Development of an electro-optical longitudinal bunch profile monitor for the future electron-positron collider FCC-ee

Zur Erlangung des akademischen Grades eines

DOKTORS DER NATURWISSENSCHAFTEN (Dr. rer. nat.)

von der KIT-Fakultät für Physik des
Karlsruher Instituts für Technologie (KIT) angenommene

DISSERTATION

von

M.Sc. Micha Reißig
aus Karlsruhe

Tag der mündlichen Prüfung: 31. Juli 2026

1. Referentin: Prof. Dr. Anke-Susanne Müller
2. Korreferent: Prof. Dr. Günter Quast

Abstract

The Future Circular Lepton Collider (FCC-ee) is a planned electro-positron collider with 91 km circumference to provide highest luminosity for precision particle physics experiments of electroweak interactions, Higgs-boson properties, Top-quark mass and more. To achieve the desired physics programme, FCC-ee foresees four different operation modes with different beam parameters. The collision conditions in every mode must be precisely determined to enable experiments at highest precision, which requires pushing the limits of high-precision particle beam diagnostics. In particular, a bunch profile monitor is required to provide high resolution bunch length measurements of every bunch to assess the impact of beamstrahlung on the collision conditions. This thesis investigates the feasibility of an in-vacuum electro-optical (EO) longitudinal bunch profile monitor and provides a concept to cope particularly with FCC-ee's wide range of bunch durations in the order of picoseconds and high bunch charges in the order of 30 nC. A simulation procedure was set up based on experiments at the EO monitor of the Karlsruhe Research Accelerator (KARA) to serve as a baseline and to identify design issues under FCC-ee's demanding beam conditions. To resolve the identified problems with long bunches and high charges, a novel prism-based design has been developed and simulated. Its functionality has been successfully demonstrated with a first prototype at the CERN Linear Electron Accelerator for Research (CLEAR).

Kurzfassung

Der FCC-ee ist ein geplanter Teilchenbeschleuniger mit 91 km Umfang für Kollision von Elektronen und Positronen bei höchster Luminosität für präzise Teilchenphysik-Experimente zur elektroschwachen Wechselwirkung, den Eigenschaften des Higgs-Bosons, der Top-Quark-Masse und weiteren Themen. Um diese Ziele zu erreichen, wird FCC-ee in vier Operationsmodi betrieben. Die Kollisionsbedingungen müssen in jeden Operationsmodus präzise bestimmt werden, um Experimente mit höchster Präzision zu ermöglichen. Daraus resultieren hohe Anforderungen an die Strahldiagnostik. Insbesondere wird ein Monitor zur Bestimmung des longitudinalen Profils jedes Teilchenpakets benötigt, um die Auswirkungen der Beamstrahlung auf die Kollisionen zu beurteilen. Diese Arbeit untersucht die Machbarkeit eines elektro-optischen (EO) Monitors zur Messung des longitudinalen Teilchenpaketprofilesund präsentiert ein Konzept, um mit der der Breite an verschiedenen Teilchenpaketdauern in der Größenordnung von Picosekunden, sowie den hohen Teilchenpaketladungen in der Größenordnung von 30 nC umzugehen. Ein Simulationsprozess wurde basierend of Experimenten mit dem EO-Monitor am Forschungsbeschleuniger KARA entwickelt, was als Design-Basis und zur Beurteilung der Probleme eines EO monitors mit den Strahlparametern von FCC-ee diente. Um die resultierenden Schwierigkeiten mit den langen Teilchenpaketen und hohen Bunchladungen zu beheben, wurde ein neues Prismen-basiertes Design entwickelt und simuliert. Dessen Funktionalität wurde mit einem ersten Prototypen am linearen Elektronenbeschleuniger CLEAR am CERN demonstriert.

Contents

1 Introduction

Particle accelerators for research applications commonly produce particle bunches with typical lengths in the range of millimeters to centimeters, which are accelerated to velocities close to the speed of light. Typically, multiple particle bunches are generated in short succession, which are collectively described as a particle beam [21]. A crucial part of particle accelerators are dedicated diagnostic instruments (beam diagnostics) to monitor the trajectory and properties of the particle beam and individual particle bunches [22]. Particle accelerators with shorter bunches in particular require ultra-fast measurement techniques to measure the length and the longitudinal profile of single particle bunches, because the short particle bunches pass the diagnostic instruments within picoseconds or less. Hence, resolving the bunch profile drives the need for beam diagnostics with a time resolution towards the femtosecond regime [23, 24]. To match the challenging requirements, non-destructive longitudinal beam diagnostics are typically experimental instruments that are tailored to the specific needs of the accelerator [25–27].

This thesis investigates the development of an in-vacuum electro-optical (EO) monitor for longitudinal bunch profile measurements of particle bunches in the Future Circular Lepton Collider (FCC-ee). In-vacuum EO monitors enable non-destructive single-shot bunch profile measurements with a sub-picosecond time resolution [26, 28]. Related measurements of the particle bunch duration (bunch length) can achieve an absolute uncertainty as low as tens of femtoseconds [29]. As these are experimental devices with a dedicated laser and read-out system, they are typically custom-made for each accelerator. Optimizations and new EO analysis techniques are developed continuously to improve its resolution [30–32]. While EO monitors are mostly installed at linear accelerators, the Karlsruhe Research Accelerator (KARA) at Karlsruhe Institute of Technology (KIT) provided the first in-vacuum EO monitor at a synchrotron, enabling single-shot turn-by-turn bunch profile measurements with a repetition rate of 2.7 MHz [27, 33–35].

The general measurement principle of an EO monitor is based on the electro-optical effect in a crystal, that changes its optical properties proportionally to the strength of an applied electrical field. When the EO crystal is exposed to the Coulomb field of a passing particle bunch, the introduced change in its optical properties modulate the polarization of a laser pulse traveling through the crystal. The resulting laser pulse has the bunch profile encoded into its polarization, which can be detected with techniques like electro-optical spectral decoding (EOSD). EOSD enables single-shot bunch profile measurements with MHz repetition rate, because a chirped laser pulse is used, where the wavelength of the laser light increases or decreases within a single laser pulse. Thus, the bunch profile is also encoded in the spectrum of the laser pulse, which can be analyzed with a spectrometer.

As a result, an EO monitor is a promising beam diagnostic instrument for Future Circular Lepton Collider (FCC-ee), which is a planned highest-luminosity electron-positron collider with 90.7 km circumference to serve as Higgs, top-quark and electroweak factory for precision experiments [36]. As studies of the FCC-ee design are progressing, boundary conditions for the bunch profile monitor development are subject to change. A starting point was provided with the conceptual design report in 2019, which discussed the physics opportunities and concept design of the lepton collider FCC-ee as an intermediate step to the Future Circular Hadron Collider (FCC-hh) within the same $\sim$91 km tunnel [37–39]. This

Table 1.1: FCC-ee beam parameters for its Z, WW, ZH and $\mathrm{t\bar{t}}$ operation modes, based on [9].

Parameter	Unit	Z	WW	ZH	$\mathrm{t\bar{t}}$
Beam energy	GeV	45.6	80	120	182.5
Beam current	mA	1292	135	26.8	5.1
Bunches / beam		11200	1856	300	60
Bunch population	10^{11}	2.14	1.45	1.15	1.55
Bunch charge	nC	34.90	21.95	27.01	25.7
Bunch length σ_z	mm	5.2	3.5	3.3	1.9
...with beamstrahlung	mm	15.2	5.3	5.6	2.3
Bunch duration $\sigma_t \approx \sigma_z/c$	ps	17.2	11.7	11.0	6.3
...with beamstrahlung	ps	50.7	17.7	18.7	7.7
inter-bunch period	ns	25			
Synchrotron power / beam	MW	50			

thesis is part of the feasibility study, which started in 2021 to asses the financial and technical feasibility of FCC-ee as a first stage, followed by FCC-hh. The feasibility study report was published in 2025 [8–10], and provides a reference for the machine parameters that are used in this thesis.

FCC-ee requires a bunch length monitor, particularly to assess the effects of beamstrahlung on the collision conditions. Beamstrahlung is a synchrotron-like radiation that is caused by the deflection of particles in the strong electromagnetic field of the opposing bunch during collisions. It affects the energy spread and the length of the particle bunches, which are crucial parameters for the precision of the physics experiment, as they impact the center-of-mass energy and the luminosity, respectively. Additionally, the bunch profile monitor is supposed to provide on-demand bunch profile measurements during commissioning of the accelerator and to monitor the top-up injection of new particles into the circulating beam.

The most promising diagnostic techniques to fulfill these challenging requirements are: a streak camera, an in-vacuum monitor based on Cherenkov diffraction radiation (ChDR), or an in-vacuum EO bunch profile monitor. A streak camera detects the longitudinal profile of visible part of synchrotron radiation spectrum, which can be used to deduct the longitudinal bunch profile. It would require a synchrotron beamline with dedicated optics to guide the visible part of the synchrotron spectrum to the camera. With the large bending radius of the FCC-ee dipole magnets of $\sim$10 km, the extraction of synchrotron light needs designated infrastructure. Discussions are ongoing, but a synchrotron beamline was not part of the accelerator design in the feasibility report.
A bunch profile monitor based on ChDR is a recent concept that is still under development. ChDR is created when the particle bunch passes next to a dielectric medium which produces radiation that propagates through the medium at the Cherenkov angle. This principle could be used to design a bunch profile monitor, which has been studied in Ref. [40].

This thesis investigates the feasibility of an EO bunch profile monitor for FCC-ee and how it needs to be designed to specifically address the unique and extreme particle beam properties and infrastructure of FCC-ee. The boundary conditions for the EO monitor development are set by the beam parameters presented in the FCC-ee feasibility study report [9]. A selection of beam parameters relevant for the development of the EO monitor is listed in Tab. 1.1. The bunch length is presented for colliding and non-colliding bunches, which highlights the bunch lengthening through beamstrahlung during collisions. The FCC-ee feasibility study report suggests four operation modes with unique particle energies to maximize the production of certain particles and particle interactions. The circulating particle bunch emits synchrotron radiation at every bending magnet, which results in an energy loss for the particles. The energy loss is compensated by accelerating the particles with radio frequency (RF) structures in a technical straight section. However, the synchrotron power scales with the particle energy to the fourth power, which sets a limit to the maximum feasible particle energy. For the development of FCC-ee a maximum synchrotron power of 50 MW per beam was set as a boundary condition for all four operation modes.

The first operation mode starts with a beam energy of 45.6 GeV, which results in a center-of-mass energy during collisions at the Z-pole for precision measurements of the Z-boson. Due to its low particle energy compared to the other modes, it allows 11 200 bunches per beam for the given limit in synchrotron radiation power and has the highest luminosity. It also provides the longest bunches of up to 15.2 mm, which poses a challenge for bunch profile measurement with an EO monitor, because it is typically optimized for sub-mm bunch lengths. The second operation mode operates at a beam energy of $\sim$80 GeV to reach the WW-threshold to enable precision measurements of the W-boson mass and its coupling. The third operation mode aims to maximize the Higgsstrahlung production ($e^+e^- \rightarrow ZH$) at $\sim$120 GeV per beam for precision measurements of the Higgs-particle. Finally, the last operation mode reaches highest energies at the Top-pair threshold at with $\sim$182.5 GeV per beam to measure the Top-quark mass and its coupling. This mode has the highest bunch charge density with the shortest bunches, but only 60 bunches in the ring to stay below the synchrotron radiation power limit.

Following the provided beam parameters and boundary conditions, the feasibility study report states, that the bunch length monitor needs to enable measurements for a wide range of bunch lengths from $\sim$2 mm to $\sim$15 mm across operation modes and provide bunch-by-bunch measurements with up to 40 MHz to accommodate the inter-bunch period of 25 ns. A bunch length uncertainty of 1 % of the total bunch length is desired to allow precise estimations of the collision conditions and the energy spread. The monitor must be non-destructive with a minimal beam impedance, to minimize the impact on the beam dynamics and the energy deposition in the crystal. The effects of heat on the EO crystal need to be investigated in particular, because a large heat load is expected at FCC-ee, due to the exposure to high intensity electromagnetic fields from the high bunch charges at high repetition rates.

The goal of this thesis is to study the feasibility of an EO monitor for FCC-ee and propose a conceptual design to cope with FCC-ee's unique and extreme particle beam properties and infrastructure requirements. Experiments and simulations with the EO monitor at Karlsruhe Research Accelerator (KARA) served as a baseline for further simulations with FCC-ee beam parameters to identify the challenges of an FCC-ee EO monitor design. The simulations revealed that KARA's EO monitor design is not suitable for the long bunches of FCC-ee's Z operation mode. Therefore, a novel crystal holder has been designed using two prisms next to the EO crystal instead of a metal mirror. The prism-based design has a reduced impedance and provides a single-pass of the probe laser through the crystal, which additionally enables bunch profile measurements at the longer bunch lengths of FCC-ee. Simulations of the EO setup under FCC-ee conditions have been used to benchmark the new design. Finally, a prototype was built and successfully tested at the in-air test stand at CERN Linear Electron Accelerator for Research (CLEAR) to demonstrate the feasibility of the new prism-based layout.

2 Basics of beam dynamics and electro-optical beam instrumentation

Particle accelerators rely on a wide range of instrumentation to monitor various aspects of the particle beam and its dynamics. This chapter introduces the basic concepts relevant for the understanding of goals and challenges to develop a longitudinal bunch diagnostic and provides an introduction to the principle of electro-optical bunch profile monitors. In particular, electro-optical sampling (EOS) and electro-optical spectral decoding (EOSD) are introduced, including a discussion of the different resolution limiting factors

2.1 Beam dynamics

Understanding particle beam dynamics is a crucial aspect for the operation of a particle accelerator and the development of relevant beam instrumentation. Understanding instabilities to avoid or deliberately control them is particularly important for circular accelerators like the Karlsruhe Research Accelerator (KARA) or the Future Circular Lepton Collider (FCC-ee), which could otherwise lead to beam loss. This section introduces the most important factors to describe the dynamics of the longitudinal bunch profile to get an understanding of what the electro-optical monitor tries to measure. This summary is mostly based on the comprehensive accelerator physics introduction in Wiedemann [21] and Wille [41], and on the treatment of longitudinal beam dynamics by Tecker [42].

2.1.1 Fundamentals of longitudinal beam dynamics in synchrotrons

For the development of a bunch profile monitor, it is essential to understand both the Coulomb field of a relativistic particle and the trajectories of particles in an accelerator. The particle trajectories eventually determine the shape of the bunch profile and the electro-optical (EO) monitor measures its Coulomb field. Since this thesis addresses the development of an EO diagnostic instrument for the Future Circular Lepton Collider (FCC-ee), the following introduction focuses on the basics of longitudinal beam dynamics of synchrotrons.

2.1.1.1 Lorentz force and its consequence for particle accelerators

The Lorentz force F_L acts on a particle with charge q and velocity $\vec{v}$ while moving through a magnetic field $\vec{B}$ and electrical field $\vec{E}$ [21]

$$F_\mathrm{L} = q\left(\vec{E} + \vec{v} \times \vec{B}\right). \tag{2.1}$$

First, it expresses that the Lorentz force from a magnetic field is perpendicular to the field and the direction of movement of the particle, which makes it unsuitable for forward acceleration. However, it enables a constant magnetic field to force a charged particle on a circular trajectory, which is already the first step toward a circular particle accelerator. The radius R of the trajectory is calculated for $\vec{v} \perp \vec{B}$ by setting the Lorentz force equal to the centripetal force F_{Cen}

$$\begin{aligned} F_{\text{L}} &= F_{\text{Cen}} \\ \Leftrightarrow qvB &= \frac{\gamma m v^2}{R} \\ \Leftrightarrow R &= \frac{\gamma m v}{qB} \end{aligned} \tag{2.2}$$

with the particles rest mass m and the Lorentz factor γ. The dependency of the bending radius R to γ and hence the kinetic energy K of the particle will become important in the next section about longitudinal beam dynamics.

Second, the Lorentz force from a magnetic field scales with the velocity of the particle, while the force of an electric field does not. Thus, for circular accelerators with particles at relativistic speeds of $v \approx c$, a magnetic field of 1 T produces the same force amplitude as an electric field with $\sim 3 \times 10^8\,\text{V/m}$.

In summary, magnets are a good choice to keep charged particles at relativistic velocities on a circular trajectory, while for the forward acceleration, it must use electric fields. As a result, a circular accelerator typically includes multiple bending magnets to keep the beam on a circular orbit and radio frequency (RF) cavities to provide an alternating electrical field to accelerate the particles.

2.1.1.2 The Frenet-Serret coordinate system and the synchronous particle

A typical electron bunch in a storage ring for a light source like Karlsruhe Research Accelerator (KARA) contains in the order of 10^{10} particles. To describe the dynamics of its individual particles, it is convenient to describe their properties via the deviation from a reference particle.

The reference orbit is typically defined by the design orbit, which describes the closed trajectory of a particle with constant kinetic energy (design energy) in the particle accelerator. The design orbit is specific to the layout of the magnets along the ring, called the magnetic lattice.

The position of individual particles in a particle bunch is defined with a Frenet-Serret coordinate system. The origin of the system is placed on a reference particle along the reference orbit, thus the positions of other particles are described in relation to a reference particle.

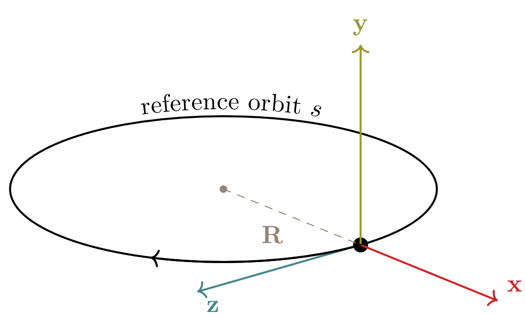

Figure 2.1: Schematic of the Frenet-Serret coordinate system, which has the origin at a reference particle moving along the reference orbit.

A schematic of the Frenet-Serret coordinate system is presented in Fig. 2.1. It defines the forward direction $\hat{z}$ longitudinal to the reference orbit s, the horizontal direction $\hat{x}$ and vertical direction $\hat{y}$. In discussions of the longitudinal profile of particle bunches, the relative arrival time t at the detector is often used instead of the longitudinal coordinate z. These two longitudinal variables are negatively proportional $z \propto -t$, which can be illustrated with the following example: If a particle A arrives earlier than a particle B ($t_A < t_B$), then particle A is positioned more toward the head of the bunch and particle B is closer to its tail ($z_A > z_B$).

A particle with kinetic energy K_0 that circulates in a storage ring with length L_0 loses energy every turn. To maintain a stable trajectory, it must gain an equal amount of energy each turn. This energy is provided by RF accelerating structures, which provide an oscillating voltage

$$V_{\text{RF}}(\psi(t)) = A \cdot \sin(\psi(t)) \tag{2.3}$$

with phase $\psi = 2\pi f_{\text{RF}} \cdot t$ and oscillation frequency f_{RF} (RF frequency). Thus, a particle with charge q needs to arrive with the same synchronous phase ψ_{S} at every turn for a consistent energy gain

$$U(\psi_{\text{S}}) = qV_{\text{RF}}(\psi_{\text{S}}), \tag{2.4}$$

which balances its energy loss. Such a particle is called the synchronous particle.

Thus, the revolution frequency of the synchronous particle is defined by the RF frequency

$$f_{\text{RF}} = h \cdot f_{\text{rev}} = h \cdot \frac{1}{T} = h \cdot \frac{v}{L_0}, \tag{2.5}$$

with the harmonic number h (integer), the revolution time T, the length L_0 of the reference orbit and the particle velocity v (with typically $v \approx c$).

2.1.1.3 Off-momentum particles and phase focusing

The momenta of particles in a particle bunch are typically distributed around the momentum of the synchronous particle, which is quantified as momentum spread σ_p.

If the momentum p of a particle deviates by Δp from the synchronous particle momentum p_0, its orbit length L deviates from the synchronous orbit length L_0 by

$$\Delta L = \alpha_c \cdot \frac{\Delta p}{p_0} \cdot L_0, \tag{2.6}$$

where α_{c} describes the momentum compaction factor. The value of α_{c} depends on the integrated dispersion function D along the orbit s

$$\alpha_{\text{c}} = \frac{1}{L_0} \oint \frac{D(s)}{R(s)}\, ds \tag{2.7}$$

with the bending radius $R(s)$ [21].

The integrated dispersion along the orbit is positive, when only the bending (dipole) magnets in a storage ring are considered. For a constant magnetic field perpendicular to the particle velocity $\vec{B} \perp \vec{v}$, the bending radius follows $R \propto \gamma$ (see Eq. 2.2) and therefore, the orbit length ΔL increases for particles with $\Delta p > 0$ and decreases for those with $\Delta p < 0$. However, quadrupole magnets are typically used to focus the particle beam and to additionally change the dispersion. They can be used to reach a negative dispersion and even achieve a negative momentum compaction factor [43]. To simplify the following explanations, the typical case of a positive momentum compaction factor is assumed.

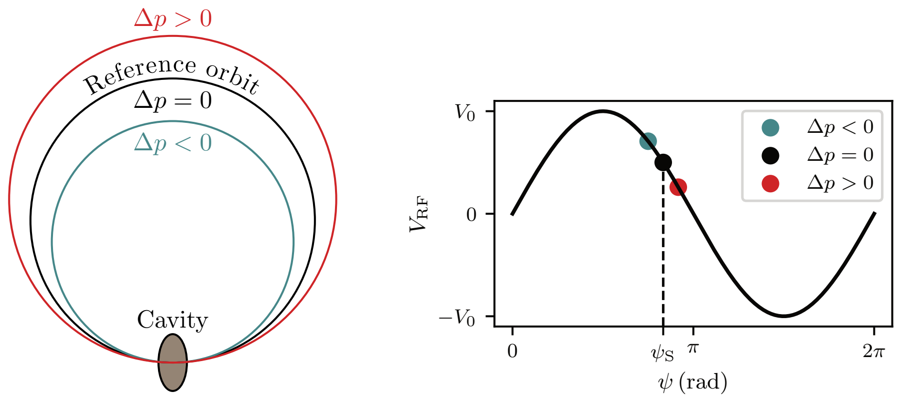

(a) Orbit length

(b) RF voltage in the cavity

Figure 2.2: Illustration of the phase focusing effect for particles above transition energy. For illustration purposes, all three example particles start with the same initial phase ψ_S at the RF but with different particle momenta. Compared to the synchronous particle with $\Delta p = 0$, particles with $\Delta p > 0$ have a larger orbit and after one turn, they arrive later at the cavity with phase $\psi > \psi_S$, which leads to a smaller energy gain through the RF voltage. $\Delta p < 0$ results in a smaller orbit and early arrival $\psi < \psi_S$ after one turn with larger energy gain.

The deviation ΔT of the revolution time T_0 from the reference particle is determined by the velocity v and the orbit length deviation ΔL of a particle via $\Delta T = \Delta L / v$. As both, the orbit length and the particle velocity can vary, the relative change follows from the total differential and yields

$$\frac{\mathrm{d}T}{T_0} = \frac{\mathrm{d}L}{L_0} - \frac{\mathrm{d}v}{v} = \alpha_\mathrm{c} \frac{\mathrm{d}p}{p_0} - \frac{\mathrm{d}v}{v} = \left(\alpha_\mathrm{c} - \frac{1}{\gamma^2} \right) \frac{\mathrm{d}p}{p_0}, \tag{2.8}$$

which is described in more detail in [42, p. 7]. The scaling factor between the relative change of the revolution time $\frac{\mathrm{d}T}{T_0}$ and the relative momentum change $\frac{\mathrm{d}p}{p_0}$ is called the phase slip factor η with

$$\eta = \alpha_\mathrm{c} - \frac{1}{\gamma^2}. \tag{2.9}$$

The phase slip factor shows that the revolution time T of a particle reaches a transition energy at $\gamma_\mathrm{t} = \sqrt{\alpha_\mathrm{c}^{-1}}$, where the revolution time does not change for small momentum deviations. Below transition energy ($\gamma < \gamma_\mathrm{t}$), the increase in orbit length following Eq. 2.6 is outweighed by the increase in particle velocity, resulting in a lower revolution time. Above transition energy for $\gamma > \gamma_\mathrm{t}$, relativistic effects constrain the velocity increase, making the orbit lengthening the dominating factor, thus increasing the revolution time.

Considering the relation between arrival time change and momentum change, the time dependent voltage of the RF structure can be used to apply higher voltages for particles with lower momentum and vice versa, which is called the phase focusing effect. Figure 2.2 illustrates the phase focusing effect for a synchronous particle above transition energy, where the synchronous phase is located on a downward slope of the oscillating electrical field. For two particles with the same initial phase as the synchronous particle, after one turn, the particle with higher energy arrives at a later phase, resulting in less energy gain compared to the synchronous particle. A particle with lower energy arrives earlier and has an increased energy gain. Thus, the phase focusing leads to dynamic changes of the longitudinal particle position and its energy, which is best described in the longitudinal phase space.

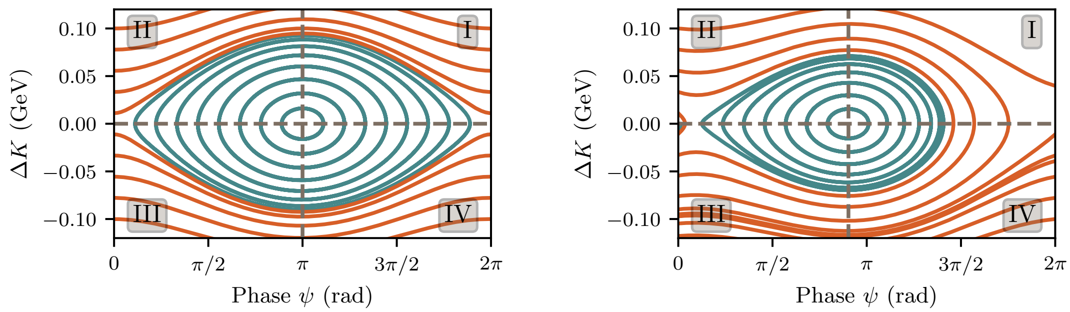

(a) $\psi_s = \pi$ (stationary case) **(b)** $\psi_s \approx 0.9\pi$

Figure 2.3: Schematic view of the trajectory of example particles in the longitudinal phase space [42]. Stable trajectories are drawn as solid blue lines and unstable trajectories as orange lines. The border between both cases is called separatrix, and the stable region RF bucket. In this case, the stable particles rotate clockwise in phase-space, and the quadrants I-IV are highlighted to serve as references in the text. In the ideal stationary case (a), the synchronous particle has a constant energy with RF phase $\psi_S = \pi$. The synchronous phase changes, when the particle loses energy, e.g., by emitting synchrotron radiation, which leads to an asymmetric shape of the separatrix (b).

2.1.1.4 Longitudinal phase space

The longitudinal particle dynamics can be visualized in phase space diagrams, which in general show a longitudinal coordinate on the x-axis and the energy on the y-axis. For continuity with the example from Fig. 2.2, the phase space in this example is spanned using the phase ψ of the particle arriving at the accelerating structure on the x-axis and the kinetic energy deviation from the synchronous particle $\Delta K = K - K_S$ on the y-axis. An example is presented in Fig. 2.3 for the simplified case of no energy loss (a) and the case for a constant energy loss per turn ΔW_{const} (b). These calculation parameters of these plots are roughly based on KARA with an electron energy of 2.5 GeV, but with an arbitrary energy loss per turn in Fig. 2.3b for illustration purposes.

Within a certain range of particle phase and energy, the particle trajectory is a stable closed loop. The border between the stable and unstable region is called separatrix and the stable region is called RF bucket. The energy loss causes a shift of the phase of the synchronous particle from $\psi_S = \pi$ to a slightly smaller phase to achieve a larger RF voltage (see Fig. 2.2b), which compensates the energy loss. The result is an asymmetric separatrix, because the synchronous phase on the RF voltage moved away from the symmetry point.

Multiple particles (e.g., in the order of 10^{10} electrons at KARA and 10^{11} electrons or positrons at FCC-ee) within the RF bucket form a particle bunch. In context to the Frenet-Serret coordinate system (see Chapter 2.1.1.2), the phase axis is inverse to the longitudinal coordinate z, because the particle arrival time at the RF increases with the phase angle. Thus, the tail of a particle bunch is positioned in phase space toward larger phase angles and the head of the bunch toward smaller phase angles.

$$U_S = q \cdot V_{\text{RF}}(\psi_S) = q \cdot V_0 \cdot \sin(\psi_S) = \Delta W_{\text{const}} \tag{2.10}$$

with the additional constraint to be on a downward slope similar to the example in Fig. 2.2 in order to enable phase focusing.

In the phase space diagram, the synchronous particle is a stationary point at $(\psi, \Delta K) = (\psi_\mathrm{S}, 0)$. In order to understand the principle of particle motion in phase space, it is useful to follow a single off-momentum particle, which starts at the same phase, but a slightly higher energy $(\psi_\mathrm{S}, \Delta K_1)$. Following Eq. 2.8, after one revolution this particle will arrive in quadrant I at a slightly later time and therefore slightly later phase $\psi_1 > \psi_\mathrm{S}$ at the accelerating voltage $V_\mathrm{RF}(\psi_1)$. Consequently, the phase focusing causes a smaller energy gain $U(\psi_1) < W_\mathrm{const}$ and an effective energy loss over the next turn. As long as the particle is still in quadrant I, it gains less kinetic energy than the previous turn, but still maintains $\Delta K > 0$ and therefore the phase increases. This continues until the particle energy drops below the energy of the synchronous particle, where the phase starts to decrease again (quadrant IV). Once the phase is smaller than the synchronous phase, the particle starts to gain energy again (quadrant III). When the energy increased above zero ($\Delta K > 0$), the phase decreases again in quadrant II. Continuing this scheme every turn results in a closed trajectory in phase space around the synchronous particle.

This example is only true for small amplitudes, such that the restoring force of the RF field V_RF is approximately linear. However, particles with a large energy-phase deviation to the synchronous particle follow an open trajectory and drift away over time. The border between the stable and unstable region is called separatrix and is highlighted as a bold black line in Fig. 2.3. The inside of the separatrix is called a RF bucket and can hold multiple particles to form a stable particle bunch.

2.1.1.5 Synchrotron motion

The oscillation of a single particle in longitudinal phase space is called the synchrotron motion, with its revolution frequency called synchrotron frequency. If the centroid of a particle bunch is displaced from the synchronous particle, it also follows a closed-trajectory motion with the synchrotron frequency. This synchrotron oscillation can be measured with longitudinal diagnostics like an EO monitor, which makes it an important aspect for this thesis.

The synchrotron motion can be described by a differential equation of a damped harmonic oscillator [41]

$$\Delta\ddot{K} + 2a_\mathrm{s}\Delta\dot{K} + \Omega^2\Delta K = 0 \tag{2.11}$$

which includes an additional damping factor

$$a_\mathrm{s} = \frac{1}{2T_0}\frac{\mathrm{d}W}{\mathrm{d}K} \tag{2.12}$$

and the synchrotron frequency

$$\Omega = 2\pi f_\mathrm{rev}\sqrt{-\frac{qV_0 h\cos(\psi_\mathrm{S})}{2\pi\beta^2 K}\eta}. \tag{2.13}$$

So far, the losses per turn W_const were assumed constant. However, the losses through synchrotron radiation depend on the particle energy (see next section), which adds the damping factor a_s to the synchrotron motion. The damping rate is generally smaller than the synchrotron frequency $a_\mathrm{s} \ll \Omega$, which leads to the solution of a damped harmonic oscillator with

$$\Delta K(t) = \Delta K_0 e^{-a_\mathrm{s}t}e^{i\Omega t} \tag{2.14}$$

to describe the synchrotron motion in phase space.

The synchrotron frequency Ω is typically smaller than the revolution frequency, which enables to calculate Ω using turn-by-turn measurements of the bunch arrival time. At KARA for example, the EO measurements in Ref. [35] determined a synchrotron frequency in the order of 10 kHz at a revolution frequency of $f_{\mathrm{rev}}^{\mathrm{KARA}} \approx 2.71\,\mathrm{MHz}$ for the specific machine settings during the experiment.

2.1.1.6 Synchrotron radiation

If a charged particle is accelerated, it emits electromagnetic waves. This is described in general by the theory of classical electrodynamics, for example in Jackson [44]. In particle accelerators, this mainly occurs as synchrotron radiation, when the particles are accelerated perpendicular to their movement direction by magnetic fields. In circular accelerators, the synchrotron power is given by

$$P_{\mathrm{SR}} = \frac{q^2 c}{6\pi\epsilon_0}\frac{\gamma^4}{R^2} = \frac{q^2 c}{6\pi\epsilon_0}\left(\frac{K}{m_0 c^2}+1\right)^4 \frac{1}{R^2} \tag{2.15}$$

with the rest mass m_0, kinetic energy K and the bending radius R [41]. Due to the scaling with $1/m_0^4$, the synchrotron power is multiple orders of magnitude larger for lighter particles like electrons ($m_{\mathrm{e}}c^2 \approx 0.511\,\mathrm{MeV}$) compared to heavier particles like protons ($m_{\mathrm{p}}c^2 \approx 938.19\,\mathrm{MeV}$). Consequently, electrons are the particle of choice for synchrotron light sources, which aim to produce high intensity synchrotron radiation. However, the additional scaling with the fourth power of the kinetic energy makes energy losses through synchrotron radiation a limiting factor for accelerators aiming at highest particle energy. As discussed in Chapter 1, the FCC-ee has a set limit of $P_{\mathrm{SR}} < 50\,\mathrm{MW}$ per beam, which restricts the maximum beam current for a given particle energy [9].

The energy loss per turn can be calculated by multiplication of the synchrotron power by the time T_{b}, which the particle takes to pass the bending sections

$$\Delta W_{\mathrm{SR}} = P_{\mathrm{SR}} \cdot T_{\mathrm{b}} \tag{2.16}$$

For electrons with $\gamma >> 1$, the energy loss can be calculated using the simplified formula

$$\Delta W_{\mathrm{SR}}^{\mathrm{e}}[\mathrm{keV}] = 88.5\frac{K^4[\mathrm{GeV}^4]}{R[\mathrm{m}]}. \tag{2.17}$$

As an example, the typical measurement scenario at KARA with a particle energy of 1.3 GeV and a bending radius of $R = 5.559\,\mathrm{m}$ results in a loss per turn of $\Delta W_{\mathrm{SR}}^{\mathrm{KARA}} = 45.5\,\mathrm{keV}$.

Since the losses are energy dependent, they are the main contribution to the damping factor a_{s} of the synchrotron motion (see Eqs. (2.11, 2.12)).

2.1.1.7 Bunch length and energy spread

Energy spread and bunch length are key parameters that characterize the size of a bunch in longitudinal phase space. Understanding these parameters requires transitioning from the incoherent motion of individual particles to the statistical description (coherent motion) of a particle bunch in phase space, typically containing billions of particles.

Consequently, a large amount of particles with individual phase space trajectories can form a stable particle bunch with a certain energy distribution and bunch length. If not stated otherwise, the bunch length in this thesis is quantified as the root mean square (RMS) bunch length

$$\sigma_z = \sqrt{\frac{1}{N}\sum_{i=1}^{N}(z_i - \overline{z})^2} = \sqrt{\frac{1}{\sum_j \mathcal{I}(z_j)} \sum_i (z_j - \overline{z})^2 \cdot \mathcal{I}(z_j)}, \tag{2.18}$$

with the Number of particles N with individual position z_i and mean position $\overline{z}$. If appropriate, a Gaussian fit is often applied if the data is noisy. The resulting RMS of the Gaussian function is equal to its standard deviation and typically provides more consistent results. For short particle bunches or laser pulses, it is common to define its longitudinal variable via the arrival time t (see Chapter 2.1.1.2), which leads to a bunch duration σ_t as an equivalent metric to the bunch length σ_z. As the particle bunches are typically at relativistic speeds, the quantities are approximately linearly related via $\sigma_t \approx \sigma_z/c$ and sometimes used synonymously.

Longitudinal profile measurements of an EO monitor typically result in a discrete intensity profile, where the RMS bunch length can be calculated with the intensities $\mathcal{I}(z_j)$ as weights for the sum over each measurement point z_j.

The energy spread is defined similarly, by

$$\sigma_{\mathcal{E}} = \sqrt{\frac{1}{N}\sum_{i=1}^{N}(\mathcal{E}_i - \overline{\mathcal{E}})^2} \tag{2.19}$$

with the individual particle energy $\mathcal{E}_i$ and the mean energy $\overline{\mathcal{E}}$.

The damping rate through synchrotron radiation leads to a decreasing bunch length, until it is in equilibrium with the quantum excitation rate. The quantum excitation is a stochastic effect of quantum fluctuations caused by the emission of photons into synchrotron radiation [45]. The bunch length in this equilibrium state is called the natural bunch length (or sometimes zero current bunch length) and it is defined by [21]

$$\sigma_z = \frac{c|\eta|}{\Omega}\frac{\sigma_{\mathcal{E}}}{\mathcal{E}_\mathrm{S}} = \frac{c}{\sqrt{2\pi} f_\mathrm{rev}}\sqrt{\frac{\eta \mathcal{E}_\mathrm{S}}{q V_0 h \cos\psi_\mathrm{S}}}\frac{\sigma_{\mathcal{E}}}{\mathcal{E}_\mathrm{S}}. \tag{2.20}$$

The natural bunch length is an important parameter, because it sets the baseline for the minimum achievable bunch length, and it can be adjusted during operation. The most important variables are the inverse dependency on the RF voltage V_0 and on the phase slip factor η, which can be adjusted via the strength of quadrupole magnets.

The actual bunch length in synchrotrons will differ from the natural bunch length, since additional effects like space charge, impedance from the vacuum chamber and other structures as well as other collective effects will lead to longer bunches. The following sections will mainly concentrate on the impact of geometric impedances, as it needs to be considered for the design of an in-vacuum EO monitor. Many other effects are described in Chao [45].

2.1.2 Impedance and wake function

Impedance and wake function are two complementary representations of the same physical phenomenon: the impedance $\mathcal{Z}$ is a description in frequency domain, while the wake function $\mathcal{W}$ is a description in time domain. The various facets of wake function and impedance lie beyond the scope of this thesis and a comprehensive treatment can be found in sources such as in Ng [46], Wiedemann [21] and Li [47]. This section is intended to outline the principles necessary for understanding the influence on longitudinal beam dynamics and to recognize characteristic features that will appear in the measurement data in later chapters.

The wake function $\mathcal{W}$ characterizes the electromagnetic impulse response of a given structure as a charge normalized voltage ($[\mathcal{W}] = 1\,\mathrm{V/C}$) and is therefore a defining parameter for the effect of the vacuum chamber on the bunch profile and beam dynamics. In general, the wake function is proportional to the integrated Lorentz force experienced by a probe particle following a unit source particle through a given structure [47]. The electromagnetic fields that enable this force can be produced by a variety of different sources, typically described as collective effects.

Although the wake function is an important property of a given structure in an accelerator, it is nearly impossible to calculate it analytically for a real particle accelerator due to the complex geometry and material properties of the surrounding material. Consequentially, electromagnetic solvers such as the wakefield solver of CST Studio Suite [48] can be used to numerically compute the wake field $E_{\mathcal{W}}$ ($[E_{\mathcal{W}}] = 1\,\mathrm{V/m}$) of a particle bunch by solving Maxwell's equations for a particle bunch traveling through a given structure. By integrating the wake field over time or longitudinal position, the wake potential $V_{\mathcal{W}}$ ($[V_{\mathcal{W}}] = 1\,\mathrm{V}$) can be obtained. To retrieve the wake function, one must perform a deconvolution of the bunch profile with the wake potential. Since deconvolution in general is an ill-posed problem, it is usually addressed by transforming the signals from time domain to frequency domain. There, the deconvolution simplifies to a division of the wake potential's spectrum by the bunch profile's spectrum, yielding the structure's impedance $\mathcal{Z}$.

The impedance is a complex quantity which is often referenced to characterize the structures of an accelerator, since it can be used to directly deduct some key impacts on the particle beam dynamics. While the real part $\Re(\mathcal{Z})$ of the impedance describes the energy loss through heat, the imaginary part $\Im(\mathcal{Z})$ describes the energy storage in the wake field. This can generally have a shortening effect on the bunch for a capacitive impedance $\Im(\mathcal{Z}) < 0$ or a lengthening effect for an inductive impedance $\Im(\mathcal{Z}) > 0$. In general, the impedance for wavelengths $\lambda = c/f \gg \sigma_z$, results in a coherent effect across the bunch. It can be described as a distortion of the RF voltage waveform (potential well distortion), which can lead to a change of the synchronous phase ψ_S and the synchrotron frequency Ω [21]. Consequentially, the bunch length is also affected with $\sigma_z \propto 1/\Omega$, following Eq. 2.18. On the other hand, impedance for $\lambda \ll \sigma_z$ results in modulation within the bunch profile.

An example is the impedance of the coherent synchrotron radiation (CSR) [49], which can cause the micro-bunching instability, leading to dynamic formation of sub-structures in the longitudinal phase space [50]. The CSR impedance is the result of a self-interaction of a single bunch with its emitted synchrotron radiation. Since the synchrotron radiation is emitted within a cone tangentially to the bunch's circular trajectory, part of the synchrotron light trajectory is on the inside of the bunch's orbit. Thus, the emitted light from the tail of the bunch can catch up and hit the head of the bunch, when it crosses the bunch's orbit again after a short travel time. This effect on the bunch can be approximated with the free space CSR impedance [51]

$$Z_{\text{CSR, FS}}(n) \approx \frac{Z_0 \Gamma\left(\frac{2}{3}\right)}{3^{1/3}} \left(\frac{\sqrt{3}}{2} + \frac{i}{2}\right) n^{1/3}, \tag{2.21}$$

with $n = \frac{f}{f_{\text{rev}}}$, the vacuum impedance $Z_0 = \sqrt{\frac{\mu_0}{\varepsilon_0}} \approx 377\,\Omega$, and the mathematical gamma function Γ [52]. To include the dimensions of the vacuum chamber, an approximation with a parallel plate impedance model can be made, which is described in Ref. [51], and for KARA in particular, a description can be found in Ref. [53]. The CSR impedance can result in the micro-bunching effect, characterized by strong bursts of CSR that limits the beam current for stable operation at electron storage rings, which is studied extensively at KARA [54–58].
Geometric impedances from devices or structures within the vacuum chamber are typically estimated with numerical simulations, which will be presented in later chapters. As the impedance interacts with the particle bunches, it needs to be reduced as much as possible for FCC-ee to optimize the stability of the beam collision conditions [9, 59]. Thus, the impedance is an important parameter for the EO monitor design.

2.1.3 Electric field of relativistic particles

Beam diagnostics like electro-optical bunch profile monitors, beam position monitor (BPM)s and many more rely on direct or indirect measurements of the electrical field, which changes its shape at relativistic velocities. To get an idea of the longitudinal Lorentz contraction of the Coulomb field, the following section provides an example based on a single point-like charge.

The electric field lines of a charged particle at rest are pointing either radially away from the particle if it is positively charged, or toward it in case of a negative charge. The electric field $\vec{E}'(r')$ of a charge q_1 at rest is described by the Coulomb force $\vec{F}'(q_2, \vec{r}')$ on a probe charge q_2 with distance $r' = \sqrt{x'^2 + y'^2 + z'^2}$ divided by its charge

$$\vec{E}' = \frac{\vec{F}(q_2, \vec{r}')}{q_2} = \frac{q_1}{4\pi\varepsilon_0} \frac{\hat{r}'}{r'^2}, \tag{2.22}$$

where $\hat{r}'$ is the unit vector pointing from q_1 to q_2 and ε_0 the vacuum permittivity.

The Lorentz transformation can be used to transform the coordinates (t', x', y', z') from the rest frame of the charge to (t, x, y, z) in a laboratory frame, in which the charge is moving in z direction with velocity v. The relation between the coordinates of both frames is described by

$$\begin{aligned} t' &= \gamma(t - \frac{vz}{c^2}), \\ x' &= x, \\ y' &= y, \\ z' &= \gamma(z - vt) \end{aligned} \tag{2.23}$$

with the Lorentz factor $\gamma = 1/\sqrt{1-(v/c)^2}$.

Additionally, the transformation of the electrical field follows

$$\begin{aligned} E_x &= \gamma\left(E'_x + \frac{v}{c}B'_y\right),\\ E_y &= \gamma\left(E'_y - \frac{v}{c}B'_x\right),\\ E_z &= E'_z. \end{aligned} \tag{2.24}$$

with magnetic field $B'_x = 0$ and $B'_y = 0$ in the rest frame of the point charge [44, p. 644 ff].

In order to calculate the electric field in coordinates of the laboratory frame, the combination of Eq. 2.24 and Eq. 2.23 results in

$$\begin{aligned} E_x &= \frac{q_1}{4\pi\varepsilon_0}\frac{\gamma x}{\left(x^2+y^2+\gamma^2(z-vt)^2\right)^{3/2}},\\ E_y &= \frac{q_1}{4\pi\varepsilon_0}\frac{\gamma y}{\left(x^2+y^2+\gamma^2(z-vt)^2\right)^{3/2}},\\ E_z &= \frac{q_1}{4\pi\varepsilon_0}\frac{\gamma(z-vt)}{\left(x^2+y^2+\gamma^2(z-vt)^2\right)^{3/2}}. \end{aligned} \tag{2.25}$$

In the x-y plane at $z = 0$, the field strength scales with γ, while the width of the field scales approximately with $1/\gamma^2$ for $(\gamma x)^2 \gg x^2, y^2$. As a result, a moving particle is compressed in the direction of movement to a pancake-like shape.

In order to visualize this effect, examples are presented in Fig. 2.4, where the absolute strength of the electrical field and its components are plotted in the x-z-plane for different particle velocities. The field is calculated based on Eq. 2.25 for an electron with $q = -e$ at $t = 0$. The y-range of $[-5\,\mathrm{cm}, 5\,\mathrm{cm}]$ of the plot is chosen to be in the typical order of magnitude of the vacuum chamber of particle accelerators. To highlight the shape of the electric field, it is mapped to a symlog-scaled discrete color map, which shows regions of similar field strength in the same color. The figure contains four columns, each for a different particle velocity. Instead of the particle velocity, usually the particle energy in units of eV or the Lorentz factor is stated in context of particle accelerators, since the velocity is typically close to the speed of light. The four columns in the plot correspond to $K = \{0\,\mathrm{eV},\ 0.5\,\mathrm{MeV},\ 5\,\mathrm{MeV},\ 50\,\mathrm{MeV}\}$ ($\gamma \approx \{1,\ 1.98,\ 10.78, 98.85\}$).

With increasing energy, the total electrical field E goes from spherically symmetric in the first column to approximately a thin vertical line at the last column. This generally applies to the individual field components E_z, E_y, too, but it is important to note that E_z includes a zero crossing at $x = 0$.

The detailed shape becomes more obvious when looking at the longitudinal profile of the electrical field, which is presented in Fig. 2.5. It shows the strength of the electrical field E (solid blue line) and its components E_x (dashed orange), E_y (dotted green) along a line at $y = 1\,\mathrm{cm}$ parallel to the x-axis. The plots clearly show the longitudinal compression of the fields and the increase in peak amplitude with increasing particle energy.

This is an important effect for measurements of the longitudinal bunch profile, because the field of an electron bunch is a superposition of the field of its individual electrons. If a detector is placed for

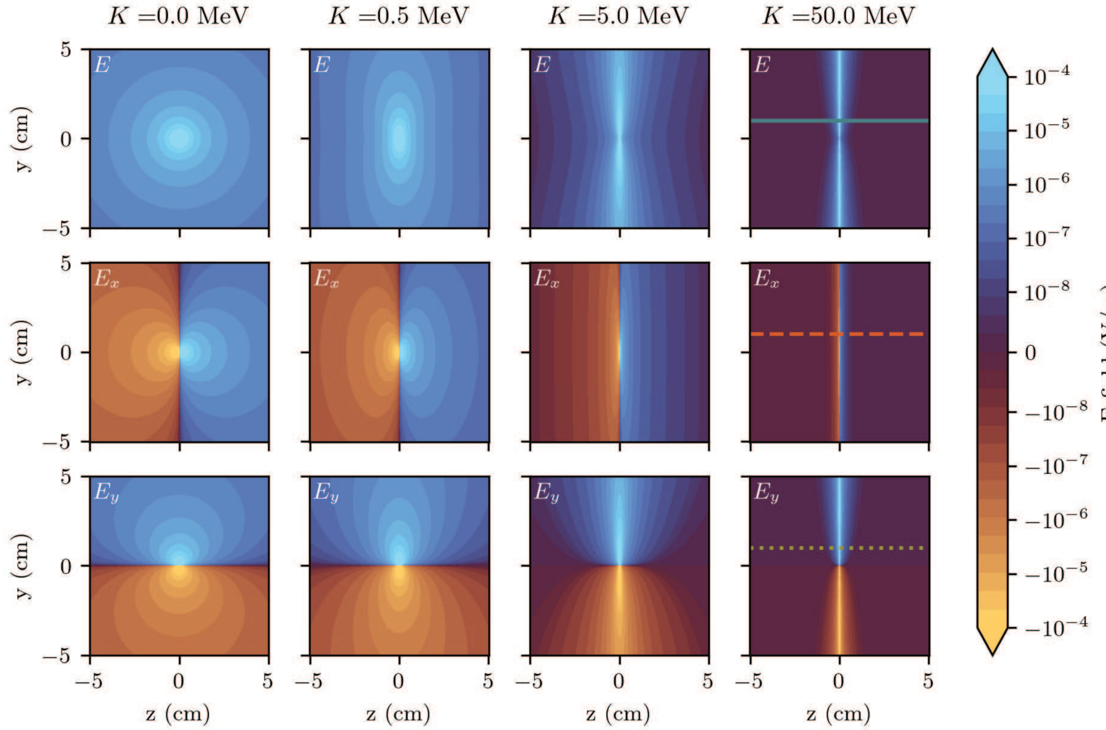

Figure 2.4: Plots of the Lorentz contraction of the Coulomb field at different kinetic energies of an electron. The higher the kinetic energy K, the stronger the field is compressed. The three rows show the strength of the total Coulomb field E_{total} and its components E_x and E_y. The columns show the electron at increasing kinetic energy K, with the electron moving in positive z direction. The field strength is mapped to a discrete symlog color map to highlight the shape of the field. The horizontal lines in the last column indicate the axis position of the plots in Fig. 2.5.

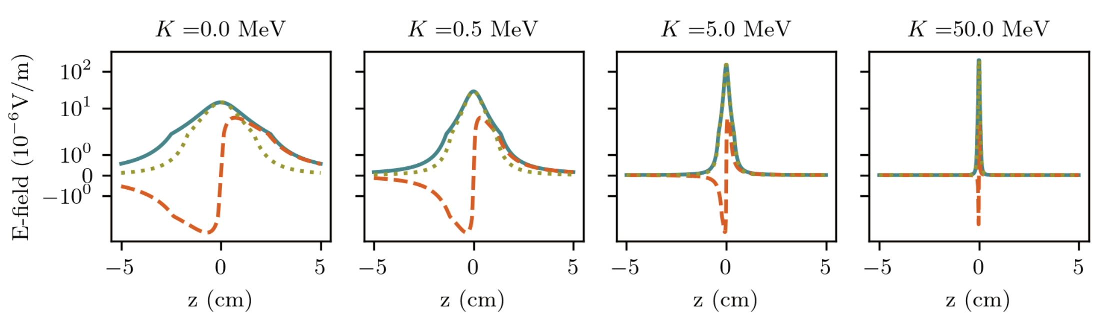

Figure 2.5: Electrical field strength and its components at a distance $y = 1\,\mathrm{cm}$ to an electron that moves along the z axis . The kinetic energy K is increasing for every plot from left to right, which also demonstrates the longitudinal Lorentz compression of the field. The solid blue line represents the total electrical field E, while E_x is displayed as a dashed orange line and E_y as dotted green line. For better readability, the y-axis has a symlog scaling.

example at $(0\,\mathrm{cm}, 1\,\mathrm{cm})$, the measured electrical field directly corresponds to the longitudinal charge density of the bunch only if the field of the single electrons is approximately a vertical line. Otherwise, the measured electrical field will be broader than the actual longitudinal charge density. As a result, for bunch profile monitors that rely on measurements of the electrical field, a low particle energy distorts the measurement and the width of the electric field needs to be considered. However, at FCC-ee, the electron and positron energies are above 45 GeV ($\gamma > 89\,000$) and the EO crystal of the EO bunch profile monitor needs to be positioned at a distance in the order of centimeters to the beam center. Thus, the effect of the vertical opening angle on the EO monitor resolution is negligible.

2.2 Electro-optical techniques

In general, electro-optical (EO) methods convert an electrical signal into an optical signal. Typically, crystals are used that change their optical properties when they are exposed to an electric field, which can be probed with a laser. The key advantage of this conversion lies in the high bandwidth and low-loss at high frequencies of optical signal transport and analysis compared to its electrical counterpart. This is particularly beneficial in the context of particle accelerator diagnostics, where often a sub-picosecond resolution is desired to resolve the longitudinal bunch profile and frequencies toward the THz regime.

While EO methods have been popular in THz spectroscopy for a long time [60], their first test as a longitudinal bunch profile diagnostic was done in 2002 [28] at the FELIX free electron laser facility in the Netherlands. In 2012, the first in-vacuum EO bunch profile monitor was installed in a storage ring at the Karlsruhe Research Accelerator (KARA) [27, 33]. In the storage ring, the EO monitor enabled to reconstruct the dynamics of the longitudinal phase space using tomography methods [13, 16, 61].

Although many improvements have been made over the years, for example enabling turn-by-turn single-shot measurements [35], the EO bunch profile monitor is still no off-the-shelf product. This is mainly due to its complexity of the laser system and its synchronization, as well as the need to adapt the system to the specific beam parameters. Parameters like bunch length and bunch charge require adjustments of the crystal thickness, its distance to the particle beam and the chirp and length of the laser pulse. The crystal material is chosen based on the laser system, the required sensitivity and desired resolution. When integrating the EO monitor in the accelerator, its design of the crystal and crystal holder needs to match the impedance requirements. Additionally, EO monitors like at KARA, free electron laser in Hamburg (FLASH), or European XFEL (European XFEL) are typically designed for short bunches, hence, a redesign is necessary to enable measurements with the longer bunches at FCC-ee.

The following sections provide an overview of how electro-optical detection works, and discusses the benefits and drawbacks of different EO techniques.

2.2.1 The electro-optical effect

In this section, the fundamental principles of the EO effect are specifically summarized to support the use case of the longitudinal bunch profile monitor. A comprehensive discussion, including other applications of the EO effect, can be found in Saleh and Teich [62], which served as the primary reference for this subsection in combination with a more specific description of EO beam diagnostics by Steffen [26].

In certain transparent materials, typically semi-conductors, the refractive index n changes if an electrical field E is applied. This is called the electro-optical effect. The change in refractive index is typically very small, but it is important to note, that even a small change in refractive index can have a large impact on the phase of light traveling through the medium. For example, for a small refractive index change of $\Delta n = \lambda/d\lambda = 10^{-4}$, a laser with $\lambda = 1\,\mu\text{m}$ wavelength will have a phase shift of $\Delta\phi = 2\pi$ over a distance of $d = 1\,\text{cm}$ in the medium[1]. Since the changes of $n(E)$ are small, it can be approximated with a Taylor expansion around $E = 0$

$$n(E) = n_0 + n_1 E + \frac{1}{2} n_2 E^2 + ... \tag{2.26}$$

However, crystals with a cubic structure like zinc telluride (ZnTe) and gallium phosphide (GaP), which are used for the EO measurements in this thesis, become anisotropic through the EO effect. Hence, the refractive index differs for different orientations of incident light and its polarization. While a single refractive index is sufficient for isotropic materials, anisotropic material requires a three-dimensional index ellipsoid

$$\vec{x}^{\mathrm{T}} S \vec{x} = \sum_{ij} S_{ij} x_i x_j = 1, \quad i, j = 1, 2, 3, \tag{2.27}$$

where S is called the impermeability tensor [62, p. 989] and $\vec{x} = \begin{bmatrix} x_1 & x_2 & x_3 \end{bmatrix}^{\top}$ are the coordinates along the principal axes, which describe the coordinates along the semi-axes of the index ellipsoid. The impermeability tensor is generally symmetric in $S_{ij} = S_{ji}$ and since the coordinate components x_i are aligned with the optical axes, it results in a diagonal matrix with $S_{ij} = 1/n_i^2$, for $i = j$. Therefore, the index ellipsoid simplifies to

$$\left(\frac{x_1}{n_1}\right)^2 + \left(\frac{x_2}{n_2}\right)^2 + \left(\frac{x_3}{n_3}\right)^2 = 1. \tag{2.28}$$

Thus, the length of the coordinates x_1, x_2, x_3 corresponds to the principal refractive indices n_1, n_2, n_3.

The index ellipsoid can be used to calculate the phase shift experienced by an incident laser light with wave vector $\vec{k}$. The cross-section of the index ellipsoid in the normal plane of $\vec{k}$ defines the index ellipse of the traveling wave, which is illustrated in Fig. 2.6. The major and minor axes of the ellipse define a slow and fast optical axes $n_\mathrm{s}, n_\mathrm{f}$ that affect laser light. The slow optical axis describes the direction with highest refractive index of the ellipse, hence the parallel polarization component of laser light propagates slower, while the fast optical axis describes the direction with lowest refractive index, where the corresponding polarization component propagates faster. A material with a fast and slow optical axis is called birefringent.

The polarization of a linearly polarized laser can be deconstructed into one component on the fast and one component on the slow optical axis. The difference between these two axes defines the phase retardation between the two polarization components of the laser light

$$\Gamma = \frac{2\pi}{\lambda} d(n_\mathrm{s} - n_\mathrm{f}) \tag{2.29}$$

along the crystal with thickness d. This phase retardation can be measured by analyzing the polarization state of a probe laser and it is the general mechanism on which the EO detection techniques are based

[1] with phase $\phi = 2\pi\frac{n \cdot d}{\lambda}$ results $\Delta\phi = 2\pi\frac{\Delta n \cdot d}{\lambda}$. Thus for $\Delta\phi = 2\pi$: $\Delta n = \lambda/d$

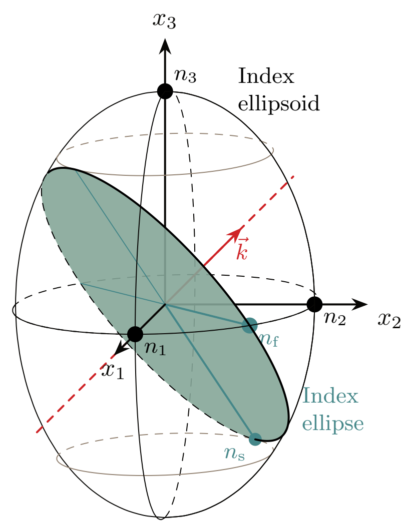

Figure 2.6: Illustration how the index ellipsoid can be used to determine the fast and slow optical axes n_f, n_s of an incident wave traveling in direction $\vec{k}$. Based on Ref. [62].

on. The following paragraphs provide an overview on the relation between the electrical field strength and the index ellipsoid, which finally defines the phase retardation.

For typical EO materials like GaP and ZnTe, the index ellipsoid becomes anisotropic if an electric field $\vec{E}$ is applied, which means that the impermeability tensor S is modified. Following Eq. 2.26, the EO effect can be described with a Taylor expansion

$$S_{ij}(\vec{E}) = S_{ij} + \sum_k \mathtt{r}_{ijk} E_k + \sum_{kl} \mathtt{s}_{ijkl} E_k E_l + \ldots, \qquad i, j, k, l = 1, 2, 3 \tag{2.30}$$

with the Pockels coefficient $\mathtt{r}_{ijk}$ and the Kerr coefficient $\mathtt{s}_{ijkl}$ [62, p. 990]. As indicated by the coefficient names, the linear effect is called Pockels effect, while the quadratic effect is called Kerr effect.

Since this thesis focuses on the application of an EO bunch profile monitor using GaP or ZnTe, some simplifications can be made based on the crystal properties and the symmetries of its cubic crystal structure. Firstly, the EO coefficients of these materials are in the order of [26, p. 33]

$$\begin{aligned} \mathtt{r}_{ijk} &\approx 1 \times 10^{-12}\,\mathrm{m/V}, \\ \mathtt{s}_{ijkl} &\approx 1 \times 10^{-21}\,\mathrm{m^2/V^2}. \end{aligned} \tag{2.31}$$

In this use case, the typical maximum electric field strength during bunch profile measurements is in the order of $\vec{E} \approx 1 \times 10^6\,\mathrm{V}$, resulting in $\sum_k \mathtt{r}_{ijk} E_k \gg \sum_{kl} \mathtt{s}_{ijkl} E_k E_l$. Therefore, the Kerr effect is about a factor 1 000 smaller than the Pockels effect and neglected in the following calculations of this thesis.

Secondly, the symmetry of S allows simplifying the Pockels coefficient tensor to a matrix with $\mathtt{r}_{wk}, \quad w = 1, 2, \ldots, 6, \quad k = 1, 2, 3$, where the index k is defined by convention through the combination of i, j. A lookup table for the conversion is presented in Tab. 2.1.

Table 2.1: Lookup table to for the index w of the Pockels coefficient $\mathtt{r}_{ijk} \to \mathtt{r}_{wk}$ [62, p. 990].

$j\backslash i$	1	2	3
1	1	6	5
2	6	2	4
3	5	4	3

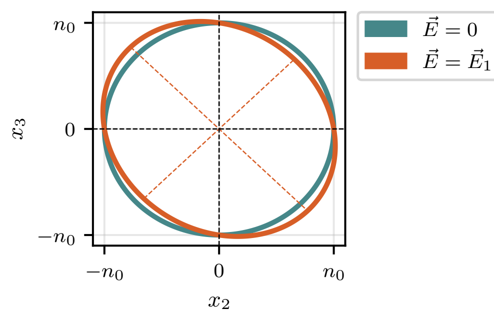

Figure 2.7: Illustrative examples of the cross-section in x_2-x_3 plane of the index ellipsoid according to Eq. 2.33. It presents the cross-section without an applied electric field (blue) compared to the cross-section with an orthogonal electrical field $\vec{E}_1$. The EO effect causes the cross-section to change from a circle to a rotated ellipse, which has its major and minor axes on the diagonal between x_2 and x_3 (orange dashed line).

The third and last simplification originates in the high symmetry of the zinc-blende structure of GaP and ZnTe, which results in on only one independent value in the Pockels coefficient matrix [62, p. 991]

$$\mathtt{r} = \begin{bmatrix} 0 & 0 & 0 \\ 0 & 0 & 0 \\ 0 & 0 & 0 \\ r_{41} & 0 & 0 \\ 0 & r_{52} & 0 \\ 0 & 0 & r_{63} \end{bmatrix}, \quad \text{with } \mathtt{r}_{41} = \mathtt{r}_{52} = \mathtt{r}_{63}. \tag{2.32}$$

The application of these simplifications to Eq. 2.27 lead to the index ellipsoid [26, p. 34]

$$\frac{x_1^2 + x_2^2 + x_3^2}{n_0^2} + 2\mathtt{r}_{41} \left(E_1 x_2 x_3 + E_2 x_3 x_1 + E_3 x_1 x_2 \right) = 1. \tag{2.33}$$

It expresses how the optical properties of the crystal change, depending on the amplitude and direction of an applied electrical field $\vec{E}$.

To clarify the meaning of Eq. 2.33, consider the following examples: If no electrical field E is applied, the resulting ellipsoid is a sphere with radius n_0. If a field $\vec{E} = \vec{E}_1$ is applied, the principle refractive index in direction x_i is still $n_i = n_0$, but the radius changes in-between the axes x_2, x_3. An example of the change in the x_2-x_3-plane is presented in Fig. 2.7, which illustrates that the applied field E_1 leads to a rotated ellipse in x_2-x_3 plane, with its major and minor axis on the diagonals between the original principle axis x_2 and x_3. The major and minor axis define the new slow and fast optical axes. Using Eq. 2.33 with $\vec{E} = \vec{E}_1$ and $x_1 = 0$, the length of the major and minor axis can be calculated by finding

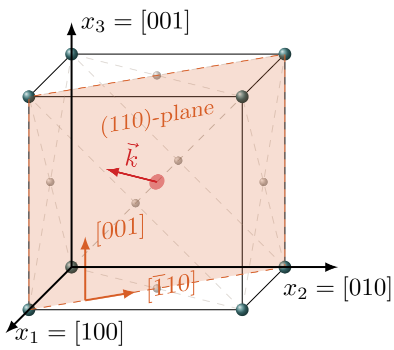

Figure 2.8: Illustration of the (110) plane in a cubic crystal lattice. It is the plane in which EO crystals are typically cut to optimize the measurement sensitivity.

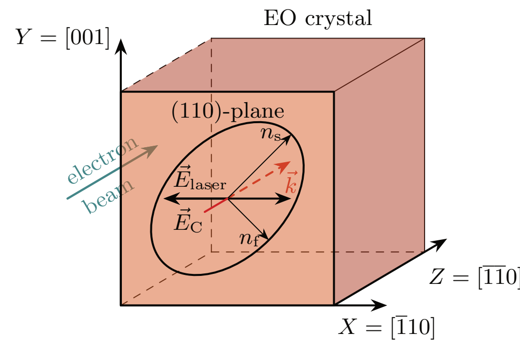

Figure 2.9: Illustration of the typical crystal axis orientation relative to the laser polarization $\vec{E}_{\text{laser}}$ and the relativistic electron beam Coulomb field $\vec{E}_{\text{C}}$. The slow and fast optical axis $n_{\text{s}}, n_{\text{f}}$ are shown as vectors within the index ellipse, which is perpendicular to the laser propagation direction $\vec{k}$. The electron beam propagates parallel to $\vec{k}$ along z, but offset in $-x$ direction next to the EO crystal.

the points for which $x_2 = x_3$, and calculate their distance to the origin. The length of the major and minor semi-axes results to

$$n_{\text{f,s}} = n_0 \sqrt{\frac{1}{1 \pm n_0^2 r_{41} E_1}}. \tag{2.34}$$

2.2.2 Optimal alignment of crystal, E-field and laser

In order to achieve optimal sensitivity of an EO bunch profile monitor, crystal structure, E-field vector and laser polarization need to be aligned such that the modulation of the laser polarization is maximized for a given E-field strength. Additionally, the laser must propagate through the crystal in parallel to the particle bunch to enable the encoding of the bunch profile onto the profile of the laser pulse. Hence, the laser pulse travels perpendicular to the direction of the Lorentz-compressed Coulomb field (see Chapter 2.1.3). This section provides an example of how an optimal alignment can be achieved with commonly available EO crystals.

The phase retardation Γ from Eq. 2.29 quantifies the accumulated phase retardation between the two polarization components on the slow and fast optical axes for a laser propagating through the crystal. In EO monitors, the change of the total laser polarization is measured, hence a larger phase retardation leads to a stronger signal. Thus, to optimize the crystal alignment for EO experiments, the phase retardation should be maximized. The strongest polarization modulation is obtained, when the laser polarization is oriented at a 45° angle with respect to the slow n_{s} and fast n_{f} axes. In this orientation, the electrical field of the laser has equal components along both axes, which maximizes the effect of the phase retardation on the total polarization state.

Since the geometry of available EO crystals and their structure is important for the crystal orientation, it is convenient to discuss directions with the common notation in Miller indices [63]. Planes are denoted by parenthesis, e.g., (hkl), while directions are indicated by square brackets, e.g., $[hkl]$, with negative indices written with a bar on top, such as $[\bar{1}10]$. Hence, the direction of x_1 is denoted as $[100]$, x_2 as $[010]$ and x_3 as $[001]$.

The previous example in the discussion of Eq. 2.33 has shown, that an applied electrical field E_1 in direction $[100]$ modulates the refractive index along the diagonals of the (100) plane such, that it develops an index ellipse with its minor (fast optical axis) and major (slow optical axis) axis along $[011]$ and $[0\bar{1}1]$. However, the crystals are usually cut and polished in the (110) plane for having a normal incident probe laser in $\vec{k} = [\bar{1}\bar{1}0]$ direction. The directions and planes of the (110) cut of the typically used Zincblende crystal lattice are illustrated in Fig. 2.8. With this crystal orientation, the E-field vector as well as the laser polarization is also found in the (110) plane.

Similarly to the previous example, the resulting fast and slow axes of the index ellipse can be calculated, but additional coordinate transforms are required to account for the different lattice orientation. Following the calculations in Steffen [26, pp. 34 ff] and Casalbuoni [64], the phase retardation in this orientation results in

$$\Gamma = \frac{2\pi}{\lambda} d(n_\mathrm{s} - n_\mathrm{f}) = \frac{\pi}{\lambda} n_0^3 r_{41} E_0 \sqrt{1 + 3\cos^2(\alpha)}. \tag{2.35}$$

This assumes the E-field vector in the (110) plane with angle α to the $[\bar{1}10]$ axis and amplitude E_0. Since the phase retardation Γ is proportional to the difference of n_1 and n_2, it is at maximum for $\alpha = 0$, which means that the electrical field vector of the Coulomb field $\vec{E}_\mathrm{C}$ should be oriented parallel to the $[\bar{1}10]$ direction.

In this orientation, the phase retardation is at maximum and simplifies to

$$\Gamma = \frac{2\pi}{\lambda} d n_0^3 r_{41} E_0. \tag{2.36}$$

Finally, Fig. 2.9 presents a typical orientation of the EO crystal relative to the Coulomb field $\vec{E}_\mathrm{C}$ and the laser polarization. The axis labels indicate the directions of an Frenet-Serret coordinate system with the transverse beam directions x, y and the longitudinal beam direction z to illustrate the crystal position at a particle accelerator (see Chapter 2.1.1.2). The direction of the laser polarization is indicated by the field vector $\vec{E}_\mathrm{laser}$ of its oscillating electric field. The maximum phase retardation for an EO crystal with a cubic structure with (110) cut is achieved, if the Coulomb field of the electron bunch $\vec{E}_\mathrm{C}$ is parallel to the $[\bar{1}10]$ axis. Given that the Coulomb field is predominantly transverse for relativistic particles, the electron beam trajectory is indicated next to the crystal along z, with a transverse displacement in $-x$ direction. To optimize the effect of the phase retardation on the resulting laser polarization, the laser propagation direction $\vec{k}$ is parallel to z and its polarization direction should lie along the bisector between the fast and slow optical axes. In this case, $\vec{E}_\mathrm{laser}$ is parallel to $\vec{E}_\mathrm{C}$, resulting in equal field components on the slow and fast optical axes $n_\mathrm{s}, n_\mathrm{f}$.

2.2.3 Principle and working point of an electro-optical monitor

A typical setup for an in-vacuum EO monitor at particle accelerators is depicted in Fig. 2.10, which is similar to what has been used for example at KARA [27], FLASH [26] and European XFEL [29]. The EO monitor contains a laser system to produce the required short laser pulses, an interaction module which includes an EO crystal and is located at the vacuum chamber of the accelerator, and a detection system. The EO monitor setups used in the context of this thesis at KARA, FLUTE and CLEAR are described in detail in the corresponding chapters (Chapters 3.1.2, 3.2.2, 5.4). An EO monitor is designed to measure

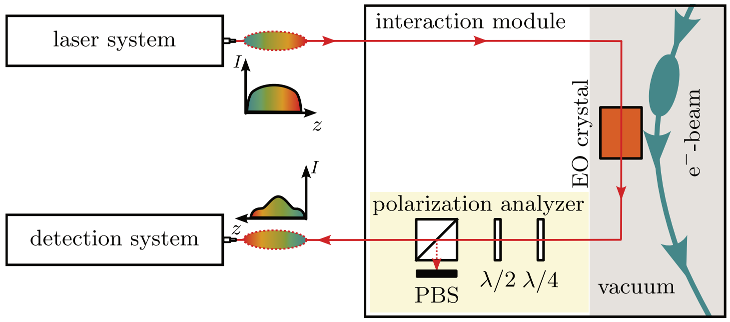

Figure 2.10: Overview schematic of a typical EO monitor setup. The EO monitor consists of a laser system, an interaction module and the detection system. The interaction module is located at the vacuum chamber of the accelerator and includes the EO crystal, which is positioned in-vacuum in vicinity of the particle beam. The electric field of the particle beam is encoded into the polarization of the laser pulse via the electro-optical effect in the crystal. The polarization analyzer converts the polarization modulation of the laser pulse into an intensity modulation, which is analyzed with a detection system.

the longitudinal bunch profile, which correlates with the longitudinal charge density distribution of charged particle bunches, by probing its Coulomb field with laser pulses via the EO effect in the EO crystal. In order to achieve a good resolution, the particles must have relativistic speeds, leading to a Lorentz-contracted Coulomb field (see chapter 2.1.3).

In the first step, a laser pulse is sent through an EO crystal, which is placed inside the vacuum chamber in the vicinity of the trajectory of charged particle bunches. In the examples listed above, a GaP crystal is used in combination with a pulsed laser with a central wavelength around 1 030 nm. The crystal orientation follows the description in the previous section to maximize the phase retardation Γ, where the laser pulses need to be linearly polarized and enter the crystal with the same orientation as the field vector of the Coulomb field. Following Eq. 2.36, the phase retardation changes linearly with the electric field strength, which is an important factor to reconstruct the bunch profile from EO measurements. The probe laser pulses are typically linearly polarized before the crystal and the phase retardation causes an elliptical polarization after the propagation through the crystal.

To enable measurements with a photodiode or a fast camera, a polarization analyzer is used to convert the polarization modulation of the laser pulse into an intensity modulation. The polarization analyzer includes a $\lambda/4$-waveplate at angle ϕ followed by a $\lambda/2$-waveplate at angle θ and a polarizing beam splitter (PBS). The $\lambda/4$-waveplate allows compensating for any intrinsic birefringence of the setup by changing an elliptical polarized laser pulse into a linear polarized pulse, if the angle ϕ is chosen accordingly. The $\lambda/2$-waveplate can change the orientation of the linear polarization and the PBS only transmits light with a certain polarization orientation, while the rest is reflected at a 90° angle.

The angles ϕ and θ of the waveplates in the polarization analyzer are adjustable and define the working point of the EO setup. Its setting determines the default laser intensity on the detector, when the laser is not modulated. For example, the waveplates can be oriented such, that the $\lambda/4$-waveplate achieves a linear polarization of the laser and the following $\lambda/2$-waveplate rotates the polarization to let the PBS reflect all the light and transmit nothing. This polarization analyzer setting is called a crossed-configuration and can be used to calibrate the waveplate orientation and define the angles to $\phi, \theta = 0$.

In general, the resulting laser intensity is described by [26, pp. 42 f]

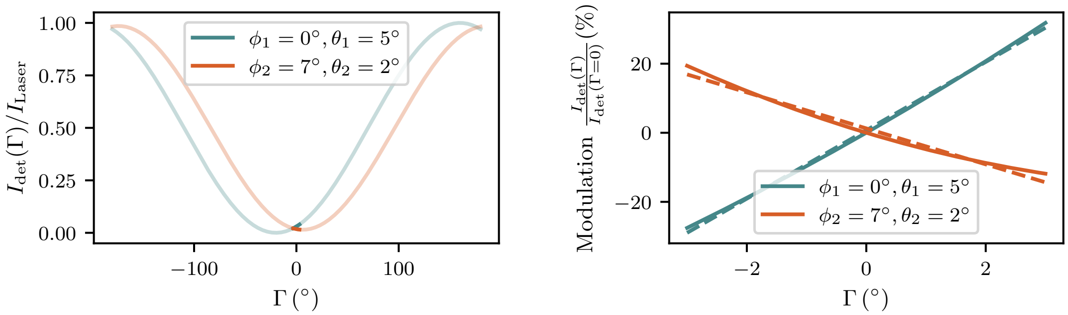

(a) Overview **(b)** Zoom to modulation in KARA's Γ range

Figure 2.11: Correlation between the laser intensity $I_{\mathrm{det}}(\Gamma)$ and the phase retardation Γ for two exemplary working points ($\phi_1 = 0°$, $\theta_1 = 5°$ and $\phi_2 = 7°$, $\theta_2 = 2°$). Subfigure (a) presents an overview of the normalized laser intensity $I_{\mathrm{det}}(\Gamma)/I_{\mathrm{laser}}$ over one phase retardation period $\Gamma = -180°$ to $180°$. The faint (desaturated) line shows the complete phase retardation period, whereas the bold coloured line marks the typical phase retardation range ($\Delta\Gamma = -3°$ to $3°$) during KARA EO measurements. Subfigure 2.11b presents the laser intensity modulation $I_{\mathrm{det}}(\Gamma)/I_{\mathrm{det}}(\Gamma = 0)$ in a zoom on KARA's typical phase retardation range $\Delta\Gamma$, as solid line and a linear fit as a dashed line. While the first working point ϕ_1, θ_1 provides a positive correlation within $\Delta\Gamma$, the second working point ϕ_2, θ_2 has a negative correlation, which is not directly an issue for EO measurements. However, the first working point provides a larger maximum modulation and it deviates less from the linear fit than the second working point ($R_1^2 > 0.99, R_2^2 \approx 0.98$), hence it would be the preferred working point for EO measurements.

$$I_{\mathrm{det}}(\theta, \phi, \Gamma) = \frac{I_{\mathrm{laser}}}{2}[1 - \cos(\Gamma - 2\phi + 4\theta)\cos^2(\phi) + \cos(\Gamma + 2\phi - 4\theta)\sin^2(\phi)], \tag{2.37}$$

assuming an initial laser intensity I_{laser}. In the search for an optimal working point, the goal is to maximize the modulation of the laser amplitude while having a decent signal-to-noise ratio and an approximately linear relation of $I_{\mathrm{det}}(\Gamma)$ within the expected range of Γ. Generally, the $\lambda/4$ waveplate is typically set to $\phi = 0°$ to only compensate for the intrinsic birefringence of the EO crystal. This simplifies the equation to

$$I_{\mathrm{det}}(\theta, \phi = 0, \Gamma) = \frac{I_{\mathrm{laser}}}{2}[1 - \cos(\Gamma + 4\theta)], \tag{2.38}$$

which highlights the sinusoidal proportionality of the laser intensity to the phase retardation Γ and the $\lambda/2$-waveplate angle θ.

Figure 2.11 presents an example of the correlation between laser intensity $I_{\mathrm{det}}(\Gamma)$ and the phase retardation Γ for a near-crossed working point with $\phi_1 = 0°, \theta_1 = 5°$ and a second working point example $\phi_2 = 7°, \theta_2 = 2°$. The first working point has been experimentally determined to roughly maximize the laser modulation for the given phase retardation during KARA experiments. The second working point represents the estimated effective working point during the presented electro-optical sampling (EOS) measurements in Chapters 3.1.3.1 and 4.2. In these experiments, a crystal temperature-related effect likely caused a drift of the working point. At KARA EO measurements, the phase retardation is typically expected to be in the range of $\Delta\Gamma = -3°$ to $3°$ (see Chapter 4.1.2). As the range $\Delta\Gamma$ is small compared to a full period, Figure 2.11a presents an overview of the position of the phase retardation range in context of a full phase rotation. For $\Gamma = 0$ (no modulation), the first working point lies to the right of the minimum, while the second working point is positioned even nearer to the minimum on its left side.

The modulation of the laser intensity $\frac{I_{\text{det}}(\Gamma)}{I_{\text{det}}(\Gamma=0)}$ over the retardation range $\Delta\Gamma$ is presented in Fig. 2.11b. To evaluate the linearity of $I_{\text{det}}(\Gamma)$, a linear function was fitted within the selected phase retardation range, resulting in a coefficient of determination of $R_1^2 > 0.99$, $R_2^2 \approx 0.98$. This result confirms, that assuming a linear correlation between I_{det} and Γ is appropriate for the first working point , which enables a linear mapping of the measured laser intensity to the longitudinal bunch profile with electro-optical spectral decoding (EOSD) measurements. However, the second working point deviates visibly from a linear function and provides a lower maximum modulation. Hence the first working point is more suitable for EO measurements, due to its higher laser intensity modulation and improved linearity across the given phase retardation range. To optimize the working point of a specific setup, the noise level of the detection system and specific measurement parameters like the bunch charge density, crystal distance to the particle beam and more need to be taken into account, which is typically done experimentally [27]. For FCC-ee, the optimal working point is expected to require additional investigation, too, because its larger bunch charge densities will increase the phase retardation range $\Delta\Gamma$.

2.2.4 Electro-optical techniques

The principle of an EO monitor can be applied to different EO techniques. An overview is presented in Ref. [24], which includes electro-optical spectral decoding (EOSD), EO spatial encoding, EO temporal decoding and EO transposition. The following explanation focuses on EOS and EOSD, because they have a less complex setup that is more suitable for prototyping. They are established techniques that are used at KARA and therefore provide a baseline for the development of an EO monitor for the FCC-ee. The different techniques require a similar setup of the interaction module including the crystal, hence the adaption of a different technique is also possible at a later stage. In particular, techniques like electro-optic spectral interferometry (EOSI) [32, 65] and diversity electro-optic sampling (DEOS) [30, 31] could be employed with small setup changes to push the resolution limit.

This section aims to provide a brief overview of the EOS and EOSD principle. Detailed technical descriptions of individual setups at KARA, Ferninfrarot Linac- und Test-Experiment (FLUTE) and CERN Linear Electron Accelerator for Research (CLEAR) are presented in context of corresponding measurements in later chapters.

2.2.4.1 Electro-optical sampling (EOS)

Figure 2.12 presents a schematic of an EO monitor with an EOS detection system. Electro-optical sampling (EOS) measurements are multi-shot measurements, because the intensity of the laser pulses is recorded and often averaged over multiple-shots, while the delay of the laser pulses is changed relative to the particle bunch arrival time. The laser pulses are sent onto a photodiode (PD), and typically the maximum of the detected pulse or the integrated pulse is used as a measure of the laser pulse intensity. Hence, each laser pulse provides a single sample point that correlates with the laser pulse intensity. As described in the previous Chapter 2.2.3, the EO crystal and the polarization analyzer of the interaction module change the resulting laser pulse intensity relative to the electric field strength at the EO crystal. Thus, the EOS technique samples the dynamics of the electrical field at the EO crystal, typically to provide an overview of the Coulomb and following wake field of the particle bunches.

Its resolution depends strongly on the length of the probe pulse (see Chapter 2.2.5), and the uncertainty of the laser delay. At setups like the one at KARA, the resolution is limited by the laser pulse length, because longer laser pulses than the electron bunch length are required for single-shot EOSD measurements (see

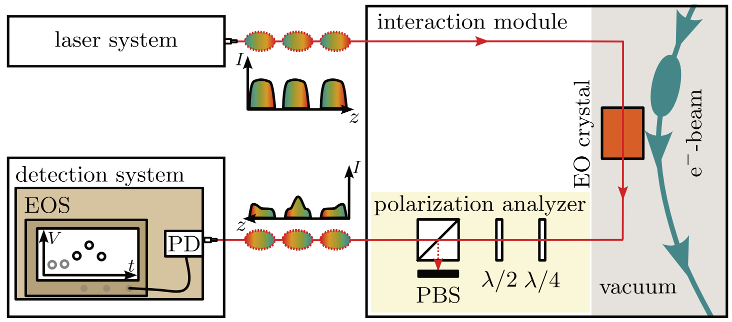

Figure 2.12: Overview schematic of a typical EO monitor setup with an EOS detection system. The intensity of multiple laser pulses is recorded with a photodiode (PD) on an oscilloscope, while their relative delay to the electron bunch arrival time changes. Each sampled datapoint is typically calculated by the maximum or the integrated intensity of the laser pulse. As the laser intensity at the photodiode (PD) changes relative to the applied electrical field strength at the EO crystal, this technique can be used to sample the Coulomb field and following wake field of the electron bunch over multiple shots.

next section). However, EOS scans are faster to acquire and analyze, which makes it a key technique for long-range wakefield scans, for the optimization and benchmarking of the EO setup, and for identifying the optimum laser pulse delay for subsequent single-shot EOSD bunch profile measurements. Thus, it is also a beneficial technique for the initial EO monitor commissioning, where long EOS time scans are used to find a first signal.

For EOS measurements, the laser pulses are typically sent onto a photodiode (PD), for the analysis, where an oscilloscope is connected to record the individual laser pulse intensity. If the laser repetition rate is high, for example at KARA with 2.7 MHz, a lock-in amplifier can be used to analyze the PD signal with an improved signal-to-noise ratio. EOS measurements and setups are discussed for KARA in Chapter 3.1.3.1, FLUTE in Chapter 3.2.2, and CLEAR in Chapter 5.

2.2.4.2 Electro-optical spectral decoding (EOSD)

EOSD is based on the idea of encoding the bunch profile in the spectrum of a single laser pulse, which enables to decode the bunch profile with a spectrometer. Generally, the longitudinal bunch profile is encoded in the longitudinal profile of the probe laser pulse via the EO effect in the crystal (see Chapter 2.2.3). To enable the encoding in the spectrum of the laser pulse, the laser pulse needs to be chirped. The chirp of a laser pulse describes, how its instantaneous optical frequency varies with its longitudinal coordinate (longitudinal position z or pulse duration t, see Chapter 2.1.1.2). For EOSD, a linear chirped is desired to achieve a linear correlation of the laser pulse spectrum and the bunch profile [26]. For example, a negative linear chirp refers to a laser pulse in which the instantaneous optical frequency increases linearly from its head towards its tail. Hence, the spectrum of the laser pulse also contains information about its longitudinal profile.

A schematic overview of an EO monitor setup for EOSD is presented in Fig. 2.13. A chirped laser pulse passes through the interaction module, where the bunch profile is encoded into its spectrum via the EO effect in the EO crystal and the following polarization analyzer. The detection system is a spectrometer with a grating that disperses the laser pulse, turning its spectrum into a spatial spread. A line camera captures the spectrally broadened pulse as an intensity profile. The resulting image with the intensity over the pixel position maps to the laser pulse spectrum, hence it also contains the encoded bunch profile.

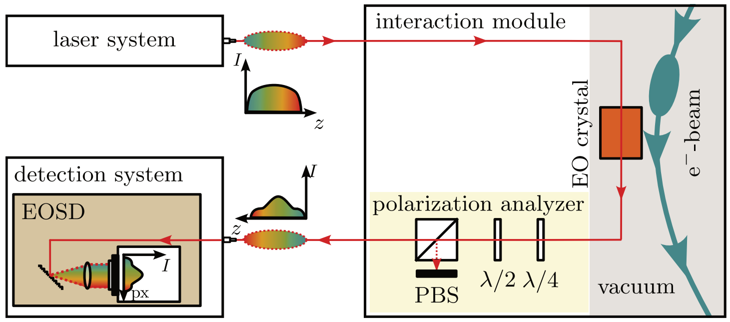

Figure 2.13: Overview schematic of a typical EO monitor setup with an EOSD detection system.

In order to decode the bunch profile, the following data is taken with the spectrometer:

- Background data BG: Taken while the laser light is blocked (no laser light on the sensor).
- Unmodulated data UD: Taken while the laser light has no interaction with the electron bunch (Laser pulse timing is shifted to before the electron bunch arrives at the crystal).
- Modulated data MD: Taken while the laser light interacts with the electron bunch (Laser pulse timing is adjusted to overlap with the electric field of the electron bunch).

The modulation M of the laser light is calculated by

$$M = \frac{MD - BG}{UD - BG} - 1. \tag{2.39}$$

The modulation directly maps to the bunch profile, if the laser pulse has a linear chirp and if laser intensity changes linearly with the bunch-induced phase retardation in the EO crystal (see Chapter 2.2.3). However, an additional calibration procedure is required to determine the bunch duration by mapping the pixels of the line camera to a time-axis.

The pixels of the spectrometer camera can be converted to the time-axis by shifting the laser delay by a known amount. The conversion factor is deducted by recording the position shift of the modulation peak on the pixels of the camera. The laser delay can be shifted for example by a delay stage, or, if possible, by adjusting the phase of the laser oscillator output directly. The resulting conversion factor enables to convert the pixels of the camera into a time axis. However, the conversion factor is only constant for a linear chirp of the laser pulse because the mentioned conversion factor is defined by the slope of the chirp. Thus, scanning the laser pulse delay while recording the position of the modulation peak also enables to estimate the chirp of the laser pulse across its spectrum. If the chirp is not linear, the conversion factor changes along the pixels of the camera, which needs to be considered for the time axis calculation.

As a result, the EOSD setup enables absolute measurements of the bunch duration and its profile, without external calibration reference.

2.2.5 Time resolution and bandwidth limitations

The EO time resolution limit τ describes the smallest resolvable temporal structure of the complete EO system, which is typically quantified by the RMS length of the signal (e.g., the bunch length in Chapter 2.1.1.7). The EO system thereby includes the full signal path, from the laser source to the final

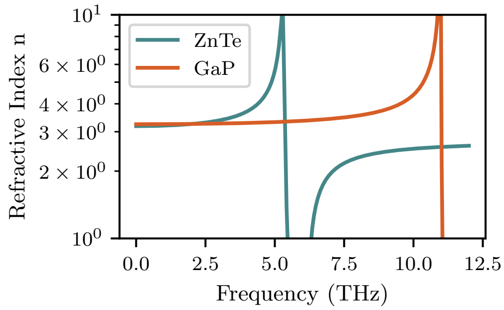

Figure 2.14: Refractive index of ZnTe (blue) and GaP(orange) in the THz frequency range. The refractive index dramatically changes at the transverse optical (TO) lattice oscillation at 5.3 THz and 10.98 THz for ZnTe and GaP respectively. The calculation is based on the description in [26, 64].

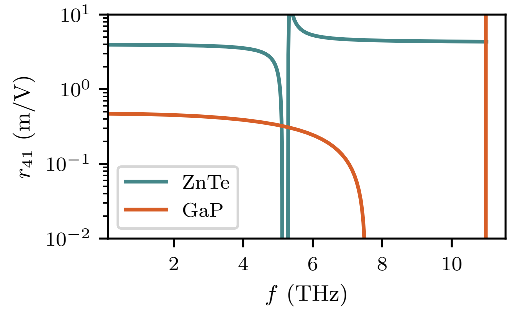

Figure 2.15: Electro-optic coefficient $r_{41}(f)$ for ZnTe (blue) and GaP. The EO coefficient is approximately constant at lower frequencies with $r_{41}^{\mathrm{ZnTe}} \approx 3.95 \times 10^{-12}\,\mathrm{m/V}$ and $r_{41}^{\mathrm{GaP}} \approx 0.47 \times 10^{-12}\,\mathrm{m/V}$, until it decreases exponentially and falls below half its initial value at 4.95 THz and 6.09 THz. The calculation is based on the description in [26, 64].

data acquisition. A related quantity of the time resolution limit is the system bandwidth BW, which is typically defined as the frequency range of a system, over which the frequency remains within −3 dB of its maximum value (equivalent to full width at half maximum (FWHM)).

The shape of the detected pulse is determined by a convolution of the signal shape and the system's frequency response, which is bandwidth-limited. As a result, the resolution limit is generally inversely proportional to the effective bandwidth of the system, and also depends on the Fourier transform of the signal shape. For a given pulse shape, the time-bandwidth product is constant and describes the smallest achievable pulse length for a given bandwidth. This pulse length is called a transform-limited pulse length. For example, the time-bandwidth product for a Gaussian pulse is given by [66]

$$\tau^{\mathrm{FWHM}} \cdot BW^{\mathrm{FWHM}} \approx 0.44 \;\Rightarrow\; \tau^{\mathrm{RMS}} \cdot BW^{\mathrm{FWHM}} \approx 0.187. \tag{2.40}$$

It is important to distinguish between the resolution limit and measurement uncertainty, which can be smaller than the resolution limit. An example is provided in [29], where a bunch length of around 400 fs was measured with an uncertainty of $\sim$17 fs, while the EO system had a resolution limit of 160 fs.

The resolution of EO measurements can be limited by multiple different factors, depending on the specific setup and the EO technique. For example, it can be limited by the size and material of the EO crystal, the laser properties, and the data acquisition. This section aims to provide an overview of the general limitations, while resolution limits of specific setups are discussed in the corresponding chapters later in this thesis. The following resolution limitations serve as an estimation of the upper resolution limit, but additional effects like laser pulse broadening in the crystal, or interactions with other electromagnetic fields from intracrystalline reflections or Cherenkov diffraction radiation (ChDR) can further impact the resolution limit.

2.2.5.1 Crystal material and size

The crystal material provides a fundamental limitation, because its lattice has certain resonance frequencies. If an electromagnetic pulse with a matching frequency excites the lattice oscillation, its energy is absorbed, causing a strong variation of the refractive index around the resonance frequency.

Concerning EO experiments, the Coulomb field of the electron bunch can excite transverse optical (TO) lattice oscillation, which prohibit EO measurements at this frequency [64]. Thus, the bandwidth of EO measurements is limited by the crystal material to its lowest TO resonance. Figure 2.14 presents a model of the refractive index in the THz range for the commonly used materials ZnTe and GaP, based on description in [26, 64]. For low frequencies, the refractive index is approximately 3.18 for ZnTe and 3.24 for GaP, but it changes dramatically close the TO resonances at approx. 5.3 THz and 10.98 THz for ZnTe and GaP, respectively.

Additionally, the EO coefficient $r_{41}(f)$ of the crystal material is frequency-dependent, particularly at frequencies close to the TO resonance. The phase retardation Γ of the probe laser scales linearly with the EO coefficient r_{41} (see 2.36), hence $r_{41}(f)$ can have an impact on the overall EO measurement bandwidth. Figure 2.15 presents the EO coefficients for ZnTe and GaP in the THz range, following the calculations of [26, 64].

ZnTe has an approximately constant EO coefficient $r_{41}^{\mathrm{ZnTe}} \approx 3.95 \times 10^{-12}\,\mathrm{m/V}$ at lower frequencies, until it sharply decreases close to the TO resonance, reaching half its initial amplitude at ~4.95 THz. GaP has a lower initial EO coefficient $r_{41}^{\mathrm{GaP}} \approx 0.47 \times 10^{-12}\,\mathrm{m/V}$ and a broader decrease toward its TO resonance. Its EO coefficient is therefore slowly decreasing and reaches half its original amplitude at 6.09 THz. Thus, the effective bandwidth for EO measurements with GaP is reduced, but remains greater than with ZnTe. This frequency dependent model of the EO coefficient $r_{41}(f)$ of GaP is derived from a model based on experimental data in the THz range, as presented in Ref. [26]. The model accounts for the dispersion near the TO resonance and yields a reduced EO coefficient at low frequencies of $r_{41} \approx 0.47 \times 10^{-12}\,\mathrm{m/V}$ compared to the commonly cited constant value of $r_{41} \approx 0.97 \times 10^{-12}\,\mathrm{m/V}$ [67, 68]. The latter value is often used in simulations and comparative studies and likely originates from reference value in a lower frequency range. However, the discrepancy between these two values remains an open question in the literature, as far as the author is aware. In the following chapters of this thesis, and in the simulations in particular, the spectral components in the lower GHz range typically dominate the spectrum. Thus, the constant EO coefficient $r_{41} \approx 0.97 \times 10^{-12}\,\mathrm{m/V}$ is assumed for GaP and the approximately four times larger EO coefficient $r_{41} \approx 4.04 \times 10^{-12}\,\mathrm{m/V}$ is assumed for ZnTe, as suggested in [67].

Additionally, the bandwidth of the response function is reduced further by the phase mismatch of the probe laser pulse and the THz-pulse of the electron bunch. The commonly used probe laser systems for EO applications have a center wavelength of either ~800 nm (~375 THz), ~1 060 nm (~283 THz) or ~1 550 nm (~193 THz), while the broad spectrum of the bunch-induced THz pulse is typically below the 10 THz mark. Thus, the frequency-dependent refractive index of the crystal differs for the probe pulse and the THz pulse, causing a phase mismatch. The crystal material and probe laser wavelength are deliberately chosen to minimize the difference and optimize the phase mismatch. For example, a ZnTe crystal has a low phase mismatch in combination with a 800 nm probe laser, a GaP crystal with a 1 060 nm laser, or a gallium arsenide (GaAs) crystal with a 1 550 nm laser [68].

When matching the crystal material and the laser wavelength, a small phase mismatch remains, and it accumulates over the propagated distance of the THz pulse and probe pulse within the crystal. In EO monitors, this distance is typically determined by the thickness of the crystal. Hence, the phase mismatch scales with the crystal thickness, making it a crucial factor when designing an EO setup. The impact of the crystal thickness on the bandwidth of the EO signal is described with the geometric response function

$$G(f) = \frac{\exp\left(i2\pi\Delta k(f, f_{\mathrm{probe}})d\right) - 1}{i2\pi\Delta k(f, f_{\mathrm{probe}})} \tag{2.41}$$

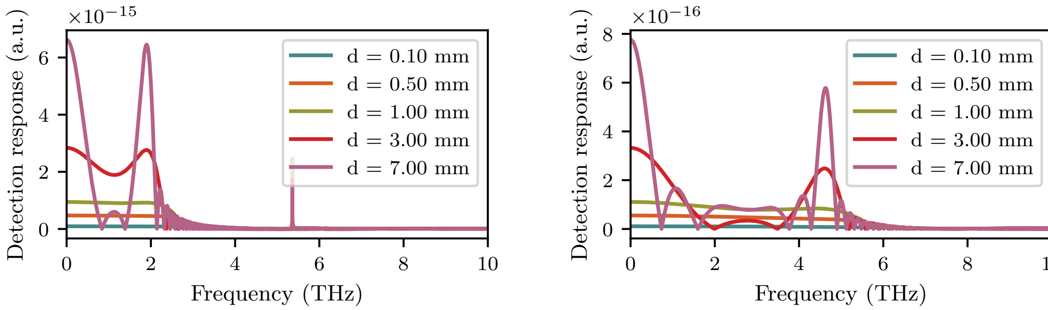

(a) ZnTe **(b)** GaP

Figure 2.16: Detection response $R(f)$ of ZnTe and GaP for a selection of different crystal thickness d. To optimize the phase matching, a probe laser wavelength of 800 nm for ZnTe and 1 060 nm for GaP is assumed. The detection response shows a reduction of the bandwidth for $d = 3\,\mathrm{mm}$ and 7 mm, which is caused by additional minima in the lower frequency region. However, a larger crystal thickness also increases the amplitude of the detection response. While GaP has a larger bandwidth, especially at smaller crystal thickness, ZnTe has a larger detection response amplitude due to its larger EO coefficient r_{41}.

with the frequency f, the probe laser frequency f_{probe}, the crystal thickness d, and the complex phase mismatch

$$\Delta k(f, f_{\text{probe}}) = \frac{f}{c}\left(n_g(f_{\text{probe}}) - n(f)\right), \tag{2.42}$$

where the $n_g(f_{\text{probe}})$ describes the group refractive index of the probe laser, and $n(f)$ the complex refractive index for the THz frequencies [67]. To simulate the EO detection response

$$R(f) = G(f)T(f)r_{41}(f), \tag{2.43}$$

the geometric response is multiplied by the surface transmittance of the crystal

$$T(f) = \frac{2}{n(f) + 1} \tag{2.44}$$

and the EO coefficient $r_{41}(f)$ [64].

Figure 2.16 presents the detection response $R(f)$ in the THz region for ZnTe and GaP at multiple crystal thicknesses d. For ZnTe, an 800 nm probe laser is assumed with a refractive index $n_g(800\,\mathrm{nm}) = 3.24$, while a 1 060 nm probe laser is assumed for GaP with the refractive index $n_g(1\,060\,\mathrm{nm}) = 3.3$ [67]. Generally, ZnTe has a lower bandwidth for thinner crystals, but the detection response amplitude is larger due to the greater EO coefficient. For the crystal thicknesses of 3 mm and 7 mm, additional minima in the detection response appear toward lower frequencies, which drastically reduces the bandwidth. The 3 dB bandwidth is plotted in Fig. 2.17, which highlights the initially larger bandwidth of GaP and the drastic drop in bandwidth for $d = 3\,\mathrm{mm}$ and $d = 7\,\mathrm{mm}$.

Finally, the crystal quality needs to be taken into account as well. Defects in the crystal are sometimes visible as black spots in the material, which likely impact the laser transmission through the crystal and decreases the sensitivity. From personal experience, ZnTe crystals tend to have more visible defects than GaP, but it also varies across different vendors. Additionally, the surface finish and potential coatings have an impact on the final EO signal. Anti-reflective coatings can be used to improve the overall laser transmission through the crystal, while reflective coatings can be used to guide the probe laser onto a specific path.

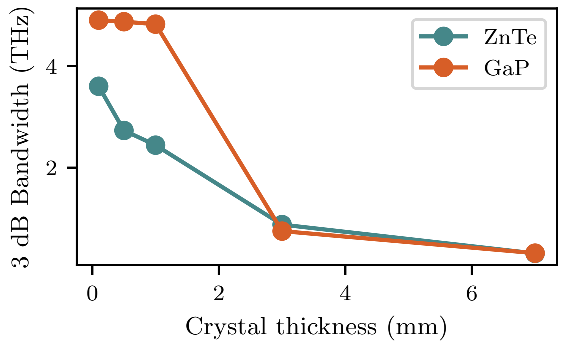

Figure 2.17: 3 dB bandwidth of the detection response (see Fig. 2.16) of ZnTe and GaP for multiple crystal thickness. The bandwidth decreases for thicker crystals, but not linearly. While GaP has a larger bandwidth for smaller crystal thicknesses, it reduces drastically for $d = 3\,\mathrm{mm}$ and $d = 7\,\mathrm{mm}$, reaching a similar level as ZnTe.

In summary, the crystal material and thickness are important parameters to balance the EO sensitivity and its bandwidth to match the specific application. The probe laser wavelength needs to be matched to the crystal material to reduce the phase mismatch and optimize the EO bandwidth. For example, a thin GaP crystal with a 1 060 nm probe laser might be ideal for high resolution measurements of short bunches, while a thick ZnTe crystal with a 800 nm has a lower bandwidth, but offers a much better sensitivity.

2.2.5.2 Laser based limitations

Depending on the EO technique, the laser properties can be the limiting factor of the overall resolution limit. In this subsection, the effects of the laser properties on the resolution of EOS and EOSD measurements are summarized. For illustration purposes, the following example calculations assume a Gaussian pulse shape. However, the resolution limit will differ for other pulse shapes.

In EOS measurements, the photodiode to detect the laser pulses typically has a rise time of more than 100 ps, but the laser pulse length is in the order of 10 ps. The electric field is sampled by changing the delay of the laser pulse in multiple steps, while measuring the amplitude of the photodiode signal at every step. The resulting amplitude of the photodiode signal is proportional to the total pulse energy. In the EOS setup, the probe laser pulse is modulated by the beam field through the EO effect. Thus, the resulting EOS signal is a convolution of the laser pulse shape in the crystal and the original electric field profile. The bandwidth is therefore limited by the spectrum of the laser pulse. It is comparable to a weighted moving average over the original electric field, where the averaging window is determined by the laser pulse length and shape.

Assuming a Gaussian laser pulse, the resulting frequency response (Fourier transform) of a Gaussian pulse is also a Gaussian [69]:

$$H(f) = e^{-2\pi^2\sigma_t^2 f^2}. \tag{2.45}$$

The 3 dB bandwidth is defined by $H(f) = 1/\sqrt{2}$, which results to

$$BW^{\mathrm{EOS}} = \frac{\sqrt{\ln 2}}{\pi\sigma_t}. \tag{2.46}$$

For example, a Gaussian pulse with length $\sigma_t = 10\,\mathrm{ps}$ would limit the bandwidth in EOS measurements to $BW \approx 26.5\,\mathrm{GHz}$. For very short laser pulses, EOS can also achieve high bandwidth, e.g. $BW \approx$

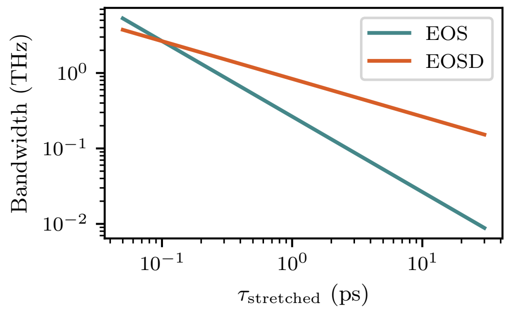

Figure 2.18: Comparison of the laser-based bandwidth limitation of EOS (blue) and EOSD according to Eqs. 2.46, 2.48. It is an exemplary illustration, where a transform-limited pulse length of $\tau_{\text{trans.-lim}} = 50\,\text{fs}$ is assumed for the EOSD bandwidth calculation. On the double logarithmic scale, the bandwidth limit appears to have a linear relation for a given laser pulse length $\tau_{\text{stretched}}$ at the EO crystal for both, EOS and EOSD. The lines cross at ~0.1 ps, but the bandwidth of EOS has a steeper downward slope, which leads to a drastically higher bandwidth of EOSD for laser pulse lengths on the picosecond scale.

530.0 GHz for $\sigma_t = 0.5\,\text{ps}$, but its multi-shot nature also requires an appropriate sampling rate to resolve the bunch profile.

EOSD typically provides a higher bandwidth for longer laser pulses with the additional benefit of enabling single-shot measurements. The profile of the electric field is encoded in the spectrum of the laser pulse, hence the bandwidth of the laser pulse spectrum provides a resolution limit. The time resolution τ for a Gaussian pulse is described by the geometric mean of the transform-limited pulse length $\tau_{\text{trans-lim}}$ and the stretched pulse length $\tau_{\text{stretched}}$ in the EO crystal [70]

$$\tau = \sqrt{\tau_{\text{trans-lim}} \cdot \tau_{\text{stretched}}}\,, \tag{2.47}$$

corresponding to the bandwidth limit (see Eq. 2.40

$$BW^{\text{EOSD}} \approx \frac{0.187}{\sqrt{\tau_{\text{trans-lim}} \cdot \tau_{\text{stretched}}}}. \tag{2.48}$$

The typical mode-lock laser systems for EOSD have a transform-limited pulse length in the order of 50 fs, which, for example for $t_{\text{stretched}} = 10\,\text{ps}$, would result in a resolution limit of $\tau \approx 707\,\text{fs}$. This corresponds to a bandwidth of ~252 GHz according to the time-bandwidth product of Eq. 2.40, and is an order of magnitude larger than an EOS measurement with similar pulse length.

Figure 2.18 provides a visualization of the laser-based bandwidth limitation of EOS (Eq. 2.46) and EOSD (Eq. 2.48. For EOSD, a transform-limited pulse length $\tau_{\text{trans.-lim}} = 50\,\text{fs}$ is assumed [29]. Both curves appear linear due to the double-logarithmic scale, and they cross at a pulse length of ~0.1 ps. The EOS bandwidth limit has a steeper downward slop, leading to a drastically higher bandwidth for EOSD in the picosecond pulse length region. Additionally, and in contrast to EOS, EOSD enables single-shot measurements, which makes it the typically preferred choice for a high resolution and high repetition rate longitudinal beam diagnostic for particle accelerators.

Techniques like diversity electro-optic sampling (DEOS) [30, 31] and electro-optic spectral interferometry (EOSI) [32, 65] are actively developed and enable to improve the resolution limit beyond the limitations of Eq. 2.47. While these techniques typically require more complex data processing to retrieve the bunch profile, they only require minor hardware changes. Thus, an upgrade of an existing EOSD system to either of these systems is possible, if an improved resolution is required. However, this thesis focuses on EOSD, because the resolution of EOSD is expected to be sufficient for the longer bunches of FCC-ee.

2.2.5.3 Data acquisition

The data acquisition system needs to match to the requirements of the EO setup or it can contribute to a resolution limit.

In EOS measurements, an oscilloscope detects the photodiode output. If an oscilloscope is used with sufficient bandwidth and sampling rate to resolve the photodiode signal, the oscilloscope is typically not the limiting factor for the resolution of EOS measurements.

EOSD requires a spectrometer to retrieve the electron bunch profile from the spectrum of the laser pulse. It is typically a custom design for the specific setup to match the laser repetition rate and laser pulse spectrum (e.g. [71]). Its main components are a grating to disperse laser pulse and a line-array camera to detect the resulting spectrum. The number of illuminated pixels on the camera sensor determines the resolution of the detected spectrum, hence the grating should be combined with optical lenses and mirrors to optimize the illumination of the camera sensor. Single shot detection can provide a technical challenge for the camera, as it needs to combine high sensitivity for the single, low-power laser shots at a near-crossed working point of the EO system with a high repetition rate at facilities like KARA. For example, to enable turn-by-turn measurements with 2.7 MHz at KARA, the Karlsruhe Institute of Technology (KIT)-developed special camera system Karlsruhe line array detector for MHz-repetition rate spectroscopy (KALYPSO) [35, 72] is used.

3 Studies with the EO beam monitor at KARA and FLUTE

The electro-optical (EO) monitor for the Future Circular Lepton Collider (FCC-ee) needs to fulfill unique and demanding requirements, which are set in particular by FCC-ee's high bunch charges at high repetition rates with a wide range of bunch lengths across its four operation modes. For this thesis, the Karlsruhe Research Accelerator (KARA) provided a platform to gain experience and perform tests with an existing EO monitor at a synchrotron. It was used to study the general functionality and operation of an electro-optical spectral decoding (EOSD) bunch profile monitor and provided a baseline for the development of FCC-ee's EO monitor concept design.

To illustrate the EO monitor principle and its capabilities, this section provides example electro-optical sampling (EOS) and EOSD measurements at Karlsruhe Research Accelerator (KARA). The EOS measurements additionally revealed a signal drift, which is likely correlated to bunch-induced crystal heating. As the high beam currents at FCC-ee will amplify this effect, a dedicated experiment has been set up to demonstrate and investigate the correlation between crystal temperature and the signal drift.

Furthermore, an EO system was installed at the linear accelerator Ferninfrarot Linac- und Test-Experiment (FLUTE) towards the end of 2025, providing additional experience and insight into the commissioning of an EO monitor. The process of setting up the system and first EOS and EOSD measurement results are presented.

3.1 EO diagnostic studies at the Karlsruhe Research Accelerator

KARA is a synchrotron and accelerator test facility at Karlsruhe Institute of Technology (KIT), which provides a platform for beam diagnostics development. The EO monitor at KARA was first suggested in 2011 [33] and initially installed in 2013 [27]. It is the first in-vacuum EO monitor for single-bunch profile measurements in a storage ring, and it has been improved in multiple iterations to enable single-shot, turn-by-turn bunch profile measurements at the KARA revolution frequency of 2.7 MHz [34, 35, 61]. This extensive operational experience with a circular particle accelerator provides a solid foundation for the development of an EO monitor for the FCC-ee.

3.1.1 Introduction to EO measurements at KARA

KARA is mainly operated in one of two different modes: The standard operation with an electron energy of ∼2.5 GeV and a dedicated short-bunch operation with low momentum compaction factor $\alpha_c \sim 1 \times 10^{-4}$ at ∼1.3 GeV [73, 74]. An overview of the typical KARA parameters in the short-bunch mode is presented in Table 3.1.

Table 3.1: Typical beam parameters at KARA in short-bunch (low-α_c) operation

Parameter	Value
Circumference	110.4 m
Radio frequency (RF) frequency	499.7 MHz
Particle energy	1.3 GeV
Momentum compaction α_c	$\sim$1 × 10^{-4}
Revolution frequency	2.716 MHz
Bunch charge	<2 nC
Bunch length	0.6 mm to 4.5 mm (1.9 ps to 15 ps)
Min. bunch spacing	2 ns

The EO monitor at KARA is designed to measure in the short-bunch mode, with typical bunch lengths $\sigma < 10\,\mathrm{ps}$ and bunch charges $q < 1\,\mathrm{nC}$. The short bunch length in combination with high bunch charge drives the micro-bunching instability, which occurs through the self-interaction of the electron bunch with its coherent synchrotron radiation (CSR). It is a longitudinal, single-bunch collective effect, that causes dynamic changes and deformations of the bunch charge density, resulting in a deterioration of the electron beam properties [50]. The EO monitor is part of the diagnostics network at KARA to study the dynamics of the micro-bunching instability, aiming towards its mitigation or control [55, 75–77]. With tomography techniques, EOSD data can be used to reconstruct the longitudinal phase space, revealing characteristic features of the micro-bunching instability [61].

3.1.2 Experimental setup of the EO system at KARA

A schematic of the overall EO monitor setup is presented in Fig. 3.1, which is generally divided in three parts:

1. Laser system: A femtosecond pulsed laser system with its synchronization electronics in a laboratory.
2. Interaction module: Located directly at the KARA vacuum chamber, including the in-vacuum crystal assembly and an optics box with a polarization analyzer on the outside.
3. Detection system: The data acquisition in the laboratory with either a photodiode for EOS, or a spectrometer for EOSD measurements.

A 35 m long PM fiber delivers the laser pulses from the laboratory to the EO interaction module with the in-vacuum EO crystal at the KARA ring. Afterwards, the leaser pulses are returned back through a 35 m SM fiber to the detection system in the laboratory.

In the EO laboratory, the laser oscillator operates at a repetition rate of $\sim$62.5 MHz and utilizes grating compressor to adjust the laser pulse chirp at its output, before it is sent to the laser amplifier. The amplifier then reduces the repetition rate with a pulse picker to typically 2.7 MHz to match the revolution frequency of KARA, and it amplifies the remaining pulses. Afterwards, the pulses are transported through optical fibers to the EO interaction module at the KARA vacuum chamber, where they are guided through a EO crystal in vicinity to the electron beam. The dispersion of the optical fibers stretches the laser pulses during the transmission, hence they typically are 1.5 to 5 times longer than the electron bunch. If the laser pulse arrival time is synchronized with the electron bunch, the electron bunch profile

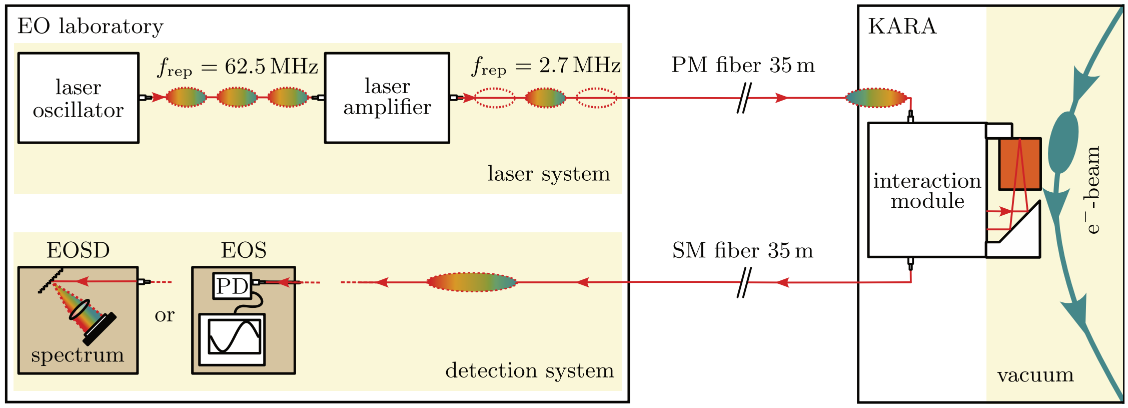

Figure 3.1: Schematic overview of the EO monitor at KARA. The laser oscillator in the EO laboratory produces laser pulses with a repetition rate of around 62.5 MHz and an integrated compressor enables to adjust the chirp and pulse length. An exemplary development of the chirp along the laser path is indicated by a color gradient from red at the trailing edge to blue at the leading edge of a laser pulse (negative chirp) or vice versa (positive chirp). After the laser oscillator, the repetition rate is reduced with a pulse picker to ∼2.7 MHz before entering a gain fiber in the laser amplifier. The amplified pulses are transported to the EO interaction module through a 35 m polarization-maintaining (PM) fiber with normal dispersion, therefore shifting the pulses towards a positive chirp. At the interaction module, the laser pulses are guided into the KARA vacuum chamber through the EO crystal, where they are modulated by the electric field of the electron bunches. Finally, the laser pulses are sent back to the EO laboratory for data acquisition through a single-mode (SM) fiber. For EOS measurements, the laser pulse intensity is measured with a photodiode (PD) and oscilloscope, and for EOSD measurements, a spectrometer consisting mainly of a grating and a line array camera is used.

is encoded in the laser pulse polarization through the EO effect. The subsequent polarization analyzer converts the modulated polarization into an intensity modulation (see Chapter 2.2.3, before the laser pulses are transported back to the EO laboratory for the data acquisition.

For EOS measurements, a photodiode in combination with a lock-in amplifier and an oscilloscope is used to detect the laser pulse intensity. For EOSD measurements, the laser pulses are connected to a free-space spectrometer, mainly consisting of a grating to disperse the laser pulses, and the KIT-built camera KALYPSO [72]. This spectrometer enables single-shot measurements of each laser pulse spectrum (at 2.7 MHz), resulting in turn-by-turn data of the longitudinal bunch profile.

3.1.2.1 Laser system

The laser system for the EO monitor at KARA is a passive mode-lock laser with an Ytterbium gain fiber, which produces femtosecond pulses around a central wavelength of ∼1 030 nm. General information about mode-locked lasers and fiber lasers can be found in [78, 79], and information about the first use of a similar laser system at KARA is presented in [27]. The laser at KARA has a custom built oscillator and amplifier, which was developed at the Paul Scherrer Institute (PSI) and the University of Bern [80, 81]. To match the revolution frequency of KARA, it has been adapted to achieve a repetition rate of 2.7 MHz. The oscillator cavity from the setup at KARA initially produces a laser pulse rate of ∼62.5 MHz, which enables a reduction to KARA's repetition rate of ∼2.7 MHz by selecting every 23rd laser pulse with a pulse picker before entering the gain fiber in the amplifier.

Figure 3.2 presents a photograph and corresponding schematic of the laser oscillator. It has an in-fiber and a free-space section, which are coupled via fiber collimators. The in-fiber section provides

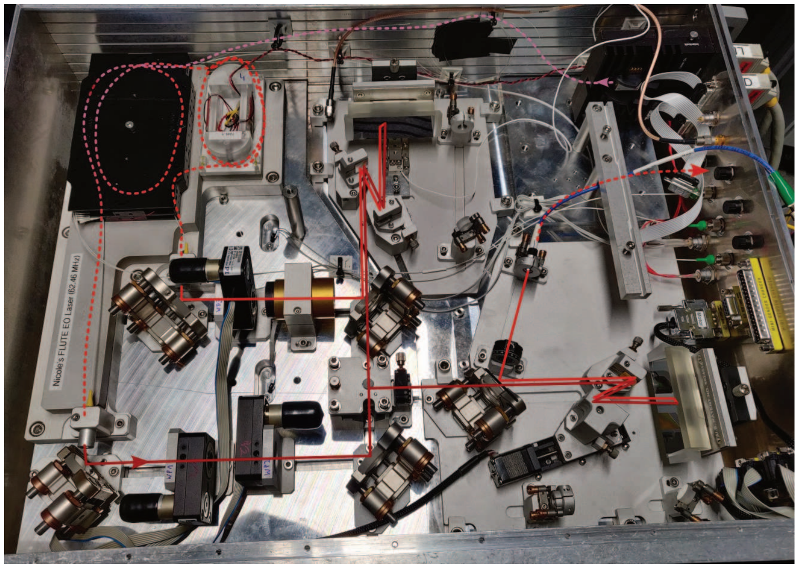

(a) Photo

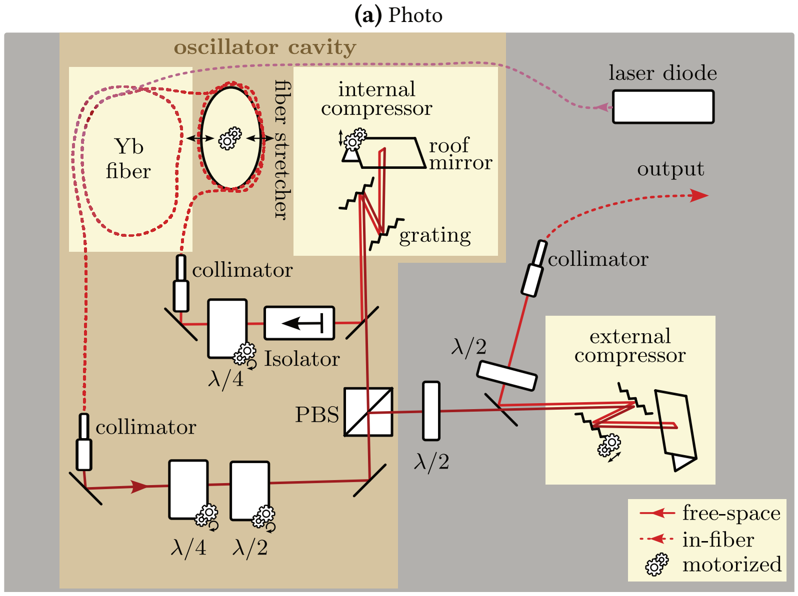

(b) Schematic

Figure 3.2: Photograph (a) and corresponding schematic (b) of the laser oscillator for the EO system at KARA (originally described in [27, 80]). The oscillator provides femtosecond pulses at a central wavelength of 1 030 nm with a repetition rate of ∼62.5 MHz. In both figures, the free-space laser path is indicated as a solid red line, and the in-fiber laser path as a dashed line. Motorized elements are marked with a small gear pictogram. The oscillator ring cavity contains the Ytterbium (Yb) gain fiber, which is pumped by a laser diode. Two motorized $\lambda/4$ waveplates and a $\lambda/2$ waveplate can be used to initiate and stabilize mode-locking. A piezo fiber stretcher enables fine adjustment of the cavity size, and a linear piezo stage under the roof mirror of the internal compressor enables a coarse adjustment of the cavity size to tune the laser pulse repetition rate. A polarizing beam splitter (PBS) is installed for out-coupling of a fraction of the intra-cavity pulses. These output laser pulses are guided onto an external grating compressor with a movable grating to adjust their chirp and pulse length. The final oscillator laser output is transported through a PM fiber to a laser amplifier (see 3.3).

integrated fiber optic splitters (not included in the schematic) that redirect a small part of the laser light to diagnostic outputs. These outputs can be used to monitor the spectrum or power of the laser oscillator, or it can be used as a reference for the synchronization to the KARA RF (see next section). Part of the main fiber is an Yb doped gain fiber, which is pumped with a fiber coupled laser diode with ∼980 nm wavelength. Additionally, a piezo stretcher is installed to to remotely fine-tune the overall length of the oscillator cavity by stretching a part of the optical fiber, which is used to fine tune the laser pulse repetition rate.

In free-space, the oscillator cavity includes two motorized $\lambda/4$ and one motorized $\lambda/2$ waveplate to set the intra-cavity polarization and to initialize mode-locking and stabilize the laser pulses. An isolator is installed to avoid back-reflections. Two gratings and a roof mirror on a motorized linear stage form a grating compressor, where the movement of the mirror is used to adjust the optical path length within the oscillator cavity. Thus it provides a mechanism for coarser laser pulse repetition rate adjustment, complementing the fine-tuning capability of the fiber stretcher.

A polarizing beam splitter cube is used to as an output coupler, where a controlled fraction of the circulating pulses can exit the cavity, depending on its polarization. The mentioned waveplates can be used to manipulate the polarization, thus adjusting the output-coupling ratio.

The oscillator output is sent through a $\lambda/2$ waveplate to rotate its polarization for optimal efficiency of the following grating compressor. The grating compressor is made similar to the intra-cavity compressor of two gratings and a roof mirror. But this external compressor has the second grating on a motorized linear stage, to enable stretching or compressing the pulses. The main goal of this compressor is to (partly) pre-compensate the dispersion of the following optical fibers, that transport the laser pulses to the EO crystal. While the normal dispersion of the optical fiber leads to a stretched pulse with a positive chirp, the compressor provides an anomalous dispersion, producing a negative chirp. By increasing the distance between the two gratings with the linear stage, the magnitude of the anomalous dispersion can be adjusted. This enables to pre-compensation for the stretching in the fiber within the limits of the linear stage and within beam alignment limitations to avoid beam-clipping.

Finally, an additional $\lambda/2$ waveplate is used to align the linear polarization to optimize the coupling efficiency for the following PM fiber. The PM fiber guides the laser light to the pulse picker and following laser amplifier.

A photograph and corresponding schematic of the amplifier is presented in Fig. 3.3. The amplifier is fully in-fiber and positioned directly above the oscillator. The oscillator output is used as input and guided through an isolator to an acousto-optic modulator (AOM), which serves as a pulse picker. Per default, the AOM does not transmit the laser pulses, if no signal is applied at the electric RF input. The laser pulses from the oscillator are spaced by ∼16 ns, hence the RF driver at KARA is typically set to provide a signal window with a duration of 15 ns at KARA's revolution frequency of ∼2.7 MHz. Thus, it reduces the pulse repetition rate of the laser to match KARAs revolution frequency. After the pulse picker, the laser pulse is amplified with a Yb gain fiber, which is pumped by a 980 nm laser diode.

A typical spectrum of the oscillator and amplifier output is presented in Fig. 3.4. The spectra depend on the mode-lock state of the oscillator, which can can change over time. However, the presented spectra are the result of the most commonly used mode-lock state for KARA EO measurement. The bandwidth of the amplifier (∼25.3 nm FWHM) is slightly larger than the bandwidth of the oscillator (∼24.7 nm FWHM), and extends further towards lower wavelengths. The center wavelength is typically defined as the wavelength of maximum intensity, which is similar for the oscillator (∼1 031 nm) and amplifier (∼1 034 nm). However, the center wavelength can be misleading, if the maximum intensity originates

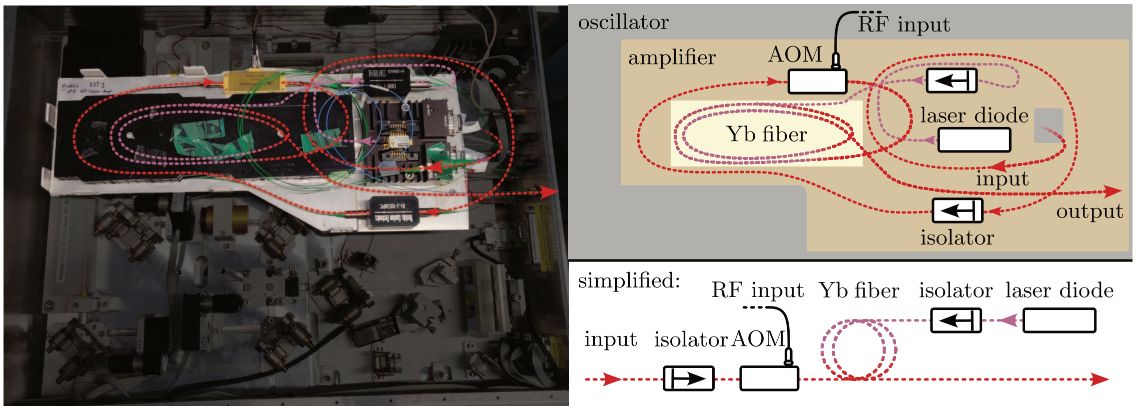

(a) Photo **(b)** Schematic

Figure 3.3: Photograph (a) and schematic (b) of the amplifier from the EO laser system (originally described in [27, 80]). A simplified schematic was added below the original schematic for better readability. The amplifier receives the laser pulses from the oscillator with 62.5 MHz, reduces the repetition rate with a pulse picker and amplifies the resulting pulses. The input pulses first pass an isolator to suppress any back-reflections from the following pulse picker and Yb gain fiber. The pulse picker is made of an acousto-optic modulator (AOM), which is controlled with an electric RF trigger signal. Similar to the oscillator in Fig. 3.2, the gain fiber of the amplifier is pumped with a 980 nm laser diode, with another isolator in-between.

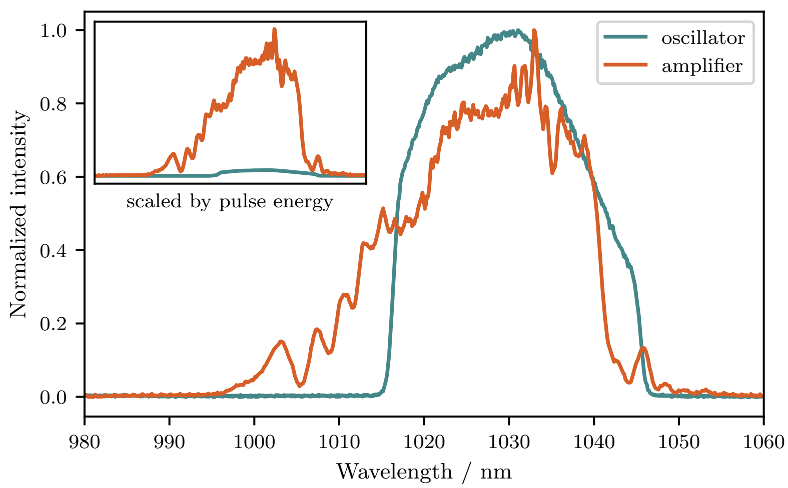

Figure 3.4: Typical normalized spectra of the laser oscillator (blue) and amplifier (orange) of the EO laser system at KARA. The oscillator spectrum has a slightly smaller bandwidth (∼24.7 nm (full width at half maximum (FWHM))) than the amplifier (∼25.3 nm (FWHM)) and center wavelength of the oscillator (∼1 031 nm) is very close to the center wavelength of the amplifier (∼1 034 nm). The inset plot shows the spectra scaled according to their relative laser pulse energy, which highlights the ∼23-fold increase in pulse energy of the amplifier. This is an example of a typical laser spectrum for measurements at KARA, but the spectrum can change drastically for different mode-lock states and for small differences in the laser setup [26, 80]

from a narrow spike in the spectrum, which is the case for the presented amplifier spectrum. To better represent the range of the spectrum, the centroid of a discrete spectrum with N samples

$$\text{centroid} = \frac{\sum_{i=0}^{N-1} \lambda_i \cdot I(\lambda_i)}{\sum_{i=0}^{N} I(\lambda_i)} \tag{3.1}$$

provides a measure for the central wavelength weighted by the intensity spectrum. The centroid of the oscillator spectrum (∼1 030 nm) is close its wavelength of maximum intensity, but the amplifier centroid (1 026 nm) is shifted to lower wavelengths due to its intensity spectrum.

The output power also depends on the mode-lock state, and in the presented state, it typically achieves 10 mW at 2.7 MHz, which corresponds to a laser pulse energy of 3.7 nJ. This implies an amplification factor of approximately 23, since the oscillator typically achieved around 10 mW at 62.5 MHz. The inset plot in Fig. 3.4, shows the spectra scaled according to their respective pulse energy to illustrate the amplification. Thus, the laser power and the bandwidth are lower than the corresponding values in Ref. [27, 80, 81], which show amplification up to a factor 100 and a bandwidth up to 100 nm. The main reason for different spectra and output power likely originates in the aging of the different components of the laser system and different laser path alignment, which lead to different stable mode-lock states and increased power loss in the oscillator cavity. The presented bandwidth and power output is a result of many optimization efforts and is considered to be sufficient to perform EOS and EOSD measurements.

The amplifier output provides pulses with an approximate duration of ∼55 fs FWHM (∼23 ps σ), as measured using a GRENOUILLE (Swamp Optics GRENOUILLE, a single-shot frequency-resolved optical grating (FROG) device for ultrashort pulse characterization [82]). The short pulse duration aligns with the expectation of the mode-locked laser system, and its time bandwidth-product of ∼0.4 is close to the theoretical value of ∼0.44 for a Gaussian pulse (see Eq. 2.40). To estimate the pulse duration at the EO crystal, the amplifier output was coupled into two consecutive PM fibers with a total length of 42 m within the EO laboratory. Due to the fiber dispersion, the pulse is stretched, falling outside the measurement range of the GRENOUILLE. Instead, an autocorrelator (APE pulseCheck) yielded a pulse duration of approximately 60 ps (FWHM, $\sigma \approx 25.5\,\mathrm{ps}$). Although the statistical uncertainty in these measurements is negligible, the instruments are very sensitive to optical misalignment, which may introduce large systematic errors. Hence, the reported pulse durations should be regarded as rough estimates only.

To crosscheck the feasibility of the measured pulse length, the stretched pulse can be calculated via the unchirped pulse length before the fiber ($\tau_{\text{trans-lim}} \approx 55\,\mathrm{ps}$) and the group delay dispersion D_2 of the fiber

$$D_2 = \frac{\sqrt{\tau^2_{\text{stretched}} - \tau^2_{\text{trans-lim}}}}{\Delta\omega} \Rightarrow \tau_{\text{stretched}} = \sqrt{(D_2\Delta\omega)^2 - \tau^2_{\text{trans-lim}}} \tag{3.2}$$

with the angular-frequency bandwidth

$$\Delta\omega \approx \frac{2\pi c}{\lambda_0^2}\Delta\lambda, \tag{3.3}$$

with the central wavelength λ_0 and wavelength bandwidth $\Delta\lambda$.

This calculation yields a stretched pulse length $\tau_{\text{stretched}} \approx 52\,\mathrm{ps}$ FWHM (22 ps σ), using the measured pulse duration directly after the amplifier $\tau_{\text{trans-lim}} = 55\,\mathrm{fs}$ FWHM (23 fs σ) with the fiber length $L = 42\,\mathrm{m}$ and the provided fiber dispersion[1]by the manufacturer for a wavelength of $\lambda_0 = 1\,025\,\mathrm{nm}$ [83] . Thus, the calculated pulse length deviates by ∼9 % from the measured pulse length, indicating that the magnitude is captured correctly, but the large uncertainties do not allow a more precise assessment.

[1] The dispersion of optical fibers with the fiber length L.is typically denoted as the conventional fiber-optic dispersion

$$D = -\frac{2\pi c}{\lambda_0^2 L} D_2 \qquad \text{(typ. in ps nm}^{-1}\,\text{km}^{-1}\text{)}.$$

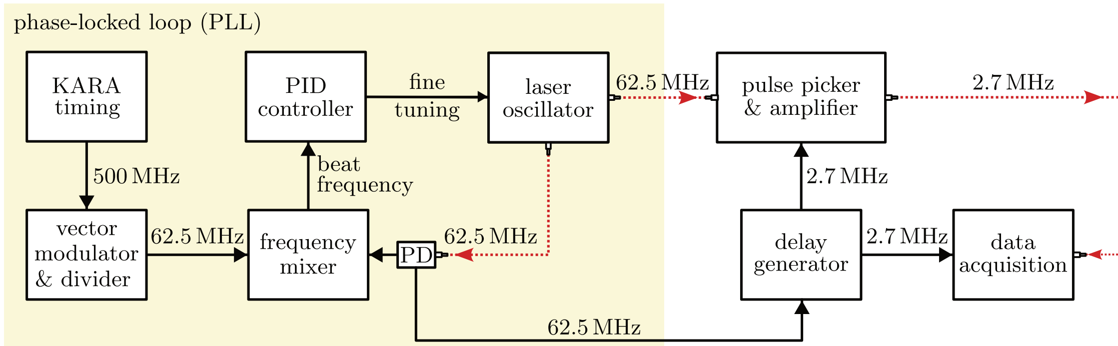

Figure 3.5: Schematic overview of the synchronization of the EO laser system and the data acquisition. Electric signals are drawn as solid black arrows, while optical fibers for the laser light are drawn as dotted red arrows.

3.1.2.2 Synchronization

The laser pulses and Coulomb field of the electron bunches need to have a temporal overlap in the EO crystal to enable EO measurements. Hence, the laser pulse repetition rate needs to be synchronized with the revolution frequency of KARA. KARA has a timing distribution system, which provides a reference frequency in the EO laboratory, that is synchronized with the KARA master oscillator. The master oscillator also serves as a reference clock for the $\sim$500 MHz RF frequency to drive the RF cavities of the KARA storage ring. Since the revolution frequency is an integer fraction of the RF frequency (see Equation 2.5), the distributed timing system is used as a reference frequency to synchronize the laser repetition rate.

The laser synchronization system has been updated iteratively during this thesis to improve its stability and usability. The following description refers to the setup in use since 2022, which was used for the following example measurements.

A simplified schematic overview of the synchronization system for the EO system at KARA is presented in Figure 3.5. The laser oscillator is synchronized with the KARA master oscillator in a phase-locked loop. The laser oscillator has a repetition rate around 62.5 MHz, and a diagnostic laser output is used to feed a signal with the current repetition rate into a frequency mixer via a photodiode. The other input of the frequency mixer is a 500 MHz signal from the KARA timing system, which went through a frequency divider with factor 8, to get the reference frequency close to 62.5 MHz. The mixing of the laser repetition rate with the reference frequency results in a beat frequency, which is low-pass filtered and used as input for a proportional-integral-derivative (PID) controller. The output of the PID is connected to the driver of the piezo stretcher within the laser oscillator. The piezo stretcher can slightly increase or decrease the oscillator cavity length by stretching part of the optical fiber, thus tuning the repetition rate of the laser. This feedback loop forms a phase-locked loop (PLL) that keeps the laser repetition rate and phase locked to the reference.

For coarse adjustments of the repetition rate, the motorized roof mirror of the internal compressor (see Figure 3.2) can be used. Typically, the coarse adjustment is done manually, until the beat frequency drops below 20 Hz. Below this threshold, the phase-locked loop (PLL) is activated to automatically fine tune the laser repetition rate and lock it to the reference frequency. Additionally, the voltage for the piezo stretcher is monitored and if it increases above a certain threshold, a coarse step of the roof mirror is initiated. This enables to reduce the voltage on the piezo stretcher again and therefore compensate for fast or long-term drifts of the beat frequency.

In addition, a delay generator (Stanford Research Systems DG645) is used to provide synchronized signals for different purposes. It gets a 62.5 MHz trigger input via a photodiode from a diagnostic output of the laser oscillator, and its internal pre-scaler is set to 23 to divide the frequency to 2.7 MHz. As a result, the signals generated by the delay generator are synchronized with the laser repetition rate. One of its outputs provides the trigger signal for the pulse picker, hence reducing the laser repetition rate from 62.5 MHz to 2.7 MHz. Another output is used as a trigger signal for Karlsruhe line array detector for MHz-repetition rate spectroscopy (KALYPSO) during EOSD data acquisition to synchronize the camera frame rate with the laser repetition rate.

The PLL also enables to change the phase, and therefore the delay of the laser pulses. A vector modulator (VM) is installed to change the phase of the reference frequency, before entering the frequency mixer. The VM can adjust the phase of the reference signal in small steps, and when the phase of the reference signal changes, the PLL will change the phase of the laser pulses accordingly. This is a very important aspect for time scans with EOS, and for the time calibration of EOSD, where the laser delay needs to be changed in small and precisely known steps.

3.1.2.3 EO interaction module

A photograph and schematic of the EO interaction module of KARA is presented in Figure 3.6. It has an optics box, which is a metal enclosure that contains free-space optics components with a fiber coupled input and output. The photo shows a mock-up in the EO laboratory, without the surrounding vacuum chamber to provide better accessibility for testing purposes. The EO optics box at KARA is connected to a metal arm with the crystal holder at its tip. At KARA, the arm and crystal holder are fully enclosed in KARA vacuum chamber, and a fused silica vacuum window at a CF flange between the optics box and the arm enables the laser transport from and to the EO crystal. Additionally, a vacuum-tight bellow below the vacuum window in combination with a linear stage enables moving the whole interaction module up and down to adjust the distance between the EO crystal and the electron beam.

The laser input of the interaction module is a PM fiber with a collimator to couple the laser from the fiber into free-space. To guarantee the linear laser polarization in the EO crystal (typically parallel or perpendicular to the Coulomb field, see Chapter 2.2.2), the laser pulses are guided through a $\lambda/2$ waveplate and a PBS, before they are sent through the arm to the EO crystal. Silver mirrors are used to align the laser path, which can introduce a slight ellipticity to the linearly polarized laser light due to imperfections causing a phase shift between p- and s-polarized light. This effect is mitigated by aligning the laser polarization to be either fully s- or p- polarized, which is done by rotating the input collimator and the mentioned $\lambda/2$ waveplate accordingly.

At the crystal assembly, the laser is reflected off a small mirror through the EO crystal. The EO crystal at KARA is a 5 mm × 5 mm × 7 mm GaP crystal, with the front surface in the (110) plane of the crystal structure. The laser enters the crystal in $[110]$ direction through the front surface, which has an anti-reflective coating to maximize the laser pulse transmission. Its linear polarization axis is aligned with the crystals $[001]$ axis, perpendicular to the Coulomb field of the passing electron bunches (see Chapter 2.2.2). After traveling through the full crystal thickness of 7 mm, it is reflected on its backside due to an applied reflective coating. On the way back through the crystal, the laser pulses travel parallel to the electron beam at KARA, before leaving the crystal through its front side, reflecting off the small mirror and propagating back through the arm into the optics box.

The optics box contains a polarization analyzer consisting of a motorized $\lambda/4$ waveplate and $\lambda/2$ waveplate followed by a PBS to adjust the working point of the EO measurement (see Chapter 2.2.3). The PBS transmits only the p-polarized part of the light and reflects the remaining part at a 45° angle. In

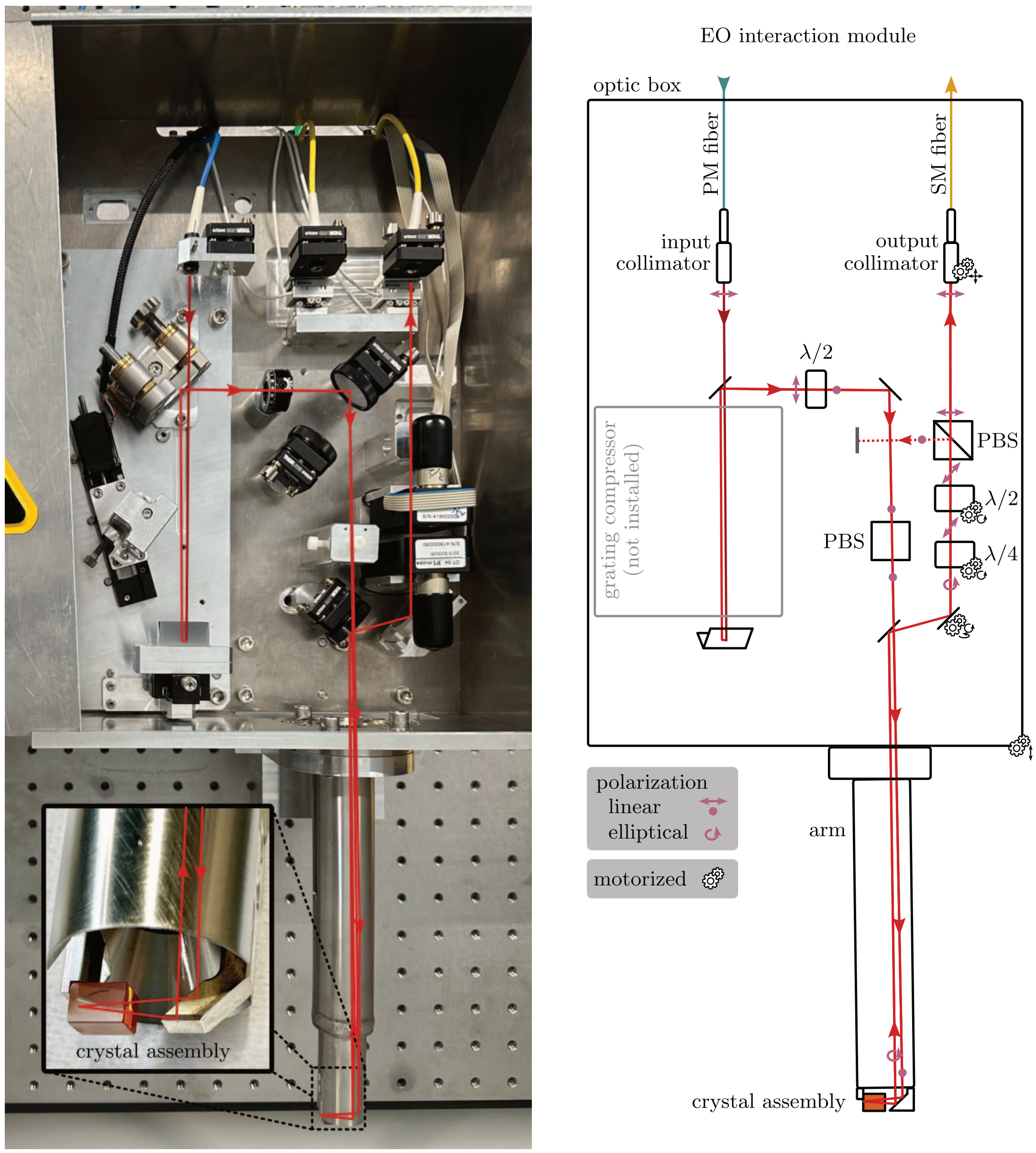

(a) Photograph **(b)** Schematic

Figure 3.6: Photograph (a) and schematic (b) of the EO interaction module at KARA (originally described in Ref. [27]). The photograph shows a duplicate in the laboratory, because the original interaction module is positioned at the KARA ring, where the arm and crystal holder are hidden inside the vacuum chamber. The optics box contains free-space optical components, except for an input and output fiber, which is coupled with a collimator. The input laser pulses are guided through a $\lambda/2$ waveplate and PBS to ensure the correct polarization before it is sent through the arm onto the mirror and EO crystal (crystal assembly). The backside of the 7 mm thick gallium phosphide (GaP) crystal has a reflective coating to send the laser pulses back to the mirror, through the arm and into the optics box. The following series of a motorized $\lambda/4$ and $\lambda/2$ waveplate in combination with a PBS builds a polarization analyzer and is used to set the working point for the EO measurements, before it is coupled into a SM fiber to transmit the laser pulses back to the EO laboratory. The laser polarization and its changes along its trajectory, caused by the waveplates and the intrinsic birefringence of the crystal, is indicated with purple arrows. The setup generally has the option to install an additional grating compressor to modify the laser pulse length, but it was not used for the measurements at KARA.

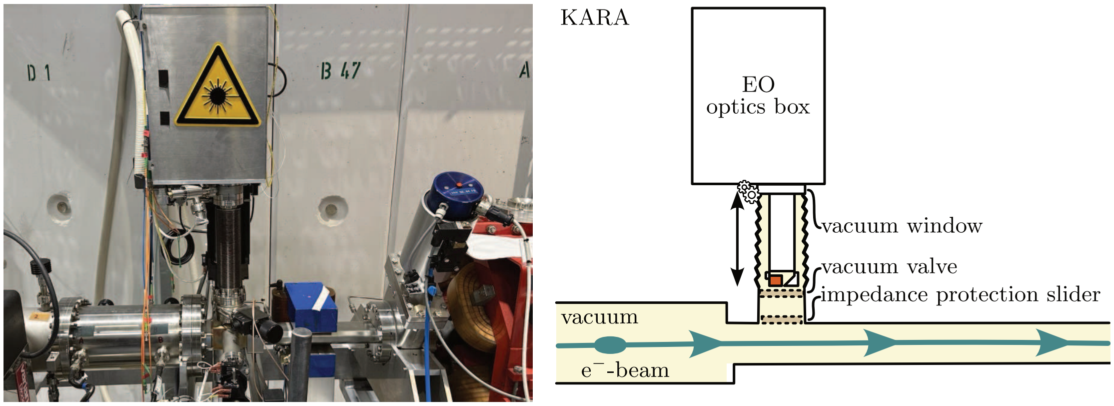

(a) Photograph **(b)** Schematic

Figure 3.7: Photo (a) and simplified schematic (b) of the newly installed EO vacuum chamber at KARA in summer 2025. It is installed above the KARA vacuum chamber and includes a new vacuum valve above the impedance protection slider. This enables to exchange the EO crystal and its holder without ventilating the KARA beam pipe directly. Similar to the previous setup (see Ref. [27, 34]), the EO interaction module with its crystal assembly is installed on a motorized linear stage to adjust the distance between the electron beam and the EO crystal. During EO measurements, the vacuum valve and impedance protection slider are opened, but otherwise the slider is closed to reduce the impedance for the electron beam.

principle, the p-polarized and s- polarized part can both be coupled into fibers and used for a balanced detection setup. However, for the following experiments, only the p-polarized part is coupled into a SM fiber by a collimator and used as output of the interaction module, as it simplifies the data acquisition and was found to provide a sufficient signal-to-noise ratio. A second collimator is installed to couple the s-polarized part into a fiber in preparation for balanced detection schemes, but it has not been used in this thesis.

The coupling efficiency into a SM fiber is very sensitive to the position and orientation of incoming laser light and requires precise alignment of the optical components on the µm scale. Since the interaction module is mounted on a motorized linear stage to adjust the distance between the crystal and the electron beam, its movements can cause slight misalignments of the laser path, leading to a reduced coupling efficiency at the output collimator. However, the interaction module is not accessible during KARA operation. Thus, the output collimator and one mirror are motorized to enable precise remote adjustments of the laser alignment.

In summer of 2025, the EO vacuum chamber was updated and fully replaced to add a vacuum-valve in the vertical direction between the arm of the EO interaction module and the beam pipe of KARA. A photo and corresponding schematic of the new setup is presented in Figure 3.7. The previous setup already included an impedance protection slider, which could be opened for EO measurements, while being closed during user operation to reduce the impedance for the electron beam. The new additional vacuum valve enables to exchange the EO crystal without ventilating the KARA beam pipe, and instead only ventilate a small section around the arm of the EO interaction module. This reduces the time needed for a crystal exchange from multiple weeks to only a couple of days, making the EO monitor at KARA a versatile EO test bench for different crystals and crystal holder designs. While I took part in the successful commissioning of the EO monitor with the new vacuum chamber, further experiments, for example with the EO prototype design for FCC-ee, are planned in the future but outside the scope of this thesis.

3.1.2.4 Data acquisition

The data acquisition devices of the EO system are located in the same laboratory as the EO laser system. The laser pulses are transported from the EO monitor output to the EO laboratory with a 35 m SM fiber. For EOS measurements, it is connected to a fiber-coupled photodiode (EOT ET3010) with an indium gallium arsenide (InGaAs) sensor. With a rise time of 175 ps ($\sim$2 GHz bandwidth), the photodiode cannot resolve the temporal profile of single laser pulses, but the signal amplitude correlates with the laser pulse intensity. For typical EOS scans, the signal amplitude is monitored with an oscilloscope (LeCroy HDO9404-MS), while scanning the laser pulse delay. Since the measured laser intensity changes, if the laser pulse is modulated by an electric field in the EO crystal, this method enables time scans of the Coulomb field and following wakefield of the electron bunch. In addition, it is typically used to determine the laser pulse delay at which the laser pulse overlaps with the Coulomb field of the bunch in the EO crystal.

To improve the signal-to-noise ratio (SNR) of EOS scans a lock-in amplifier (Anfatec eLockIn 205/2) can be used to further process the photodiode signal. It multiplies the signal with a 2.7 MHz reference signal that matches the repetition rate of KARA and applies a low-pass filter to the result. For example, for EOS time scans at KARA, the laser pulse delay is adjusted every $\sim$1.25 s and the time constant of the laser pulse is set to 1 s. This acts similarly to a narrow band-pass filter that isolates the slow dynamics of the signal component, which matches the repetition rate of KARA. Hence, it drastically reduces noise, while keeping slow changes of the laser pulse amplitude during EOS time scans.

For the single-shot bunch profile measurements with EOSD, the 35 m fiber is connected to a spectrometer instead of the photodiode. The spectrometer is a free-space setup based on a reflective grating that disperses the laser light. The angular dispersion is focused with a spherical lens and recorded with the KIT-built line-array camera KALYPSO (Karlsruhe line array detector for MHz-repetition rate spectroscopy) [72]. The spectrometer is based on Ref. [71], but the commercial camera was replaced by KALYPSO with a 256 pixels silicon (Si) sensor array to enable turn-by-turn single-shot EOSD measurements at 2.7 MHz [20, 35].

3.1.3 Example measurements at KARA

This chapter presents an example measurement of EOS and EOSD at KARA, respectively. These EO measurements were used to gain experience with the EO monitor's capabilities and limitations and provide a baseline for the development of an EO monitor for FCC-ee. It also serves as a reference for a new simulation procedure, which is later used to test and develop the new conceptual EO monitor design for FCC-ee (see Chapter 4). The exemplary EOS measurement in this section has also been summarized and presented in Refs. [1, 3].

3.1.3.1 EOS measurements at KARA

For this EOS scan, KARA was operated in it short bunch (low-α_c) mode at 1.3 GeV with a single bunch in the storage ring. The bunch charge started at approximately 0.35 nC and decreased to 0.27 nC by the end of the scan. Before the scan, the linear stage at the EO monitor was used to slowly decrease the distance of the EO crystal to the electron beam, until a slight increase in the signal of a nearby beam loss monitor was detected. The beam loss monitor is positioned close to the KARA vacuum chamber downstream of the EO monitor. It detects the Cherenkov light of charged particles through a lead-glass radiator with a photomultiplier tube (see Ref. [84, pp. 26 ff]). Once it shows a slight increase in the

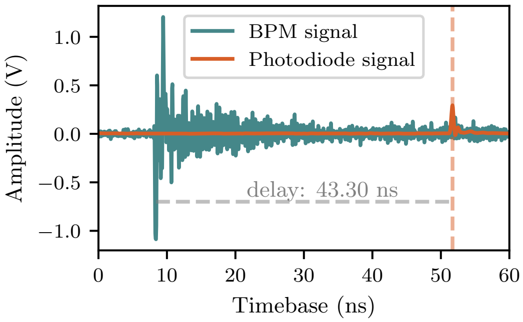

Figure 3.8: Waveforms of the BPM signal and laser pulse signal from the photodiode (PD) on the oscilloscope in the EO lab. From prior experience, a ~39.5 ns delay between BPM signal and laser pulse signal achieves temporal overlap of the laser pulse and the Coulomb field of the electron bunch in the EO crystal. In this case, the delay is 43.3 ns, because the following EOS scan covers a range of −4 ns to stop at 39.3 ns delay, hence the temporal overlap with the Coulomb field and following wakefield is included in the EOS scan range.

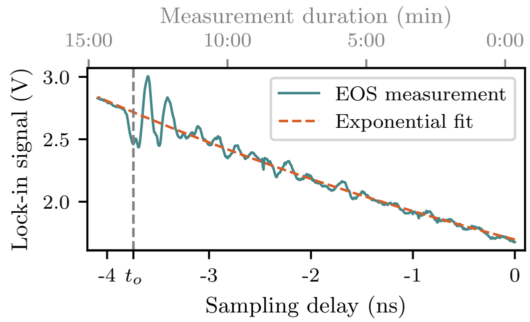

Figure 3.9: Example of a lock-in amplifier signal during an EOS scan at KARA. The laser delay is shifted in steps of ~−6 ps for a total range of 4 ns, while the laser pulse signal of the photodiode is processed with a lock-in amplifier and recorded with an oscilloscope. With ~1.25 s per step, the total measurement duration is ~15 min and the time constant of the lock-in amplifier's low-pass filter was set to 1 s to provide step-to-step laser signal changes. The baseline of the raw data increases over the duration of the measurement, which is probably caused by a temperature drift of the EO crystal [3]. An exponential fit is used to estimate the baseline drift, yielding $y \approx 1.70\exp(-0.13x)$. (Also presented in [1, 3])

signal counts while moving the crystal closer to the beam, it is assumed that some of the electrons at the outer edge of the electron bunch are deflected into the beam loss detector. Thus, the distance between the EO crystal and the electron beam is considered to be a good balance between minimal distance for high sensitivity and sufficient distance to avoid impacting the trajectory of the electron bunch. In this example, a slight beam loss increase was detected at 7 mm distance between the crystal center line and the geometric center of the KARA vacuum chamber. This value is expected to be similar to the distance between the crystal center and the electron beam center, because fast-feedback systems at KARA keep the beam typically close to the geometric center of the vacuum chamber.

With KARA's revolution frequency of ~2.716 MHz, the electron bunch arrives at the EO crystal every ~368 ns, and the laser repetition rate is synchronized to the same frequency. Since the electron bunch and laser pulse duration is typically of the order of 10 ps, the temporal overlap between the electron bunch and the laser pulse in the EO crystal is very short compared to the time span in-between the electron bunches. Thus, the electric signal of a beam position monitor (BPM) on the oscilloscope in the EO laboratory provides a reference timing of the electron bunch arrival time. The photodiode of the EOS data acquisition is connected to the same oscilloscope, providing a signal of the EO laser pulse after it propagated from the laser system to the EO monitor and back to the EO laboratory. Rough estimations of the signal propagation time from the BPM to the oscilloscope in comparison to the laser pulse signal from the EO crystal to the oscilloscope can be used to approximate the required delay between the BPM and laser pulse signal on the oscilloscope to achieve temporal overlap of the electron bunch with the laser pulse in the EO crystal. Previous long EOS time-scans suggest that the laser pulse starts to overlap with the bunch's Coulomb field in the EO crystal at a delay of ~39.5 ns between BPM signal and laser pulse signal.

Figure 3.8 presents the waveforms of the BPM signal and laser pulse signal on the oscilloscope, before the following EOS scan started. The delay between BPM signal and laser pulse signal is 43.3 ns, hence the EOS scan was set to cover a time range of 4 ns in negative direction to include part of the wakefield and stop shortly after passing the temporal overlap at a delay of ∼39.5 ns.

The raw lock-in amplifier signal of the EOS scan is presented in Figure 3.9. In the scan, the laser pulse starts at the delay of 43.3 ns to the BPM signal and is shifted in ∼−6 ps steps to a total range of 4 ns. The delay shift is realized by changing the phase of the reference frequency with a vector modulator, as described in Section 3.1.2.2. The x-axis of the plot shows the relative sampling delay to the starting point in ns. Every step of the delay scan took approximately 1.25 s, leading to a total measurement duration of approximately 15 min. The time constant of the lock-in amplifier was set accordingly to 1 s to highlight changes in the photodiode signal from one time step to the next (see 3.1.2.4). The resulting signal represents changes of the laser pulse intensity. Its first peak (the earliest in time) at $t_\mathrm{o} \approx -3.74\,\mathrm{ns}$ indicates the laser modulation induced by the Coulomb field of the electron bunch. The following oscillations are caused by the wakefield that follows the electron bunch.

However, the signal baseline increases during the scan. The baseline drift has been characterized by fitting an exponential function, yielding $y = (1.697 \pm 0.005)\,\mathrm{V} \cdot \exp((-0.126 \pm 0.001)\,\mathrm{ns}^{-1} \cdot x)$, with y corresponding to the lock-in amplifier signal and x the sampling delay. The drift also has been observed in experiments, where the sampling delay has not been changed. Hence, it does not correlate with the sampling delay directly, but with the measurement duration. The drift is hypothesized to arise from an electron-bunch-induced temperature change of the EO crystal, which causes a change in the intrinsic birefringence of the EO crystal. The hypothesis is investigated with a qualitative experiment presented in Chapter 3.1.4 and Ref. [3].

In the experiment, it was found that the drift behaves similarly to a shift of the working point, because it is mainly caused by a laser polarization change at the EO crystal. In the EOS measurement, the initial working point was set to the $\lambda/2$ waveplate angle $\theta = 4.6°$ and $\lambda/4$ waveplate angle $\phi = 0°$, which is a typical setting to optimize the modulation amplitude at KARA [27]. However, the heat-induced shift of the laser polarization changes the effective working point over time, which needs to be considered when trying to replicate the results in simulations (see Chapter 4.2).

To determine the current effective working point, one needs to determine how far θ and ϕ need to be shifted to achieve the minimum laser pulse amplitude (crossed configuration, see Chapter 2.2.3). Thus, a scan of θ was done directly after the EOS scan, while recording the laser pulse intensity with the photodiode. When the minimum $\theta = \theta_\mathrm{min}$ is found, the $\lambda/4$ waveplate angle ϕ requires a similar scan to find the angle ϕ_min, where the laser pulse amplitude is minimal. This process is typically repeated multiple times to iteratively decrease the minimum laser pulse amplitude and get closer to the crossed configuration, because θ and ϕ are not independent variables of the laser intensity $I(\theta, \phi)$ (see Equation 2.37). However, as the effective working point is changing over time during these example measurements, the working point of $\theta = 2°, \phi = 7°$ has been estimated for the sampling point at t_o by interpolating between a working point determination before and after the experiment.

The modulation of the signal is calculated by dividing the signal by the exponential baseline fit, which is presented in Figure 3.10. To compensate for the decreasing bunch charge q during the measurement, the modulation is also multiplied by $q(t_\mathrm{o})/q(t)$. Additionally, the uncertainty of the modulation is estimated by propagating the uncertainty of the exponential fit $\sigma_\mathrm{fit}(t)$ and calculating the noise as standard deviation of the modulation σ_noise before the bunch arrives ($t < 0.2\,\mathrm{ns}$). Both uncertainties are combined $\sigma = \sqrt{\sigma_\mathrm{fit}^2(t) + \sigma_\mathrm{noise}^2}$ and included as a 1σ error band in the plot. The estimated uncertainty is small compared to the modulation minimum at −9.77 %, which yields a decent peak amplitude with

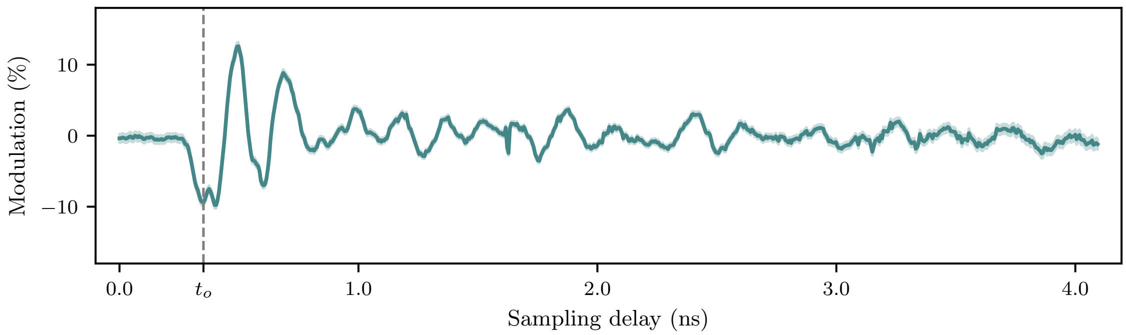

Figure 3.10: Modulation of the EOS signal after processing the data of Fig. 3.9. The modulation is calculated by dividing the raw signal by the baseline. The first peak of the modulation at t_o is induced by the Coulomb field of the electron bunch, and the following oscillations originate in the wakefield. The effective working point at t_o is approximated at $\phi = 7°$, $\theta = 2°$ and leads to a negative modulation by the Coulomb field. However, the effective working point drifts over time, due to the laser polarization drift (see Figure 3.9). This EOS scan provides an overview of the Coulomb- and wakefield-induced EO modulation, which is compared to simulations in Chapter 4.2 for further analysis. (Also presented in Ref. [3, 5])

$SNR \approx 19.95$. Direct measurements of the photodiode typically yield a lower SNR, but the lock-in amplifier drastically reduces the noise and increases the SNR.

The Coulomb peak of the EOS scan at t_o overlaps with a neighboring peak with similar amplitude. The next peak is positive and has the largest modulation amplitude of 12.6 %, while the following peaks decrease in amplitude and appear similar to a dampened oscillation. In summary, the EOS scan provides an overview of the timing and amplitude of the Coulomb peak and the following wakefield with a less complex setup and data acquisition than EOSD. Hence, EOS will also be a crucial technique for the EO monitor at FCC-ee for its commissioning, for providing an overview of the wakefield and for finding the overlap with the Coulomb field (t_o). Once the overlap is found, the detection system can be changed from a photodiode to a spectrometer for single-shot high-resolution EOSD bunch profile measurements.

3.1.3.2 EOSD measurements at KARA

For EOSD measurements at KARA, the laser pulses are analyzed with a custom spectrometer for the detection of single laser pulse spectra at high repetition rate [27, 35, 71]. This enables single-shot bunch-profile measurements due to encoding of the longitudinal profile in the spectrum of a chirped laser pulse. KARA was operated in short-bunch mode (low-α_c), with a single bunch in the ring. At the moment of the following EOSD measurement, the electron bunch had a charge of ∼430 pC (equivalent beam current 1.19 mA). The working point of the EO monitor was set to a near-crossed polarizer setting with $\theta = 3°$ ($\lambda/2$ waveplate) and $\phi = 0°$ ($\lambda/4$ waveplate). In preparation of EOSD measurements, 1 000 line-profile images were taken with the line-array camera (KALYPSO [72]) of the spectrometer, but with the laser pulse blocked to only detect the background signal. Hence, the background images only contain electric noise and stray light from the environment, and the average over all background images is subtracted from the following measurements of the laser pulse spectrum.

Figure 3.11a presents a single modulated I_mod and single unmodulated I_unmod laser pulse image of the spectrometer camera with the background image already subtracted. The variance over all measured modulated and unmodulated images was calculated, resulting in a mean standard deviation of the intensity $\overline{\sigma}_\text{mod}$, $\overline{\sigma}_\text{unmod} \sim 12$ arb. u. for both curves. Hence, the standard deviation is too small in

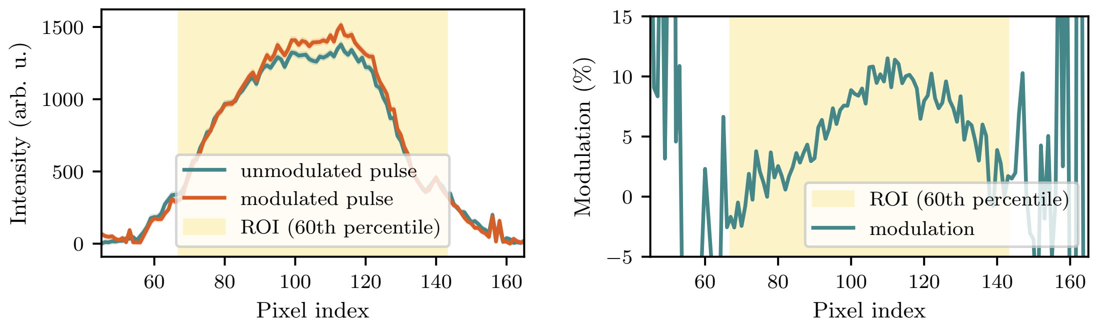

(a) modulated vs. unmodulated laser pulse

(b) modulation

Figure 3.11: KALYPSO images of an unmodulated and modulated laser pulse (a) and its calculated modulation (b). The pixel range is cropped to the section of the sensor that is illuminated by the laser pulses. The background with a blocked laser beam has been subtracted from the both images. The modulation is calculated as a division of the modulated and unmodulated laser pulse image. An error-band around the modulation shows its propagated standard deviation (1σ), which increases as the laser intensity decreases. Later plots will focus on a region of interest (ROI), which is defined as the 60th percentile of the unmodulated laser image, resulting in a pixel index range from 67 to 143.

comparison to typical maxima of the order of 1 500 arbitrary units to be visible in the plot. The laser pulse approximately illuminates the pixels from index 55 to index 165 out of the 256 available pixels. Generally, more illuminated pixels would improve the resolution, but it would reduce the intensity per pixel. The illuminated area changes with the laser pulse spectrum (e.g. for a different laser mode-lock state), and can be adjusted with the layout and components of the spectrometer setup (e.g. grating and lens properties, and the distances in between the components). The presented setup aims to provide a balance between decent resolution and sufficient sensitivity, based on the previous setup in Refs. [27, 71].

Figure 3.11b presents the modulation M following Eq. 2.39

$$M = \left(\frac{I_{\text{mod}}}{\overline{I}_{\text{unmod}}} - 1 \right),$$

which is proportional to the modulated signal I_{mod} divided by the average over 1 024 unmodulated signals $\overline{I}_{\text{unmod}}$. The plot also includes the propagated uncertainty

$$\sigma_M = \sqrt{\left(\frac{1}{\overline{I}_{\text{unmod}}} \sigma_{\text{mod}} \right)^2 + \left(\frac{-I_{\text{mod}}}{\overline{I}^2_{\text{unmod}}} \sigma_{\text{unmod}} \right)^2} \tag{3.4}$$

in the form of an error band to illustrate the standard deviation (1σ). The uncertainty of the modulation appears large in comparison to the uncertainty of the intensity of the modulated and unmodulated signal in Figure 3.11a, and it increases towards low intensity amplitudes. This is a result of calculating the modulation as a division of the modulated and unmodulated signal, hence, the propagated uncertainty is roughly proportional to the inverse intensity of the laser pulse (see Eq. 3.4).

When the laser intensity decreases, small deviations between the modulated and unmodulated signal can lead to large modulation percentages, hence a ROI needs to be defined, in which the noise of the modulation is on an acceptable level. In the following discussions, the ROI is defined by the 60th percentile of the full unmodulated laser pulse image, which results in the pixel index range in this

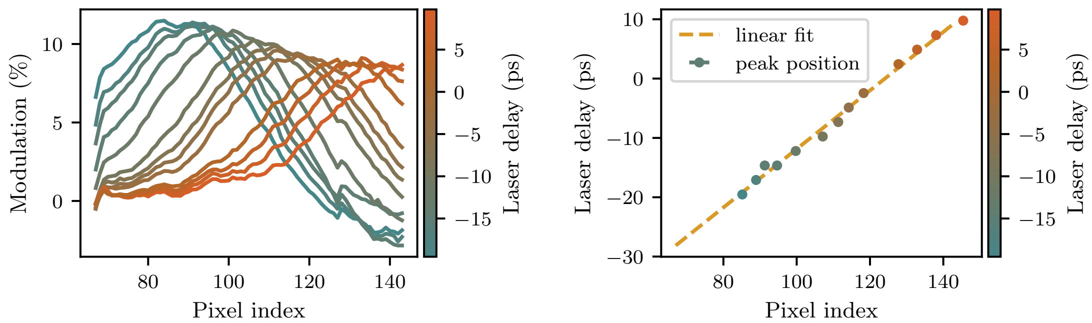

(a) average modulation during a time scan

(b) modulation peak position

Figure 3.12: For the pixels-to-time calibration of the spectrometer, the average modulation at multiple laser delays was measured (a), and the shift of the modulation peak on the camera sensor compared to the laser delay was calculated (b). The shift of the laser delay is indicated with a color gradient from blue (earlier) to red (later), and each curve is the result of an average over 100 000 camera images at a frame rate of ∼2.7 MHz. The color gradient in (b) redundantly encodes the laser delay, and it was added to maintain consistency with (a). A Gaussian function was fitted to the average modulation at every delay step to determine the pixel position of the peak maximum. The inverted correlation between the laser delay and the peak position determines the calibration of the time-axis, and the inverse slope of a linear fit yields the pixel-to-time calibration factor $k_{\text{pt}} \approx (-0.50 \pm 0.01)\,\text{ps/pixel}$.

example from 67 to 143. This ROI definition was determined experimentally, as it provides a decent pixel range with an acceptable noise level.

For the pixel-to-time conversion, the following definition of the time axis is used: The time refers to a relative arrival time of the electric signal in the EO crystal, e.g. the head of the electron bunch profile arrives before the tail, hence the time t_0 of the head is smaller than the time t_1 of the tail. As the laser delay is changed instead of the electron bunch delay during the time-scan, calculating the time axis from the time scan data is counter-intuitive. A positive laser pulse delay causes the same shift of the modulation peak position on the EOSD camera image, as a corresponding negative delay of the electron bunch. Thus, the conversion of the pixel position to the time axis is inverse to the conversion from the pixel position to the laser pulse delay.

For the time scan, the laser pulse delay was shifted with stepwise changes of the VM to adjust the reference signal phase of the PLL (see Chapter 3.1.2.2). 100 000 images were taken at every step, which takes approximately 37 ms per step at the 2.7 MHz frame rate. While the delay of the laser pulse changes, the arrival time of the bunch stays constant, hence the modulation peak on the laser pulse signal appears to shift relative to the laser pulse delay on the spectrometer image.

Figure 3.12a presents the average modulation at every step during the time scan within the previously defined ROI. Due to the large number of samples $N = 100\,000$, the standard error of the mean (SEM) ($\sim \sigma_M/N$) of the averaged modulation is small. To quantify the peak position, a Gaussian function was fitted to the averaged modulation at every step. With an average width of ∼20 pixel (σ), the displayed ROI contains only about 4σ width of the peak. Additionally, the amplitude of the modulation peak changes slightly from one time scan step to the next, which could be caused by wavelength-dependent effects of optical components like the waveplates [27]. It would cause a dispersion of the working point, which would change the modulation amplitude depending on the wavelength within the spectrum. In addition, a modulation shift could be caused by the beam-induced heating of the EO crystal, that causes an effective working point shift over time. However, the impact of the amplitude change on the

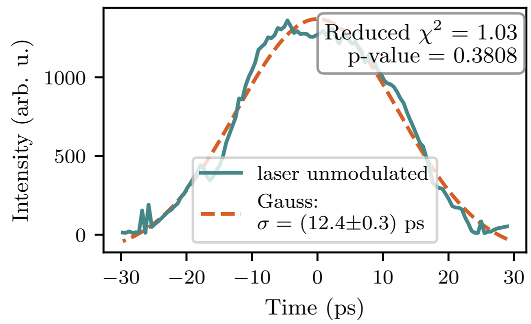

Figure 3.13: Averaged temporal profile of the unmodulated laser pulse with the calibrated time axis. Multiple measures can be used to quantify the laser pulse length: The profile has a FWHM of ∼28.6 ps and yields a root mean square (RMS) width of ∼10.5 ps. The temporal profile was approximated by a Gaussian function to obtain the width parameter $\sigma = (12.6 \pm 0.3)$ ps. The fit achieves a coefficient of determination $R^2 = 0.978$, meaning that 97.8 % of the total variance is reproduced by the Gaussian. However, the residuals show systematic deviations, because the Gaussian function is an approximation and does not perfectly represent the underlying temporal profile.

time calibration is small, because it does not affect the position of the modulation peak on the camera sensor directly.

Figure 3.12b presents the laser delay shift over the pixel-position of the modulation peak (μ from the Gaussian fit). The uncertainty (σ) on the Gaussian fit center is generally too small to be visible in the plot, but it increases towards the edges of the ROI, as an increasing part of the peak is cut off. A linear fit was added to the plot and its inverse slope provides the first-order pixel-to-time calibration factor

$$k_{\mathrm{pt}}{}^{\mathrm{KARA}} = (-0.501 \pm 0.011)\,\mathrm{ps/pixel}. \tag{3.5}$$

The relation between pixel index and time depends on the chirp of the laser pulse and does not necessarily need to be linear. In this case, the linear fit yields a reduced $\chi^2 \approx 0.4$ (p-value ∼0.93), which suggests that the linear function is fully compatible with the data, but the uncertainties might be overestimated.

Figure 3.13 revisits the averaged KALYPSO image of the unmodulated pulse from Figure 3.11a, but with a calibrated time axis instead of the camera pixels. Thus, the plot presents the temporal profile of the unmodulated laser pulse in the EO crystal. To quantify the laser pulse length, a Gaussian function was fitted to the data, yielding

$$\sigma_{\text{laser pulse}} = (12.4 \pm 0.3)\,\mathrm{ps}. \tag{3.6}$$

The pulse shape is typically non-Gaussian, but the Gaussian function is a common approximation to simplify the quantification. In this case, the Gaussian function provides a decent fit to the data, with a coefficient of determination $R^2 = 0.978$. However, small systematic deviations of the data from the fit hint at the fundamental non-Gaussian shape of the laser pulse profile. The difference also appears in the calculated RMS width of ∼10.5 ps, which is smaller than the Gaussian σ. If the signal was perfectly Gaussian, the RMS and the Gaussian σ would be identical. Finally, the pulse width can be quantified as $\mathrm{FWHM} \approx 28.6\,\mathrm{ps}$, which is a commonly used quantity for arbitrary laser pulse shapes.

The electron bunch profile in KARA is changing dynamically due to the synchrotron oscillation, the rotation in the longitudinal phase-space and charge density modulations through collective effects like the micro-bunching instability (see Chapter 2.1.1, and Ref. [50, 57, 61]). Single-shot turn-by-turn EOSD measurements can capture these changes by measuring for example 100 000 images within 37 ms. To

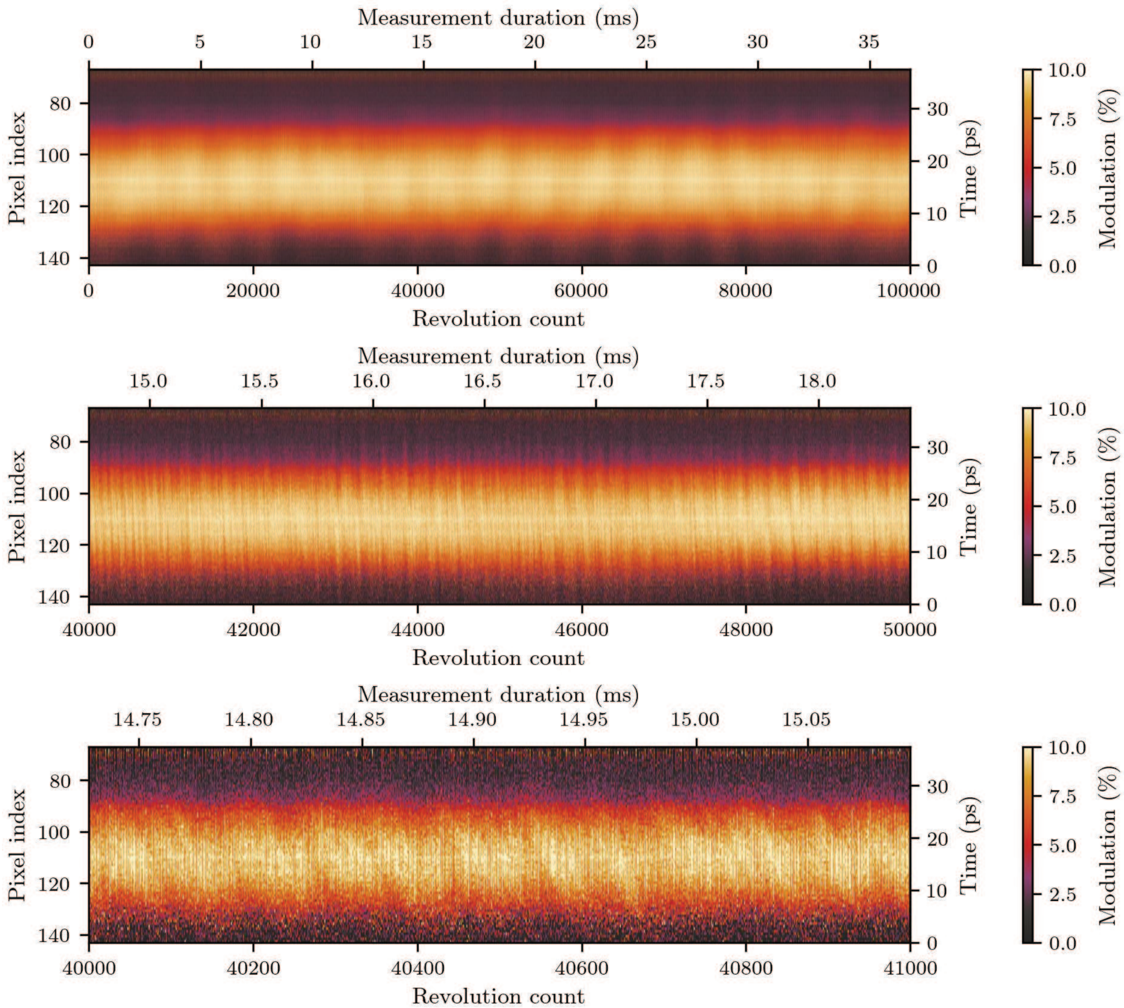

Figure 3.14: Modulation of 100 000 consecutive EOSD images taken the KARA revolution frequency of 2.7 MHz (turn-by-turn). The plots y-axes show the ROI of the camera pixels (left side) and its corresponding calibrated time axis (right side), and its x-axis shows the revolution count of the electron bunch (top axis) and its corresponding measurement time (bottom axis). The top plot presents the full dataset with 100 000 revolutions, the second ranges over 10 000 revolutions and the third plot ranges over 1 000 revolutions. The different x-axis limits highlight the different time scales of different features.

visualize this amount of images, the EOSD modulation data is typically displayed as revolution plots, where the modulation amplitude of the image is color-coded and stacked horizontally [20, 35, 50, 61].

Figure 3.14 presents three revolution plots with decreasing ranges of total revolution counts, providing a zoom on a selected revolution count range. The zoomed-in plots highlight effects at smaller time scales, which are lost in the plots with larger time scales, due to the limited plot resolution and aliasing. The x-axis represents the revolution count of the electron bunch in the KARA ring, which corresponds to the count of the consecutive KALYPSO images. The top-axis provides a conversion of the revolution count to the measurement duration, using the revolution frequency of 2.716 MHz. The ROI of the camera image is presented on the y-axis, together with the corresponding time-axis on the right side. The top plot provides an overview of all 100 000 revolution counts and reveals a slow oscillation of the modulation peak with a period in the order of 2 ms. The second plot ranges over 10 000 revolution

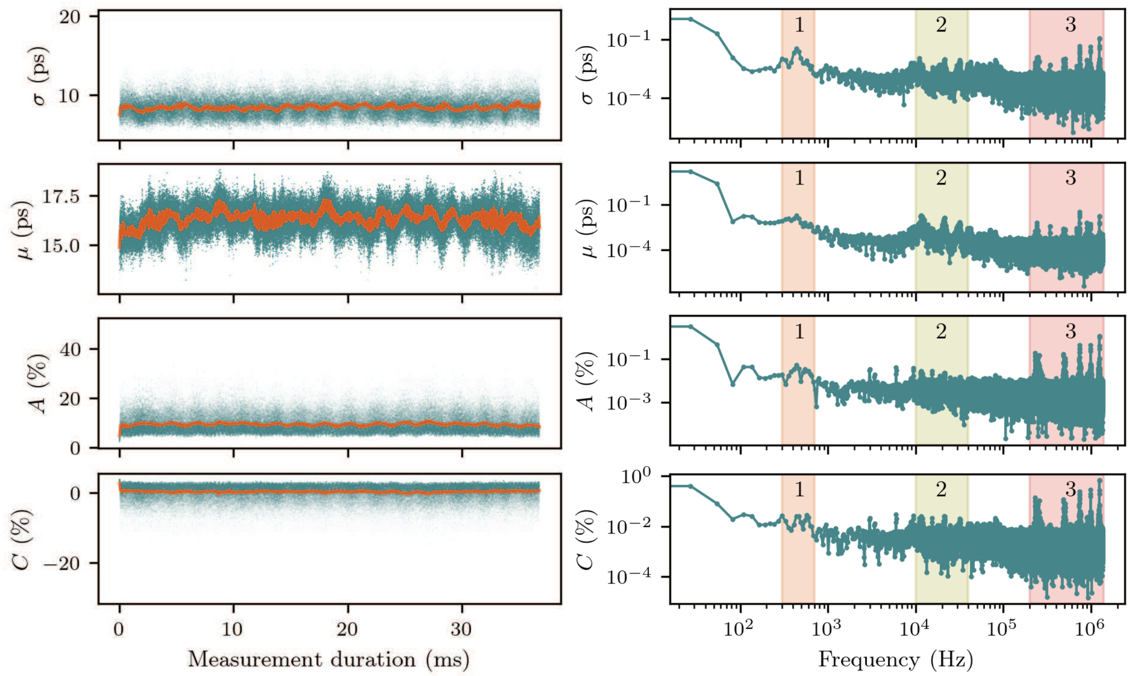

(a) time series **(b)** FFT

Figure 3.15: Time series (a) and FFT (b) of the evolution of parameters from a Gaussian function $A \exp\left(-\frac{1}{2}\left(\frac{x-\mu}{\sigma}\right)^2\right) + C$, which was fitted to every single-shot modulation of the EOSD images presented in Figure 3.14. The time series shows the raw data over ~100 000 revolutions (blue), and low-pass-filtered data (orange), were a Gaussian filter with a width of $\sigma = 50$ frames was applied. The first 500 images were omitted due to a reproducible unknown issue during the beginning of the data acquisition, that caused an nonlinear intensity increase over the whole pixel range. Due to the large number of images, oscillations at higher frequencies are difficult to identify. The FFT enables the frequency analysis and yields large amplitude variations at different frequencies. The large contribution below 100 Hz likely originates in the parameter offset and slow drifts caused by the environment of the data acquisition. Despite the use of a logarithmic scale, it is difficult to see individual peaks in the highlighted regions, due to the large amplitude difference. Hence, Fig. 3.16 presents the FFT data on a cropped linear scale to analyze the peaks in the highlighted regions.

counts, revealing faster oscillations with periods on the order of 0.1 ms. The third plot ranges over 1 000 revolution counts and reveals dynamic changes within the modulation profile, which appear similar to oblique, parallel lines. To further quantify the mentioned oscillations and dynamic changes, the evolution of the modulation peak is parametrized and a Fast Fourier Transform (FFT) is applied to reveal the oscillation frequencies.

To quantify the width σ, center position μ, amplitude A and offset C of the modulation peak, a Gaussian function

$$f(x) = A \cdot e^{-\frac{1}{2}\left(\frac{x-\mu}{\sigma}\right)^2} + C \tag{3.7}$$

was fitted to every single-shot image. This method was preferred over calculations of the centroid or RMS, because it was found to be less sensitive to random outliers and noise. The increasing noise towards the edges of the ROI impacts the calculation of the centroid and RMS, leading to results that are more difficult to interpret. A Gaussian fit was found to provide more stable results. A non-linear least-squares fit algorithm includes the propagated standard deviation of the modulation data, resulting in a weighted fit that prioritizes a good fit to data points with lower standard deviation over data with

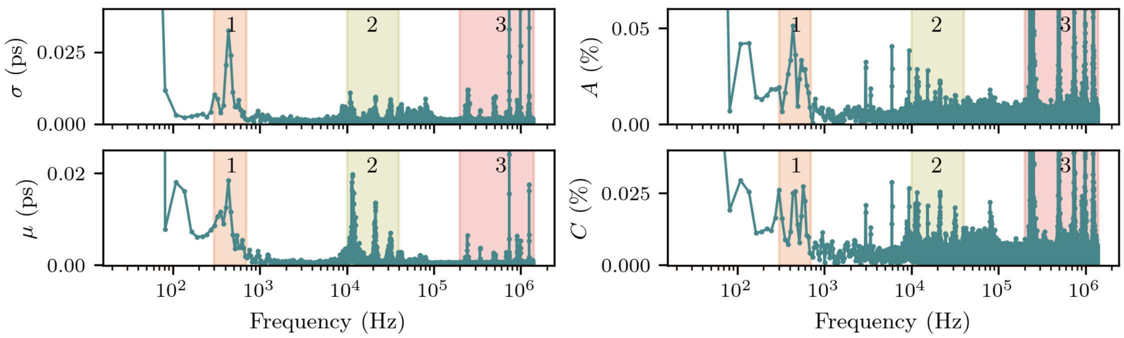

Figure 3.16: FFT of the Gaussian fit parameters from EOSD modulation with a cropped and linear y-axis to highlight certain peaks in the spectrum. The data corresponds to Figure 3.15b, where the full spectrum on a logarithmic axis is presented. The main features are sorted into three regions: First, the low frequency peak around ∼437 Hz (orange area), which is likely related to the bursts of the micro-bunching instability, which is especially prominent in σ, μ and A, but also shows potential cross-correlation in the offset C [50, 61]. Second, the ∼11.4 kHz peak and potentially its higher harmonics (green area), which occur mainly at the center position μ and are likely caused by the synchrotron oscillation. Third, multiple peaks above 200 kHz that occur at every parameter, which could be caused by electrical noise or issues of the data acquisition electronics.

higher standard deviation. It also yields the covariance matrix of the fit parameters in absolute values, which can be used to calculate the standard deviation of single parameters and their correlation.

Figure 3.15a presents the evolution of the Gaussian fit parameters over the duration of the EOSD measurement, totaling 100 000 data points per fit parameter. The transparency of each data point P_i is scaled inversely with its squared uncertainty ($1/\sigma^2_{P,i}$) to reduce visual clutter and highlight the fit parameters with small uncertainties. In addition, the result of a weighted Gaussian filter with a width of $\sigma_{\text{filter}} = 35$ data points is plotted, which corresponds to a cutoff frequency of ∼12 kHz. The plotted data shows a strong variance with many outliers, which is drastically reduced with the Gaussian filter. Thus, it hints at strong variations at high frequencies, which is discussed further in the following paragraphs. The data also reveals slower oscillations, which is expected from the revolution plots in Figure 3.14.

To generally quantify the parameter values and its variance, a weighted mean is calculated with

$$\overline{P} = \frac{\sum_{i=0}^{N-1} w_i P_i}{\sum_{i=0}^{N-1} w_i}, \quad w_i = \frac{1}{\sigma^2_{P,i}}. \tag{3.8}$$

The resulting weighted average parameter values

$$\begin{aligned} \overline{\mu} &= (16.3 \pm 0.7)\,\text{ps}, \quad \overline{\sigma} = (8.4 \pm 1.2)\,\text{ps}, \\ \overline{A} &= (9.4 \pm 3.8)\,\%, \quad \overline{C} = (0.3 \pm 2.4)\,\% \end{aligned} \tag{3.9}$$

provide a characterization of the average temporal modulation profile. The standard deviation of the averaged fit parameters is non-negligible and likely originates from three main causes:

1. Noisy data: As presented in Figure 3.11b, the modulation is very sensitive to noise of the camera data.
2. Gaussian fit: The covariance matrix reveals an absolute correlation > 0.75 among σ, A, C. The correlation increases the uncertainty of the final fit parameters, because changes of correlated parameters have a similar effect on the optimization of the fit. Additionally, σ and A of the electron bunch profile are expected to be correlated, because its number of electrons is approximately constant. Hence, a smaller width σ would result in a larger amplitude A and vice versa.

3. Beam dynamics: Effects like the synchrotron motion and the micro-bunching instability cause dynamic changes of the electron bunch. Thus, the corresponding EOSD signal is expected to change accordingly.

To analyze the different oscillation frequencies, the FFT of the parameter time series is presented in Figure 3.15b. Both axes are scaled logarithmically to accommodate the great frequency and amplitude range. In addition, Figure 3.16 shows the same data, but on a cropped linear y-axis to highlight certain peaks in the spectrum. Three exemplary frequency ranges with prominent peaks are highlighted as colored regions to discuss their potential origin.

Region 3 marks the region above 200 kHz and contains multiple sharp peaks in all four Gaussian parameters. The first two peaks mainly occur in the amplitude A and the offset C, which could be caused by intensity variations of the laser or changes of the background. Additionally, variation in amplitude A could also be caused by changes of the distance of the crystal to the electron beam, e.g. through the betatron oscillation, or by changes of the transverse beam size. However, further studies are required to evaluate the magnitude and impact of these effects. Other peaks across all parameters could hint to high frequency noise from the readout electronics or the laser system. The Gaussian filter in Figure 3.15a, suppresses these features to highlight oscillations at lower frequencies.

Region 2 includes a prominent peak at $\sim 11.4\,\text{kHz}$, which mainly occurs at the modulation peak position parameter μ, but is also visible in the modulation width σ. Thus, it might originate in the synchrotron oscillation (see Chapter 2.1.1.5), which typically occurs with a frequency of the order of 10 kHz for this operation mode [85]. It is followed by frequency peaks with decreasing amplitude at ∼21.4 kHz and ∼31.6 kHz. As these frequencies are close to multiples of the suggested synchrotron frequency, it might be caused by microstructures in the electron bunch density, which appear during the micro-bunching instability [50, 55, 61, 86]. Due to the synchrotron motion, these microstructures rotate in the longitudinal-phase space, causing a modulation of the longitudinal electron bunch profile close to harmonic frequencies of the synchrotron frequency. The instability frequency appears to be slightly below the harmonics of the synchrotron frequency, which also appeared in EO far-field experiments of the CSR, where it was attributed to a change of the potential-well distortion, causing a temporary change of the synchrotron frequency [87].

Finally, region 1 contains a peak most prominent in σ, μ and A at ∼437 Hz, but it is also visible and only slightly less prominent in the offset C. This could hint at the bursting frequency, which corresponds to regular bursts of high intensity CSR due to the formation of small structures from the micro-bunching instability. Therefore the bursting frequency is expected to potentially impact the parameters σ, μ and A of the modulation, but it should not impact the offset directly. The observed peak in the offset could be caused by the mentioned cross-correlation between C, A and σ.
Besides longitudinal effects, peaks in the spectrum could also originate in effects of the read-out electronics, cross-correlations of the fit parameters, or coupling with the transverse beam dynamics, e.g. creating peaks related to the betatron frequency and corresponding side bands. To confirm these hypotheses, future investigations with parallel betatron tune measurements are required, as synchronous data of the betatron tune was not available for the presented example.

In summary, the EOSD data presented in this section highlight the potential of this measurement method to investigate and monitor longitudinal bunch dynamics of structures in the electron bunch density in the entire range from long-term changes to turn-by-turn dynamics. It could be tailored to specific applications with sophisticated analysis methods (e.g. phase-space tomography [61]), performing synchronized measurements with other beam diagnostics [55], and optimizing the experimental setup (e.g. reducing the crystal size to achieve better resolution [29]). In the context of FCC-ee, the setup at KARA serves as a foundation for the development of a versatile EO system to monitor longitudinal beam dynamics during different operation modes with a wide range of bunch length and bunch charge densities.

3.1.4 Qualitative study of crystal heating

During EOS measurements at KARA, a drift of the laser intensity over time was often observed of unknown origin. This drift does not occur without an electron beam, or when the EO crystal is hidden from the electron beam behind the impedance protection slider. For example, the signal drift is present in the EOS measurement in Chapter 3.1.3.1, where the recorded EOS signal on the photodiode increased from ∼1.6 V to ∼2.7 V within the 15 min measurement duration. The drift is also mentioned in previous publications (Refs. [27, Ch. 6.3] and [88]), where a decrease in signal amplitude was observed during measurements with multiple bunches in the ring, in particular. It was suggested that it might be caused by beam-induced heating of the EO crystal and its holder, which causes slight misalignments of the laser trajectory. As the laser is coupled into a single-mode fiber and the coupling efficiency is very sensitive to misalignment, the heating causes a change of the laser intensity on the photodiode at the end of the fiber. Thus, it is an important factor for the development of an EO monitor for FCC-ee, because a greater heat load is expected caused by its high beam currents.

Across multiple EO measurements at KARA, it was noticed that the signal drift can be compensated by readjusting the working point of the EO setup. This effect hints at a change in the laser polarization over time, which causes an effective shift of the working point. This leads to the hypothesis that heating of the EO crystal and its holder causes a laser polarization change, in addition to possible misalignments of the laser trajectory. The temperature change could cause localized mechanical stress on the EO crystal through a temperature gradient within the crystal, or through differences in thermal expansion rate between the crystal, its holder and its coatings. Mechanical stress can change the birefringence of the EO crystal via the photo-elastic effect [89, 90], and therefore change the polarization of the probe laser.

This section presents an estimation of the typical heating power of the electron beam at KARA and a dedicated experiment to heat the EO crystal and investigate its impact on the laser signal at the output of the EO monitor.

3.1.4.1 Heating power estimation

The EO crystal poses an impedance to the electron beam, which causes an energy loss of the beam and creates a wakefield. This energy loss is characterized by the loss factor [21]

$$k_l = \frac{2}{q^2} \int_0^\infty Re(Z(\omega)) Q^2(\omega) \,\mathrm{d}\omega, \tag{3.10}$$

with bunch charge q, impedance $Z(\omega)$ and longitudinal bunch form factor $Q(\omega)$ (Fourier transform of the longitudinal charge distribution). The loss factor describes the generalized energy loss of a single particle per turn, hence the total deposited power (heating power) results in

$$P = \frac{I_{\text{total}}^2}{f_{\text{rep}} \cdot n_b} \cdot k_l = q^2 \cdot f_{\text{rep}} \cdot n_b \cdot k_l = f_{\text{rep}} \cdot n_b \cdot 2 \cdot \int_0^\infty Re(Z(\omega)) Q^2(\omega) \,\mathrm{d}\omega, \tag{3.11}$$

with the total beam current I and number of bunches n_b.

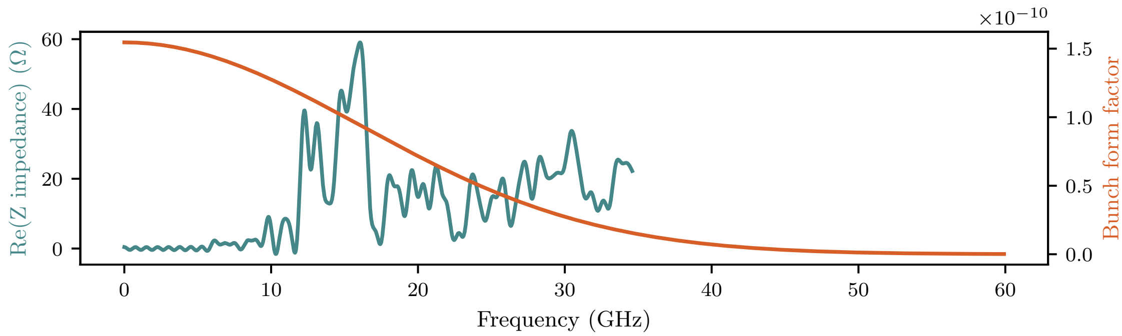

Figure 3.17: Real part of the longitudinal impedance and the longitudinal bunch form factor (Fourier transform of the longitudinal bunch charge density) from a simulation of the EO crystal at KARA. The wakefield solver of CST studio suite was used to simulate the impedance of only the EO crystal without its holder for typical beam parameters at KARA to estimate the heat load. The maximum frequency of the impedance calculation is limited by the computing power, as higher frequencies require the simulation of shorter bunch lengths, which is computationally expensive. However, the impedance is scaled with the bunch form factor squared for the calculation of the heating power (see Eq. 3.10), which drastically reduces the impact of the impedance at high frequencies.

Figure 3.17 presents the impedance $Re(Z(\omega))$ of the EO, resulting from a simulation of the CST wakefield solver [48], which numerically calculates the wakefield and impedance of a given bunch charge distribution within a three dimensional structure. Additionally, the form factor of an Gaussian bunch profile with length $\sigma = 2.96\,\mathrm{mm}$ ($\sim$9.8 ps) is presented, which is the approximate bunch length during the EOS measurement of Chapter 3.1.3.1. With the corresponding bunch charge $q = 274\,\mathrm{pC}$ and its 2.716 MHz repetition rate, the simulated impedance results in a deposited power $P \approx 15\,\mathrm{mW}$.

With an estimated mass $m = 0.72\,\mathrm{g}$ of the 5 mm × 5 mm × 7 mm GaP crystal of the EO setup at KARA, and an assumed specific heat $c_T \approx 0.44\,(\mathrm{J/gK})$ at room temperature [91], the crystal temperature would increase by $\Delta T \approx \frac{P \cdot 60}{m \cdot c_T} \approx 2.8\,°\mathrm{C\,min}^{-1}$. However, this temperature increase is a rough estimate of the upper limit, because heat losses to the environment will reduce the temperature increase and, at some temperature, lead to an equilibrium, where the crystal temperature no longer increases. Additionally, the specific heat slightly increases with temperature [91], which also leads to a reduced temperature change through heating. However, the result shows that the order of magnitude of the generated heating power on the EO crystal at KARA is non-negligible and could cause noticeable temperature changes.

3.1.4.2 Experiment to investigate the impact of crystal heating

To observe the impact of EO crystal temperature changes on EO measurements, a mock-up of the KARA EO interaction module was set up in the EO laboratory. This setup enables heating of the EO crystal with hot air, while monitoring the power of the unmodulated laser pulses at the output of the mock-up monitor. Additionally, the polarization analyzer in the EO monitor allows to determine if the temperature change also causes a polarization change of the laser pulses. A brief summary of this experiment was published in Ref. [3].

A photograph of the mock-up interaction module is presented in Fig. 3.6a of Chapter 3.1.2. In contrast to the installed EO interaction module at KARA, the mock-up module is not enclosed by a vacuum chamber, which makes the crystal and its holder accessible. A hot-air blower was fixed at a distance of $\sim$2 m and aimed at the EO crystal at the end of the monitor arm to enable slow consistent heating.

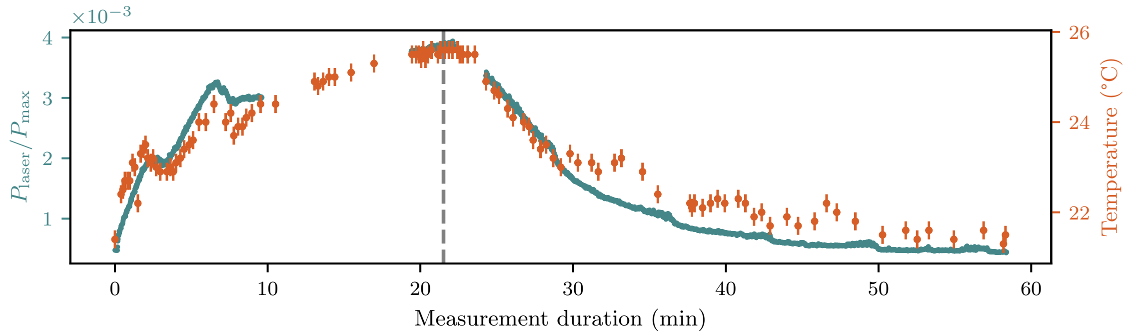

Figure 3.18: Measured temperature (orange) of the EO crystal and normalized laser power output P_{laser}/P_{max} (blue) of the mock-up EO interaction module during heating the crystal and its holder with hot air. P_{max} is the maximum achievable laser power output, when the working point is set to parallel configuration of the polarization analyzer. The data points show an estimated statistical uncertainty as error bar, but additionally, the temperature measurement has a large systematic uncertainty due to unclear calibration of the thermal imager. For the experiment, The working point was initially set to a crossed configuration to minimize the laser output power. To detect an effective drift of the working point, a scan of the $\lambda/4$ and $\lambda/2$ waveplate angles was done between the 10 min to 20 min mark, hence the power measurements are missing during that period. (Also presented in Ref. [3])

The crystal temperature was recorded with a thermal imager (Testo 868), which was mounted ~20 cm above the EO crystal. The thermal imager provides a 2D temperature map with 160 px × 120 px pixels, of which the temperature at the center of the EO crystal was recorded. The systematic uncertainty on the absolute temperature values is large, because the imager was not calibrated for the GaP crystal. A precise calibration would require the emissivity of the EO crystal, which is not known and depends on the material and its surface preparation. Thus, the measurement is not suitable for a detailed assessment of absolute temperatures but it is sufficient for a rough estimate of the temperature trend in this experiment during the heating and cooling process.

To detect the drift of the laser pulse power, the same laser system as for KARA EO measure was used, but the laser amplifier output was connected to the input of the mock-up module in the EO lab via a 5 m optical fiber. After the laser pulses in the mock-up module pass through the EO crystal and the following polarization analyzer ($\lambda/4$-, $\lambda/2$ waveplate and PBS, see Fig. 3.6b), the average output laser power is measured with a fiber-coupled power meter (Thorlabs S120C).

The working point was initially set to a crossed configuration with $\phi = 0°$, $\theta = 0°$, hence the output laser power is at minimum. In this configuration, the output power is typically slightly above zero Watts, due to imperfections and dispersion of the polarization analyzer.

Figure 3.18 presents the trend of the crystal temperature and relative laser power P_{laser}/P_{max} over a heating cycle. The relative laser power represents the fraction of the laser power P_{laser} compared to the maximum P_{max} at parallel configuration of the polarization analyzer. The temperature and laser power reach a global maximum at 22 minutes 31 second, which coincides with turning the heating off. During the heating period, the temperature and laser power increases on average, but it also has two local minima, where the temperature and laser power decreased briefly. These local minima are likely caused by the air conditioning system of the EO laboratory, which occasionally provides cool air that decreases the room temperature and disturbs the air flow of the hot-air blower. The partly missing data approximately from 10 min to 20 min is caused by additional waveplate scans, which were conducted to compare the relative working point at high temperature to the initial working point.

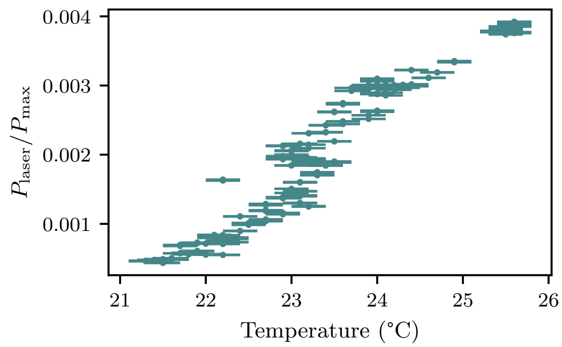

Figure 3.19: Crystal temperature over relative laser power from the measurement presented in Fig. 3.18. The original temperature and laser power time series were merged with a nearest-neighbor approach with a one-second matching tolerance. The errorbars indicate the statistical uncertainty, but the temperature measurements have an additional unknown systematic uncertainty due to the missing calibration of the thermal imager. The plot indicates a correlation between temperature and laser power, which also shows in the Pearson correlation coefficient of 0.971, meaning that 97 % of the laser power variance can be explained by a positive linear correlation to the crystal temperature. Its small p-value on the order of 1×10^{-119} additionally highlights the existence of a statistically significant correlation between the relative laser power and the crystal temperature.

After the heating was turned off, the temperature and laser power return to the initial value before the heating. The decrease is similar to an exponential decay towards an asymptote, but it also exhibits some small steps. the steps are more pronounced in the temperature and slightly offset to the relative power measurements. The steps are likely caused by the occasional cool air from the air conditioning system of the EO laboratory. The differences in time and amplitude of the steps between temperature and power measurements is not clear. A possible cause is systematic errors of the thermal imager, of which the temperature readings might be influenced by the cardboard that was placed behind the crystal as background. The cardboard probably cools faster than the EO crystal, or it is impacted more directly by the air flow of the air conditioning.

Figure 3.19 presents a plot of the relative laser power over the crystal temperature. Since both variables were measured as separate time series (see Fig. 3.18), they have been merged by matching each laser power measurement to its nearest temperature measurement (nearest-neighbour approach), within a one second interval. If no matching measurement was found within the interval, the data point was omitted.

The graph indicates that the relative laser power increases with the crystal temperature. As explained previously, the thermal imager is not calibrated properly to the material and surface of the crystal material, which introduces an unknown systematic uncertainty on the temperature readings. Thus, the data does not allow to determine a direct relation between the laser power and absolute crystal temperature, but it can be used to test for a correlation. To quantify the correlation, the Pierson correlation coefficient was calculated, which yields 0.971 with a small p-value on the order of 1×10^{-119}. Hence, $\sim$97 % of the laser power variance can be explained by a linear correlation to the crystal temperature and therefore the Pearson correlation coefficient reveals a statistically significant correlation between both quantities.

To test if the relative laser power change originates in a change of the laser polarization, a scan of the $\lambda/4$ and $\lambda/2$ waveplate angles ϕ, θ of the polarization analyzer was done once before, after and during the heating cycle. Scanning the ϕ and θ while monitoring the laser power after the polarization analyzer can reveal changes in the effective working point, which hints at a polarization change of the laser (see Chapter 2.2.3). For example, if the working point is initially in a crossed configuration with $\phi_0 = 0°$, $\theta_0 = 0°$, no laser light passes through the analyzer. When the laser polarization changes, light passes through the analyzer, increasing the laser power at the output. A following scan of the waveplate angles reveals new waveplate angles to achieve a minimum output power at ϕ_1, θ_1. Shifting the working point to ϕ_1, θ_1 mitigates the laser polarization shift and returns the working point to a crossed configuration. Thus, a change of the laser polarization effectively changes the working point and leads to changes of the output laser power.

Before the start of the heating cycle, the working point was set to a crossed configuration with $\phi_0 = 0°$, $\theta_0 = 0°$. Thus, the waveplate angles were set to the position of minimum output power. After the heating cycle, when the temperature returned to the initial room temperature, the minimum laser power was still at the same working point with ϕ_0, θ_0. However, the waveplate scans during the heating cycle in the time range from 10 min to 20 min (see Fig. 3.18 revealed a shift of the minimum of the $\lambda/4$ waveplate angle to $\phi \approx -2°$ and of the $\lambda/2$ waveplate angle to $\theta \approx 0.6°$.

In summary, the experiment proved the correlation between the crystal temperature and the output laser power, which supports the hypothesis of temperature-induced drift of laser power during EO measurements at KARA. Additionally, scans of the waveplate angles during the heating cycle hint at a heat-induced polarization change of the laser. The polarization change is equivalent to a change of the EO working point, hence it is likely part of the reason for the laser power drift. Its origin could be mechanical stress caused by gradients in thermal expansion rate within the EO crystal and between the crystal and its holder. Generally, strain on the crystal lattice is known to cause changes in its birefringence [89, 90], and the birefringence influences the laser polarization after the crystal.

During single-shot EOSD measurements, the bunch-induced modulation can change the laser amplitude by a couple of percent within picoseconds or less (see KARA EOSD in Chapter 3.1.3.2), which is orders of magnitude faster in comparison to the slow temperature induced drift (e.g. $\sim$30 % baseline intensity decrease over 15 minutes during EOS at KARA in Fig. 3.9). Therefore it is possible to mitigate its effect by readjusting the working point directly before the measurement. To quantify and possibly predict the effect, an improved experimental setup with a calibrated temperature probe is necessary. As the extent of the heating depends on the beam current and the impedance of the crystal (see Eq. 3.10), it is important for the implementation at FCC-ee to decrease the impedance as much as possible to reduce the heat load. Due to FCC-ee's high bunch charges, a significantly lower impedance might be possible, because the EO crystal can be positioned further away from the beam while keeping a similar signal strength. However, especially the high beam current during Z-operation provides a challenge which might require addition thermal management. Additionally, it might be possible to extrapolate the laser power drift and use it to calculate the corresponding effective change of the working point. This would enable automatic adjustments of the the working point to keep the laser output stable and thus mitigate the effect of the crystal heating. Furthermore, optimizations of the crystal holder to reduce localized mechanical stress during thermal expansion could help to mitigate the effects of the crystal heating on EO measurements.

3.2 EO at the Ferninfrarot Linac- und Test-Experiment (FLUTE)

At FCC-ee, the commissioning of an EO monitor is particularly challenging due to its large-scale infrastructure and corresponding long transmission lines in combination with the required precise arrival time synchronization of the laser pulses and particle bunches on a picosecond level. The commissioning of the EO monitor at FLUTE provided valuable experience in achieving precise frequency and phase

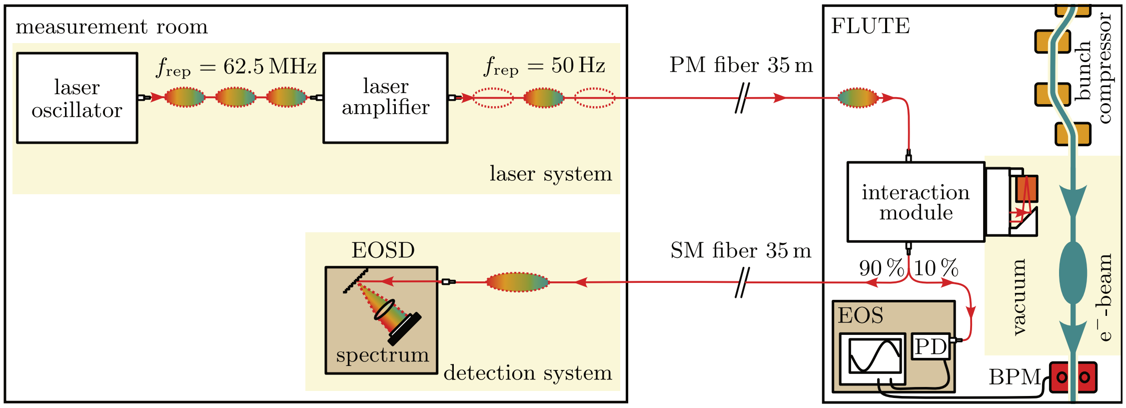

Figure 3.20: Schematic overview of the EO monitor at FLUTE, which is installed after the bunch compressor. The general principle is similar to the system at KARA (see Chapter 3.1.2), and uses the same laser oscillator, amplifier and a similar EO interaction module. The laser system is positioned in the measurement room next to the experimental hall of FLUTE, and a PM and SM optical fiber with 35 m length is used to transport the laser to the interaction module and back to the measurement room for the EOSD detection system. In contrast to the setup at KARA, the laser is split at the output of the interaction module with a fiber optic splitter to send ∼10 % of the laser pulse power onto a photodiode within the experimental hall, while the other ∼90 % of the light is transported to the measurement room to a spectrometer for EOSD measurements.

synchronization and enabled to identify potential challenges and methods for the commissioning at FCC-ee.

The Ferninfrarot Linac- und Test-Experiment (FLUTE) is a linear accelerator and test facility for accelerator physics at KIT, with a focus on the production of ultra-short electron-bunches and corresponding ultra-short THz-pulses and their applications [92, 93]. The short bunches of FLUTE serve as a test bench for the development of new diagnostic methods and tools for future accelerators, like single-shot femtosecond diagnostics with a compact transverse deflecting structure (compact TDS) [94–96], and an in-vacuum EO monitor [97], with their required synchronization on a femtosecond level. This section outlines the challenges and solutions that enabled first successful EOSD measurements at FLUTE and it highlights the lessons learned for the FCC-ee EO monitor commissioning. In addition, first EOSD bunch profile measurements are presented, utilizing FLUTE's bunch compressor to achieve different bunch lengths.

3.2.1 Experimental setup of the EO system at FLUTE

The electron bunches of FLUTE are generated with a photo-injector, which utilizes the photo-electric effect to produce short bursts of electrons by hitting a copper cathode with high intensity laser pulses. For the EO measurements, the low-energy section provided electron energies of up to 7 MeV with repetition rates of 10 Hz or 50 Hz and the following S-band linac accelerated the electrons to energies of 30 MeV to 40 MeV. The following bunch compressor contains a chicane made of four dipole magnets, which enables longitudinal compression of a chirped electron bunch. The chirp can be changed by changing the RF phase in the linac, thus adjustments of the RF phase and the dipole strength in the bunch compressor enable bunch length variations [98, 99]. The interaction module of the EO monitor is positioned after the chicane to enable measurements at different bunch lengths.

Figure 3.20 presents a schematic overview of the EO monitor at FLUTE. The setup is similar to the system at KARA and uses the same laser oscillator and amplifier and EO interaction module, which is described in Chapter 3.1.2. The synchronization of the laser repetition rate with the bunch repetition rate of FLUTE follows a principle similar to that at KARA (see Chapter 3.1.2.2, but uses different hardware based on the MicroTCA standard [100]. The synchronization system creates a phase-locked loop (PLL), where the oscillator cavity length is continuously adjusted to match the laser pulse repetition rate with a timing signal of FLUTE's master oscillator. The pulse picker is included in the laser amplifier and reduces the original laser repetition rate from 62.5 MHz to 50 Hz to match the repetition rate of FLUTE.

The laser light is transported through a 35 m long PM fiber from the measurement room to the EO interaction module in the experimental hall of FLUTE with the EO crystal installed in the vacuum chamber after the bunch compressor. Similarly to the setup at KARA, it is mounted on a linear stage to adjust the distance between the EO crystal and the electron beam (see Chapter 3.1.2.3). A vacuum valve enables installation or crystal change without directly ventilating the beam pipe. The EO interaction module is almost identical to the module at KARA (see Fig. 3.6b) and also includes a 5 mm × 5 mm × 7 mm EO crystal. However, the optics box has an additional grating compressor installed before the EO crystal to further adjust the laser pulse length.

The laser output of the interaction module is split with a fiber optic splitter to obtain $\sim$10 % of the laser light onto a fiber-coupled photodiode (EOT ET3010) in the FLUTE experimental hall for EOS measurements. The remaining $\sim$90 % of the laser light is transported through a 35 m long SM fiber to the measurement room, where the laser is out-coupled via a collimator and led to a grating-based spectrometer for EOSD measurements.

The photodiode of the EOS setup is connected to an oscilloscope (R&S RTO64) directly in the experimental hall. The signal of a BPM downstream of the EO interaction module is also connected to the same oscilloscope to serve as a timing reference, in combination with a reference signal from the timing distribution system of FLUTE. This setup is positioned in the experimental hall to keep the fiber and cable lengths short, which simplifies the approximation of signal arrival times. Thus, the EOS setup focuses on the initial synchronization of the laser pulse arrival time to achieve temporal overlap with the electron bunch field in the EO crystal.

The spectrometer in the measurement room enables single-shot EOSD measurements of the laser pulse spectrum to decode the longitudinal electron bunch profile. The setup is again similar to KARA, with a grating to disperse the laser pulse and a lens to focus the spectrum onto a line-array camera [71]. Instead of the ultra-fast camera KALYPSO, a commercial line-array camera with an 512 pixel InGaAs sensor (Andor iDus DU490A-1.7) is used, because it is sufficient for the low repetition rates of FLUTE.

For the following presented EOSD measurements, the working point was set by the angles of the $\lambda/4$ waveplate $\phi = 0°$ and $\lambda/2$ waveplate $\theta = 2°$. This near-crossed setting was experimentally determined with additional EOS measurements at multiple working points to provide both high modulation and a decent SNR.

3.2.2 Commissioning and first EOSD measurements at FLUTE

One of the major challenges during the commissioning of the EO system at FLUTE is the synchronization of the electron bunch with the laser pulse arrival time to achieve a first EO signal. Precise timing is crucial, as the time window for temporal overlap is on the order of 20 ps (a convolution of the longitudinal bunch and laser profile), which is one billion times shorter than the delay between two electron bunches ($\sim$20 ms at 50 Hz repetition rate). Hence, a simple search for the overlap with an EOS scan that covers the full time range between two bunches by changing the laser pulse delay is too time-consuming for practical use.

There are multiple strategies to narrow down the search window for signal overlap. For example, using a continuous wave (CW) laser instead of the pulsed laser allows to trigger on the modulation directly with an oscilloscope (see Chapter 5.4.6). However, this requires an additional laser system and a high modulation intensity to achieve a good signal-to-noise ratio (SNR). Alternatively, drastically increasing the laser repetition rate to reduce the time between two pulses reduces the required scan range. E.g., using the full 62.5 MHz repetition rate of the laser oscillator reduces the required scan range to the interval between two pulses of 2 ns. This guarantees to get a modulated laser pulse during the laser delay scan with a range of 2 ns, but since there would be 10 million laser pulses in the time between two electron bunches, it remains difficult to find the one modulated laser pulse.

Thus, a different approach was used, where a reference signal from a BPM was used to estimate the required laser pulse timing to achieve temporal overlap with the electron bunch (similar to the commissioning at KARA [27]). The electron bunch induces an electrical signal in the metal pick-up of the BPM in the vacuum chamber, which is connected to an oscilloscope. The photodiode of the EOS setup is also connected to this oscilloscope to provide a signal of the probe laser pulse. The delay between the BPM signal and the expected beam-induced modulation of the EOS measurement can be estimated by approximating the EO signal propagation delay from the EO crystal to the oscilloscope and subtracting the reference signal propagation delay of the BPM to the oscilloscope. Since the BPM is located $\sim$1 m downstream of the EO crystal, the propagation time of the electron bunch must also be taken into account.

To simplify the estimation and reduce systematic errors, short cables and fibers were chosen, and the oscilloscope was positioned directly in the experimental hall. This led to an estimated delay of $\sim$22 ns between the BPM signal and the bunch-induced EO modulation of the laser pulse. Thus, the oscilloscope was set to trigger on the BPM signal and the laser pulse delay scanned around the 22 ns mark. As the estimation is expected to have a relatively large uncertainty, a scan range on the order of 10 ns was chosen, resulting in a scan duration of a couple of minutes. With the persistent mode enabled, the oscilloscope overlays all measured waveforms during the scan, which helped to finally detect a modulation of the amplitude of the laser pulse signal at a laser pulse delay of $\sim$25.7 ns to the BPM signal.

In preparation of the following measurements, the EO crystal was moved closer to the electron beam, until a decrease in bunch charge was measured with an integrating current transformer (ICT) downstream of the EO crystal. The EO measurements were conducted with an approximate bunch charge of 250 pC, and the crystal was positioned as close to the electron beam as possible without reducing the bunch charge.

Figure 3.21 presents EOSD measurements of the spectrometer camera during a laser delay scan close to 25.7 ns delay to the BPM. The presented heatmap is similar to the revolutions plots of Fig. 3.14 at KARA, where the modulation amplitude of each camera image is displayed as a vertical strip of pixels. The calculation of the modulation follows Eq. 2.39 and the EOSD analysis of the KARA example in Chapter 3.1.3.2. However, in contrast to KARA, the trend of multiple images along the x-axis represent the laser delay change instead of the revolution count. The resulting images are cropped to a region of interest, which is defined by the 70 percentile of an unmodulated laser pulse image.

Since the delay of the laser pulse is scanned, but the arrival time of the electron bunch stays constant, the modulation of the electron bunch creates a diagonal line on the heatmap. It also reveals a pattern of following alternating diagonal dark and light lines, which are caused by the positive and negative

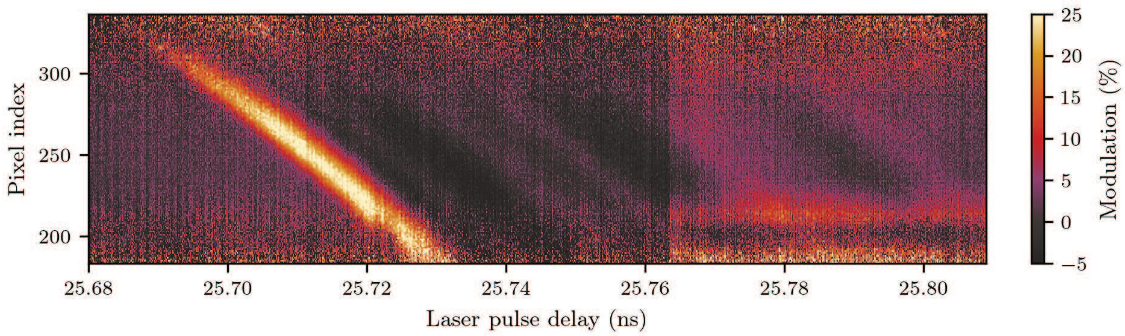

Figure 3.21: Modulation heatmap of EOSD images during a laser delay scan. The modulation of a single EOSD image is displayed as a vertical stripe, and successive images are stacked from left to right during a scan of the laser pulse delay. The pixel range is cropped to a ROI, which contains the 70th percentile of an image with the unmodulated laser pulse. As the delay increases, the modulation from the electron bunch field moves through the laser pulse profile from top to bottom, creating a diagonal stripe. This data is used to calculate the pixel-to-time calibration factor ${k_{\mathrm{pt}}}^{\mathrm{FLUTE}}$, using the pixel position change of the modulation peak during the given laser delay shift.

modulations from the wakefield. In comparison to the revolution plots at KARA, the modulation has a smaller width, hinting at a small electron bunch length in comparison to the laser pulse length.

The data of the laser delay scan was also used to convert the pixel position into a time-axis. The principle of this conversion is based on how much the pixel position of the modulation peak changes for a known change of the laser delay, and it is described in more detail in the previous Chapter 3.1.3.2. For these FLUTE EOSD measurements, the conversion is approximately linear with a pixel-to-time calibration factor

$$ {k_{\mathrm{pt}}}^{\mathrm{FLUTE}} = (0.288 \pm 0.020)\,\mathrm{ps/pixel}. \tag{3.12} $$

Applying the conversion factor to spectrometer images of an unmodulated laser pulse reveals a laser pulse length of $\sigma_{\text{laser pulse}} = (10.06 \pm 0.07)\,\mathrm{ps}$ (FWHM $= 19.68\,\mathrm{ps}$). Hence, the laser pulse length is approximately 2.5 ps (9.9 ps FWHM) shorter than at KARA, which is expected due to the additional compressor in the optics box of the EO interaction module.

Figure 3.22 presents the modulation of a single-shot measurement at FLUTE and its standard deviation across multiple measurements. It shows the increasing standard deviation towards the edges of the ROI, because the laser signal intensity decreases (see also Chapter 3.1.3.2). The peak modulation amplitude reaches $\sim$25.2 % with a peak width of $\sigma = (2.7 \pm 0.1)\,\mathrm{ps}$ (FWHM $= 5.8\,\mathrm{ps}$). Thus, the bunch length is shorter than at KARA and the EO modulation of the Coulomb field only covers a small part of the laser pulse. The bunch length at FLUTE depends on multiple machine parameters, in particular the RF phase and the magnet settings of the bunch compressor [98, 99]. For this particular measurement, the RF phase was set to be 10° off crest, which is expected to result in a slight bunch compression compared to an on-crest (0°) RF phase.

The first application of the EOSD setup followed directly after its commissioning, with measurements of the bunch profile at different settings of the RF phase in combination with the bunch compressor. Starting from the on-crest (0°) RF phase, the RF phase was increased to 5° and 10° with constant angle and magnetic fields of the bunch compressor, which was expected to shorten the bunch due to the corresponding change of its chirp. Finally, the RF phase was slowly increased to 29° while optimizing the bunch compressor to achieve a small bunch length, based on live EOSD data in the control system.

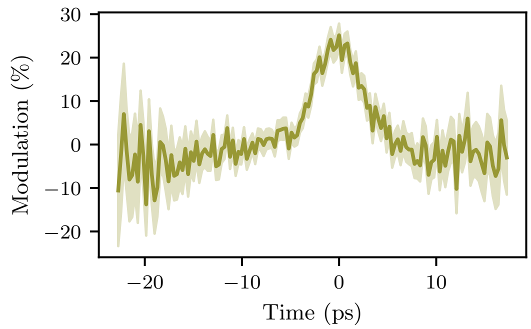

Figure 3.22: Modulation of single EOSD image with calibrated time-axis. A light blue error band shows the calculated standard deviation from 100 consecutive measurements. The uncertainty increases towards the edges, because the range of the x-axis corresponds to the previously defined ROI, where the laser intensity decreases towards the edges. The modulation has a peak width of $\sigma = (2.7 \pm 0.1)$ ps (FWHM $= 5.8$ ps), suggesting a much shorter bunch length than the measurement at KARA in Chapter 3.1.3.2.

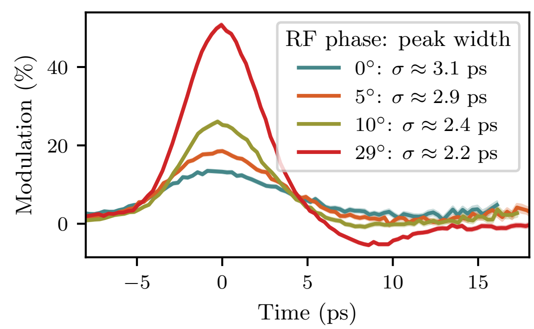

Figure 3.23: Modulation of averaged EOSD images for different bunch lengths at FLUTE. The standard error of the mean is illustrated as an error band, but it is very small due to the averaging over 100 measurements. The bunch length changes are caused by a electron bunch chirp changes through RF phase adjustments in combination with a following bunch compressor. The RF phase angle is defined relative to the on-crest setting, and the magnets of the bunch compressor were constant except for the setting with RF phase 29°, where it was optimized to achieve short bunches.

The remote operation was made possible by integrating its motors, synchronization and data acquisition in the control system.

Fig. 3.23 presents averaged EOSD measurements at the mentioned different RF phase settings of 0°, 5°, 10° and 29°. To reduce the uncertainty, the measurements are averaged over 100 images, providing a small standard error of the mean. The peak width σ was calculated by fitting a Gaussian function, yielding $\sigma = (3.08 \pm 0.07)$ ps, (2.92 ± 0.05) ps, (2.43 ± 0.03) ps and (2.23 ± 0.03) ps. Hence, the resulting EO modulation peak width decreases with increasing RF phase, while the modulation amplitude increases with approximately 14 %, 19 %, 26 % and 51 %. This evolution of the peak width and amplitude generally follows the expectation, because the RF phase changes increase the chirp of the electron bunch, which improves the compression of the bunch compressor, resulting in shorter bunches. Since the bunch charge is not affected, shorter bunches lead to an increased charge density, causing a stronger Coulomb field, which results in a stronger EO modulation. The modulation at the RF phase of 29° shows a negative modulation shortly after the positive main peak. The negative peak likely originates from the wakefield, because a higher charge density amplifies the wakefield amplitude, making it more visible towards shorter bunch lengths. While the statistical uncertainty of the averaged measurements is small, systematic uncertainties might require further investigation, as the length of the 7 mm thick GaP crystal in combination with the long laser pulse durations relative to the bunch duration could lead to additional broadening of the signal (see Chapter 2.2.5, and Refs. [26, 64]).

In summary, the commissioning of the EO monitor at FLUTE provided some challenges, in particular with the precise synchronization of the laser pulse arrival time with the electron bunch. Using the EOS setup in combination with a reference signal from a BPM on the same oscilloscope helped to finally achieve the measurement of a first EO modulation. After successful commissioning, a study with EOSD measurements at different bunch lengths was performed, using FLUTE's bunch compressor.

The EO monitor commissioning at FLUTE highlighted the importance of a reference signal to estimate the required laser pulse delay for achieving temporal overlap with the electron bunch. This will also be crucial for FCC-ee, because the high radiation levels and limited space in the accelerator tunnel, and especially the arc sections, likely requires the laser system and detection system to be located in a cavern of a straight section. It leads potentially to long fibers and cables for the signal transmission, which, next to potential issues with laser pulse lengthening from the fiber dispersion, additionally increases the difficulty for the arrival time synchronization. The experiments at FLUTE showed that it is possible to set the EO monitor up for remote operation and that it will be crucial to keep fiber lengths as short as possible in addition to providing a bunch arrival time reference signal for the EO monitor commissioning at FCC-ee.

4 Numerical simulations of an EO beam monitor

The beam parameters of the Future Circular Lepton Collider (FCC-ee) are unique and provide challenges for the development of an electro-optical (EO) longitudinal bunch profile monitor, especially due to its wide range of bunch lengths and high bunch charges. To evaluate the specific challenges for an EO monitor and develop solutions with a concept design, a simulation procedure has been set up based on the EO monitor at Karlsruhe Research Accelerator (KARA).

This chapter provides a comprehensive explanation of the simulation procedure, a comparison of its results to electro-optical sampling (EOS) measurements at KARA, followed by an evaluation of the challenges for an EO monitor under FCC-ee's beam conditions and the development of a novel crystal holder design for FCC-ee. Thus, this chapter expands upon the concise descriptions in previous publications [1, 3, 5, 6], but the simulation parameters have been updated in this thesis to match the published parameters of the FCC-ee feasibility study report [9].

4.1 Simulation environment

The simulation procedure aims to replicate EOS and electro-optical spectral decoding (EOSD) measurements at KARA (see Chapter 3.1) and later extrapolate by simulating with FCC-ee's beam parameters. Hence, the simulation procedure follows the EO monitor principle of Chapters 2.2.3, of which the major simulation steps are presented as a flow diagram in Fig. 4.1. It starts with a numerical simulation of EO crystal in the beam field of a passing particle bunch in the vacuum chamber, which us conducted with the Wakefield solver of the CST Particle Suite [48]. The resulting electric field in the crystal is further processed with Python scripts to simulated the laser pulse to probe the EO effect in the crystal, the following polarization analyzer that defines the working point, and the subsequent detection system.

The simulation steps are discussed in detail in the following sections with example parameters from the KARA EOS measurement of Chapter 3.1.3. The corresponding input parameters for the simulation are summarized in Table 4.1, and are explained at corresponding locations during the following explanations.

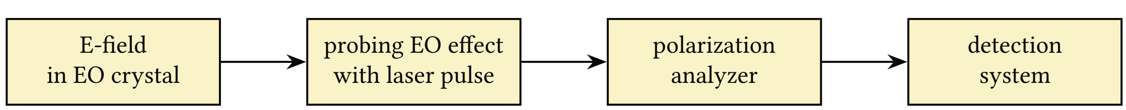

Figure 4.1: Flow diagram of the simulation procedure.

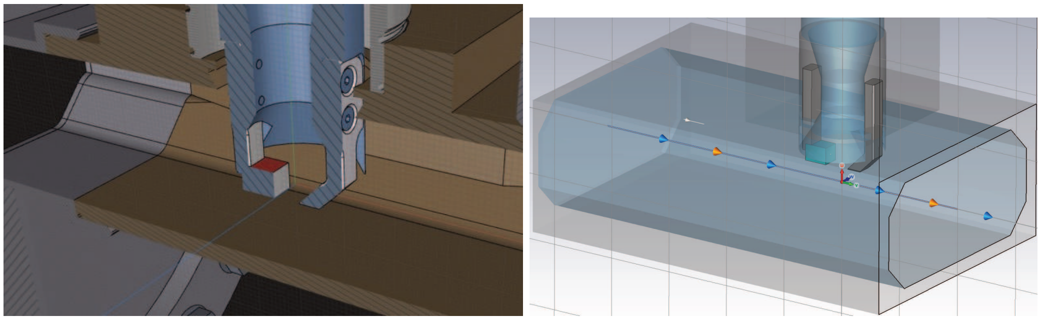

(a) CAD model (Courtesy of S. Schott) **(b)** Simplified model in CST Studio

Figure 4.2: Comparison of the original KARA CAD (a) and the simplified 3D model for CST simulations (b). It shows the in-vacuum crystal assembly with the EO crystal and a small mirror protruding into the vacuum chamber. In CST, the crystal is colorized in turquoise, while it is orange in the CAD model. The vacuum chamber is displayed transparent in CST, while in the CAD model, the vacuum chamber is cut along the y-z plane to make the crystal visible. The blue line with arrow-heads represents the electron beam trajectory in the CST model.

4.1.1 Numerical simulation of the electric Field

To simulate the electric field within the EO crystal, the Wakefield Solver of the CST Particle Suite [48] is used. This numerical solver requires a 3D model of the in-vacuum EO section and the longitudinal charge distribution and trajectory of the propagating particle bunch. The solver computes the electromagnetic field of the particle bunch and its interactions with the surrounding material in time domain on a 3D mesh. The resulting fields are expressed in terms of wake potentials, and probe points can be placed in the 3D model to directly retrieve the electric field. This enables the simulation of EO measurements, as it models the electric field dynamics within the EO crystal.

4.1.1.1 Approximations and resulting limitations

One of the central challenges in setting up the simulation is to balance computational efficiency with accuracy of results, which inevitably leads to some approximations in the simulation procedure. In this thesis, both qualitative and quantitative approaches have been applied, to evaluate the impact of different simulation parameters:

1. The mesh size has been systematically varied until the resulting wake potential converged. For instance, when the mesh size is sufficiently small, further refinement leads to only tiny changes in the shape of the resulting wake potential. Thus, the mesh size is set to the largest acceptable value, thereby reducing computation time with minimal impact on accuracy.
2. Certain parameters, such as simplifications of the vacuum chamber geometry, were determined based on informed assumptions. The validity is evaluated qualitatively in an a posteriori comparison of the simulation results to measurements at KARA, as discussed in Chapter 4.2 enabling a qualitative evaluation.

The following paragraphs explain the most prominent applied approximations and discuss its impact on the simulation accuracy.

For this thesis, the 3D model of the KARA EO monitor was created directly in the CST software based on the original CAD design. The geometry has been simplified in the process, while keeping the large scale dimensions as accurate as possible. Figure 4.2 presents a comparison of the original KARA CAD design and the simplified 3D model for the simulation. Parts far away from the crystal or outside the vacuum have been neglected, as well as screws and other small details. The exceptions are the crystal and its holder, which remain reasonably detailed parts. Since simulations of EO measurements are based only on the electric fields inside the EO crystal, parts in close vicinity of the crystal have been designed with more details. This is also reflected in the mesh resolution, which varies across the 3D model and is finer close to the crystal. In frequency domain, a coarser mesh limits the maximum frequency of the simulation and missing details in the 3D model will show up as missing or shifted peaks in the spectrum of the simulated data. On the other hand, the computing time increases with a finer mesh and a detailed geometry. To find a balance, scans with decreasing mesh size and increasing details of the geometries have been done until the electric field dynamics in the EO crystal did not show any major changes. This resulted in a maximum frequency of 100 GHz for the simulation examples in this thesis, which was also used for the comparison to measurement data from an EOS scan at KARA(see Chapter 4.2).

Another limitation of the Wakefield Solver is the approximation of the particle beam as a rigid 1D current distribution (longitudinal bunch profile) moving along a given beam axis. It leads to accurate simulations of the electric field strength, if the probe distance r to the beam center is much greater than the transverse beam size σ_{xy}, and if no self-interaction of the bunch is expected. However, evaluating the accuracy of this approximation for the simulated electric field strength in the EO crystal requires knowledge of the transverse charge density profile of the beam, the position of the EO crystal and the probe laser trajectory within the crystal. These values are often not available in experiments. As the crystal is usually at a certain distance to the beam to avoid affecting the beam dynamics and to avoid damage from direct impact of the particle beam, the impact of the line charge density approximation is expected to be small. However, it depends on the specific measurement scenario and can increase the uncertainty of the resulting simulated field strength.

The longitudinal bunch profile is an input parameter for the simulation. It can be parametrized with a predefined Gaussian function, or it can be defined as a custom profile from discrete data. Since the solver is optimized for Gaussian bunches, custom profiles increase computing time. High-resolution custom profiles, in particular, substantially slow down the simulation, as their high frequency components require additional mesh refinement. This thesis employs Gaussian profiles, as it provides reasonable approximations of key quantities such as the bunch length and peak charge density. Fine structures in the bunch profile and other effects on the beam are neglected at this stage, as they are not critical for developing a general EO monitor concept. The Gaussian parametrization is directly defined by the baseline parameters (bunch charge and bunch length) provided by FCC-ee optics studies. Thus, it enables systematic investigations on how the EO setup at KARA must be adapted to the high-intensity beams of the various FCC-ee operation modes, which is essential for the development of a first prototype.

4.1.1.2 Probing the electric field for EO measurements

Figure 4.3 presents an example for the simulated total electric field on a cross-section of the EO monitor model. In this frame, the electron bunch is located directly below the crystal assembly. The electric field is strongest close to the electron bunch and stretches mostly in y-direction. This shape of the electric field is caused by high Lorentz factor $\gamma \approx 2500$, which leads to a strong Lorentz compression (see Chapter 2.1.3). The crystal, the mirror and the crystal holder protrude into the vacuum chamber and interact with the electric field, causing a complex dynamic of the electric field inside the crystal.

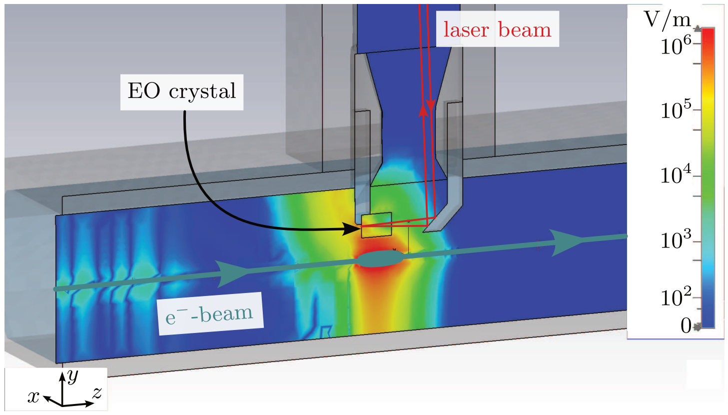

Figure 4.3: Cross-section of the simplified model of the KARA EO in-vacuum setup in the simulation program CST Particle Studio [48] the color-coded total electric field strength. For illustration purposes, An indicator for the laser beam and electron beam trajectory has been added.

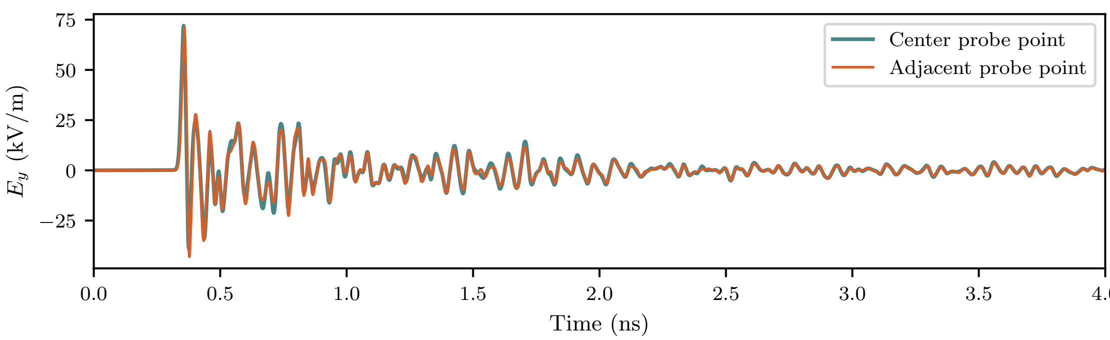

Figure 4.4: Simulated electrical field strength in y-direction of a probe in the center of the crystal and an adjacent probe at $\sim 0.3\,\mathrm{mm}$ distance. These are two adjacent example probes out of the 23 probes, which are placed equidistant along a line in the crystal. As the change of the electric field is small, the total number of probes is considered sufficient to sample the electric field at the trajectory of the laser light, which is essential for simulations of the EO effect.

For EO measurements, laser pulses are sent through the crystal. The electric field strength at the laser trajectory leads to a polarization modulation of the laser light through the EO effect (see Chapter 2.2). In the simulation, probe points are placed on a line through the crystal to monitor the electric field over time along the virtual laser trajectory.

Figure 4.4 presents the data from one field probe at the crystal center and data from the neighboring probe at a distance of $\Delta d \approx 0.3\,\mathrm{mm}$. The probe data is the vertical component E_y of the electrical field, because the crystal and laser polarization are oriented such that E_y provides the strongest modulation of the laser light (see Chapter 2.2.2). To simulate EO measurements, 23 of these probes are spaced at equal intervals on a line through the crystal, thus sampling the electric field along the laser trajectory. This is the maximum number of probes of which the data can be conveniently exported with the CST user interface, and, as the example in Fig. 4.4 shows, the change from one probe to the next is small. Therefore, the number of probes is considered sufficient for further calculations of the EO effect.

4.1.2 Simulation of EOS measurements at KARA

The simulated electric fields in the EO crystal need to be processed further to simulate EOS measurements. As indicated by the flow chart in Fig. 4.1, the laser pulse probes the electric field strength via the EO effect in the EO crystal. The EO effect causes a birefringence modulation of the crystal, leading to a polarization modulation of the laser pulse, which is quantified by the phase retardation Γ. The subsequent polarization analyzer transforms the polarization modulation into an intensity modulation, which is measured with the detection system.

4.1.2.1 Probing the EO effect with a propagating laser pulse

The electric field at the probe point in the crystal changes over time, and it changes with the position of the probe. In EOS measurements, a laser pulse propagates through the crystal to probe the electric field through the EO effect. This laser pulse propagation needs to be taken into account for the modulation of the laser pulse polarization. It is quantified with the total phase retardation Γ between two perpendicular polarization axes. This has been discussed in Chapter 2.2 for the case of a homogeneous static electric field, resulting in Eq. 2.36, which states a proportionality of the phase retardation Γ to the crystal thickness d times the electric field strength E_y ($\Gamma \propto d \cdot E_0$).

However, in the simulation, the field data is restricted to discrete probe points $i \in \{0, 1, 2, \ldots, N-1\}$, which have a constant spacing Δd and are labeled with increasing numbers in upstream direction. Hence, the phase retardation Γ is approximated with a sum over all probes, assuming a constant electric field $E_y^{(i)}$ between the probes over the length Δd. This approximation provides an additional error in the simulation results, but since the change of the electric field from one probe to the next is small (see Figure 4.4), it was considered acceptable. Due to the propagation of the laser pulse, the electric field $E_y^{(i)}$ also depends on the arrival time t_i of the laser pulse at each probe. Putting these requirements together, the phase retardation results in

$$\Gamma = \frac{2\pi}{\lambda} n_0^3 r_{41} \cdot \Delta d \sum_{i=0}^{N-1} E_y^{(i)}(t_i) \tag{4.1}$$

The arrival time t_i can be calculated in relation to the arrival time t_0 at the first probe via

$$t_i = t_0 + i \cdot \frac{\Delta d}{c/n_0}. \tag{4.2}$$

In this context, n_0 is assumed to be constant, because the Pockels coefficient r_{ij} is small (see Chapter 2.2.1) and the resulting changes of n_0 caused by the EO effect are negligible for the arrival time calculation.

At KARA, the laser pulse is reflected on the backside of the crystal, hence traveling twice through the length of the crystal: First against the electron beam direction (upstream) and after the reflection in beam direction (downstream). Equation 4.1 enables the calculation of both signals by adding a sum over the probes in reverse order, while still increasing the arrival time t_i:

$$\Gamma = \frac{2\pi}{\lambda} n_0^3 r_{41} \cdot \Delta d \left(\underbrace{\sum_{i=0}^{N-1} E_y^{(i)}(t_i)}_{\text{upstream}} + \underbrace{\sum_{i=N}^{2N-1} E_y^{(2N-1-i)}(t_i)}_{\text{downstream}} \right). \tag{4.3}$$

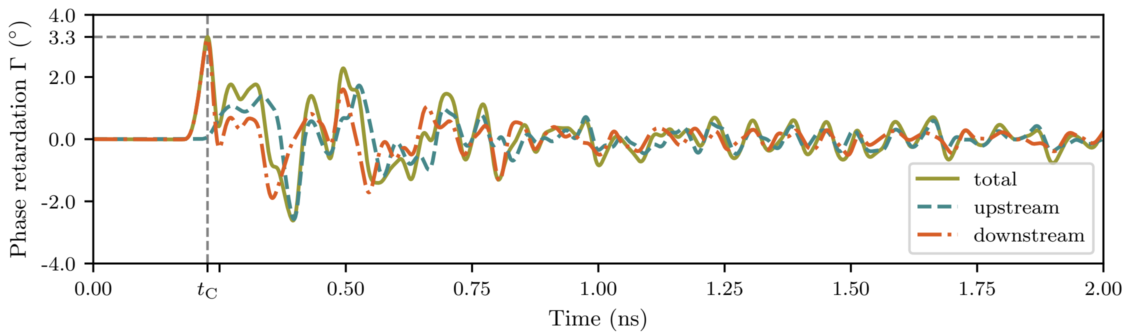

Figure 4.5: Simulation of the total phase retardation Γ at KARA in green, with the upstream component in orange (dash-dotted) and downstream component in blue (dashed). t_C highlights the time of Coulomb peak from the bunch overlapping with the laser. The subsequent peaks of the phase retardation originate in the wake field. Around the time of the overlap t_C, the unwanted upstream signal has a low amplitude.

This requires that the last probe $(N-1)$ has a distance of $\frac{\Delta d}{2}$ to the reflective surface of the crystal. Thus, the distance from one probe to the along the laser trajectory is constant (d), because after the last probe point $N-1$, the laser is reflected at the crystal back side and passes probe point $N-1$ again.

Figure 4.5 presents the total phase retardation Γ for a simulation of the KARA EO setup, and its up- and downstream component. The time on the x-axis describes the arrival time of the laser at the first probe, which is defined to be zero at the simulation start. The position t_C is marked to highlight the peak caused by the Coulomb field of the bunch, while the following peaks are caused by the wake field.

The bunch profile is encoded in the downstream component, because the Coulomb field and the laser pulse co-propagate through the crystal. However, the EO setup measures the total phase retardation, thus bunch profile measurements require a negligible upstream component at the Coulomb peak around t_C. In the example presented in Fig. 4.5, the upstream component is small around t_C and increases afterward. As a result, the total phase retardation is dominated by the downstream component at the first peak, enabling EO bunch profile measurements.

4.1.2.2 Simulation of the polarization analyzer

The phase retardation corresponds to a polarization modulation of the probe laser, which is converted to an intensity modulation with the polarization analyzer. It contains a $\lambda/4$-, a $\lambda/2$-waveplate and a polarizing beam splitter (see Chapter 2.2.3). The simulation uses Eq. 2.37 to calculate the laser intensity I_{det}, which states [26, pp. 42 f]

$$I_{\text{det}}(\theta, \phi, \Gamma) = \frac{I_{\text{laser}}}{2}[1 - \cos(\Gamma - 2\phi + 4\theta)\cos^2(\phi) + \cos(\Gamma + 2\phi - 4\theta)\sin^2(\phi)],$$

with the angle ϕ of the $\lambda/4$-waveplate and θ of the $\lambda/2$-waveplate. These angles define the working point of the EO setup, which is discussed in Chapter 3.1.2.

An example of the laser intensity is presented in Fig. 4.6 with a near-crossed working point with $\phi = 2°$, $\theta = 7°$. The working point was chosen to fit to an example EOS measurement at KARA, in which crystal heating issues lead to an unintended drift of the working point (see Chapter 3.1.4). This measurement example has been discussed in Chapter 3.1.3.1 and is compared to the EOS simulation later in Chapter 4.2.

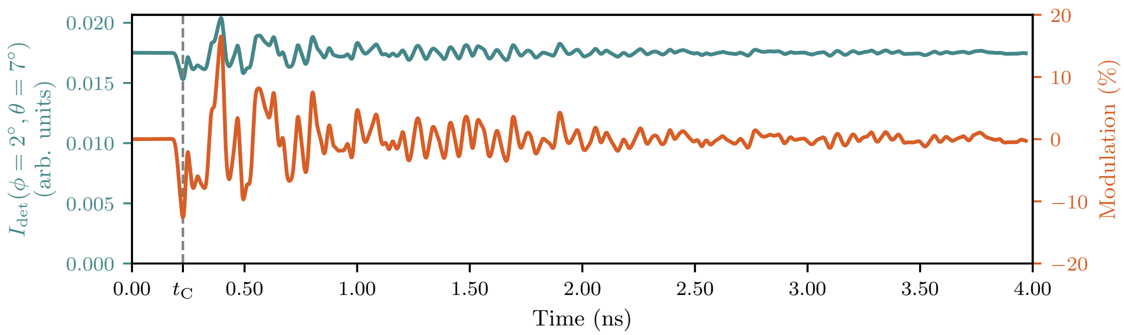

Figure 4.6: Laser intensity modulation derived from Eq. 2.37 in blue, and corresponding relative modulation in orange. The working point is set to $\phi = 2°$ and $\theta = 7°$, to match the working point of the EOS example measurement at KARA, which is discussed in Chapters 3.1.3.1 and 4.2.

In the presented Fig. 4.6, the initial laser intensity is given in arbitrary units and normalized to $I_{\text{laser}} = 1$, resulting in a normalized laser intensity after the polarization analyzer in the order of ∼0.02. The selected working point causes a reduction in laser intensity I_{det} for a positive phase retardation Γ and vice versa. Hence, EO effect of the bunch's Coulomb field around t_{C} causes a reduction of the laser signal (negative modulation).

EO measurements are often presented via the relative laser intensity modulation, which describes the ratio of the modulated laser intensity to the unmodulated laser intensity $\frac{I_{\text{det}}(\Gamma)}{I_{\text{det}}(\Gamma=0°)}$. In general, the working point is optimized to achieve a maximum relative modulation for the given electric field strength, while keeping an approximately linear correlation of the laser intensity and the phase retardation $I_{\text{det}} \propto \Gamma$ (see Chapter 2.2.3). The working point in this example ($\phi = 2°$, $\theta = 7°$) leads to a noticeable non-linear correlation between the phase retardation Γ and the laser intensity I_{det}, which has been explained in more detail in Chapter 2.2.3. As a result, a positive phase retardation of e.g., $\Gamma = 3°$ leads to a negative modulation with smaller absolute amplitude than its negative equivalent $\Gamma = -3°$. This effect is visible in the modulation in Figure 4.6, where the amplitude of the largest peak of the wake field at $t \approx 0.4\,\text{ns}$ is $\sim 23\,\%$ larger than the positive peak at t_{C}, while in the phase retardation, the wake field peak was $\sim 25\,\%$ smaller (see Fig. 4.5). This comparison demonstrates, that the chosen working point is not optimal for bunch profile measurements, where a higher modulation at t_{C} would improve the signal-to-noise ratio.

4.1.2.3 Simulation of the detection system

EOS measurements use multiple laser pulses with increasing arrival time to sample the electric field of consecutive bunches in the EO crystal. During EOS measurements at KARA, there is typically only one electron bunch in the storage ring, hence a maximum of one sample per turn is taken. The resolution of the final EOS measurement can be limited by the sampling rate, the laser pulse length and the bandwidth of the data acquisition (see Chapter 2.2.5). The same laser settings are used at KARA for EOS and EOSD measurements, thus the results mainly differ in the data acquisition. For the simulation of either EO technique, the modulation of single laser pulses needs to be calculated first.

At KARA, EOS measurements were typically performed by changing the laser delay in steps of $\sim 6\,\text{ps}$ approximately every 1.25 s, yielding a sampling rate of 128 steps/ns over the laser delay. The laser pulse length at the EO crystal was approximated with separate auto-correlator measurements to be $\sigma_{\text{laser}} \approx 20.2\,\text{ps}$ for this EOS measurement . In the simulation, these parameters are used to calculate

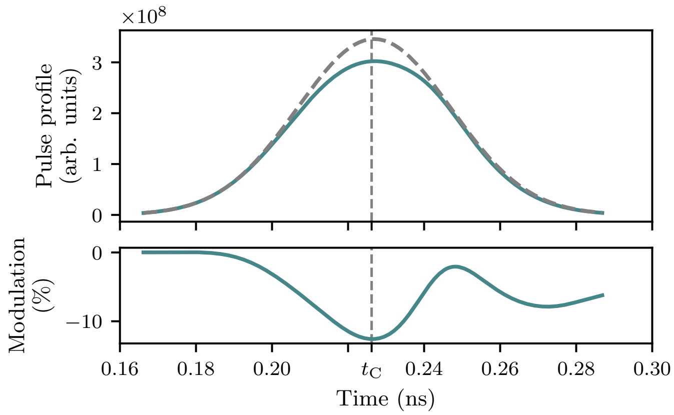

Figure 4.7: Comparison of the simulated modulated laser pulse profile at t_C (blue) versus the unmodulated laser pulse profile (gray). The bottom plot shows the modulation M, which is the division of the modulated and the unmodulated laser pulse.

the modulation of a single laser pulse at a certain delay based on the previously calculated continuous laser intensity simulation. The laser pulses are approximated as normalized Gaussian functions of width σ_{laser}, which are multiplied with the modulation M at a certain arrival time.

An example for the resulting modulated laser pulse is presented in Figure 4.7. It shows a simulated laser pulse modulated by the Coulomb field at the time t_C in comparison to the unmodulated Gaussian. In EOSD measurements, this modulated profile is measured, and its relative modulation reveals the electron bunch profile and parts of the following wake field. For EOS simulations, these laser profiles need to be processed further to account for the data acquisition.

The data acquisition consists of a photodiode, which is connected to a lock-in amplifier. The photodiode has a bandwidth of 3 GHz and is approximated in simulation as a low-pass filter. For the principle of the lock-in amplifier, it is important to distinguish two different time axes, which are connected to the EOS measurements:

- The sampling delay, which is the relative arrival time shift of the laser pulse between each sampling step. Its total range for one EOS scan is in the order of ns, with individual steps typically in the order of ps.
- The measurement duration, which describes the total time that an EOS scan takes. The total duration is typically in the order of 10 min.

In general the lock-in amplifier mixes the photodiode signal with a KARA revolution frequency of 2.7 MHz as reference signal, and applies a low pass filter with a time constant $\tau_{\text{lock-in}}$. During EOS measurements, each sampling step takes about 1.25 s, hence the time constant is set to $\tau_{\text{lock-in}} = 1\,\text{s}$. The resulting lock-in signal therefore only shows the changes from on sampling step to the next and averages over multiple shots per step. Thus, the lock-in amplifier leads to a noticeable improvement of the signal-to-noise ratio compared to the EOS scans with only the photodiode. In the simulation, the lock-in amplifier is approximated by calculating the maximum amplitude of each scan step and applying a low pass filter with a time constant of $\tau_{\text{lock-in}}$ over the measurement duration.

Figure 4.8a presents a comparison of the simulated laser intensity I_{det} and the simulated EOS measurement, which includes the laser pulse length and data acquisition. The EOS simulation has a reduction in detail, where for example overlap of the Coulomb peak at t_C and the following first peak of the

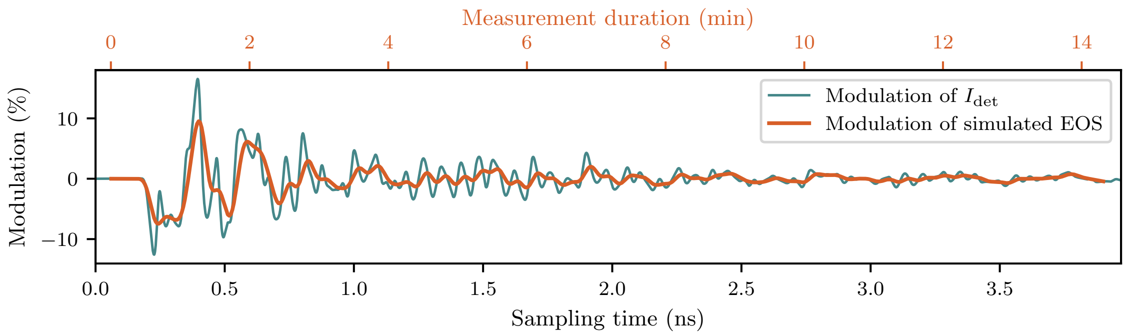

(a) Time domain

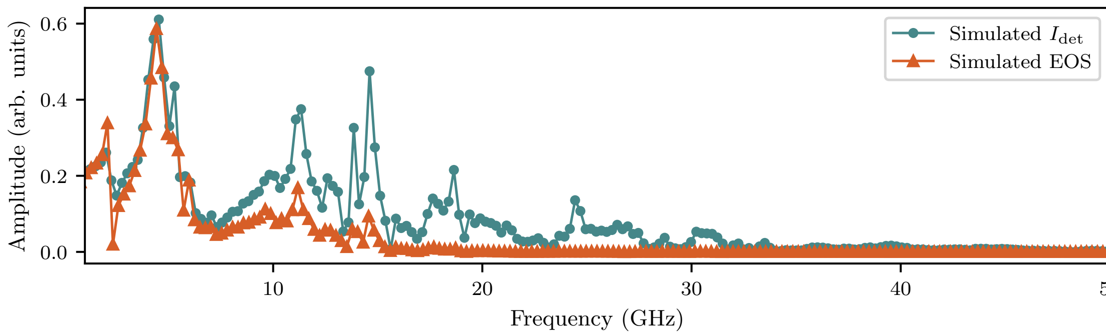

(b) Frequency domain

Figure 4.8: Comparison of the simulated modulation of the laser pulse (blue) and the modulation of a simulated EOS measurement (orange), including filtering by the photodiode and the lock-in amplifier. The time domain EOS signal in (a) shows a smoothing of the laser pulse modulation, which appears in its spectrum in (b) as a suppression of frequencies above ~8 GHz. (Also presented in Ref. [2])

wake field has increased. It still enables to visually distinguish both peaks and identify the first peak as the Coulomb peak, but it does not correspond directly to the bunch profile. To analyze the reduced bandwidth, the corresponding spectrum for both traces is calculated with an Fast Fourier Transform (FFT) and presented in Fig. 4.8b. The peak around 4.5 GHz is the most prominent peak and similar in both signals. Additional simulations suggest that it originates in a resonance of the vacuum chamber, since it changes with its width and with the position of the crystal inside the chamber. The raw modulation of the laser intensity I_{det} also shows multiple frequency peaks between 8 GHz and 45 GHz, which are suppressed in the full EOS simulation. This reduction in bandwidth for EOS measurements is expected, as it acts similar to a moving average where the laser pulse profile provides the weighted averaging window (see Chapter 2.2.5). Thus, EOS measurements are suitable to provide an overview over the bunch's Coulomb and Wakefield or to benchmark the EO setup for working point optimizations, because the detection system and data acquisition is relatively simple. However, the more complex readout for EOSD measurements is required for single-shot bunch profile measurements.

4.2 Comparison of simulation and experiment

Figure 4.9 presents a comparison of the EOS simulation and the corresponding EOS measurement at KARA. It shows the simulated and measured modulation of the laser signal. The details of this EOS measurement and its uncertainty have been described previously in Chapter 3.1.3.1. The uncertainty is

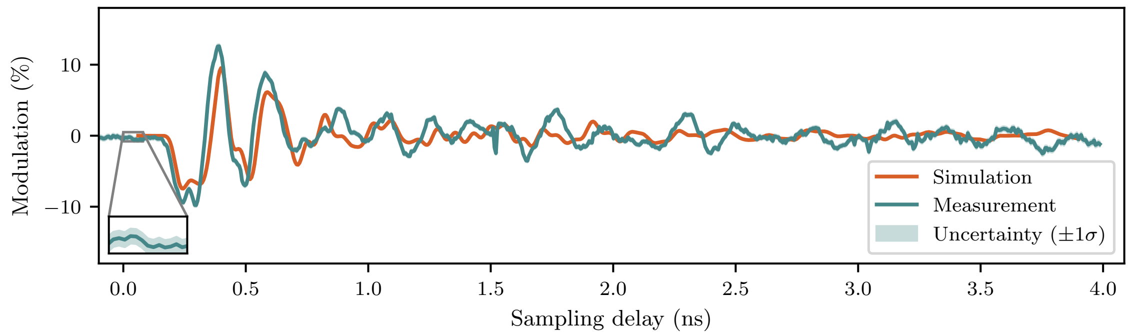

(a) Time domain

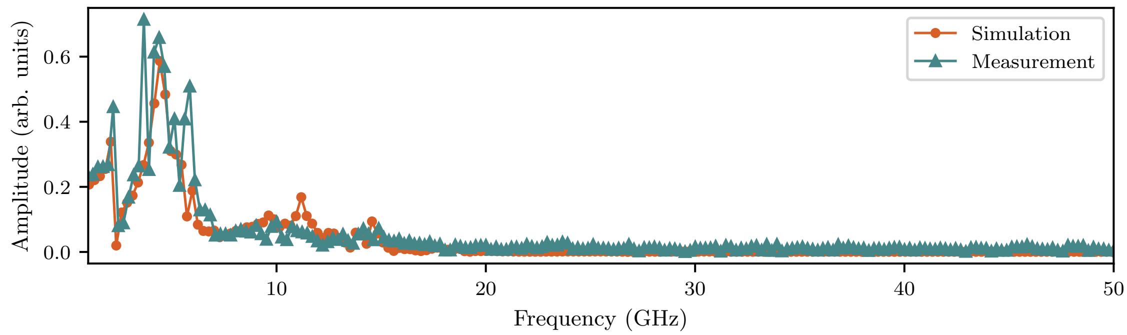

(b) Frequency domain

Figure 4.9: Comparison of the simulated (orange) and measured (blue) EOS modulation. The modulation in time domain is presented in (a), while (b) shows the corresponding result of a FFT. The measurement data was taken at KARA and the measurement and the uncertainty calculation is described in Chapter 3.1.3. The Coulomb peak at t_C and the following most prominent peaks have a lower amplitude in the simulation, but the general shape matches well. The FFT reveals some frequencies, which are not represented in the simulation. (Also presented in Refs. [1, 3])

highlighted in a small additional zoomed-in plot, because it disappears behind the line thickness of the full plot. The input parameters of the simulation are derived from the example measurement and summarized in Tab. 4.1. A small offset was added to the sampling delay of the measurement to have the first peak for both signals at the same time t_C.

For the first, most prominent peaks from t_C to $\sim 0.8\,\mathrm{ns}$, the modulation of measurement and simulation match in their general shape. For example, the characteristic double peak is present in both signals. It starts at the negative Coulomb peak and transitions to the next negative peak, which is mainly caused by the upstream signal (see Figure 4.5). However, the amplitude at t_C in the simulation is $\sim 2.3\,\%$ below the measured modulation. In general, the simulation underestimates the modulation amplitude, which could be caused by a mismatch of the working point. The settings of the wave plate angles ϕ and θ relative to the initial laser polarization have a large impact on the modulation amplitude and had to be estimated for the measurement (see Chapter 3.1.3.1). In addition, the distance of the laser trajectory in the crystal to the electron orbit was not directly measured, but estimated based on the crystal position and the geometric center of the vacuum chamber. An overestimation of the crystal distance could also lead to the smaller simulated amplitude.

In comparison to the simulation, the measurement shows additional oscillations after the first prominent peaks ($t \gtrsim 1.5\,\mathrm{ns}$). It could be caused by additional impedances within the KARA vacuum chamber, like strip lines, vacuum pump ports, beam position monitors and others, which are upstream of the EO monitor, but not represented in the simplified geometry in the simulation.

The resulting spectrum from a FFT of the modulation is presented in Fig. 4.9b. It reveals a similar spectrum of the simulation and experimental data with one main peak at around $\sim 4.5\,\mathrm{GHz}$. However, the measurement has three additional sharp peaks at $\sim 3.7\,\mathrm{GHz}$, $\sim 5.1\,\mathrm{GHz}$ and $\sim 5.3\,\mathrm{GHz}$ directly next to the main peak. They could be missing in simulation due to the simplifications in the geometry of the vacuum chamber and crystal assembly.

In summary, the similarities of the simulated large-scale features to the EOS measurement at KARA show the capability of the simulation procedure and support its suitability as a tool for the development of an EO bunch profile monitor. Although it shows its limits towards smaller features, it captures the major wakefield features and enables gaining insight about the impedance (and wake field), the modulation amplitude and the resolution limitations caused by the laser pulse length and the data acquisition system. The simulations also enable to study the up- and downstream component of the phase retardation, which cannot be measured directly with EOS. Since the upstream signal could disturb bunch profile measurements with EOSD when it overlaps with the Coulomb peak of the downstream signal, it is an important factor to monitor, if the beam parameters change. Overall, the simulation procedure is suitable to aid with the development of an EO monitor for FCC-ee, as it enables the estimation of crucial parameters like the impedance, the modulation amplitude, and the interference of the up- and downstream EO signal.

4.3 Concept design for FCC-ee

The EOS simulation procedure is used in this section to identify challenges of the EO monitor design for the unique and demanding beam parameters of FCC-ee. To mitigate the identified challenges, a new conceptual design is proposed and evaluated with the simulation. The beam parameters that mostly affect EO measurements are the bunch charge, which is in the order of $\sim$30 nC and the bunch length, which ranges from $\sim$2 mm to $\sim$15 mm for the different operation modes [9]. The higher beam energy of 45 GeV to 180 GeV only has a minor influence, since it changes the opening angle of the Coulomb field proportionally to $1/\gamma^2$. The opening angle was already small at KARA ($\gamma^{KARA} \approx 2\,500$) and is even smaller for the high beam energies of FCC-ee, hence it is not expected to have a notable impact on the EO monitor resolution.

The development of the EO monitor concept design in this section has partially been published in Refs. [1, 5, 6], but since then, the simulations have been updated to use the new vacuum chamber dimensions with 60 mm diameter instead of 70 mm, and the beam parameters from the feasibility study report [9] (see Table 1.1).

4.3.1 Simulation of the KARA EO monitor under FCC-ee beam parameters

To benchmark the KARA EO setup under FCC-ee beam conditions, the simulation procedure of Chapter 4.1.2 is repeated using the FCC-ee beam parameters at Z-pole energy. The example of the parameters at Z operation is presented in particular, because long bunches are suspected to be a major issue for the design of the KARA EO setup and the Z operation mode has the longest bunches. An evaluation of the other operation modes follows in Chapter 4.3.2 with the simulation of a new conceptual crystal assembly design for FCC-ee.

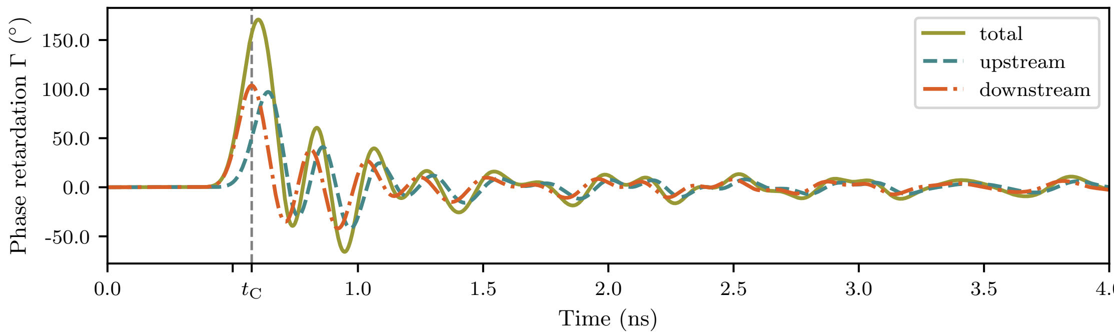

Figure 4.10: Simulated phase retardation of the KARA EO setup under FCC-ee beam conditions. The simulation parameters are similar to Table 4.1, which was used for Fig. 4.5, but with the high bunch charge and length of the FCC-ee Z-operation (see Table 1.1). The Coulomb peak at t_C of the downstream component overlaps with the first peak of the upstream signal, which masks the Coulomb peak in the total phase retardation. This is problematic for bunch profile measurements with EOSD, because only the total phase retardation is measured.

The presented simulation uses the same input parameters as the previous KARA EOS simulation, which are described in Table 4.1. The exceptions are the bunch charge and bunch length, and beam energy. In the Z operation mode, FCC-ee has its longest bunches, with $\sigma_z = 15.2\,\mathrm{mm}$ at a bunch charge of $q = 34.9\,\mathrm{nC}$.

Figure 4.10 presents the simulated phase retardation and its up- and downstream component. In comparison to Figure 4.5 with KARA beam parameters, the long bunches of FCC-ee lead to broader peaks and an overall smoother curve. A FFT analysis reveals that the main frequency still is at 4.5 GHz, but the higher frequency components are missing. Due to the high bunch charge, the total phase retardation Γ of the first peak increased from ∼3.3° to ∼170.9°. This leads to a nonlinear modulation of the probe laser intensity I_{det}, which has a sinusoidal correlation to the phase retardation Γ (see Eq. 2.38). The working point is usually set to provide an approximately linear correlation for small phase retardations (see Chapter 2.2.3), which is not valid for large Γ. As a result, the spectrum in EOSD measurements would not have a linear correlation to the bunch profile and would require additional processing to retrieve it.

The high bunch charge also leads to high electrical fields strengths inside the EO crystal. The simulated field strength at KARA peaked at around ∼70 kV/m (see Figure 4.4) in the crystal center, but it reaches ∼1 140 kV/m for the FCC-ee beam parameters. As discussed in Chapter 3.1.4, some part of the energy of the electric field (Coulomb and wake field) is absorbed and transformed to heat, which can lead to a drift of the laser polarization through changes of the intrinsic birefringence in the crystal. This drift does not prohibit EOSD bunch profile measurements directly, but it requires continuous adjustments of the $\lambda/4$ and $\lambda/2$ wave plate after the crystal to keep the optimal working point. This effect also scales with the repetition rate of bunches passing the crystal. For Z operation, in the order of 11 000 bunches per beam are planned, which results in a beam current of ∼1 300 mA. This is around a factor 1 000 more than during EOS measurements at KARA, with a typical current of ∼1 mA to 2 mA.

Figure 4.10 also reveals, that the long bunches lead to an overlap of the first peak of the downstream signal with the first peak of the upstream signal. The downstream signal peak at t_C corresponds to the bunch profile, but due to the overlap with the upstream signal, the bunch profile is obscured in the total phase retardation Γ. This is a major issue, because EOSD only measures the total phase retardation and is therefore unable to measure the bunch profile under these conditions.

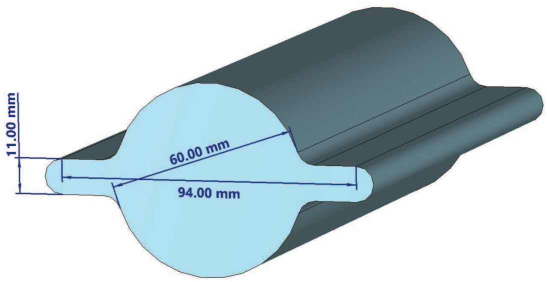

Figure 4.11: 3D schematic of the FCC-ee vacuum chamber. Dimensions are deducted from Ref. [9]

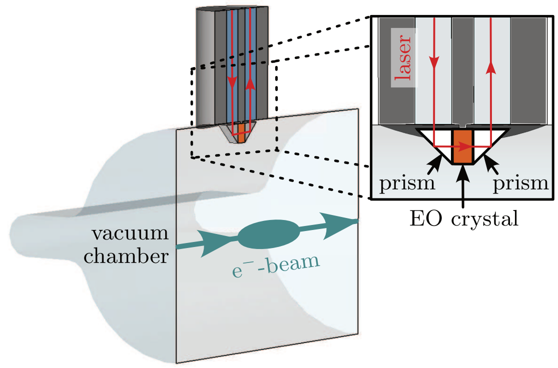

Figure 4.12: Concept design of an EO monitor for FCC-ee. The model is designed in CST studio [48]. The EO crystal is placed between two prisms at the top of FCC-ee's vacuum chamber. The prisms provide total internal reflection to guide the incoming laser pulses (red line) once through the crystal (single pass) before it is sent back for analysis. This conceptual design has been presented first in Ref. [6].

In summary, the simulation revealed multiple challenges with the EO monitor design under FCC-ee conditions, and especially a major issue that prohibits bunch profile measurements with long bunches. Thus, the design needs to be adapted for FCC-ee and requires a new design of the crystal assembly.

4.3.2 New design of the crystal assembly for FCC-ee

As established by previous simulations, the new design of an EO monitor for FCC-ee needs to be adapted for high bunch charges in the order of 30 nC and especially long bunch lengths of up to 15.2 mm. As discussed in Chapter 1, the setup should be compact with a low impedance to minimize the impact on FCC-ee's beam dynamics. Since the four operation modes of FCC-ee come with notable changes in the beam parameters (see Table 1.1), the setup also needs to be be placed in FCC-ees vacuum chamber and cope with the different operation modes with as few hardware changes as possible.

These challenges are addressed with a new concept design, which is discussed and tested in simulations in the following sections.

4.3.2.1 Design considerations

As the EO monitor requires an EO crystal that is exposed to the electric field of the particle bunches in-vacuum, the geometry of the vacuum chamber plays a crucial role in its design. All operation modes share most of the same hardware components, including the vacuum chamber. A short section of the vacuum chamber volume is presented in Fig. 4.11, which has a round cross section with radius $r = 60\,\mathrm{mm}$ with horizontal winglets [9]. As the synchrotron radiation radiates tangentially from the beam trajectory, it mainly impacts the outer winglet of the ring and causes a temperature increase of the vacuum chamber wall. Hence, the winglets provide space for additional synchrotron absorbers to dissipate the additional heat.

Figure 4.12 presents a simplified 3D model, which was created in CST Studio [48] to enable first tests of the new design with simulations. The concept design of the crystal assembly for FCC-ee addresses the challenges with multiple changes compared to the KARA EO setup. As a first proof-of-principle design, it assumes the same 1 030 nm laser as used at KARA and a GaP crystal. The image shows a crystal with dimensions of 5 mm × 5 mm × 7 mm, but the crystal thickness can be varied to further reduce or increase the phase retardation (see Eq. 4.1).

To decrease the phase retardation amplitude, the crystal is placed at a greater distance to the beam. Hence, the EO concept takes full advantage of the height of the vacuum chamber, and the crystal is attached at the top to maximize the distance to the particle beam and to reduce exposure to the intense synchrotron radiation (SR) in the horizontal plane.

To avoid the upstream signal, the laser pulses are guided only once through the EO crystal. This single-pass setup is realized with two prisms, which are attached to the sides of the crystal. They are oriented such, that the incident laser pulse experiences a total internal reflection, leading to a refection angle of 90°. The first prism guides the incoming laser (from the top) downstream through the crystal, and after the crystal, the second prism reflects the laser pulses upwards out of the vacuum chamber. Hence, the setup requires changes of the interaction modulate, but the laser and detection system could be similar for example to the EO monitor setup at KARA (see Chapter 3.1.2).

The prisms enable a compact, single-pass setup without using a reflective coating on the crystal, which is needed for the setup at KARA. This benefits the use in environments with higher beam currents, because it can lead to cracks in the coating, reducing its performance. Cracks in the crystal coating have been observed at KARA, which were likely caused by temperature changes of the crystal during tests at higher beam currents [27, p. 112 f.]. The anisotropic crystal has a different thermal expansion rate than the coating, and the resulting mechanical stress is expected to cause the coating to break. FCC-ee will operate at high beam currents, thus avoiding the reflective coating in the EO concept is an important feature.

The prisms and the crystals are attached to a metal plate, which has a hole above each prism to serve as an opening for the laser pulses. In contrast to the setup at KARA, where the crystal was mounted to an arm with a large opening in its center (see Fig. 4.2), the holes in the EO concept for FCC-ee are smaller to reduce the impedance in the GHz range.

4.3.2.2 Simulation results

This section discusses the simulation results based on beam parameters at FCC-ee during Z operation as a first example, but a comparison of the different operation modes is provided later. The beam parameters in the simulation are taken from Table 1.1. The crystal at KARA has a thickness of 7 mm, but has been reduced to 3 mm for the simulation of the EO concept to further reduce the phase retardation. The prisms are assumed to be common fused silica prisms, which provide decent radiation hardness [102] and the optical properties to be used with total internal reflection for the given 1 030 nm laser.

The maximum strength of the electric field in the center of the crystal is 300 kV/m, which is only 25 % of the 1 200 kV/m from simulations with FCC-ee beam parameters in the KARA setup (see Chapter 4.3.1). However, it is still $\sim$3 times higher than the simulated 72 kV/m during typical EO measurements at KARA (see Fig. 4.4)

The simulated phase retardation Γ of the EO concept for FCC-ee is presented in Fig. 4.13 in comparison to the simulated total phase retardation of the typical EO measurement at KARA (taken from Fig. 4.5).

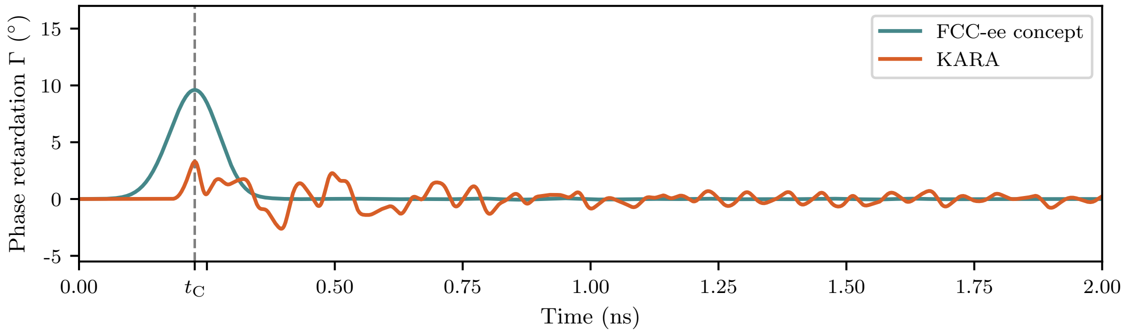

Figure 4.13: Simulated phase retardation Γ of the EO monitor concept for FCC-ee during Z operation (blue) in comparison to Γ from the setup at KARA during a typical measurement (orange, taken from Fig. 4.5). The phase retardation of the FCC-ee concept has a maximum amplitude of 9.6° at the Coulomb peak t_C, which ~3 times higher compared to KARA, but still feasible for EO bunch profile measurements. The wake field and upstream signal are a potential concern to disturb EO bunch profile measurements, but neither are visible in the simulation of the EO concept for FCC-ee.

A time offset was added to the phase retardation of the FCC-ee concept in order to visually align the first peak of both signals at t_C.

The Coulomb peak at t_C has a maximum phase retardation of $\Gamma_{max}^{(\text{FCC-ee Z})} \approx 10.5°$, about three times larger than at KARA ($\Gamma_{max}^{(\text{KARA})} \approx 3.3°$, see Chapter 4.1.2). The larger Γ_{max} requires adjusting the $\lambda/2$-waveplate angle θ to maintain an approximately linear correlation between I_{det} and Γ (see Chapter 2.2.3). For example, the working point $\phi = 0°$, $\theta = 10°$ produces a linear fit to $I_{det}(\Gamma) \in [0, \Gamma_{max}]$ with a coefficient of determination $R^2 > 0.999$, indicating sufficient linearity.

Increasing θ also reduces the relative modulation $M = I_{det}(\Gamma)/I_{det}(0) - 1$, which affects the signal-to-noise ratio. Nevertheless, due to the high Γ_{max}, the maximum modulation still reaches $M_{max} \approx 50\,\%$, which is higher than what was simulated for KARA.

The wake field is a prominent feature in the simulated KARA setup, which produces an oscillating total phase retardation after the Coulomb peak t_C. The oscillation amplitude is a sum of the upstream and downstream phase retardation, which is caused by the wake field in the EO crystal (see Fig. 4.5). The amplitude is in the order of the Coulomb peak in the beginning, but it is dampened over time. For the FCC-ee setup, this following oscillation is reduced and barely visible in Fig. 4.13. The main reasons are the missing upstream signal and the reduced impedance of the setup, which is discussed later in this section.

Figure 4.14 presents a summary of the simulated phase retardation of the different FCC-ee operation modes. To account for the increasing bunch charge density from Z, W, ZH and $t\bar{t}$ operation modes, the crystal thickness was reduced to $d^{(\text{Z, W, ZH, } t\bar{t})} = 3\,\text{mm},\ 1\,\text{mm},\ 1\,\text{mm}$ and $0.5\,\text{mm}$. This enables to keep the maximum phase retardation at a similar magnitude, with $\Gamma_{max}^{(\text{Z, W, ZH, } t\bar{t})} \approx 10.5°,\ 10.9°,\ 12.6°$ and $13.7°$. The linearity of $I_{det}(\Gamma) \in [0, \Gamma_{max}]$ is still sufficient across all operation modes for example for the working point $\phi = 0°$, $\theta = 10°$, as a linear fit yields a coefficient of determination $R^2 \geq 0.999$ for all.

Towards shorter bunch lengths, a negative peak becomes more pronounced after the Coulomb peak and reaches a maximum negative amplitude of −4.7° at $t\bar{t}$ operation. This negative peak is likely the first occurrence of an oscillating wake field, which is damped quickly after one period to an amplitude below 0.4°. As the wake field is a result of the impedance (see Chapter 2.1.2),

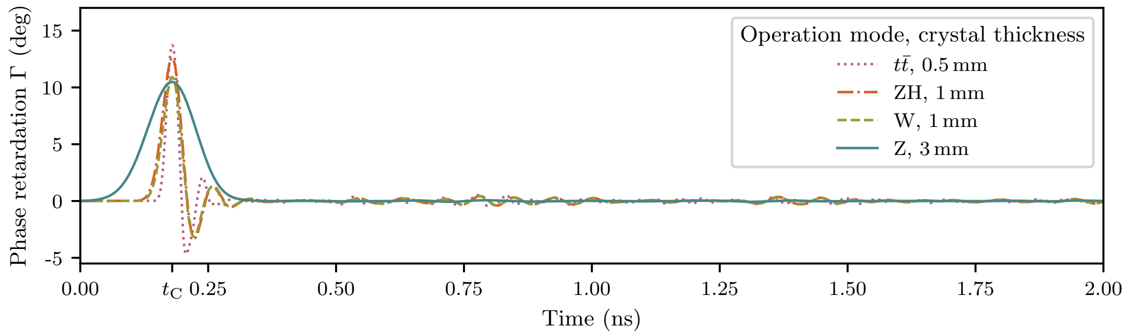

Figure 4.14: Comparison of the simulated phase retardation Γ of the different FCC-ee operation modes. The mode-specific particle beam parameters are listed in Table 1.1 and the general simulation parameters are taken from Table 4.1, but the crystal thickness is reduced to $d = 3\,\text{mm},\ 1\,\text{mm},\ 1\,\text{mm}$ and $0.5\,\text{mm}$ for the Z, ZH, W and $\text{t}\bar{\text{t}}$ operation modes respectively.

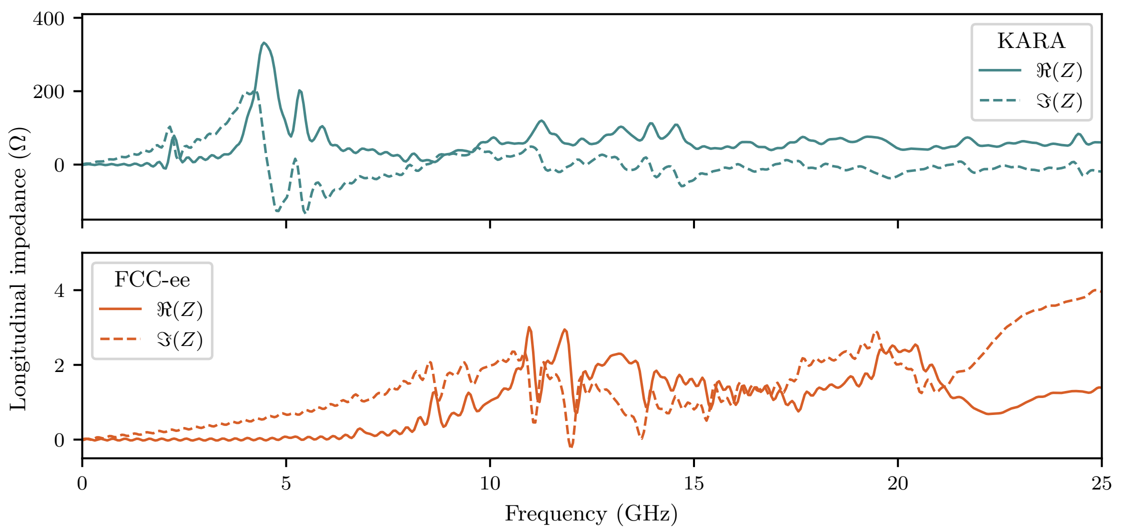

Figure 4.15: Simulated longitudinal impedance Z of the KARA EO setup and the FCC-ee concept. The real (solid line) and imaginary part (dashed line) result from simulations with the CST Wakefield Solver [48]. The plot on top corresponds to the EO monitor setup at KARA, as described in section 4.2, and the bottom plot corresponds to the EO monitor concept for FCC-ee with a 3 mm thick EO crystal. Both cases are displayed on separate axes, because the different geometry of the FCC-ee concept and its greater distance between the crystal and the particle beam result in an impedance reduction of two orders of magnitude.

Fig. 4.15 presents the longitudinal impedance of the KARA EO monitor and the FCC-ee concept, enabling a comparison independent of bunch length and charge. Like the simulation of the electric field, the impedance is simulated numerically using the CST Wakefield Solver [48]. For both cases, the real and imaginary part of the longitudinal impedance is presented, where the real part represents resistive impedance resulting in energy loss of the beam, and the imaginary part generally represents inductive ($\Im(Z) > 0$) and capacitive ($\Im(Z) < 0$) impedance that can affects the bunch profile and can cause instabilities (see Chapter 2.1.2).

The presented frequency range from 0 GHz to 25 GHz captures the major features within the main part of the bunch's spectrum (bunch form factor), of which the bandwidth approximately ranges from

3.7 GHz (FWHM) in Z-operation to 24.5 GHz (FWHM) in $t\bar{t}$ operation. The simulated frequency range was chosen as a balance that captures most features within the main spectrum of the bunch's form factor, while simulations towards higher frequencies would have an increased computing time and would require more detailed 3D models with a finer mesh size.

The simulated real part of the impedance at the KARA EO monitor has a major peak at ∼4.45 GHz with an amplitude of ∼332 Ω, next to a major peak of the imaginary part at ∼4.25 GHz with an amplitude of ∼203 Ω. Additionally, the imaginary part has a two neighboring negative peaks around 5 GHz with an amplitude of ∼−135 Ω. Multiple smaller peaks follow towards higher frequencies from 10 GHz to 25 GHz, resulting in an average real part impedance of ∼63 Ω, and a low average imaginary part of −6 Ω.
The impedance peaks causes the wakefield oscillations that are visible in the simulated EOS scans, which was discussed previously in section 4.1.2.3. Per definition, the frequency of the impedance peaks also fits to the peaks in the FFT of the wakefield. The resistive impedance ($\Re(Z)$) describes the energy loss of a given particle bunch, hence it also describes the deposited power in the vacuum chamber. A fraction of this heat load also affects the EO crystal, which was discussed in Chapter 3.1.4 with a corresponding simulation of the crystal only, without its holder and the surrounding vacuum chamber.

The FCC-ee EO monitor concept has generally a lower impedance with less pronounced peaks, with an impedance maximum at ∼11 GHz with an amplitude of 3 Ω and very broad peak of the imaginary part at ∼4.25 GHz with an amplitude of ∼2.2 Ω. For frequencies from 15 GHz to 25 GHz, the impedance real part averages to ∼1.4 Ω, and the imaginary part averages ∼2.2 Ω.
Thus, the impedance for the FCC-ee concept is about two orders of magnitude smaller than the KARA EO monitor, which is mainly achieved by increasing the distance of the crystal assembly to the beam, and replacing the protruding metal mirror and crystal holder with prisms attached to the crystal. The reduction of the impedance is a crucial part for FCC-ee, as it is important that the EO monitor affects the beam properties as little as possible. On the other hand, the deposited power and resulting heating of the crystal also needs to be reduced as much as possible to avoid a drift of the signal baseline and, in extreme cases, damage to the crystal (see Chapter 3.1.4). Although the impedance was drastically reduced, FCC-ee's great beam currents still lead to an estimated deposited power of 0.3 W during Z-operation (following the calculations in Chapter 3.1.4), which is an order of magnitude larger that what was estimated for the crystal at KARA. However, the uncertainty on this value is large, as it is unclear how much of this power is deposited in the crystal itself and it strongly depends on the final technical design of the crystal assembly.

The reduction of the impedance is a great milestone for the development of the EO monitor design for FCC-ee and can be used as a baseline for future estimations of the total impedance of FCC-ee. The impedance of different structures around the FCC-ee accelerator ring are discussed in the FCC-ee feasibility study report [9, pp. 28 ff], where the presented total longitudinal impedance of the whole accelerator ring is in the order of 10 000 Ω. The great impedance is mainly caused by the accumulation over the great length of around 91 km of the overall accelerator structure and in this context, the contribution of the EO monitor impedance is expected to be small. However, the impedance remains a very important factor to consider when progressing toward a technical EO monitor design, because localized impedance peaks at certain frequencies can have a negative impact on beam stability. Additionally, the transverse impedance is an important subject for future studies, to particularly avoid excitation of the transverse mode coupling instability [59].

In summary, the longitudinal impedance could be reduced by two orders of magnitude. The main contributors to the reduction are: the greater distance of the crystal assembly to the electron beam (enabled by the larger vacuum chamber and high signal amplitude through FCC-ee's great bunch charges), the removal of the mirror next to the crystal, and the reduction of the hole diameter of the vertical metal arm, which is holding the crystal. The simulation of the new concept for FCC-ee shows a larger, but reasonable phase retardation amplitude, which is suitable for EO bunch profile measurements. The crystal thickness can be used as a fine-adjustment of the sensitivity and to adapt to the different operation modes. The added prisms enable this compact, single-pass setup to cope with the long bunches during Z operation, as well as the high charge densities with short bunches during $t\bar{t}$ operation. Since this design has never been tested before, the following chapter describes the design of a first prototype and EOS measurements as a proof-of-principle.

Table 4.1: Typical input parameters for the simulation procedure. These example parameters are chosen to correspond to the example EOS measurement at KARA from Chapter 3.1.3.1.

Parameter	Value		Description
CST Parameters			
Max. frequency	100	GHz	Maximum frequency of the simulation
Bunch length σ_{bunch}	2.96	mm	σ of a Gaussian profile, derived from streak camera measurements
Bunch charge q	274	pC	Total bunch charge of a Gaussian particle bunch
Laser parameters			
λ_0	1 030	nm	Central wavelength
f_{rep}	2.7	MHz	Repetition rate
σ_{laser}	20.2	ps	Pulse duration
Crystal parameters (GaP)			
d	7	mm	Crystal thickness
n_0	3.179		Initial refractive index (derived from Ref. [101])
r_{41}	0.97	pm/V	Pockels coefficient [67]
Working point			
ϕ	2	°	Angle of $\lambda/4$ wave plate directly after the crystal
θ	7	°	Angle of $\lambda/2$ wave plate directly before the PBS
Data acquisition			
Photodiode bandwidth	3	GHz	Used to approximate the PD as a low-pass filter
Time constant $\tau_{\text{lock-in}}$	1	s	Used to approximate the lock-in as low-pass filter

5 Prototype test at CLEAR

A first prototype has been built to test the electro-optical (EO) bunch profile monitor concept for Future Circular Lepton Collider (FCC-ee). It aims to validate the general functionality of the novel crystal holder design with its prisms to guide the laser pulses using total internal reflection. The CERN Linear Electron Accelerator for Research (CLEAR) was chosen for a first proof-of-principle test, because of its in-air test stand, where the setting up of a prototype was possible in a short timescale.

This chapter describes the development of the first prototype, the experimental setup and methods, and the measurement results. These first measurements are summarized in [1, 2], but are treated in this chapter in greater detail with additional measurement results.

5.1 Introduction to CLEAR

The CERN Linear Electron Accelerator for Research (CLEAR) is a linear accelerator with the primary focus on prototyping and validating accelerator components. It also serves as a user facility for irradiation studies of electric components and medical applications [103]. It is composed of the 25 m-long CALIFES injector, followed by a 16 m-long beamline. The in-air test stand is located at the end of the beamline, with a length of approximately 1 m.

Table 5.1: Typical beam parameters at CERN Linear Electron Accelerator for Research (CLEAR), partly adapted and extended from [104]

Parameter	Value
Particle energy	60 MeV to 220 MeV
Bunch charge	0.01 nC to 2.0 nC
Bunch length	0.3 mm to 2.5 mm (1 ps to 7.5 ps)
Bunch train repetition rate	0.8 Hz to 10 Hz
Micro-bunches per train	1 to 150
Micro-bunch repetition rate	1.5 GHz or 3 GHz
Intra-bunch spacing	666.7 ps or 333.3 ps

CLEAR offers a wide range of beam parameters for different use cases. Typical parameter ranges are presented in Table 5.1 [104]. For the experiments with the EO monitor prototype for FCC-ee, a particle energy of $\sim$200 MeV was used. As discussed in Chapter 2.1.3, the opening angle of the Coulomb field scales with $1/\gamma^2$, hence high beam energies are preferred for EO bunch profile measurements, because a large opening angle can limit its resolution. Additionally, high bunch charge densities are desired to achieve a large phase retardation (see Eq. 2.29), thus enabling a better signal-to-noise ratio (SNR). For the EO concept design for the FCC-ee, a very high phase retardation was a concern, due to the very high charge densities at FCC-ee (see Chapter 4.3.1). Since the range of bunch charges at CLEAR is substantially lower, a maximum bunch charge was targeted for the electro-optical sampling (EOS) measurements. The optimization of the bunch charge resulted in relatively long bunches measured to be up to ~7.5 ps during the EOS measurements.

The photoinjector is driven by a Nd:YLF based laser system with a repetition rate of 1.5 GHz in the laser oscillator [105]. The following pulse picker and amplifier stages can typically lead to up to 150 micro-bunches with a spacing of ~666.7 ps. With an optional double pulse generator, the bunch spacing can be cut in half by splitting the pulses into two and adding a delay to one part [105, p. 13f]. For the EOS experiment, the generation of a train of bunches is useful for commissioning. The multiple micro-bunches and therefore longer bunch trains increase the chances of finding the temporal overlap between the probe laser pulse and the Coulomb field in the EO crystal.

Besides regular use of beam position monitors (BPMs) and beam screens to monitor the beam position, an integrating current transformer (ICT) and a wall current monitor (WCM) has been used to monitor the bunch charge. In addition, a spectrometer was occasionally used to monitor beam energy and a transverse deflecting cavity to measure the bunch length.

The EOS experiments have been conducted within two separate weeks of beam time in July 2023 and March 2024, of which the first beamtime mainly served for preparations and tests. Between the beam times, the photoinjector cathode has been exchanged, which is likely the main contributor of the increased bunch charges from around 0.4 nC towards 1 nC in the second beam time.

5.2 Prototype design

The EO monitor prototype serves as a proof-of-principle for the novel crystal holder design with two prisms to guide the laser light. Starting from the interaction module of the EO monitor at Karlsruhe Research Accelerator (KARA) (see Refs. [27, 34] and Chapter 3.1.2) custom parts have been designed and included to enable a prism-based crystal assembly. Many spare parts for the KARA EO monitor were used for building the prototype, which enabled a short construction time of a couple of months.

5.2.1 Overview of the compact prototype

The prototype is based on the interaction module of theEO monitor at KARA (see Chapter 3.1.2), and a photograph and corresponding schematic is presented in Fig. 5.1. It consists of an aluminum box (optic box) and a stainless steel arm. The optic box handles the input and output of the laser through fibers and offers space for various optical components in the free space laser beam path. The mechanical arm is attached to the optic box and ends in the custom crystal holder for the dual prism setup. The direction of the laser light through the crystal can be reversed by slightly changing the position of a few optical components, which enables the installation on either side of the electron beam. This compact and sturdy setup allows for safe transport of the fully assembled prototype from KIT in Karlsruhe, Germany to the CLEAR facility at CERN (CERN) in Geneva, Switzerland.

The laser input is handled through a pigtail style collimator for a wavelength of 780 nm, (OZOptics LPC-04-780) with an aspheric lens to ensure a collimated laser beam with a divergence angle of 1 mrad in free space. Its 1 m long polarization-maintaining (PM) fiber is terminated with an FC/APC connector, which enables the connection via optical fibers to the laser setup. The optic box provides space for an optional motorized grating compressor or stretcher directly after the collimator to enable adjustments of the laser pulse length.

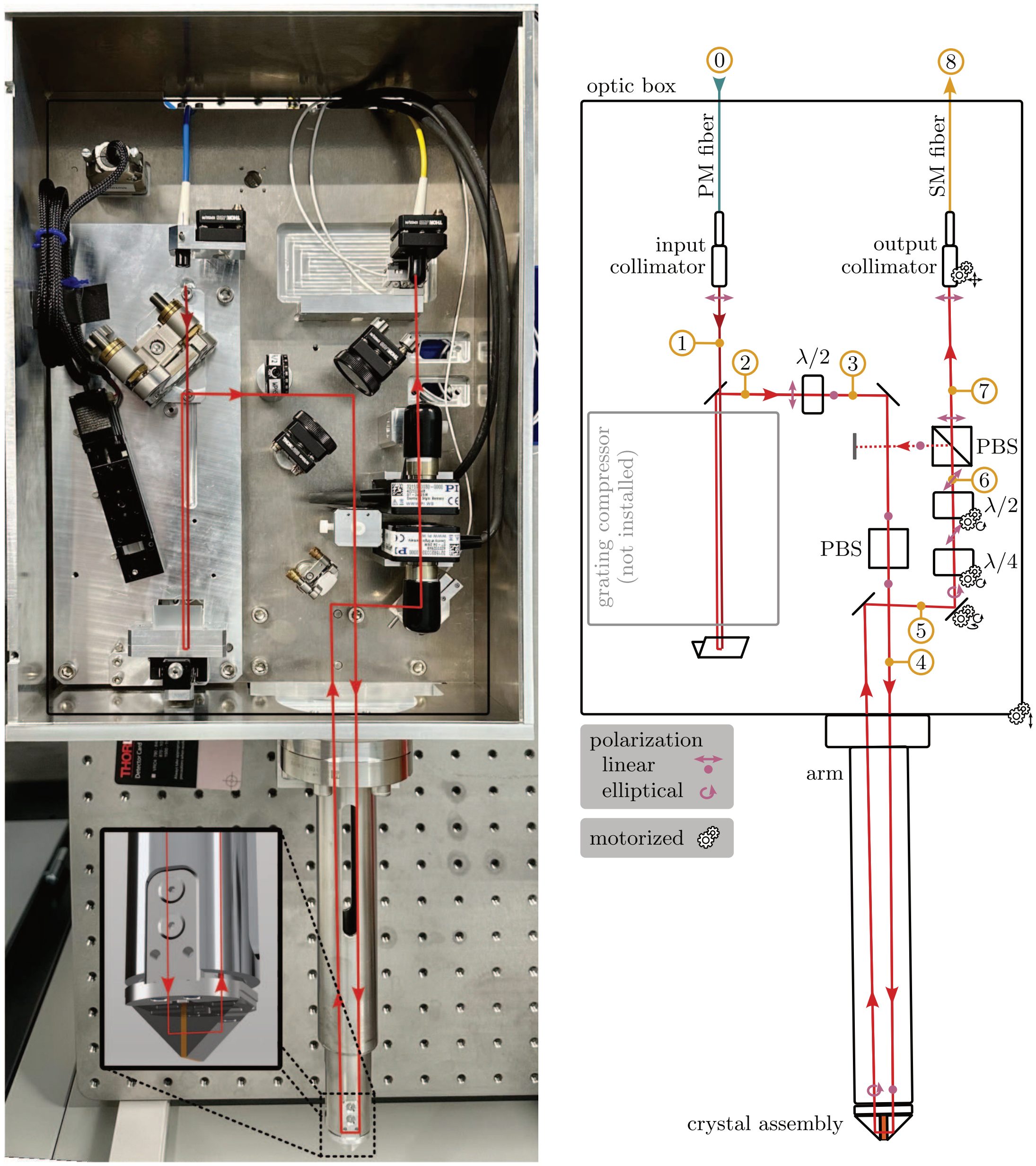

(a) Photograph of the prototype **(b)** Schematic of the prototype

Figure 5.1: Photograph (a) and schematic (a) of the FCC-ee EO prototype for testing at CLEAR. The prototype is based on the interaction module of the KARA EO monitor (see Ref. [27] and Chapter 3.1), which has been modified to accomodate a novel prism-based crystal assembly. The optics box handles the transition of the laser light from the fibers to free-space and it includes the polarization analyzer to set the working point of the EO monitor. It has an arm attached, which ends in the crystal assembly with the novel prism setup. The position of some components are adjustable to reverse the direction of the laser light through the crystal, if needed. The design laser polarization is indicated with purple arrows before and after relevant optical components. Yellow position markers show typical spots for laser power measurements, which are discussed in Chapter 5.4.3. Motorized components are marked with a gears symbol. The setup is installed on a translation stage to adjust the distance between EO crystal and electron beam. The grating compressor for reducing the pulse length was briefly tested, but omitted due to substantial laser power loss. The optics box can be closed with a lid, making the whole setup stable and easy to transport from Karlsruhe Institute of Technology (KIT) to CLEAR.

The laser pulses at the in-air test stand are long ($\sim$25 ps) compared to the expected electron bunch length (<7.5 ps), because they are stretched by the normal dispersion of the long optical fibers (typ. >75 m). The anomalous divergence of the optional compressor could reduce the laser pulse length and partly compensate the pulse stretching from the normal dispersion of optical fiber. However, the limited space in the optic box also limits the achievable compression, because the anomalous dispersion depends on the distance of the gratings [106]. During tests on-site at CLEAR, the compressor leads to a substantial loss of laser power. Due to the time constraints during the beamtime at CLEAR, this issue was not further investigated, and the compressor was omitted in favor of increased laser power.

Without the compressor, the free space laser first hits a roof mirror, serving as a periscope to get the laser on a lower level. Generally, the laser should be either s- or p-polarized on reflection on a mirror because it minimizes a mirror-induced ellipticity [107, pp. 739 ff.]. The example shows s-polarized light, because with the protected silver coating of the roof mirror (Thorlabs HRS1015-AG), it leads to slightly better reflectance $R_\mathrm{s} > 99.5\,\%,\ R_\mathrm{p} > 99\,\%$ according to the manufacturers' specifications. As a result, the following silver coated mirror reflects p-polarized light through a $\lambda/2$-waveplate, which is used to turn the linear polarization by 90 degrees.

Together with the following polarizing beam splitter (PBS), the waveplate defines the polarization angle of the probe laser in the EO crystal. Inside the crystal, the probe laser needs to have a 45° angle to the fast and slow optical axes to maximize the modulation. Ideally, the (110) cut crystal is aligned such that the Coulomb field points in the $[\bar{1}10]$ direction and the beam direction is normal to the cutting plane. In this configuration, the laser polarization needs to be oriented either parallel or perpendicular to the Coulomb field in the (110) plane (see Chapter 2.2.2). In Fig. 5.2b, the laser is s-polarized at the prism to minimize the risk of an additional phase retardation, hence it is aligned parallel to the $[001]$ axis in the crystal and perpendicular to the Coulomb field.

If an electric field such as the Coulomb field was applied, the laser light polarization is slightly elliptical after the crystal (see Chapter 2.2.1). The following prism reflects the light back into the optic box, where after two additional mirrors, it passes through the polarization analyzer with a $\lambda/4$-waveplate, a $\lambda/2$-waveplate and a PBS to enable adjusting the working point for EO measurements (see Chapter 2.2.3). The $\lambda/4$-waveplate is typically used to compensate for any polarization ellipticity caused by the intrinsic birefringence of the crystal, or phase retardation errors introduced by mirrors or other components. The $\lambda/2$-waveplate in combination with the subsequent PBS transforms the polarization modulation from the EO effect into an intensity modulation of the laser light. The waveplates are motorized to allow remote control of their rotation angle and, therefore, adjust the working point from the control room.

Finally, the linearly polarized light is captured by a pigtail collimator, which couples the light into a single-mode (SM) fiber. The coupling efficiency is very sensitive to the laser alignment and requires mirror adjustments on the micrometer scale. To increase alignment precision, the collimator is mounted on a x-y-positioner stage (2 stacked SmarAct SLC-1720-lc) in combination with a motorized tip-tilt mirror (SmarAct STT-25.4) before the $\lambda/4$-waveplate. Both components are based on piezoelectric motors and enable resolutions of <1 nm and <1 n°, respectively (according to the manufacturer).

The total dimensions of the prototype are approximately 56.5 cm × 26.0 cm × 10.0 cm with a total weight of approximately 8.5 kg, making it sufficiently compact for transport by vehicle and straightforward installation in the in-air test stand. The experimental area at CLEAR provides an optical table, where the electron beam passes at a height of approximately 25 cm. To match the position of the EO crystal to the electron beam trajectory, the setup is mounted on a horizontal stage (Thorlabs NRT100) with additional stands to adjust the height of the prototype. The motorized stage enables the distance between the crystal and the electron beam to be adjusted during the experiment.

5.2.2 Crystal holder

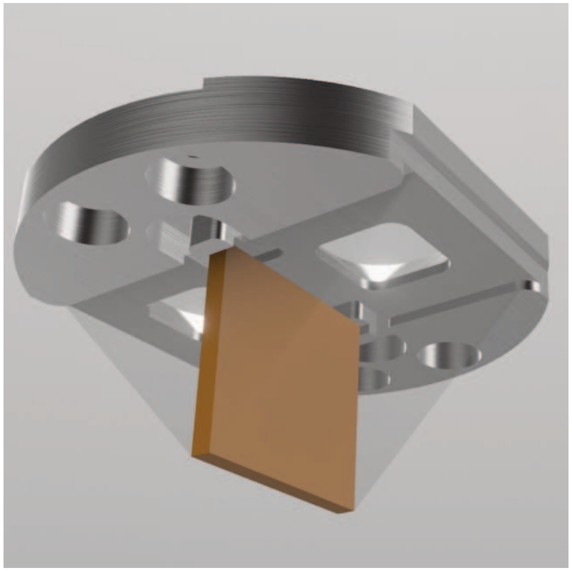

(a) Crystal holder plate

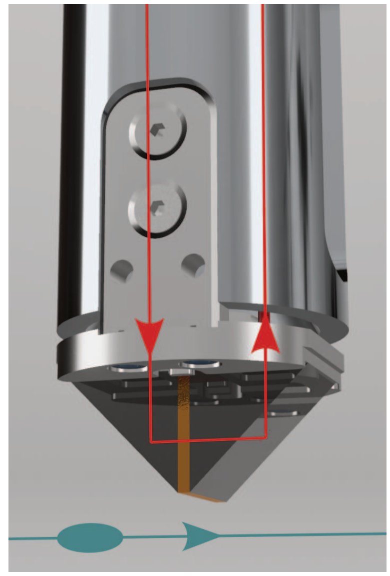

(b) Assembled crystal holder

Figure 5.2: Rendered images of the crystal holder plate of the EO prototype for CLEAR (a) and the fully assembled crystal holder (b). The baseplate has grooves to enable precise alignment of the crystal (orange) and prisms (transparent gray), and the small contact points of the crystal aid the glueing process. A slightly enlarged clearance accounts for thermal expansion. The baseplate is compatible with the arm from the KARA EO setup, but it needs to be rotated by 90° to get the probe laser (red line) parallel to the electron beam (blue line) in the crystal. The images are based on a CAD model by S. Schott, first published in [1, 2].

A special crystal holder has been designed to hold the crystal in-between two prisms. Its baseplate is presented in Fig. 5.2a, which has grooves to align the prisms and the crystal. The slots for the prisms and the crystal have an enlarged clearance to account for thermal expansion of the material. Two holes in the holder enable the probe laser light to enter the prism on one side, getting reflected through the EO crystal and exit after the total internal reflection (TIR) at the other prism. An overview of the assembled arm with crystal holder is provided in Fig. 5.2b, including the laser path and exemplary electron beam trajectory.

The crystal is in direct contact with the prisms to improve laser transmission by reducing additional laser reflections, which could occur if a gap is left in between the prisms and the crystal. This requires well polished and clean surfaces to establish a direct contact between the crystal and the prisms. Small imperfections can lead to air bubbles, which reduce transmission efficiency and could lead to inconsistent results. Direct contact enables a simple assembly for this first prototype test, but for a fixed installation at FCC-ee, it is recommended to investigate alternative methods. For example index-matching vacuum-compatible optical glue should be considered to provide a consistent contact with high transmission efficiency, or intentionally leaving a gap between the prisms and the crystal to account for thermal expansion.

The crystal sits on top of two small protrusions, and it is designed to be glued to only one of them. The small protruding contact point aids the glueing process, because excess glue is able to run off without enlarging the bonded area on the crystal. The small single glued surface area helps to reduce mechanical stress in the crystal during thermal expansion, which otherwise could cause additional polarization changes of the probe laser (see Chapter 3.1.4).

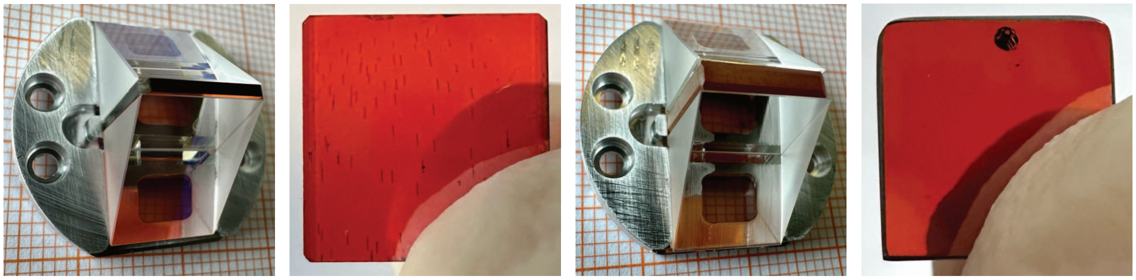

(a) 1 mm holder **(b)** 1 mm zinc telluride (ZnTe) **(c)** 2 mm holder **(d)** 2 mm ZnTe

Figure 5.3: Photos of the crystal holder for 1 mm (a) and 2 mm (c) thick crystals with photos of the corresponding crystals (b), (d). The ZnTe crystal with 1 mm thickness has visible defects, which could disturb measurements. Thus, the crystal with 2 mm thickness was preferred for the CLEAR measurements.

However, thermal issues are not expected at CLEAR, because the charge density is similar to KARA, while the repetition rate is a factor $\sim 10^5$ lower. In addition, the surrounding air helps to dissipate the heat from the crystal in contrast to the in-vacuum setup at KARA. Nevertheless, it is an important topic for the high beam currents at FCC-ee, hence the prototype already includes these measures for potential future tests at other machines (e.g. KARA) with higher beam currents.

For the prisms, commonly available fused silica prisms with an adjacent side length of 10 mm were used (Thorlabs PS610). Fused silica offers a transmission of ∼93.4 % for a 10 mm thick sample at 780 nm. Compared to other typical materials like N-BK7, it offers a lower coefficient for thermal expansion and a lower reflective index $n_{\text{prism}}^{(\text{fused silica})} \approx 1.45$. The minimum angle of incidence to achieve TIR is called the critical angle and is defined by

$$\sin(\vartheta_{\text{c}}) = \frac{n_0}{n_{\text{prism}}}, \quad \Rightarrow \vartheta_{\text{c}}^{(\text{fused silica})} \approx 43.6^\circ. \tag{5.1}$$

Therefore, the EO prototype requires careful laser alignment with a high precision, because the design angle of incidence of $\vartheta_1 = 45^\circ$ is close to the critical angle $\vartheta_{\text{c}}^{(\text{fused silica})}$. If the angle ϑ_1 is smaller than ϑ_{c}, for example through misalignment, the reflectivity decreases, which leads to an effective loss in laser power for the EO experiment. Since there are two prisms at a relative angle of 90°, the incident angle of the second prism ϑ_2 is determined by the incidence on the first prism ϑ_1 by

$$\vartheta_2 = 90^\circ - \vartheta_1. \tag{5.2}$$

Thus, $43.6^\circ < \vartheta_1 < 46.4^\circ$ is required to guarantee a TIR in both prisms. Due to the small holes in the crystal holder metal plate and the long distance through the arm between the prisms and the previous / next mirror, the geometric aperture is fairly small, which helps to achieve a precise laser trajectory alignment. Nevertheless, the alignment should be optimized by adjusting the two mirrors before the prisms to maximize the laser power after the prisms.

5.2.3 Crystal selection and determination of crystal axes

Figure 5.3 presents photos of the two different crystal holder prototypes, which were made for crystal sizes of 10 mm × 10 mm × 2 mm and 10 mm × 10 mm × 1 mm. ZnTe is chosen as the preferred crystal material, because in comparison to other common materials, it provides the best phase matching with the 780 nm laser at CLEAR, and it has a roughly four times higher Pockels coefficient than gallium phosphide (GaP), in the order of $r_{41} \sim 4 \times 10^{-12}\,\text{m/V}$ [68].

Unfortunately, the newly ordered 1 mm-thick crystals in Fig. 5.3b had visible defects in the form of multiple black dots in the material. According to the manufacturer, this is common in ZnTe and likely caused by air, which is trapped inside the crystal during the manufacturing process. However, the later presented measurements were conducted with the 2 mm crystal holder and an existing 2 mm-thick ZnTe crystal with no visible defects (see Fig. 5.3d), because the increased increased sensitivity of a thicker crystal been preferred for the commissioning of the EO monitor at CLEAR.

The crystal is cut in the common (110) plane, but the orientation of the $[\bar{1}10]$ and $[001]$ axes were not defined. Since a precise orientation is important for EO measurements, a grazing incident X-ray diffraction (XRD) setup was used to determine the crystal axes. The details of this method are well described in [108]. In summary, an X-ray beam is sent onto the crystal at a shallow angle to its cutting plane and, depending on the crystal orientation, a detector can measure characteristic Bragg peaks in the diffraction pattern. To find appropriate Bragg reflections that yield peaks with sufficient intensity, calculations using the x0h program of the X-Ray Server have been used [109, 110]. These calculations revealed that two Bragg peaks at certain diffraction angles are expected from the (200) and (400) plane, if the incident X-ray beam points in the $[\bar{1}10]$. As a cross-check, the crystal was rotated by 90° to an incidence angle pointing in the $[001]$ direction. According to the simulations, a scan in this configuration should reveal the Bragg peaks in the (-440) and (-220) plane. In the measurement results, the relative diffraction angles of the detected Bragg peaks were matched to the calculated peak positions, which allowed to determine the $[\bar{1}10]$ and the $[001]$ axes of the crystal. A black dot has been applied close to one edge of the crystal, marking the $[\bar{1}10]$ direction.

In addition to the newly bought 1 mm-thick crystals, the older 2 mm-thick crystal was available at CERN. A photo is presented in Fig. 5.3d. It did not have any visible defects, was nicely polished and from factory, it had rounded corners and a black dot to mark the $(\bar{1}10)$-plane (thus, the marked edge is in $[001]$ direction). This crystal did fit between the prisms in one of the crystal holders and was the preferred option for the measurements at CLEAR. With a thickness of 2 mm, the expected phase retardation is approximately two times larger than for a 1 mm thick crystal, which could help to find a fist EO signal at CLEAR.

5.3 EOS simulations

To complement the EOS measurements with the prototype at CLEAR, an EOS simulation was performed, following the principle described in Chapter 4, but with parameter and 3D model adjustments to match the EO prototype at CLEAR. This section briefly describes the simulation setup and its results, which serve as a reference for the discussion of the EOS measurements in the later sections of this chapter.

5.3.1 3D-model and other input parameters

The simplified 3D model is presented in Fig. 5.4. The experimental area is not in a vacuum chamber and the surrounding space is filled with air. The boarders of the model are defined as open ends to avoid any reflections, except for the bottom surface, which has the boundary condition of a perfect electrical conductor ($E = 0$) to approximate the metal surface of the optical table. The EO prototype is simplified to just a metal plate holding the prisms and the EO crystal, because these parts mainly affect the dynamics of the electrical field inside the EO crystal.

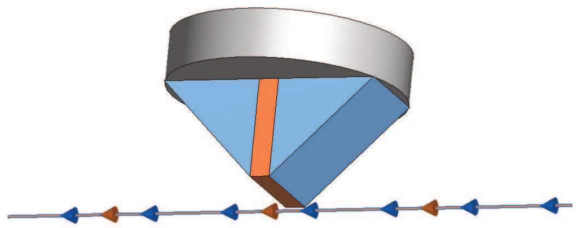

Figure 5.4: Simplified 3D model of the EO prototype at CLEAR for CST simulations. Its main components are the ZnTe crystal (orange) in-between two prisms, which are attached to the metal holder. The setup is in-air, where the electron beam passes the crystal in 2 mm distance.

The crystal has the dimensions of 10 mm × 10 mm × 2 mm with ZnTe as a material. Its dispersion function is modeled as a Lorentz oscillator, following the description in [64]

$$\varepsilon(\omega) = \varepsilon_{\text{el}} + \frac{S_0\omega_0^2}{\omega_0^2 - \omega^2 - i\Lambda_0\omega}, \tag{5.3}$$
$$\varepsilon_{\text{el}} = 7.4,\ w_0/(2\pi) = 5.3\,\text{THz},\ S_0 = 2.7,\ \Lambda_0/(2\pi) = 0.09\,\text{THz}.$$

For example, this results in a refractive index of around $n \approx 2.70$ at 100 GHz, and $n \approx 2.86$ at the probe laser wavelength $\lambda = 780\,\text{nm}$.

As in previous simulations, the maximum frequency of the CST simulation is set to 100 GHz to keep an acceptable computing time, but still provide sufficient detail. For a simulation in the sub-100 GHz regime, the fused silica prisms are assumed to have a constant refractive index $n = 1.95$ [111, 112].

Most input parameters are set to match the conditions of the CLEAR EOS measurements of 2024 (see Chapter 5.5.1). The electron bunch is approximated as a Gaussian with $\sigma_z = 2.25\,\text{mm}$ ($\sigma_\tau \approx 7.5\,\text{mm}$) and a bunch charge of 1 nC. The distance between the EO crystal and electron beam is set to 2 mm.

To calculate the phase retardation Γ, 25 equidistant electric field probes are placed in the crystal along its center line. For the propagation of the probe laser along this line, a wavelength of 780 nm and corresponding refractive index of $n = 2.86$ is assumed, and the EO coefficient of the ZnTe crystal is set to $r_{41} = 4.04 \times 10^{-12}\,\text{V/m}$.

5.3.2 Simulation results of the prototype at CLEAR

The resulting phase retardation is presented in Fig. 5.5, over a time of 2 ns. The first peak at t_C has the highest retardation $\Gamma_\text{C} \approx 18.3°$ and is caused by the Coulomb field of the electron bunch. The following ringing corresponds to the wake field, which amplitude decreases over time. While its first negative amplitude reaches $\sim$−12.1°, the oscillation amplitude stays below 2.5° after 1 ns.

Due to the small distance of the crystal to the electron beam, the phase retardation is strong and has approximately the same order of magnitude as the simulations of the EO concept for FCC-ee (e.g. Fig. 4.14). However, for the EO concept, the wake field was barely noticeable, due to the reduced impedance from a greater distance of the crystal and its holder to the beam.

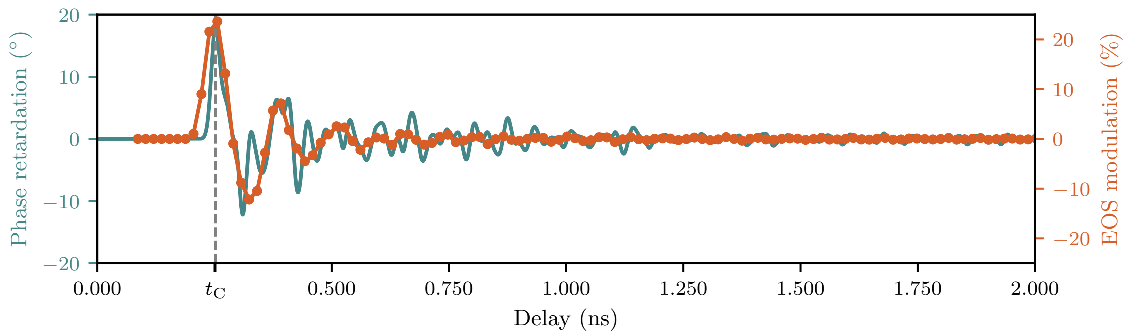

Figure 5.5: Simulated phase retardation (blue) and simulated EOS measurement (orange) with the EO prototype at CLEAR. The photodiode was simulated as a low-pass filter with 3 GHz cutoff-frequency, leading a reduction of the high-frequency components in the EOS signal compared to the phase retardation.

Additionally, Fig. 5.5 includes a simulated EOS measurement, which is later compared to the CLEAR EOS measurement in Chapter 5.5.1. The laser modulation is simulated for a working point of $\phi = 0°, \theta = 15°$ to match the CLEAR measurement conditions. To simulate the photodiode with 3 GHz bandwidth, a low-pass filter with 3 GHz cutoff-frequency was applied . Since the delay scan for the EOS measurement at CLEAR has been performed in discrete steps, the modulation is sampled with a step size of $\Delta t = 17$ ps for the EOS simulation. The laser pulse length has not been measured during the beam time, but a laser pulse length $\sigma = (25.9 \pm 0.5)$ ps is estimated based on the calculation in Ref. [40], where the same laser system was used for a different experimental setup.

The simulations suggest a maximum modulation amplitude of ∼24 %, followed by a negative peak from the wake field with ∼12 % modulation amplitude. The rest of the wake field is strongly suppressed by the limited bandwidth through the long laser pulse and the data acquisition. For the same reason, the first peak is broadened and can include three to four sampling points within its width $\mathrm{FWHM_{sim}} \approx (49 \pm 12)$ ps. The full width at half maximum (FWHM) was calculated with linear interpolation, hence the sampling rate determines the uncertainty $\delta\mathrm{FWHM} = \Delta t/\sqrt{2}$.

In summary, the simulation predicts a strong bunch-induced modulation for the EOS measurements at CLEAR. Its main peak is expected to span around three to four data points within the FWHM, and it is followed by slightly weaker negative peak from the wake field. These signal characteristics were used during the EOS measurements, when searching for the bunch-induced modulation. The following section presents the measurement results and includes a brief comparison with the simulation results.

5.4 Experimental setup and methods

This section introduces the experimental prototype setup at the in-air test stand of CLEAR and the utilized laser system. It provides an overview of the experimental steps in preparation of the final EOS measurements, which includes the laser alignment, setting the crystal distance to the beam, setting the EO monitor working point and the method to achieve the arrival time synchronization of the laser pulses and electron bunches. The data analysis methods for the EOS measurements are explained along an illustrative example of the final test measurements during the first beam time at CLEAR.

The EO prototype was tested during two separate beam times at the in-air test stand at CLEAR: the first in July 2023, the second in March 2024. The first beam time mainly served for preparations and tests of the prototype integration in the full EO monitor setup and resulted in a first indication of a

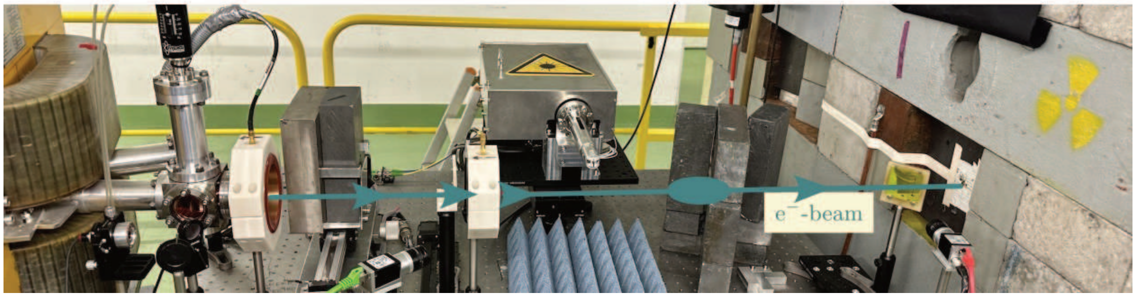

(a) Photo

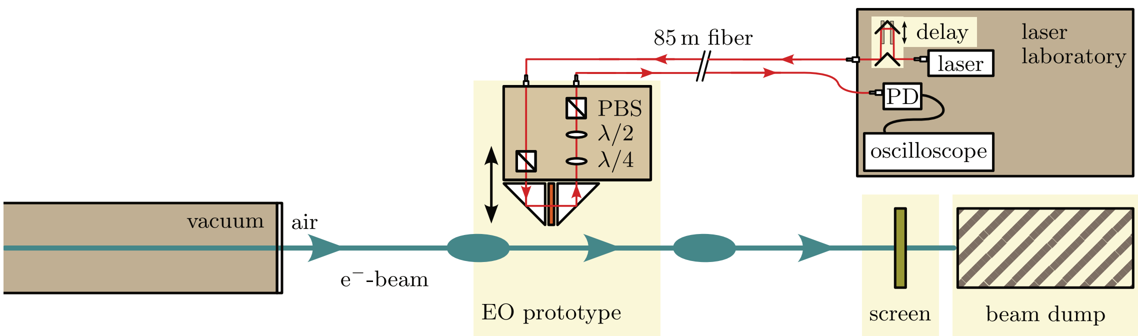

(b) Schematic overview

Figure 5.6: Photo (a) and corresponding schematic (b) of the EOS setup with the prototype at the CLEAR in-air test stand. The electron beam leaves the vacuum chamber through a Kapton window, where the EO prototype is set up on a horizontal linear stage on an optical table. The laser system and EOS detection system is located in a nearby laser laboratory and connected to the prototype via ∼85 m of optical fibers. to monitor the transverse position of the electron beam, a beam screen is located in front of the near-by beam dump.

potential EO signal of two consecutive electron bunches with low SNR. During all these experiments, the setup was modified multiple times, using different crystals, prisms, fibers and mirrors in the optics box to improve the laser path alignment. This chapter focuses on the description of the final prototype setup, using the 2 mm thick ZnTe crystal with the corresponding crystal holder.

Finally, the measures for noise reduction during the second beam time are described, which were the key to the final EOS measurements.

5.4.1 Overview of the prototype setup

A schematic overview of the entire experimental setup is presented in Fig. 5.6, with the EO prototype at the in-air test stand. For better visibility, the laser and EO prototype are simplified. For each of these, a detailed schematic was presented previously, in Fig. 5.7 and Fig. 5.1b.

After the electron beam exits the CLEAR vacuum chamber through a thin Kapton window, it passes through air above an optical table, until it hits the beam dump. The EO prototype was installed on a motorized linear stage, which enabled to remotely change the distance between the crystal and the electron beam. Additionally, two cameras and YAG beam screens were available to be placed somewhere in the in-air test stand on demand. During the time of the measurements at CLEAR, they have been used at different positions. In the example of the photo, a YAG screen was placed before the beam dump, and monitored with a camera to measure the transverse beam position. The beam dump is suspected to be the most intense source of ionizing radiation, hence some available lead blocks were used to shield the prototype.

In the laser laboratory, the light is coupled into a PM fiber, after it passes the delay stage, the grating compressor and the pulse picker (see Figure 5.7). The laser light is transported through multiple optical fibers from the laser laboratory to the EO prototype, with a total length of approximately 85 m. In the prototype, the laser is guided through the EO crystal in a free space setup, but the output is coupled into an optical fiber, again (see Figure 5.1b). From there, the light is transported through multiple fibers back to the laser laboratory, with a total length of approximately 80 m.

The laboratory contained a grating spectrometer with an intensified camera, which could be used to try bunch profile measurements with electro-optical spectral decoding (EOSD). However, the long laser pulses at the crystal in comparison to the relatively short electron bunches would drastically limit the resolution. In addition, EOS is a simpler setup, enabling an on-the-fly analysis of the measurements, which is beneficial in the initial search for temporal overlap of the laser pulse and the Coulomb field in the crystal. Unfortunately, EOSD was not used during the described measurement campaign, because the first EOS signal was detected just at the last evening of beam time. Nevertheless, EOS measurements can demonstrate the functionality of the new prism-based crystal assembly and thus provide a baseline for the future development towards a technical EO monitor design for FCC-ee.

For EOS measurements, the fiber with the returning laser light is connected directly to a photodiode with a specified bandwidth of 12 GHz (Thorlabs DXM12DA), and its output was connected to an oscilloscope with a bandwidth of up to 10 GHz (Tektronix MSO648). This simple setup enables monitoring the modulation of the laser intensity, which is caused by changes of the applied electrical field at the EO crystal. With the crystal in close vicinity to the electron beam, it can be used to sample the Coulomb field of the electron bunch with the laser pulses. This data acquisition is not expected to resolve the bunch profile directly, but it serves as a first proof-of-principle test to measure a first EO signal with the novel prism design. The first results are presented later in Chapter 5.5.

5.4.2 Laser system for EO applications

Table 5.2: Overview of the pulsed laser system output (Toptica FemtoFiber pro NIR) for EO applications at CLEAR. Adapted from [40].

Parameter	Value	Unit
Center wavelength	780	nm
Spectral width (FWHM)	$\sim$10	nm
Average output power	<200	mW
Pulse energy	<2.7	nJ
Pulse length	<120	fs
Repetition rate	75	MHz

For different beam instrumentation tests, CLEAR has a femtosecond pulsed laser (Toptica FemtoFiber pro NIR) that can be synchronized to a subharmonic of the accelerating radio frequency (RF) structures. It is suitable for EO applications and has been used for tests of different setups. This section provides an overview of the laser system in the context of the EO prototype experiments. A more comprehensive description is presented in [40, pp. 74 ff.].

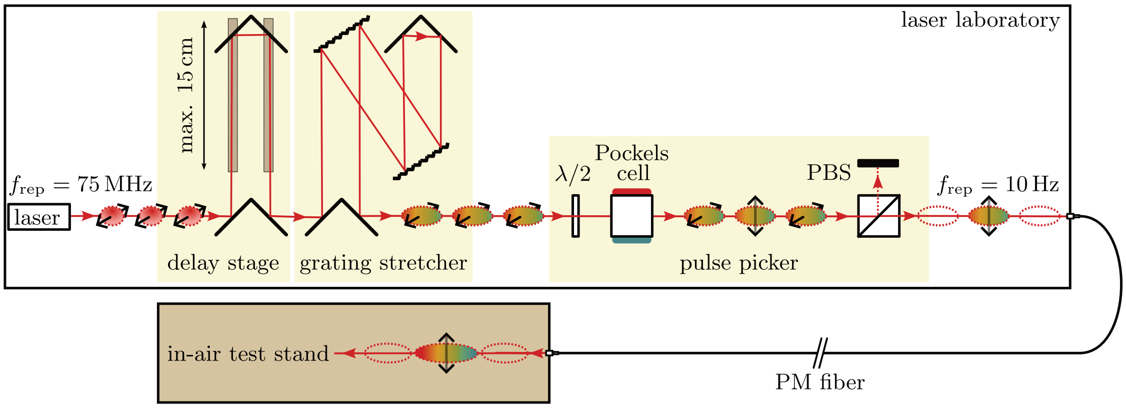

Figure 5.7: Schematic overview of the 780 nm femtosecond laser system for EO applications at CLEAR. Three exemplary laser pulses are illustrated as three ovals, with their length representing changes of the pulse length. Arrows indicate the orientation of the linear polarization, and only vertically polarized pulses can pass the PBS in the pulse picker. The anomalous dispersion of the grating stretcher lengthens the pulse with a negative chirp, which is indicated with a color gradient from red to blue. However, the normal dispersion in the fiber leads to a stretched pulse with a positive chirp at the in-air test stand.

An overview of the laser pulse parameters is presented in Table 5.2. It is an Erbium-doped fiber laser with a center wavelength of 1 560 nm, which uses a Lithium-Niobate crystal for second-harmonic generation of the final laser center wavelength of 780 nm. It produces pulses with a length of <120 fs (FWHM) at a free space output. The repetition rate is tailored to 75 MHz to fit the 40$^{\text{th}}$ subharmonic of the 3 GHz frequency of the RF accelerating structures. To synchronize with the RF frequency, a proportional-integral-derivative (PID) controller adjusts the laser repetition rate by changing the oscillator cavity length.

Figure 5.7 presents a schematic overview of the laser pulse modifications along the transport from the output of the Toptica laser system to the in-air test stand. The free space output first leads the laser pulses to a delay stage, composed of a rooftop mirror on a motorized linear stage. It can change the optical path by up to 30 cm, resulting in a maximum arrival time shift of the laser pulses by up to 1 ns.

The Toptica laser system is located in a nearby laser laboratory on the klystron gallery of CLEAR, where a fiber patch panel is connected to a patch panel at the CLEAR beamline with a fixed 75 m long PM fiber to transport the laser light. Depending on the use case, additional fibers are used to transport the laser light from the laser system to the patch panel in the laser lab, and from the patch panel at CLEAR to the experiment. A typical material for these fibers is fused silica, which has a normal dispersion $D < 0$. Thus, a grating stretcher with an anomalous dispersion $D > 0$ is installed before the fiber to partly compensate for the stretching of the laser pulses. Nevertheless, the total length of the fibers leads to pulses with a calculated length of approximately $\sigma_z \approx 7.5\,\text{mm}$ ($\sigma_\tau \approx 25\,\text{ps}$) at the in-air test stand [40, p. 85].

A pulse picker based on a Pockels cell is installed after the grating stretcher. It enables to adjust the repetition rate of the laser pulses to match the 10 Hz repetition rate of CLEAR. In the pulse picker, the linear polarization of the laser light is rotated with a $\lambda/2$ waveplate to be reflected at a PBS into a laser dump. A short electrical signal can be applied to the Pockels cell before the PBS to rotate the polarization of a selection of laser pulses. As a result, only a selection of pulses is transmitted through the PBS. It is typically set to a repetition rate of 10 Hz, omitting most of the laser pulses from the native repetition rate of 75 MHz. This is an advantage for EO measurements, because every selected laser

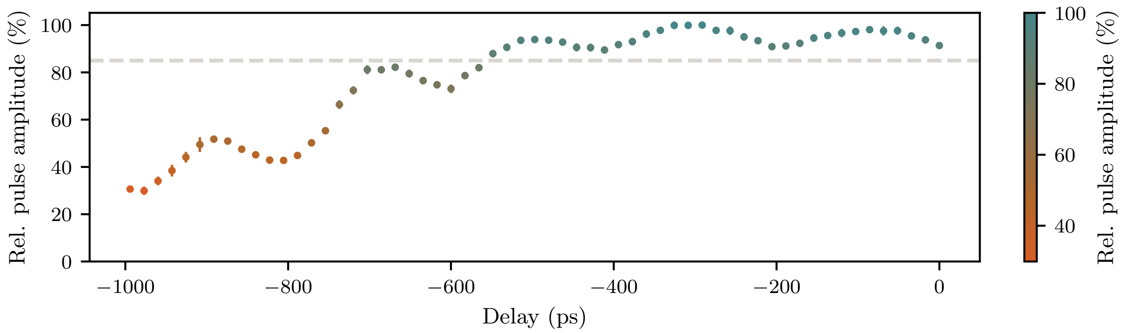

Figure 5.8: Normalized laser intensity at the output of the EO laser system during a delay scan from 0 ns to −1 ns. The data was recorded with a photodiode during the beam time at CLEAR, using the EO prototype setup (see Chapter 5.4.1). The color gradient redundantly encodes the y-value to maintain consistency with its usage in later figures. Every data point shows the average laser pulse amplitude over 50 shots, with the corresponding standard deviation indicated by error bars. The variation is very small, hence the error bars are mostly hidden behind the data point markers. The normalized laser intensity stays above the dashed gray 85 % mark for the first half of the scan, but decreases to a minimum of ∼29 % in the second half. (Also presented in Ref. [1])

pulse can overlap in time with an electron bunch. However, it makes laser alignment and setting up experiments more difficult because the average laser power is reduced drastically. To mitigate this issue, the angle of the $\lambda/2$ waveplate is changed during the laser alignment, allowing the transmission of all pulses through the PBS.

5.4.2.1 Effect of the delay stage on laser intensity

The setting of the laser delay can change the effective output intensity of the laser, because a movement of its linear stage leads to small laser path misalignments. This changes the output intensity because the coupling efficiency into the PM fiber is very sensitive to angular and positional alignment.

Figure 5.8 presents the laser pulse amplitude during a scan of the delay stage, normalized to the maximum pulse amplitude. The measurement data was taken with a photodiode during an EOS delay scan with the EO prototype, which is described later in Chapter 5.5. The plot shows the mean pulse amplitude during 50 shots, with error bars indicating the standard deviation. The color-code for the amplitude will also be used in later plots of the EOS measurement results. During the measurement, the delay stage was moved in a range from 0 cm to 15 cm in 59 equidistant steps, effectively reducing the laser path length before the detector. The movement corresponds to a delay of 0 ns to −1 ns with a step-width of ∼17 ps.

The normalized pulse amplitude stays above the 85 % mark for more than the first half of the delay scan, approximately from 0 ps to −550 ps. The amplitude oscillates during the delay change with a period length of approx. 200 ps (∼3 cm), possibly arising from geometric inconsistencies of the linear stage, for example a tilt error of the stage itself, or a periodic pitch error of the leadscrew. The amplitude of the oscillation increases in the second half of the scan, in addition to an overall amplitude decrease, which reaches its minimum approximately at −978 ns with ∼29 % of the maximum pulse amplitude. A lower pulse intensity decreases the SNR of EOS and EOSD measurements, hence the usable scan range could be limited, depending on the noise level of the individual measurement. However, this issue only arises during delay scans, since once the laser delay is fixed to a desired delay, the laser alignment can be optimized manually for the specific setting.

Table 5.3: Exemplary power budget table with multiple measurement points along the laser trajectory (positions are marked in Fig. 5.1). The measurements were taken during the alignment process with a handheld silicon photodiode of a common power meter (Thorlabs PM100D), with an estimated absolute uncertainty of ±10 %. The values correspond to the transmission from the previous listed position to the given position in percent.

Position	Description	Transmission
1	Fibers from laser to input collimator	∼57 %
2	Before first $\lambda/2$ waveplate	∼90 %
3	After first $\lambda/2$ waveplate	∼96 %
4	Before the arm	∼67 %
5	After the arm (prisms + crystal)	∼44 %
6	After $\lambda/4$ and second $\lambda/2$ waveplate	∼88 %
7	After second PBS	∼91 %
8	After output collimator (in fiber)	∼81 %
9	In the laser lab (in fiber)	∼47 %
Total transmission		∼4.4 %

The fluctuation over time of the laser pulse amplitude is generally low, with an average standard deviation of ∼1.6 % and a maximum of 3.1 % across the steps of the delay scan. Additionally, small shot-to-shot variations do not affect EOS measurements strongly, because the average over multiple shots can be used to decrease the standard error of the mean (SEM).

5.4.3 Alignment of the laser path and the crystal position

The laser trajectory was prealigned at KIT, but with the available 1 030 nm laser. At CLEAR, a realignment was required, because the dispersion of all the components lead a slightly different path for the 780 nm at CLEAR. Additionally, the transport from KIT to CERN might have caused misalignments, considering that especially the coupling efficiency into the SM fiber at the output is very sensitive to the incidence angle and position.

One week before the beam time at CLEAR, the fully assembled EO prototype (see Fig. 5.1) was brought to the laser laboratory at the klystron gallery above the CLEAR experimental hall. This enabled a first alignment with the 780 nm pulsed laser (see Chapter 5.4.2) by connecting it to the input fiber of the prototype. In the EO prototype, the motors of the $\lambda/4$ and $\lambda/2$ waveplates have been integrated in the control system of CLEAR to remotely control the working point. For the laser alignment, the waveplates were set to transmit maximum laser power in the output fiber. Finally, the setup was installed at the CLEAR in-air test stand on the first day of beam time. Over the time at CLEAR, multiple modifications have been made to the setup to finally achieve successful EOS measurements, hence the laser alignment was repeated multiple times.

Table 5.3 presents one exemplary measurement of a power budget table across different sample points along the laser trajectory. For this measurement, the monitor was already installed at the CLEAR in-air test stand and connected to the laser via two consecutive fibers with a length of 75 m and 10 m. The measurements were taken with a handheld silicon photodiode, connected to a power meter (Thorlabs PM100D). The estimated absolute uncertainty is around ±10 %, hence the measurements only serve as an orientation.

One of the largest power losses of around occurs during the transport to and from the EO prototype to the laser laboratory, with a transmission of approximately 57 % on the connection from the laboratory to the prototype input and 47 % transmission from the prototype output back to the laboratory. This transmission includes three FC/APC connectors for the connection of a 10 m fiber from the laser to the patch panel within the laser laboratory, a 65 m fiber from the laboratory to the patch panel at CLEAR, and a 10 m fiber from the patch panel to the pigtail-style collimator at the prototype input, with its 1 m long fiber. The same scheme is applied from the prototype output towards the photodiode in the laser laboratory.

The FC/APC connectors between two fibers are suspected to be major contributors to the losses. Qualitative transmission measurements with multiple combinations of available fibers and connectors showed drastic differences in transmission efficiency. Some combinations with a 10 m fiber had losses >50 %, while others were below 20 %. These differences hint at issues with the manufacturing tolerances of the FC/APC connectors or the fibers. However, due to the large number of possible combinations and the limited time, not all connector and fiber combinations could be tested. As a result, the best combinations out of a couple of sample measurements were chosen for the final setup.

The input requires PM fibers to enable a linear polarization at the crystal, but it is not required for the output, because the EO modulation is encoded in the laser intensity. The output pigtail collimator has a SM fiber, which was connected to the available PM fibers for transport to the laser laboratory. The connection between the SM and PM fiber is less efficient, which is likely part of the reason for the reduced transmission efficiency from the prototype to the detection system.

The transmission efficiency from the EO prototype input to its output totals to $\sim$17 %, of which the greatest power loss occurs at the mechanical arm with the crystal assembly. The 44 % transmission efficiency in the prisms and crystal is less than expected. It could be caused by imperfections in the crystal and prism surface, which cause additional reflections. If the crystal and prism surface are not fully flat, small air pockets occur, which could lead to additional losses. A transmission of up to 74 % could be achieved during previous tests with a different 1 mm thick crystal. However, the higher sensitivity of the 2 mm thick crystal was preferred for the final measurements.

In summary, the total transmission efficiency from the laser system to the EOS detection system was approximately 4.4 %, which is less than expected. However, the laser power at the photodiode was sufficient for reliable detection, hence further optimizations were not pursued due to the limited beam time. Future experiments could likely benefit from a detailed investigation aimed at improving transmission efficiency through realignment, cleaning or replacing optical components at locations with high losses.

For the EO measurement, the crystal needs to be positioned in close vicinity to the electron beam and aligned such that the Coulomb field vector is parallel to the $[\bar{1}10]$ crystal axis (see Chapter 2.2.2). To achieve this orientation, the prototype was installed horizontally on adjustable stands to match the height of the crystal center to height of the electron beam. To aid the alignment process, a visible, red laser can be activated by moving a mirror in the vacuum chamber. Its light path follows the ideal electron beam trajectory above the optical table at the in-air test stand, thus it can be used as a reference to align the position of the EO crystal.

Figure 5.9 presents a photo of the crystal in its holder clipping the light of the red alignment laser. The detector card downstream of the crystal shows the shadow of the prisms and crystal, and the laser spot. It was used to align the crystal on the vertical axis by changing its height until the laser spot was in the middle of the shadow of the crystal edge. Additionally, it was used for the offset calibration of the horizontal linear stage, which is supposed to adjust the distance between the center of the electron

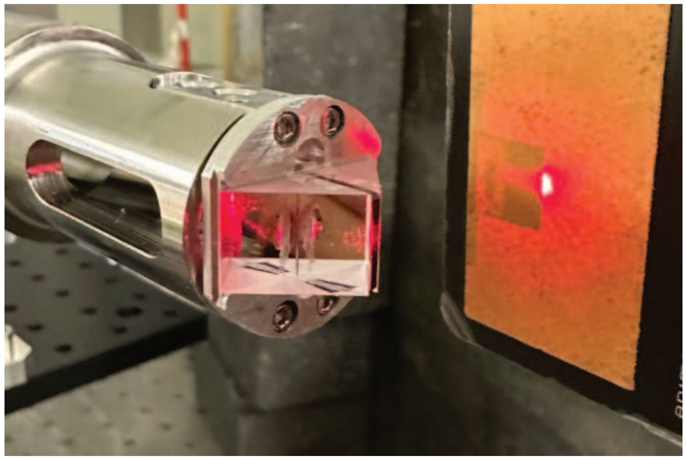

Figure 5.9: Photo of the alignment laser to calibrate the position of the crystal relative the the electron beam.

beam and the edge of the crystal. It was defined to be zero at the position where the crystal edge cuts the laser spot in half.

Finally, a scintillating yttrium aluminium garnet (YAG) screen with a crosshair was centered around the laser spot and positioned in front of the beam dump. It serves as a reference to center the electron beam during the measurements using steerer magnets.

5.4.4 Crystal distance optimization

As the bunch-induced modulation amplitude correlates with the electric field strength in the crystal, it scales with $1/r^2$ with the distance r of the electron bunch to the probe laser (see Chapter 2.1.3). Thus, bringing the crystal close to the electron beam is essential for achieving a high modulation. However, the crystal should not be put directly in the electron beam to avoid damage.

To enable controlled positioning of the crystal, an alignment laser was used to calibrate a linear stage that controls the horizontal distance between the crystal and the ideal beam center (see Chapter 5.4.3). To find a suitable position of the EO crystal during the EOS measurements, a YAG beam screen had been installed on the electron beam path close to the EO crystal. Figure 5.10 presents a screenshot of a camera image from the beam screen. The EO crystal was slowly moved closer to the electron beam, until an edge is visible on the beam screen, which originates in the EO crystal clipping the beam.

Typically, the clipping appeared at a distance of 2 mm between the crystal edge and the beam center. This position was chosen for the final EOS experiments, because it provides a balance between being close enough to the beam to have a large modulation amplitude, but avoiding having the probe laser directly in the electron beam and potentially damaging the crystal.

5.4.5 Working point of the EO monitor

The working point is defined by the angles of the $\lambda/4$ and $\lambda/2$ waveplates of the polarization analyzer, which is integrated into the optics box of the prototype (see Fig. 5.1b). The polarization analyzer converts the electron bunch induced modulation of the laser polarization into an intensity modulation, and its working point greatly affects the linearity and amplitude of this conversion (see Chapter 2.2.3).

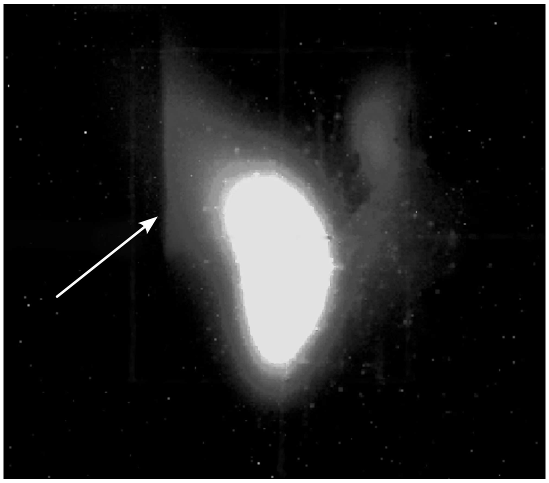

Figure 5.10: Screenshot of a camera image from a beam screen positioned shortly after the EO prototype. The EO crystal distance to the beam was slowly reduced, until an edge appears on the screen image, caused by the crystal clipping the electron beam. The colors have been adjusted and transformed to grayscale to improve contrast. This image was first published in [1].

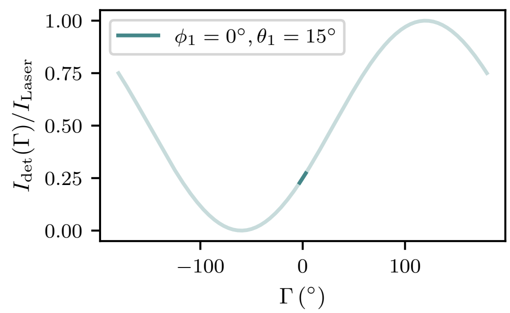

Figure 5.11: Illustration of the normalized laser intensity for the EO monitor working point that has been used at CLEAR. With the $\lambda/2$ waveplate angle $\theta = 15°$ and the $\lambda/4$ waveplate angle $phi = 0°$ of the polarization analyzer, the working point is set at a greater laser intensity and on a steeper slope in comparison to the typical near-crossed setting at KARA (see Chapter 2.2.3). The range of the phase retardation $\Gamma = -10°$ to $20°$ is estimated from the simulation results (see Chapter 5.3) and is drawn in blue in contrast to the full period overview in light blue.

At CLEAR, the motorized $\lambda/4$ and $\lambda/2$ waveplate were integrated in the control system to enable working point changes without needing to access the experimental hall. However, the scale for the waveplate angles in the control system was not calibrated initially.

The waveplate rotation angle was calibrated by running the probe laser through the EO prototype and monitoring the average laser pulse power on a power meter, while changing the working point. First, both waveplates have been adjusted to find a minimum laser power. This crossed-polarizer configuration serves as a reference point and defines the waveplate angles $\phi = 0$, $\theta = 0$. The laser amplitude is expected to be symmetric around the minimum, therefore each waveplate was rotated by a certain angle in both directions to check, if the resulting laser amplitude was approximately equal. Next, the angle θ of the $\lambda/2$ waveplate was increased, until it passes a maximum and reaches the next minimum. This defines $\theta = 45°$. The precision of this process is limited by the readings of laser power, the laser stability, the precise positioning of the reference point and many other factors. Hence, the uncertainty of both waveplate angles is estimated to be around $\sigma_(\phi, \theta) = 1°$.

This calibration was performed each time, after related changes were done to the setup. Additionally, the amplitude difference between the maxima and minima reveals the extinction ratio of the EO system, which describes the dynamic range of the detection and determines the signal clarity. It was typically measured to be ∼18.5 dB, which is a decent value that is not expected to be a limiting factor for the EOS measurements.

As described in Chapter 2.2.3 and Equation 2.38, the laser intensity at the EO prototype output is defined by

$$I_{\text{det}}(\theta, \phi = 0, \Gamma) = \frac{I_{\text{laser}}}{2}[1 - \cos(\Gamma + 4\theta)], \tag{5.4}$$

with the bunch-induced phase retardation Γ. For the measurements at CLEAR, a working point around $\phi = 0$, $\theta = 15°$ was typically chosen. The expected range of the phase retardation around the working point is deducted from the simulation in Chapter 5.3 and presented in Fig. 5.11. While smaller angles potentially increase the relative bunch-induced modulation (see Chapter 2.2.3), this working point provides a larger laser pulse signal amplitude and larger absolute modulation, because the slope of sinusoidal function is larger. A high absolute modulation was preferred, because at the time of the measurements, the signal noise was a major concern and the laser power at the photodiode was low. This working point enabled a greater laser power, which increased the SNR on the photodiode.

5.4.6 Arrival time synchronization utilizing transition radiation

Finding the temporal overlap of the laser pulse and the Coulomb field of the electron bunch is one of the biggest challenges when commissioning an EO bunch profile monitor. The laser repetition rate is synchronized to the RF frequency of CLEAR, but the low duty-cycle of the laser pulses and electron bunches provide a challenge for matching their arrival time at the EO crystal.

The laser pulse length $\sigma_z \approx 7.5\,\text{mm}$ ($\sigma_\tau \approx 25\,\text{ps}$) is small compared to the pulse spacing $T_{\text{rep}} \approx 13.3\,\text{ns}$ (for $f_{\text{rep}} = 75\,\text{MHz}$). It results in a duty-cycle of

$$P_{\text{DC}} = \frac{4\sigma_\tau}{T_{\text{rep}}}, \quad \Rightarrow P_{\text{DC}}^{(\text{laser})} \approx 0.75\,\%, \tag{5.5}$$

assuming an effective pulse length of $\pm 2\sigma$. Considering the delay stage with a maximum delay of 1 ns, the chance that the laser pulses can match a random arrival time is only ~7.5 %.

The electron bunches have a spacing of $T_{\text{rep}} \approx 0.1\,\text{s}$ ($f_{\text{rep}} \approx 10\,\text{Hz}$). With an exemplary bunch length of $\sigma \approx 7.5\,\text{ps}$, resulting in a duty-cycle of

$$P_{\text{DC}}^{(\text{CLEAR})} = n \cdot 3 \times 10^{-8}\,\%, \tag{5.6}$$

which can be multiplied by the number of micro-bunches n with a spacing of ~667 ps (see Chapter 5.1). For example, a bunch train of 20 micro-bunches has a total length of ~13.3 ns, which covers the spacing between two laser pulses. It guarantees that at least one laser pulse has a temporal overlap with a micro-bunch during a scan of the delay stage.

However, the 10 Hz repetition rate of bunch trains compared to 75 MHz of the laser pulses leads to a modulation of only every 75 000th laser pulse. The modulated pulse is difficult to find, since the modulation occurs only during a small part of the delay scan. Additionally, the laser amplitude changes with the delay, because movements of the delay stage cause small misalignments, which change the coupling efficiency into the PM fiber (see Chapter 5.4.2.1).

5.4.6.1 Transition radiation reference setup

To narrow down the search for the overlap signal, an additional setup for reference arrival time measurements was installed next to the prototype. It enabled measurements of the beam-induced transition radiation (TR) with a continuous-wave probe laser via an EO Mach-Zehnder interferometer.

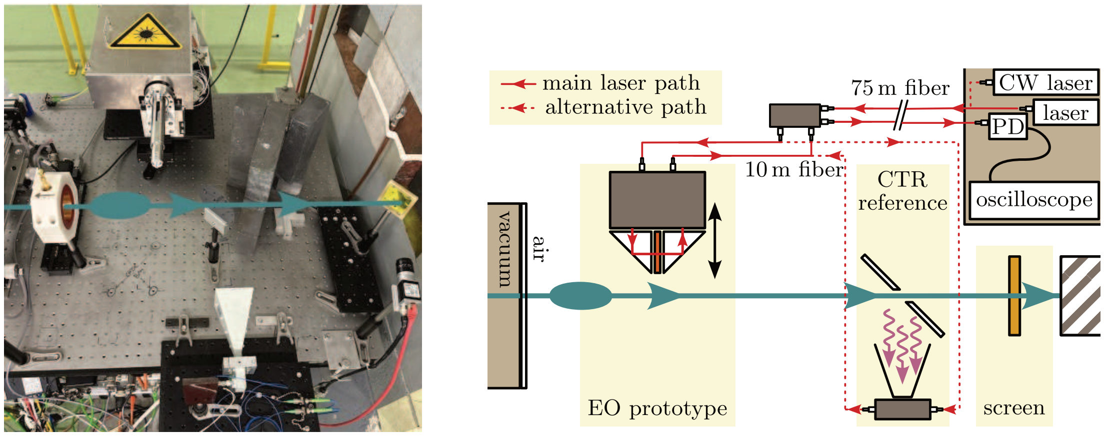

(a) Photo **(b)** Schematic

Figure 5.12: Photo (a) and schematic (b) of the arrival time reference setup using TR, based on [113]. A silicon wafer is placed at an angle in the electron beam, to produce and direct TR into a horn antenna. The horn antenna transmits the corresponding signal to an EO Mach-Zehnder interferometer. A continous wave laser is connected to the interferometer, using the same fibers and finally the same photodiode and oscilloscope as the EO prototype. The TR produces a peak in the final laser signal on the photodiode, which serves as reference for the bunch arrival time on the oscilloscope.

The probe laser can use the same fibers and photodiode as the EO prototype, providing a reference signal of the bunch arrival time on the oscilloscope. The setup was used and characterized previously at CLEAR in the context of developing a Cherenkov diffraction radiation (ChDR)-based beam diagnostic, which is described in [113, pp. 128 ff.].

Instead of the direct beam field, the reference setup is optimized to measure transition radiation. TR is emitted, if an electric charge passes a transition between two media with different permittivity [44, 114]. It features a broadband spectrum, with coherent emission for wavelengths greater or equal to the bunch length. It is typically used as an intrusive bunch length diagnostics in linear accelerators, which use the coherent transition radiation (CTR) from a metal disc or foil inserted in the particle beam path [115–117].

A photo and corresponding schematic of the experimental setup at CLEAR is presented in Fig. 5.12. A silicon wafer is installed in the electron beam path at an angle of $\sim 45^\circ$ to direct the backwards TR onto a broadband horn antenna (A-INFO LB-65180-15-C-SF). It is connected to a Mach-Zehnder EO modulator (iXblue NIR-MX800-LN), which modulates the probe laser intensity relative to the electric signal from the horn antenna. The laser intensity is measured with the same photodiode and oscilloscope as the EO prototype. The same optical fibers can be used, too, which leads to a similar arrival time of the bunch-induced laser modulation on the oscilloscope for both experiments.

The benefit of the CTR setup is the use of a continuous wave (CW) laser (Thorlabs S1FC780PM), which inherently does not require delay scans to detect temporal overlap. Instead, the overlap is found by searching for a peak in the otherwise constant laser intensity on the oscilloscope. Common CW lasers have a drastically smaller peak power than the pulsed laser system and therefore require a sufficient modulation amplitude to achieve a good signal-to-noise ratio (SNR). Tests of the EO prototype with the CW were not successful, hence the CTR setup was used to provide a stronger laser modulation.

The EO Mach-Zehnder modulator in the CTR is a fiber coupled device, with an RF input for the horn antenna and a DC bias voltage. It divides the laser pulse into two parts, which are guided separately

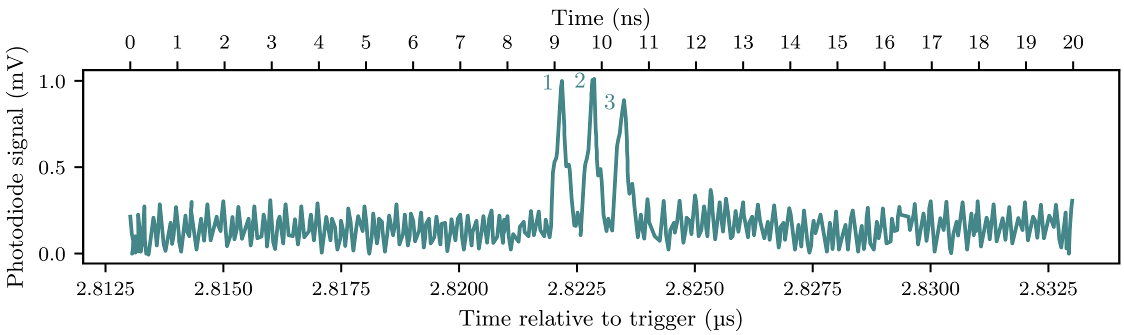

Figure 5.13: Photodiode signal of the CTR measurements with three micro-bunches per train. The bottom axis refers to the timebase of the oscilloscope, while the top axis shows the time in ns for better readability. A CW laser was connected to the calibration setup using the same return fiber as for the EO prototype. The timing of the three peaks on the oscilloscope serves as a reference time for later EOS measurements with the prototype for FCC-ee.

through a lithium niobate ($LiNbO_3$) crystal and recombined before its output. An applied electrical field changes the birefringence of the crystal through the EO effect, resulting in a phase retardation between the two laser paths. In this case, the origin of the electrical field is a combination of a bias voltage and the signal from the horn antenna. The combination of both laser paths at the output leads to an interference, which modulates the output laser intensity.

In the ideal case, the resulting laser intensity is given by [118]

$$I_{\mathrm{CTR}} = \frac{I_0}{2} \cdot \left(1 - \cos\left(\frac{\pi}{V_\pi}(V_{\mathrm{bias}} + V)\right)\right), \tag{5.7}$$

with the bias voltage V_{bias} and the characteristic voltage V_π, which describes the voltage for a phase shift of π. Similar to the principle of the EO monitor (see Eq. 2.38) the modulation amplitude of the laser intensity depends on the working point. In this case, the working point can be adjusted with a bias voltage V_{bias}. For the time calibration, optimizing the working point for maximum modulation amplitude is not the priority, as only the arrival time of the modulation is of interest. Thus, the bias voltage was dynamically tuned to maintain an adequate SNR.

5.4.6.2 Reference CTR measurement of three bunches

Figure 5.13 presents an example photodiode signal with the CTR setup. CLEAR was set to have three micro-bunches per train, leading to three consecutive peaks in the photodiode signal. The shape of the peaks is mainly a detector-limited response and does not directly correspond to the electron bunch shape, since the bandwidth of the data acquisition is not sufficient to resolve the modulation of the picosecond short electron bunches. In addition, the working point has been arbitrarily set in a low transmission setting to achieve an adequate relative modulation amplitude, but it is not optimized to provide a linear relation to the CTR signal. Nevertheless, the CTR setup successfully provides a timing reference to help with the search for the temporal overlap with the EO prototype.

The two spacings between the three peaks are ~683 ps and ~632 ps, which are close to the expected bunch spacing of ~667 ps. The discrepancies likely originate in the peak width in combination with the noise level (root mean square (RMS) noise of ~0.07 mV), since the position of the maxima is sensitive

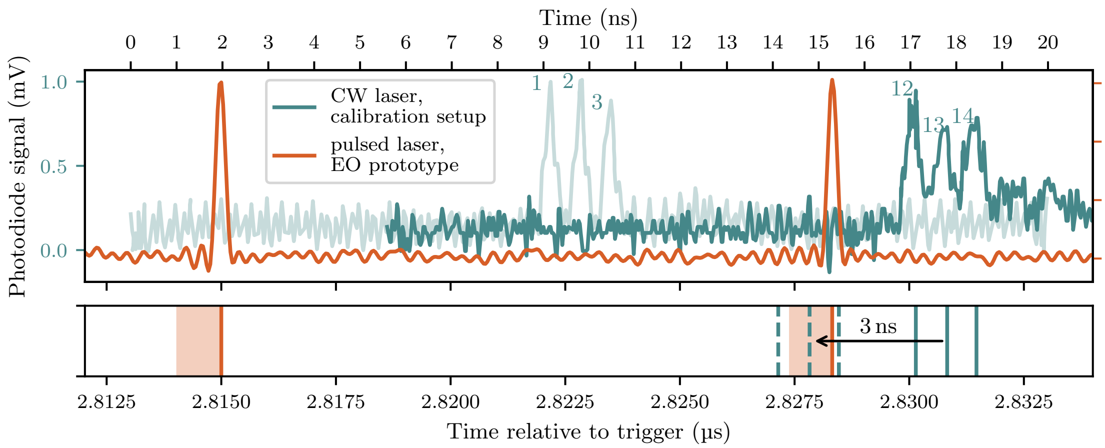

Figure 5.14: Arrival time comparison of EO prototype laser pulses (orange) and CTR measurements with a CW laser (blue). The measurements were done sequentially, switching the same fibers, photodiode and oscilloscope between the two setups. The numbers at the peaks correspond to the relative numbers of the electron bunches, in reference to Fig. 5.13. The diagram on the bottom highlights the peak positions as vertical lines and the scan range of the delay stage (light orange). The signal of an electron bunch is expected to arrive 3 ns earlier with the EO prototype compared to the CTR setup. Applying the expected delay to the CTR measurements of bunch 12 to 14 reveals, that bunch 13 is expected to overlap with a probe laser pulse during the delay scan with the EO prototype.

to noise. Overall, the level of agreement is considered sufficient to use the peaks as a reference for the bunch arrival time.

The oscilloscope was triggered on a 10 Hz reference signal, synchronized with the CLEAR repetition rate. Since the same trigger signal is used for the EO prototype measurements, the arrival time of the peaks on the oscilloscope can be used as a reference point. For later reference, the peaks and corresponding bunches are numbered 1, 2 and 3, sorted by their approximately arrival time 2.822 2 µs, 2.822 9 µs and 2.823 5 µs.

5.4.6.3 Laser pulse arrival time estimation to achieve temporal overlap with an electron bunch

To calculate the expected arrival time difference between the CTR setup and the EO prototype, the optical path length from the electron bunch to the oscilloscope was estimated. It is calculated as a sum of the path lengths with certain sections, multiplied with the refractive index of the respective medium (e.g. air, optical fibers, EO crystal, ...). In total, the EO prototype is estimated to have a shorter optical path length by $\sim$92 cm, hence the signal is expected to arrive $\sim$3 ns earlier at the oscilloscope compared to the CTR setup.

Figure 5.14 presents an exemplary photodiode signal of the EO prototype with the pulsed laser in comparison to CTR measurements with the CTR setup using a CW laser. The arrival time of the laser pulse can only be shifted in negative direction by up to −1 ns, due to the limited movement of the delay stage. The bunch arrival time is more flexible, because the pulse picker of the laser for the photoinjector enables to change the selected pulse range (see Chapter 5.1). It enables to select the RF buckets that are filled with an electron bunch, effectively enabling a phase shift of the bunch train in relation to the 10 Hz trigger signal. In the following description, the bunches are numbered according the their

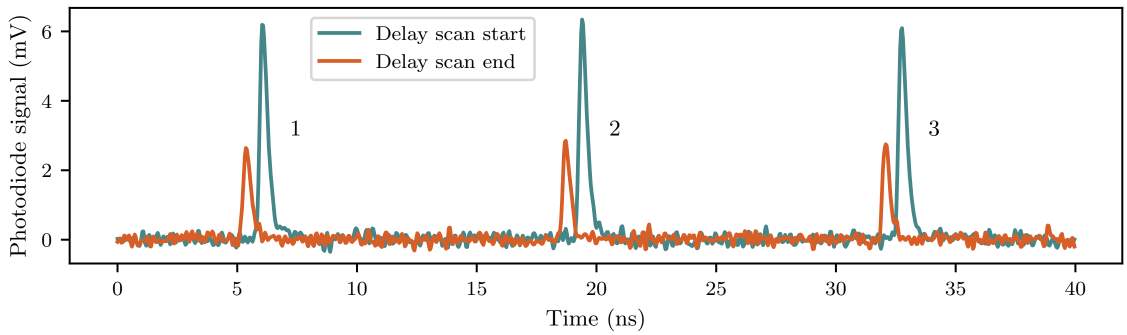

Figure 5.15: Photodiode signal at the start (blue) and end (orange) of a delay scan during EOS measurements. Three pulses are typically recorded in one waveform, with an expected modulation on pulse two during the delay scan. The timing for the overlap is estimated with the CTR reference setup (see Chapter 5.4.6. The other two pulses serve as an unmodulated reference, and can be used to calculate the relative modulation. (Also presented in Ref. [1])

relative RF bucket number in reference to the first bucket in Fig 5.13. The goal is to find the appropriate RF buckets, which lead to a temporal overlap of an electron bunch with the pulsed EO laser in the EO crystal during a 1 ns delay scan of the laser pulses.

The peaks in the CTR measurement of the bunches 12 to 14 are more uneven compared to the previous CTR measurements of the bunches 1 to 3, which is not fully understood and might originate in different bunch charges or a different working point of the CTR setup. The measurements were done a couple of hours apart, with a restart of the machine in between and a different scaling of the y-axis on the oscilloscope. However, the position of the peaks matches the expected position well, which is calculated by extrapolating from the CTR measurements of the bunches 1 to 3 assuming a bunch spacing of ∼667 ps. Hence, the peak position is considered sufficiently accurate to serve as a rough timing reference for the EO prototype.

The CTR signal of the bunch 13 has its maximum at ∼2.830 8 µs which is within the approximate range of the delay scan of the EO prototype setup (∼2.827 4 µs to ∼2.826 4 µs), when accounting for the estimated −3 ns shift from the optical path length difference. The calculated arrival times are considered to have high uncertainties, mainly due to the rough estimation of the optical path length difference between the two setups. Hence three bunches 12 to 14 were used for the initial measurements with the EO prototype to increase the chances of finding overlap. Thanks to this estimation, first EOS measurements with the prototype were performed successfully, which is described in Chapter 5.5.

5.4.7 Data analysis methods for EOS at CLEAR

The oscilloscope provides the photodiode signal, and is set to include typically three or more laser pulses per waveform. Figure 5.15 presents two example waveforms from EOS measurements of 2023. The first waveform shows the signal of three laser pulses at the beginning of the delay scan, and the other waveform shows the signal at its end. In this measurement, the maximum delay was set to approximately −850 ps. The RMS baseline noise is typically in a similar order of magnitude as the expected bunch-induced modulation, hence a direct observation on the oscilloscope is unlikely. In this example, the RMS noise of the baseline is ∼0.12 mV, which calculates to approximately 1.9 % to 4.8 % of the pulse amplitude during the delay scan.

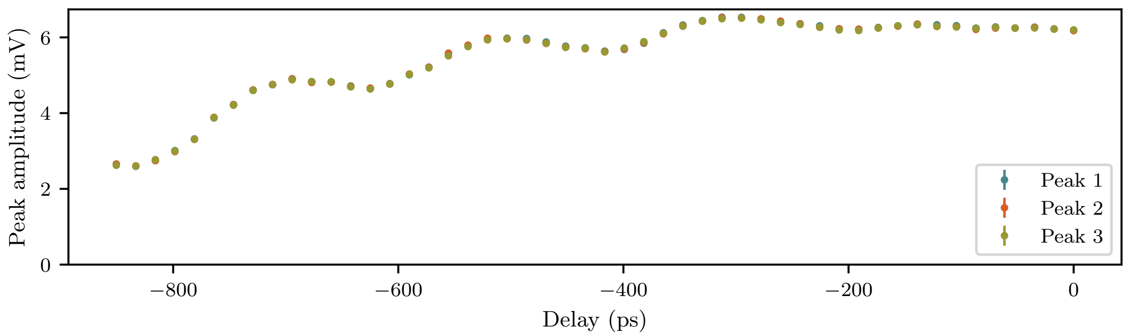

Figure 5.16: Amplitude of three recorded laser pulse peaks during the EOS scan. One data point represents the mean value over 50 shots, with its standard deviation indicated as error bars. The standard deviation is very small and not visible in this graph, but becomes more important during the following data analysis. The amplitude change is caused by the movement of the delay stage (see Chapter 5.4.2.1). The progression of the three peaks is very similar with a high absolute amplitude, hence the markers peaks 1 and 2 are hidden behind peak 3. The small difference makes observations of small deviations difficult. Thus, this plot serves as an intermediate step, but is not suitable to visualize a potentially small bunch-induced modulation.

To reduce the noise, typically the average over 50 to 100 measurements is taken per step of the delay stage. The resulting SEM is about a factor of 10 smaller than the single-shot baseline noise, achieving a level below 1 % of the peak amplitude. For example, Fig. 5.16 presents the mean amplitude of all three peaks and its SEM during a delay scan. Due to the small errors, the corresponding error bars are mostly hidden behind the data point markers. The pulse amplitude of all peaks generally decreased during the scan, with an additional slow amplitude oscillation. This behavior across all three peaks is caused by the movements of the delay stage, which is discussed in Chapter 5.4.2.1.

In a typical EOS measurement, only one pulse of the three pulses is expected to temporally overlap with the electron bunch. Therefore, a bunch-induced modulation would manifest in the plot as an amplitude deviation of one peak for a certain time span during the delay scan. The expected time span $\Delta\tau$ of the modulation can be estimated, by considering the temporal overlap of the Coulomb field of the electron bunch with the laser pulse. Assuming a Gaussian shape for the laser pulse σ_{laser} and the Coulomb field σ_{bunch}, the width of the cross-correlation curve is also Gaussian, with an effective width

$$\sigma_{\text{mod}} = \sqrt{\sigma_{\text{bunch}}^2 + \sigma_{\text{laser}}^2}. \tag{5.8}$$

In a typical EOS example from the CLEAR measurements, the laser pulse length is approximately $\sigma_{\text{laser}} \approx 25\,\text{ps}$ and a bunch length in the order of $\sigma_{\text{bunch}} \approx 4.5\,\text{ps}$, resulting in a modulation width of

$$\sigma_{\text{mod}} \approx 25.4\,\text{ps} \qquad (\text{FWHM}_{\text{mod}} \approx 59.8\,\text{ps})\,. \tag{5.9}$$

This calculated modulation width also agrees with the simulated EOS modulation width of $\sim (55.0 \pm 12.0)\,\text{ps}$ (FWHM) (see Chapter 5.3.2).

In this example, the step-width of the delay stage is set to ~52 mm, resulting in delay shifts of ~17.4 ps. This provides a balance between an acceptable scan duration of ~38 min and at least three data points within the FWHM of the bunch-induced modulation. The length of the scan duration is partly determined by the 10 Hz repetition rate and the number of measurements per step, but the internal processing of the oscilloscope also provided a bottleneck. The performance of the oscilloscope gradually deteriorated, which was likely caused by an increasingly full internal cache.

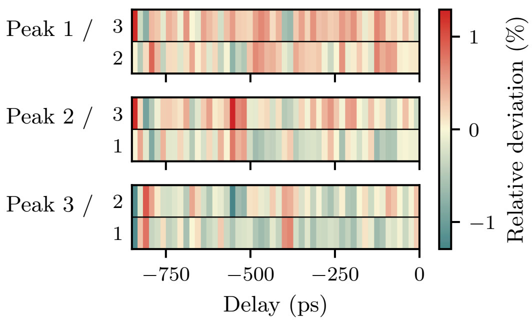

Figure 5.17: Overview of the relative deviation between peaks. The plot has a section for each peak, which compares the deviation to all other peaks. It enables to identify pulse modulations of any pulse during the delay scan. If a deviation appears across all rows within one section and is visible over a suitable delay span, it is potentially a bunch-induced modulation.

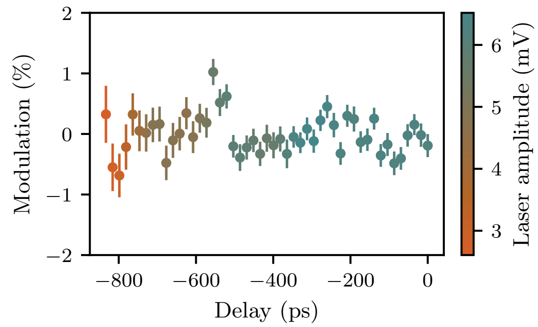

Figure 5.18: Modulation of peak 2 and its SEM during the delay scan. The changes of the absolute laser pulse amplitude are indicated with a color gradient (see Chapter 5.4.2.1). After identifying a unique modulation on a certain peak S in Fig. 5.17, all other peaks are summarized as a background signal BG to achieve a minimal SEM. The presented modulation $\mathrm{M} = \mathrm{S}/\mathrm{BG} - 1$ and its calculated uncertainty enables to characterize the modulation peak. In this example from 2023, the modulation amplitude is too small to enable any conclusions towards a bunch-induced modulation.

However, the bunch-induced modulation is potentially small compared to the absolute peak amplitude, making it difficult to observe the modulation. To improve visibility of small modulations, the amplitude ratios of the different combinations of all three peaks are calculated. To get an overview over all combinations, a 2D matrix-like image is plotted, where the rows are ratios of the peak combinations and the columns correspond to the delay step.

An example is presented in Fig. 5.17, where each pixel of the 2D plot is colorized with increasing vibrancy in correlation to the relative deviation of the peaks. The plot is divided in three sections with three rows each, showing the relative modulation of one specific peak in comparison to all the other peaks. If a one peak has a bunch-induced modulation with sufficient amplitude, it shows up as a vibrant color at the same delay range over all rows within its section. Thus, the overview plot is useful to determine the modulated peak containing. However, it doesn't show the uncertainty, hence further analysis is necessary.

In this example from the beam time in 2023, the overview plot reveals that peak 2 has a maximum in the relative deviation to peak 1 and peak 3 at a delay of around −550 ps. It spans approximately across three delay steps, which meets the expected width for a bunch-induced modulation. However, the modulation is small (∼1 %).

Assuming peak 2 (S) to have a bunch-induced modulation enables to summarize the other peaks as an unmodulated signal (BG). Hence, the modulation of peak 2 is linearly related to the division of its amplitude by the mean amplitude of all other peaks

$$\mathrm{M} = \frac{S}{BG} - 1. \tag{5.10}$$

Summarizing all unmodulated peaks to a single background signal further decreases the uncertainty of the modulation, which is calculated with an error propagation

$$\mathrm{SEM_M} = \frac{\mathrm{S}}{\mathrm{BG}}\sqrt{\left(\frac{\mathrm{SEM_S}}{\mathrm{S}}\right)^2 + \left(\frac{\mathrm{SEM_{BG}}}{\mathrm{BG}}\right)^2}. \tag{5.11}$$

As a result, the modulation M ideally has a clear peak with decent SNR that corresponds to the bunch-induced modulation of the EO prototype,

Figure 5.18 presents the modulation of the example data from 2023. Additionally, the laser pulse amplitude changes, which are caused by the delay stage, are indicated with a color gradient of the data points. It highlights that the higher SEM towards the end of the delay scan roughly correlates with reduced pulse amplitude (see Chapter 5.4.2.1). The peak around a delay of −550 ps possibly corresponds to a bunch-induced modulation, but the maximum of $\sim$(1.02 ± 0.22) % ($\mathrm{SNR} \approx 4.7$) is still small. Overall, the measurement result of 2023 was considered as a hint to a possible EO bunch-induced modulation, hence the beam time in 2024 was planned to further improve the results.

5.4.8 Noise reduction

During the measurements in 2024, the signal-to-noise ratio (SNR) could be improved by multiple different factors. A major contribution was an increase in the bunch charge from $\sim$0.3 nC to $\sim$1 nC, enabled by the installation of a new cathode for the photoinjector of CLEAR in winter of 2023/24 [119]. As the EO effect scales linearly with the electric field strength in the crystal (see Chapter 2.2.1), this improvement is expected to increase the amplitude of the modulation approximately by a factor of 3. It was also found in retrospect that the pulsed probe laser for the EO experiment probably suffered from a large jitter of the order of 5 ps (1σ) during the beam time in 2023 and had been improved to a jitter of the order of hundreds of femtoseconds [120] until the measurements in 2024. Due to averaging over multiple shots, a larger jitter contributes to a broadening and amplitude reduction of the bunch-induced modulation in the EOS measurements. Thus, the jitter reduction is expected to contribute to the improvement of the EOS measurements in 2024.

In the beginning of the beam time in 2024, the klystrons next to the laser laboratory were found to be a major source of high frequency noise in the oscilloscope data. Therefore, the klystrons that were not essential for the EOS measurements have been turned off. In addition, the bandwidth of the oscilloscope was digitally reduced from 10 GHz to 3 GHz, further reducing the baseline noise in its waveforms. As a final measure for noise reduction, the number of samples per step of the delay scan was increased to typically 100 instead of 50 measurements reducing the SEM in the EOS measurement analysis.

5.5 EOS measurements with the prototype at CLEAR

Two separate weeks of beam time, first in July 2023 and second in March 2024, were used to perform tests with the EO prototype for FCC-ee at CLEAR. The prototype was designed to serve as a proof-of-principle for the novel prism-based design of the crystal holder. To test the feasibility of this compact single-pass setup, the prototype at CLEAR was set up for an EOS experiment, following the description of Chapter 5.4.

The results of the first beam time in 2023 had a low SNR and are used in this chapter as illustrative example for the methodology of analyzing the EOS measurements. The SNR was improved during the beam time in 2024, and its results are discussed separately in the second part of this chapter.

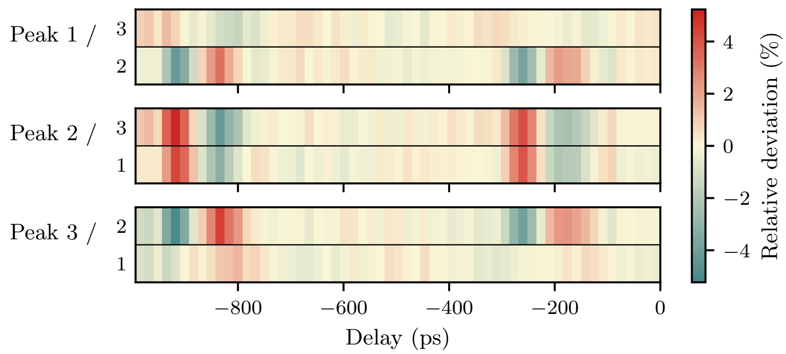

Figure 5.19: Overview of the relative amplitude deviation of the three laser pulse peaks from the photodiode signal during a delay scan. It shows the average deviation over 100 shots at each delay step. The plot reveals a ∼5 % modulation of peak 2 in the begging and towards the end of the delay scan. The spacing of the modulation peaks matches the expectation for a bunch-induced modulation.

5.5.1 Discussion of experimental results

To confirm the working principle of the EO prototype, multiple EOS measurements have been done at CLEAR in 2024. Different working points, delay scan resolution and number of bunches have been used to verify that the signal follows the anticipated behavior. This section presents the results of these measurements using the analysis methods from the previous section. The machine parameters generally follow the description of Chapter 5.1, if not stated otherwise.

5.5.1.1 EOS measurement compared to simulation

After multiple days of optimizing the setup and the arrival time synchronization, a promising signal was detected in the last afternoon of the beam time. To maximize the absolute modulation, the working point was set to $\phi \approx 0$, $\theta \approx 15°$, and the EO crystal was moved close to the electron beam at a distance of ∼2 mm.

CLEAR was operated with bunch trains at 10 Hz containing three micro-bunches. Their RF buckets were selected to achieve temporal overlap with a laser pulse during the delay scan (see Chapter 5.4.6). The bunch charge was maximized to achieve approximately 1 nC per micro-bunch, at a bunch length of $\sigma \approx 7.5\,\mathrm{ps}$.

The oscilloscope was set to record three laser pulses within one waveform, of which the second one (peak 2) was expected to experience a bunch-induced modulation during the delay scan, based on the arrival time synchronization tests with the CTR setup (see Chapter 5.4.6). 100 sample measurements were taken at each delay scan step to improve the SNR of the average.

Figure 5.19 presents the relative deviation of the three laser pulse peaks in all possible combinations. It reveals a relative deviation of peak 2 to the mean of peak 1 and peak 3. The deviation has two prominent maxima with a modulation of approximately 5 %, one close to the beginning of the delay scan at $t_{\mathrm{C1}} \approx -257\,\mathrm{ps}$ and one towards the end at $t_{\mathrm{C2}} \approx -925\,\mathrm{ps}$.

The distance between the maxima of ∼668 ps fits well to the expected ∼667 ps bunch spacing. The small deviation of 2 ps is possibly caused by the limited sampling resolution ∼17 ps. Additionally, approximately three data points seem to be part of the peak around the maximum, which matches the

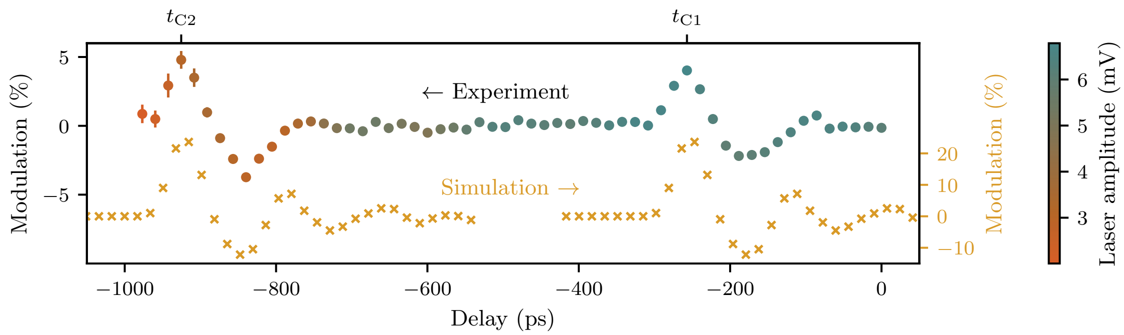

Figure 5.20: Modulation of the average peak 2 amplitude compared to the average amplitude of peak 1 and peak 3 during a delay scan. The error bars indicate the SEM, which generally increases during the delay scan and largest around the peak at t_{C1}. The change of the absolute laser amplitude change during the delay scan is indicated by a color gradient of the data points. The plot shows two maxima with a decent SNR, which likely correspond to a bunch-induced modulation. (The measurement data was also presented in Ref. [1, 2])

expectation for a bunch-induced modulation (see Chapter 5.4.7). Thus, peak 2 is assumed to be the modulated peak, while peak 1 and 3 can be summarized as a background reference.

Figure 5.20 presents the modulation of peak 2, using the mean of peak 1 and peak 3 as reference. Summarizing peak 1 and peak 3 effectively doubles the number of background samples, hence reducing the SEM. The SEM is indicated by error bars, and it increases towards the end of the delay scan (left side of the plot) due to the overall reduced laser pulse amplitude. The change of the pulse amplitude during the scan is indicated with a color gradient, which is described in detail in Chapter 5.4.2.1.

The resulting SNR of the first peak $\mathrm{SNR}_{C1} \approx 20.3$ at t_{C1} indicates a clean signal, and the second peak at t_{C2} still has a decent $\mathrm{SNR}_{C2} \approx 7.4$, despite its lower laser pulse amplitude. Both peaks are followed by a strongly dampened oscillation, which has a first negative peak with approximately half the amplitude of the peaks at t_{C1} and t_{C2}, respectively. The following peaks decrease drastically in amplitude and are barely visible. In summary, a decent SNR of the main peaks is enabled by averaging over 100 measurements at each data point, but the uncertainty might be underestimated, for example due to additional uncertainties from the laser jitter or a slow drift of beam parameters.

In Fig. 5.20, these experimental results are also compared to the EOS simulation from Chapter 5.3. The simulation results are plotted twice: First with the Coulomb peak aligned at t_{C1} and second with the Coulomb peak aligned at t_{C2} to enable a direct comparison of the simulated and measured EOS signal shape. The major difference between simulation and experiment is the modulation amplitude of the Coulomb peaks, which is approximately four times larger in simulation. To improve readability, the EOS simulation and measurement are plotted on different y-axes. The large amplitude deviation is likely caused by multiple factors, which are discussed in the following paragraphs.

One likely reason for the amplitude deviation is an underestimation of the distance between the probe laser in the EO crystal and the electron bunch. In simulation, the distance is defined by the position of the probe laser in the crystal and the distance of the crystal to the electron bunch. The simulation assumes a central position of the probe laser within the 10 mm × 10 mm cross-section of the crystal, and a crystal distance of 2 mm. Hence, a total distance of $d = 10\,\mathrm{mm}/2 + 2\,\mathrm{mm} = 7\,\mathrm{mm}$ is assumed. However, the position of the probe laser in the crystal is not known precisely in the experiment. If, for example, the laser is positioned 3 mm further away from the beam, it would approximately halve the modulation, because the electric field amplitude scales with $1/d^2$.

Additionally, a part of the deviation is caused by the transverse charge distribution of the real electron bunch. The simulation assumes a line charge density along the trajectory of the bunch, with no transverse spacial extent. For probe points close to the beam with a distance in the order of the transverse bunch size, this line density approximation overestimates the electric field strength at the probe point. The magnitude of this effect depends on the transverse shape of the electron bunch. For the EOS measurements, the horizontal beam size had been minimized to allow small distances between the crystal and the beam. The resulting transverse profile was often elongated in the vertical dimension, similar to the shape presented in Fig. 5.10. The beam screen readout was not calibrated for transverse charge distribution measurements and only enables a very rough estimation.

To get an idea of the order of magnitude of the effect, the transverse shape is approximated as a one-dimensional flat-top distribution along the vertical axis. A sum of two Gaussian distributions with $\sigma = 1\,\mathrm{mm}$, separated by a distance of 2 mm is used to approximate the flat-top charge distribution. A Monte-Carlo simulation was set up to determine the electric field strength at a probe point with a horizontal distance of 7 mm to the charge distribution center (resembling the probe laser). The results revealed that the electric field strength decreased by ~6 % with the flat-top distribution compared to a point charge at the same distance. Thus, the effect of the transverse charge distribution in the EOS experiment is expected to have a similar order of magnitude.

An additional decrease in the EOS modulation amplitude in the experiments is caused by additional reflections of the electric field before it enters the crystal. For example, if there was air trapped between the prism and the crystal, the additional change of the refractive index would lead to reflections at the borders, leading to a reduced Coulomb field strength in the crystal. Small air gaps between prisms and crystal are likely for the EOS prototype, because it was designed to support changing the EO crystal in the crystal holder and therefore account for small manufacturing errors of different crystals. Furthermore, the materials of the prism and crystal are idealized in simulation, hence additional absorption or reflections from the materials might add to a reduction of the Coulomb field transmission to the crystal.

Despite the large amplitude deviation, the width of the two main peaks $\mathrm{FWHM_{C1}} \approx (68 \pm 12)\,\mathrm{ps}$, $\mathrm{FWHM_{C2}} \approx (42 \pm 12)\,\mathrm{ps}$ match the width of the simulated Coulomb peak ($\mathrm{FWHM_{sim}} \approx (55 \pm 12)\,\mathrm{ps}$) within the uncertainty of the measurement. However, the uncertainty is large, due to the low sampling rate of only 3 peaks within the FWHM. The following oscillation after the main peaks follows a similar shape as the wake field in the simulation, with a strong negative peak first and strong dampening of the following oscillations. Overall, the dampening appears stronger in the measurement, because in contrast to the simulation, the second negative peak is not visible anymore.

In summary, the first EOS measurement revealed two bunch-induced signals, which match the expected intra-bunch spacing. In comparison to simulation, the modulation amplitude is drastically reduced, but the general shape of the Coulomb peak and following wake field match the expectation. To further increase confidence that the signal corresponds to the desired bunch-induced signal, follow-up measurements were conducted.

5.5.2 Measurement at inverse working point

Inverting the working point to $\phi \approx 0°, \theta \approx -15°$ is expected to invert the bunch-induced modulation. If the signal does not invert, or if it changes in unexpected ways, it likely did not originate in a polarization change of the probe laser in the EO crystal. Thus, this measurement serves as a simple method to check for unintended signal sources, for example cross-talk from klystron signals, or other electrical sources that are also synchronized with the electron bunch arrival time.

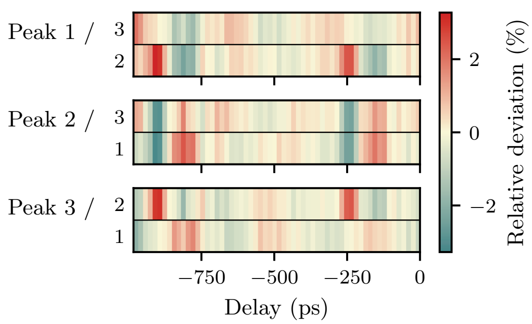

Figure 5.21: Overview of the relative laser pulse amplitude deviation from an EOS measurement. The EOS working point is inverted compared to the previous EOS measurement in Chapter 5.5.1.1, which is expected to invert a bunch-induced modulation. The generally lower deviation amplitude is likely cause by a lower bunch charge and increased distance between the crystal and the bunch center. This overview reveals a modulation of peak 2, which roughly matches the expected signal. The modulation is investigated in more detail in Fig 5.22.

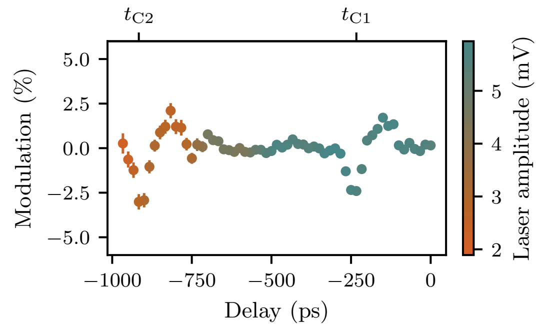

Figure 5.22: Modulation of peak 2 compared to the average of peak 1 and 3 from an EOS measurement. In comparison to the modulation in the previous measurement (Fig. 5.20), it shows similar features, but with opposite sign. Since the working point was inverted, the corresponding signal inversion confirms the origin of the modulation in a change of the laser polarization, instead of accidental pickup of electrical noise. (Also presented in Ref. [1, 2])

The measurement with inverted working point was performed several hours later and after a full restart of CLEAR, due to a combination of issues with the machine as well as with the EOS measurement procedure. Because of ongoing issues with the transport of the electron bunches at the whole length of the CLEAR beamline, the bunch charge of all three bunches was limited to approximately 0.77 nC at the in-air test stand. A slightly wider transverse beam size also required a slight increase in the distance of the crystal to the beam center from 2 mm to 2.5 mm. Besides these differences and the inverse working point, the same measurement principle was applied with 100 samples per delay step.

A first overview of the relative deviation of three recorded peaks from laser pulses on the photodiode are presented in Fig. 5.21. The plot reveals a modulation in peak 2, consisting of two prominent minima at $t_{\text{C1}} \approx -233\,\text{ps}$ and $t_{\text{C2}} \approx -916\,\text{ps}$ with amplitudes of approximately −2.4 % and −3.0 %, respectively.

Figure 5.22 presents the modulation of peak 2 with reduced uncertainty, due to averaging over peak 1 and peak 3 as reference. The most prominent features are two minima, with a decent $\text{SNR}_{\text{C1}} \approx 12$ and $SNR_{\text{C2}} \approx 7$. The two minima at t_{C1} and t_{C2} are close to the positions of the maxima from the previous measurement and with similar width of $\text{FWHM}_{\text{C1}} \approx (76 \pm 12)\,\text{ps}$, and $\text{FWHM}_{\text{C2}} \approx (46 \pm 12)\,\text{ps}$. However, the SNR of these minima is lower, and the absolute modulation amplitude is approximately 50 % smaller than the maxima from the previous measurement. The source of this deviation is not known, but due to the restart of the CLEAR accelerator, it is likely caused by a combination of lower bunch charge, increased distance of the crystal to the bunch center and a different transverse bunch shape.

Overall, this EOS signal has a similar shape compared to the previous measurement, with the exception for the opposite modulation polarity. Hence, the inverse working point also inverted the signal, which excludes the signal origin to be from any synchronized electrical noise and increases the confidence that it is a bunch-induced EO signal.

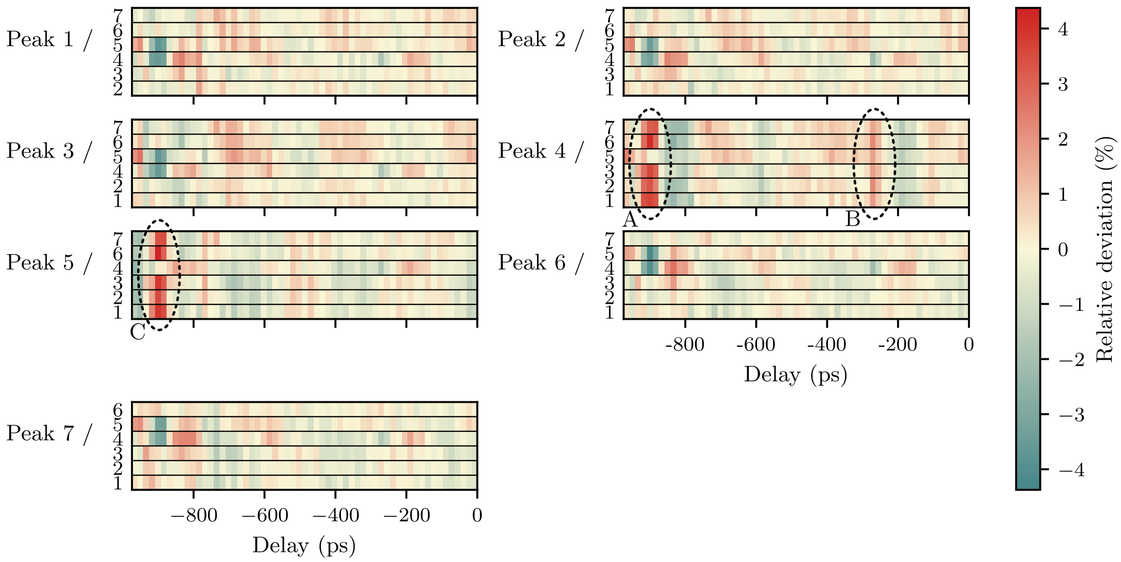

(a) Relative laser pulse deviation during delay scan

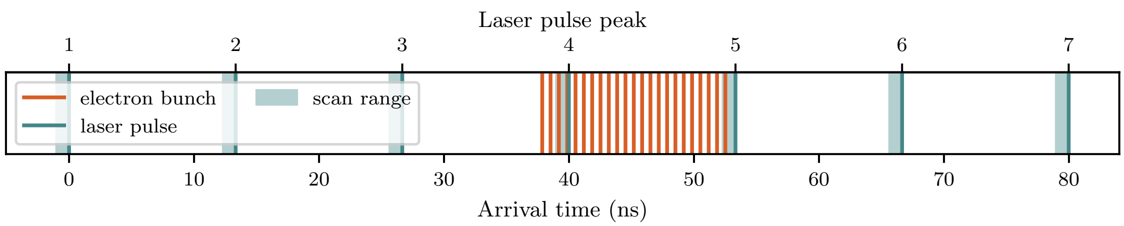

(b) Schematic overview of the laser pulse and electron bunch arrival time

Figure 5.23: Relative deviation of the recorded laser pulses during the EOS measurement with 23 micro-bunches per train (a) and corresponding schematic of their arrival time (b). The plot reveals bunch-induced modulation of peak 4 and peak 5, highlighted by a surrounding dashed ellipse and annotated as A, B and C. The occurrence of the modulation in these two laser peaks matches the expectation, because the total time span of the bunch trains is slightly longer than the spacing between two laser pulses.

5.5.3 Modulation of two subsequent laser pulses

To get an additional confirmation that the timing calculations are correct, and that multiple modulated pulses can be detected, an additional EOS measurement with 23 consecutive bunches per train was conducted. The resulting total time span of one bunch train is ∼14.7 ns, which guarantees that two consecutive laser pulses (with ∼13.3 ns spacing) experience an EO modulation during the delay scan over 1 ns.

This measurement was taken a couple of hours after the first successful EOS measurement (see Chapter 5.5.1.1, with a restart of the CLEAR accelerator in-between. The start-up required tweaking multiple machine parameters to optimize the bunch charge at the in-air section, hence parameters like the transverse bunch profile are different and the status of the machine is not perfectly comparable to the previous measurements. A total charge of the 23 micro-bunches approximately 12 nC was achieved, hence resulting in an average bunch charge of 0.5 nC. The crystal distance to the beam center was set to ∼2.5 mm and the working point of the EOS experiment was set to $\phi \approx 0^\circ$ and $\theta \approx 15^\circ$.

The timebase of the oscilloscope was extended to fit seven laser pulse peaks onto one waveform. The large number of pulses was chosen to guarantee capturing both modulated pulses. Additionally, the large number of reference pulses enables investigating the influence of the wake field or other unintended signals on subsequent laser pulses.

Figure 5.23a presents the relative deviation of all seven pulses during the delay scan. Similar to previous measurements, the step size of the delay scan is approximately 17.4 ps, and the average over 100 shots was taken each time. The most prominent modulation peaks A and C are visible on laser peak 4 and peak 5, both at a delay of approximately −907 ps with an amplitude of $\sim$3.55 % and $\sim$3.8 %. Peak 4 has the additional maximum B around −269 ps, but with a lower amplitude of $\sim$1.9 %. A schematic overview of the corresponding laser pulse and electron bunch arrival times is presented in Fig. 5.23b.

The prominent modulation C of laser peak 5 likely corresponds to the bunch-induced modulation from the last electron bunch of the bunch train, because the next bunch would be expected at −240 ps (667 ps later), but no additional modulation is visible. Since peak 4 arrives $\sim$13.333 ns before peak 5, which is equivalent to the duration of 20 bunch-spacings, it is expected to have a bunch-induced modulation for both peaks at the same time during the delay scan. The additional prominent modulation B within the scan of peak 4 occurs at a relative delay of approximately 638 ps to the previous modulation maximum A. Hence, the spacing of the maxima deviates from the expected 667 ps bunch spacing by 29 ps. Considering the low sampling rate with a step size of approximately 17 ps, this deviation is larger than expected. It could be caused by errors in the movement of the delay stage, which is assumed to have a constant step size. Additionally, the wake field of the previous bunch(es) could impact the shape of the peak, effectively moving its maximum in the final measurement.

The modulation maximum B also only has approximately half the amplitude of the other two maxima, which is not fully understood. It could originate in an overlap with the wake field of previous bunches in combination with a lower bunch charge, since the individual bunch charge is not known.

In summary, the EOS measurement with 23 micro-bunches enabled to detect modulation peaks A, B and C from multiple bunches during the delay scan of two subsequent laser pulses (peak 4 and peak 5). While the two maxima A and C match the expectation for a bunch-induced modulation, the scan of peak 4 contains an additional modulation B, which deviates slightly from the expected signal. It has a lower amplitude and slightly different arrival time, which could hint at additional issues with the arrival time estimation, a different bunch charge, or interactions with the wake field of previous bunches. Nevertheless, the occurrence of the modulation in the delay scans of two subsequent laser pulses confirms ability of the EO prototype to detect multiple electron bunches with short spacing.

5.5.4 Detailed scan

To reveal the shape of the bunch-induced modulation in greater detail, an additional EOS measurement was performed with an increased sampling rate. The delay stage was moved in steps of 6.6 ps, and 100 measurements were taken each step. Due to the time constraints of the limited beam time, the total scan range was reduced to $\sim$256 ps, resulting in a measurement duration of $\sim$47 min. Three bunches were used per train, which enabled to optimize the CLEAR beamline to achieve a total bunch charge of approximately 3 nC (average of 1 nC per bunch) at the in-air test stand. The oscilloscope was set to monitor three laser pulse peaks, where peak 2 is expected to have a bunch-induced modulation.

Figure 5.24 presents the modulation of peak 2, which is calculated by dividing the average amplitude of peak 2 by the average amplitude of peak 1 and 3. The result shows a low SEM, resulting in a decent $\mathrm{SNR} \approx 20$ of the maximum at $t_{\mathrm{C1}} \approx -211\,\mathrm{ps}$. The maximum reaches a relative modulation of

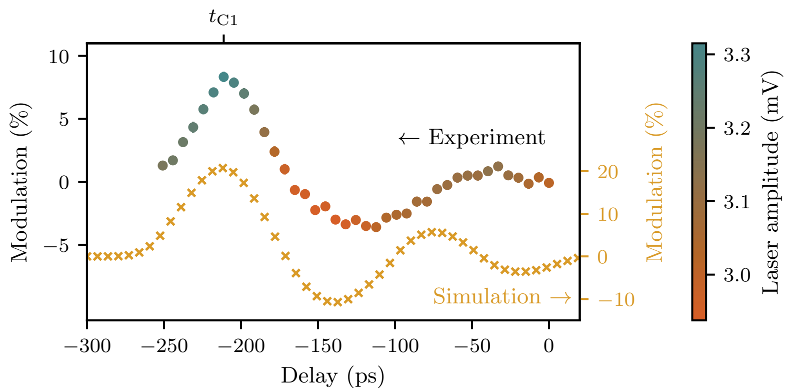

Figure 5.24: EOS measurement (orange circles) during a detailed delay scan with a step width of ∼6.6 ps and corresponding simulation results (yellow crosses). The position of the maximum of the simulation data was aligned to t_{C1}, and is plotted on a separate y-axis to account for the higher amplitude and improve readability. The experimental modulation is a result of a division of the average amplitude of the modulated laser pulse and the average of two unmodulated pulses. The resulting SEM is drawn as error bars, but it is small and mostly hidden behind the circular data markers. The color of the circular markers represents the average laser pulse amplitude, which nearly constant during this short scan. The simulation captures roughly the appearance of the measurement, but its simplifications result in an overall larger amplitude and differences in the periodicity and decay of the wake field oscillation.

∼(8.3 ± 0.4) %, which is the largest measured modulation during the measurement campaign at CLEAR. It has a width of $\mathrm{FWHM}_{\mathrm{C1}} \approx (43.6 \pm 4.7)$ ps, which is calculated with linear interpolation between the data.

In comparison to previous EOS measurements, the larger maximum amplitude is likely caused by a combination of the high bunch charge and the high sampling rate, because a smaller step size increases the likelihood of capturing the maximum of the signal. The width of the signal lies on the smaller end of the range observed in previous measurements, but remains within the statistical spread. The general shape of the signal, including the ringing of the wake field is consistent with previous experiments.

To revisit the comparison of experiment and simulation with improved resolution, Fig. 5.24 includes a plot of an EOS simulation. The simulation follows the description of Chapter 5.3 and uses the same parameters, but the sampling rate was adapted to the delay step size of 6.6 ps to match the experiment. The increased modulation amplitude was discussed previously in Chapter 5.5.1.1, and is likely caused by the assumption of a line charge density with no transverse extend in combination with simplifications of material properties and geometry of the crystal and prisms.

The simulated peak at t_{C1} has a width of $\mathrm{FWHM}_{\mathrm{C1}}^{(\mathrm{sim})} \approx (54.9 \pm 4.8)$ ps, which is slightly broader than the measured signal. This small deviation could be caused by the uncertainty through the sampling rate, and, for example, by the simplified estimation of data acquisition bandwidth limits, However, the first negative peak has a width of $\mathrm{FWHM}_{\mathrm{C1}}^{(\mathrm{sim})} \approx (61.0 \pm 4.8)$ ps, while the measurement shows $\mathrm{FWHM}_{\mathrm{C1}} \approx (80.6 \pm 4.7)$ ps. In combination with a following, more pronounced, second maximum in the simulation, the differences hint at a deviation of the simulated impedance compared to the experiment. The bandwidth limit of the data acquisition acts similar to a moving average over the original phase retardation (see Fig. 5.5), hence it obscures the underlying features of the original wake field. As a result, the deviation of the peak width could be caused by differences in the impedance, for example from details of the geometry or material properties of the experimental setup.

In summary, the detailed scan highlights the bandwidth limitation of the data acquisition, but it hints at an underlying deviation of the simulated impedance in comparison to the experiment. However, the shape of the main peak is consistent with the simulated signal and further supports the proof-of-principle of the EO prototype.

6 Summary and conclusion

The Future Circular Lepton Collider (FCC-ee) requires a bunch length monitor to assess the beamstrahlung that impacts the energy spread and luminosity of the colliding electron and positron bunches [8–10], to provide on-demand longitudinal bunch profile measurements for the commissioning of the accelerator and to monitor the top-up injection of additional particles into the circulating beam. As stated in the feasibility study report, the monitor needs to provide single-shot longitudinal profile measurements of every bunch with a bunch length uncertainty of below 1 % at a repetition rate of up to 40 MHz, enabling bunch-by-bunch measurements. The monitor needs to cope with a wide range of bunch lengths over FCC-ee's four distinct operation modes in the range of $\sim$2 mm to $\sim$15 mm (bunch duration of $\sim$6 ps to $\sim$51 ps) with high bunch charges of around 30 nC, while keeping the impedance low to minimize the energy deposition in the electro-optical (EO) crystal and its effect on particle beam dynamics.

This thesis evaluates the feasibility and presents a conceptual design for an in-vacuum EO longitudinal bunch profile monitor to cope with the demanding requirements of FCC-ee. EO monitors are used in a few linear accelerators as a custom, experimental diagnostic instrument, optimized for single-shot high-precision bunch profile measurements at sub-ps bunch durations [26, 28, 29]. In contrast to EO monitors aiming for measurements of short bunches, FCC-ee's high bunch charge and wide range of bunch lengths poses new challenges that require dedicated studies to assess its feasibility and to develop a dedicated conceptual design.

To establish a fundamental understanding of the diagnostic principle and to provide a baseline for further investigations, these studies of the EO monitor for FCC-ee have been grounded in experiments with the existing EO monitor at Karlsruhe Research Accelerator (KARA) (see Chapter 3.1). The EO monitor at KARA was the first to enable turn-by-turn bunch profile measurements at a synchrotron, with a repetition rate of 2.7 MHz [27, 33, 35]. While the existing setup provides a crucial reference for low-charge, short-bunch regimes, a new comparative simulation procedure is presented in this thesis that enabled studies of the EO monitor under FCC-ee's beam conditions (see Chapter 4). To assess the functionality of the new simulation procedure, the simulated electro-optical sampling (EOS) Coulomb and wakefield scans have been compared to KARA EOS measurements, showing a good agreement of its main features. Simulations of the KARA EO monitor under FCC-ee's beam conditions revealed a major issue with the existing design of the in-vacuum crystal assembly, because the probe laser pulses propagate twice, once upstream and once downstream, through the EO crystal. This causes a signal interference that masks the encoded bunch profile, especially for the long particle bunches of FCC-ees Z-operation mode. Hence, the design of the crystal assembly is not suitable for measurements at FCC-ee.

This thesis mainly focuses on solutions for this major issue with the development of a new single-pass design, in which the laser passes only once and in downstream direction through the crystal. A new crystal assembly is proposed, containing two prisms attached to the up- and downstream faces of the EO crystal to use total internal reflection for guiding the laser pulses without blocking the particle bunch's electric field (see Chapter 4.3). Hence, it does not require coatings and maintains a compact size. To cope with FCC-ee's high bunch charge, the crystal is now positioned at the top of the FCC-ee vacuum chamber to increase the distance between the crystal assembly and the particle beam. Furthermore, adjustments of the crystal thickness can be used to fine-tune the balance between sensitivity and resolution for FCC-ee's four operation modes. Simulations have been conducted and confirmed that the novel prism-based design provides sufficient signal amplitude with a drastically reduced impedance, hence suggesting its feasibility for FCC-ee's beam conditions.

To experimentally evaluate the functionality of the new prism-based setup, a prototype of the EO monitor's interaction module has been built (see Chapter 5), which is adapted from the KARA module to accommodate a prism-based crystal assembly. It has been tested with EOS scans at the in-air test stand of the CERN Linear Electron Accelerator for Research (CLEAR) and complementary simulations, providing a successful proof-of-principle of the prism-based crystal assembly. Thus, the new prism-based crystal design provides a baseline to build towards a technical EO monitor design for FCC-ee.

An additional issue was revealed during EOS experiments at KARA, which featured a slow drift of the baseline laser signal, that was suspected to correlate with the heat load on the crystal assembly. A dedicated experiment has been conducted, which confirmed a correlation between the crystal assembly temperature and the signal baseline drift (see Chapter 3.1.4). As the drift originates in the laser polarization and is very slow at KARA compared to the single-shot measurements at 2.7 MHz repetition rate, it can be mitigated by readjusting the EO monitor working point before the start of an electro-optical spectral decoding (EOSD) measurement. As the heating is expected to be stronger at FCC-ee, a low impedance of the crystal assembly is important to reduce the heat load, and further studies are recommended to investigate mitigation strategies like automated working point adjustments and thermal management.

For a future transition of the new conceptual EO monitor design to a corresponding technical design, the EO detection technique (see Chapter 2.2.4) and its specific resolution with the prism-based crystal assembly need to be evaluated. Past EO monitors have shown sub-picosecond resolution with uncertainties of tens of femtoseconds [29], relying on a low-jitter laser synchronization. Due to the large scale of FCC-ee and thus potentially long cables and fibers, the synchronization system and placement of the EO monitor components at FCC-ee require additional investigations.
The repetition rate of EOSD bunch profile measurements is mainly limited by the spectrometer camera's frame rate, which achieved 2.7 MHz at KARA [35, 72]. While a new camera version targets 12 MHz [121], achieving the desired 40 MHz will require further R&D. Alternatives include splitting the laser signal for multiple data acquisition systems, or deploying multiple EO setups.
Concerning the infrastructure requirements, the commissioning of an EO monitor at the linear accelerator FLUTE and the experiments at CLEAR highlighted the importance for a reference signal of the particle bunch arrival time. As the gap between bunches or bunch batches is often orders of magnitude larger than the bunch and laser pulse length, the reference signal provides an important indicator to synchronize the arrival time of the probe laser pulse and particle bunch (see Chapters 3.2.2, 5.4.6). As FCC-ee has inter-batch durations of up to tens of microseconds [9], a reference signal is recommended to be incorporated in future studies of the EO monitor's infrastructure and placement.
Furthermore, the radiation load and radiation hardness of EO monitor components, in particular the EO crystal, need to be studied and taken into account for its placement and for the laser transmission from the EO laser system to the interaction module and detection system.

In conclusion, this thesis demonstrates the feasibility of an EO monitor for bunch profile measurements at FCC-ee with the dedicated and newly developed prism-based concept to particularly enable measurements at FCC-ee's wide range of bunch lengths. The proposed compact, low-impedance conceptual design provides the baseline for transitioning towards a technical EO monitor design closely tailored to the unique demands of CERN's large-scale future lepton collider.

Acronyms

AOM	acousto-optic modulator 39, 40, 125
BPM	beam position monitor 14, 47, 48, 63, 64, 66, 90, 125
CERN	CERN 90, 95, 102, 125
ChDR	Cherenkov diffraction radiation 2, 28, 107, 125
CLEAR	CERN Linear Electron Accelerator for Research i, 3, 22, 25, 26, 89–103, 105–109, 111, 113, 114, 117–120, 124, 125
compact TDS	compact transverse deflecting structure 62, 125
CSR	coherent synchrotron radiation 13, 14, 36, 56, 125
CTR	coherent transition radiation 107–110, 114, 125
CW	continuous wave 64, 107–109, 125
DEOS	diversity electro-optic sampling 25, 32, 125
EO	electro-optical i, 1–3, 5, 10–14, 17–33, 35–49, 51, 52, 56–67, 69–75, 77, 79–86, 89–110, 113–119, 121, 123–125, 130, 131
EOS	electro-optical sampling 5, 24–26, 31–33, 35–37, 41, 43, 46–49, 57, 58, 61, 63, 64, 66, 69, 71, 73–80, 85–87, 89, 90, 95–99, 101–105, 108, 110, 111, 113–120, 123–125
EOSD	electro-optical spectral decoding 1, 5, 25–27, 31–33, 35–37, 41, 43, 46, 49, 51–56, 61–66, 69, 75–77, 79, 80, 99, 101, 124, 125, 129
EOSI	electro-optic spectral interferometry 25, 32, 125
European XFEL	European XFEL 17, 22, 125
FCC	Future Circular Collider 125
FCC-ee	Future Circular Lepton Collider i, 1–3, 5, 9, 11, 14, 17, 25, 32, 35, 45, 46, 49, 56, 57, 61, 62, 67, 69, 71, 79–86, 89, 91, 93, 94, 96, 99, 108, 113, 123–125
FCC-hh	Future Circular Hadron Collider 1, 2, 125
FFT	Fast Fourier Transform 54–56, 77–80, 85, 125
FLASH	free electron laser in Hamburg 17, 22, 125
FLUTE	Ferninfrarot Linac- und Test-Experiment 22, 25, 26, 35, 61–63, 65–67, 124, 125
FWHM	full width at half maximum 28, 39–41, 52, 65, 97, 99, 100, 111, 116, 117, 120, 125, 129
GaAs	gallium arsenide 29, 125
GaP	gallium phosphide 18–20, 23, 28–31, 43, 44, 59, 66, 82, 87, 94, 125
GHC	global hybrid correction 125
ICT	integrating current transformer 64, 90, 125
InGaAs	indium gallium arsenide 46, 63, 125
IP	interaction point 125

IR infra-red 125

KALYPSO Karlsruhe line array detector for MHz-repetition rate spectroscopy 33, 37, 43, 46, 49, 50, 52, 53, 63, 125
KARA Karlsruhe Research Accelerator i, 1, 3, 5, 6, 9, 11, 14, 17, 22, 24–26, 33, 35–40, 42–49, 52, 53, 56–59, 61–66, 69–71, 73–80, 82–85, 87, 90, 91, 93, 94, 105, 123–125
KIT Karlsruhe Institute of Technology 1, 33, 35, 37, 46, 62, 90, 91, 102, 125

$LiNbO_3$ lithium niobate 108, 125

OTR optical transition radiation 125

PBS polarizing beam splitter 23, 38, 43, 44, 59, 74, 87, 92, 100–102, 125, 131
PD photodiode 25, 26, 37, 42, 47, 62, 77, 87, 125
PID proportional-integral-derivative 42, 100, 125
PLL phase-locked loop 42, 43, 51, 63, 125
PM polarization-maintaining 36–39, 41, 43, 62, 63, 90, 99–101, 103, 106, 125
PSF point spread function 125
PSI Paul Scherrer Institute 37, 125

RF radio frequency 3, 6–10, 12, 13, 36, 39, 40, 42, 62, 65, 66, 99, 100, 106, 107, 109, 110, 114, 125, 130
RMS root mean square 12, 27, 52, 54, 108, 110, 125, 130
ROI region of interest 50–54, 65, 66, 125

SEM standard error of the mean 51, 66, 102, 111–113, 115, 119, 120, 125
Si silicon 46, 125
SM single-mode 36, 37, 44–46, 62, 63, 92, 102, 103, 125
SNR signal-to-noise ratio 46, 49, 63, 64, 89, 98, 101, 106–108, 113–115, 117, 119, 125
SR synchrotron radiation 82, 125

TIR total internal reflection 93, 94, 125
TO transverse optical 28, 29, 125
TR transition radiation 106, 107, 125

VLD visible light diagnostics 125
VM vector modulator 43, 51, 125

WCM wall current monitor 90, 125

XRD X-ray diffraction 95, 125

YAG yttrium aluminium garnet 104, 125
Yb Ytterbium 38–40, 125

ZnTe zinc telluride 18–20, 28–31, 94–96, 98, 125

Symbols

Sign	Description	Unit
$\vec{B}$	Magnetic field	B
BG	Background data	
BW	bandwidth, typically 3 dB bandwidth.	Hz
c	Speed of light in vacuum	m/s
D	Dispersion of a particle in a synchrotron	m
d	Crystal thickness	m
D_2	group delay dispersion	Hz
$\vec{E}$	Electric field	V/m
$\vec{E}$	Electrical field	V/m
E	Electric field strength	V/m
$E_{\mathcal{W}}$	Wake field	V/m
f	Frequency	Hz
F_{Cen}	Centripetal force	N
F_{L}	Lorentz force	N
FWHM	Full-width-half-maximum (full width at half maximum (FWHM))	
h	Harmonic number (integer)	
I	Current	A
K	Kinetic energy	eV
k_{pt}	Pixel-to-time calibration factor for the EOSD spectrometer	ps/pixel
L	Orbit length of a particle in a synchrotron	m
L_0	Orbit length of the reference particle in a synchrotron	m
ΔL	Orbit length difference to the reference orbit	m
M	Modulation	%
m	Rest mass	kg
MD	Modulated data	
n	Refractive Index	
p	Momentum of a particle	kg m/s
p_0	Momentum of the reference particle	kg m/s
Δp	Momentum difference to the reference particle	kg m/s
P_{SR}	Power of synchrotron radiation in a circular accelerator	W
q	Electrical charge	C
R	Radius of circular trajectory	m
$\vec{r} = (x, y, z)$	Coordinate vector in a Frenet-Serret coordinate system	(m, m, m)
S	Impermeability tensor	
s	Path of the reference orbit	m
SNR	signal-to-noise ratio	
T	Revolution time of a particle in a synchrotron	s
T_0	Revolution time of the reference particle	s

Sign	Description	Unit
T_{b}	Time that a particle takes in a bending section within one turn	s
ΔT	Revolution time difference to the reference particle	s
U	Electric potential energy	J
UD	Unmodulated data	
V	Voltage	V
v	Velocity	m/s
V_{RF}	Voltage of the accelerating fields in the radio frequency (RF) cavity	V
$V_{\mathcal{W}}$	Wake potential	V
ΔW_{SR}	Energy loss per turn due to synchrotron radiation	eV
α_{c}	Momentum compaction factor	
β	Relativistic velocity parameter defined as $\beta = \frac{v}{c}$	
ε_0	Vacuum permittivity	F m^{-1}
η	Phase slip factor	
Γ	Phase retardation	rad
γ	Lorentz factor	
γ_{t}	Lorentz factor at transition energy	
λ	Wavelength	m
Ω	Synchrotron frequency	Hz
ϕ	Angle of $\lambda/4$ waveplate. Part of the EO working point.	°
ψ_{S}	Synchronous phase of the reference particle	deg
ψ	Phase of the accelerating field in the RF cavity	deg
$\sigma_{\mathcal{E}}$	RMS energy spread of a particle bunch	eV
σ_p	RMS momentum spread of a particle bunch	kg m/s
σ_z	RMS longitudinal length of a particle bunch	m
τ	Describes the temporal resolution. Typically the root mean square (RMS) value.	s
θ	Angle of $\lambda/2$ waveplate. Part of the EO working point.	°
$\mathcal{E}$	Total particle energy	eV
$\mathcal{E}_{\text{S}}$	Total energy of the synchronous particle	eV
$\mathcal{I}$	Intensity	W/m^2
$\mathtt{r}$	Pockels coefficient tensor	
$\mathtt{s}$	Kerr coefficient tensor	
$\mathcal{W}$	Wake function	V/C
$\mathcal{Z}$	Impedance	Ω

Glossary

chirp The chirp of a laser pulse describes a change of the wavelength over the duration of the pulse. E.g. a linear chirp refers to a linear correlation between the wavelength and the temporal profile of the pulse. 36, 125

coefficient of determination The coefficient of determination is a quantity to evaluate the goodness of fit. It is defined as $R^2 = 1 - \frac{\sum_i (y_i - \hat{y}_i)^2}{\sum_i (y_i - \bar{y})^2}$, with observed values y_i, model predictions $\hat{y}_i$ and the mean of the observed data $\bar{y}_i$. It describes the fraction of how much the variance of the data is captured by the fit (perfect fit: $R^2 = 1$). 25, 52, 83, 125

polarization analyzer A series of a $\lambda/4$ and $\lambda/2$ waveplate, followed by a polarizing beam splitter (PBS). It enables the conversion of a polarization modulation of a laser pulse into an intensity modulation, and is used in the EO monitor. Its initial setting of the waveplate angles ϕ and θ determines the working point of the EO system. $\phi, \theta = 0°$ is defined by the crossed configuration, where the transmitted laser power is minimized through the analyzer. 23, 25, 36, 37, 43, 44, 58–60, 69, 74, 91, 92, 104, 105, 125, 131

symlog A modified logarithmic scale, which depicts negative values x as $-\log(|x|)$. Additionally, it switches to a linear scale for values close to $x = 0$. 15, 16, 125

working point The working point of the EO setup is defined by the angle ϕ of the $\lambda/4$ wave plate and θ of the $\lambda/2$ wave plate in front of a PBS from the polarization analyzer (see Fig. 2.10). Its setting has a crucial impact on the modulation amplitude (see Chapter 2.2.3). 23–25, 43, 44, 48, 49, 51, 57, 59–61, 63, 69, 74, 75, 77, 78, 80, 83, 87, 91, 97, 102, 104–106, 124, 125, 130, 131

Publications

[1] M. Reissig, E. Bründermann, S. Funkner, L. L. Grimm, B. Härer, G. Niehues, J. L. Steinmann, A.-S. Müller, R. Corsini, A. Gilardi, S. Mazzoni, C. Pakuza, A. Schloegelhofer, T. Lefevre, and P. Korysko. *An Electro-Optical Bunch Profile Monitor for FCC-ee*. Preprint. Submitted to Physical Review Accelerators and Beams. 2025. arXiv: 2510.02018 (physics.acc-ph). DOI: 10.48550/arXiv.2510.02018.

[2] M. Reissig, A.-S. Müller, B. Härer, E. Bründermann, G. Niehues, R. Ruprecht, S. Funkner, A. Schloegelhofer, C. Pakuza, R. Corsini, S. Mazzoni, T. Lefevre, A. Gilardi, L. L. Grimm, and P. Korysko. "First Prototype Measurements with an Electro-Optical Bunch Profile Monitor for FCC-ee". In: *Proc. IPAC'25* (Taipei, Taiwan). 16. JACoW Publishing, Geneva, Switzerland, June 2025, pp. 3125–3128. DOI: 10.18429/JACoW-IPAC25-THPS079.

[3] M. Reissig, Akira Mochihashi, Anke-Susanne Müller, Bastian Härer, Erik Bründermann, Gudrun Niehues, Johannes Steinmann, Meghana Patil, Robert Ruprecht, and Stefan Funkner. "Simulations of an Electro-Optical in-Vacuum Bunch Profile Monitor and Measurements at KARA for Use in the FCC-ee". In: *Proc. IPAC'24*. JACoW Publishing, July 2024, 2354–2357 pages. DOI: 10.18429/JACOW-IPAC2024-WEPG56.

[4] M. Reissig, Bastian Härer, Gudrun Niehues, Johannes Steinmann, Marcel Schuh, Akira Mochihashi, Anke-Susanne Müller, Stefan Funkner, Erik Bründermann, and Meghana Patil. "First Two-Bunch Measurements Using the Electro-Optical near-Field Monitor at KARA". In: *Proc. IPAC'23*. JACoW Publishing, Sept. 2023, 4756–4759 pages. DOI: 10.18429/JACOW-IPAC2023-THPL121.

[5] M. Reissig, Miriam Brosi, Erik Bründermann, Stefan Funkner, Bastian Härer, Anke-Susanne Müller, Gudrun Niehues, Meghana Patil, Robert Ruprecht, and Christina Widmann. "Development of an Electro-Optical Longitudinal Bunch Profile Monitor at KARA Towards a Beam Diagnostics Tool for FCC-ee". In: *Proc. IPAC'22*. JACOW Publishing, Geneva, Switzerland, July 2022, pp. 296–299. DOI: 10.18429/JACoW-IPAC2022-MOPOPT025.

[6] M. Reissig, Erik Bründermann, Stefan Funkner, Bastian Härer, Anke-Susanne Müller, Gudrun Niehues, Meghana Patil, Robert Ruprecht, and Christina Widmann. "Status of a Monitor Design for Single-Shot Electro-Optical Bunch Profile Measurements at FCC-ee". In: *Proc. IBIC'22*. JACOW Publishing, Geneva, Switzerland, Dec. 2022, pp. 455–459. DOI: 10.18429/JACoW-IBIC2022-WEP26.

[7] M. Reissig. "Detailed Studies of the Effects of Solenoid Misalignment and Development of Beam-Based Alignment Methods for the FLUTE Injector". MA thesis. Karlsruhe, Germany: Karlsruhe Institute of Technology, Dec. 2020.

[8] M. Benedikt, …, M. Reissig, et al. "Future Circular Collider Feasibility Study Report: Volume 1 Physics, Experiments, Detectors". In: *The European Physical Journal C* 85.12 (Dec. 24, 2025), p. 1468. DOI: 10.1140/epjc/s10052-025-15077-x.

[9] M. Benedikt, …, M. Reissig, et al. "Future Circular Collider Feasibility Study Report: Volume 2 Accelerators, Technical Infrastructure and Safety". In: *The European Physical Journal Special Topics* 234.19 (Dec. 2025), pp. 5713–6197.
DOI: 10.1140/epjs/s11734-025-01967-4.

[10] M. Benedikt, …, M. Reissig, et al. "Future Circular Collider Feasibility Study Report: Volume 3 Civil Engineering, Implementation and Sustainability". In: *The European Physical Journal Special Topics* 234.17 (Nov. 2025), pp. 5113–5383.
DOI: 10.1140/epjs/s11734-025-01958-5.

[11] S. Funkner, A.-S. Müller, A. Malygin, E. Bründermann, F. Donoso, G. Niehues, I. Wilke, J. Steinmann, M. Reissig, M. Nasse, P. Rabiei, R. Ruprecht, and S. Toroghi. "First Measurements of the Transient Electrical Near-Field of Electron Bunches in the FLUTE in-Air Section". In: *Proc. IPAC'26*. Prepress available at https://www.ipac26.org/prepress/pdf/WEP6049.pdf. JACoW Publishing, Geneva, Switzerland, May 2026, pp. 3036–3039.
DOI: 10.18429/JACoW-IPAC2026-WEP6049.

[12] F. Donoso, A.-S. Müller, E. Bründermann, G. Niehues, J. Gethmann, M. Frank, M. Reissig, M. Brosi, P. Schreiber, and S. Funkner. "Phase Space Tomography Constrained by the Vlasov–Fokker–Planck Equation Using EOSD Diagnostics at KARA". In: *Proc. IPAC'26* (Deauville, France, May 17–22, 2026). 17. Prepress available at https://www.ipac26.org/prepress/pdf/WEP5146.pdf. JACoW Publishing, Geneva, Switzerland, May 2026, pp. 2909–2912.
DOI: 10.18429/JACoW-IPAC2026-WEP5146.

[13] F. Donoso, A.-S. Müller, E. Bründermann, M. Frank, M. Reissig, and S. Funkner. "Extended Phase Space Tomography for EOSD Simulation Considering Crystal Geometry Effects". In: *Proc. IPAC'25* (Taipei, Taiwan). 16. JACoW Publishing, Geneva, Switzerland, June 2025, pp. 2818–2821.
DOI: 10.18429/JACoW-IPAC25-THPM063.

[14] C. Goffing, A.-S. Müller, M. Reissig, F. Zimmermann, and J. Keintzel. "Beam-Based Alignment Techniques for the FCC-ee". In: *Proc. IPAC'25* (Taipei, Taiwan). 16. JACoW Publishing, Geneva, Switzerland, June 2025, pp. 571–574.
DOI: 10.18429/JACoW-IPAC25-MOPM109.

[15] S. Mazzoni, A. Boccardi, A. Schloegelhofer, B. Salvachua, C. Zamantzas, D. Butti, M. Gasior, R. Kieffer, T. Lefevre, A. Nosych, L. Torino, U. Iriso, M. Reissig, E. Bründermann, B. Härer, G. Niehues, R. Ruprecht, A.-S. Müller, B. Paroli, E. Howling, M. Potenza, and M. Siano. "Overview of the FCC-ee Beam Instrumentation R&D". In: *Proc. IBIC2024* (Beijing, China). 13. JACoW Publishing, Geneva, Switzerland, Sept. 2024, pp. 1–4.
DOI: 10.18429/JACoW-IBIC2024-TUAC2.

[16] Felipe Donoso, Andrea Santamaria Garcia, Anke-Susanne Müller, Erik Bründermann, Martin Frank, M. Reissig, and Stefan Funkner. "Longitudinal Phase Space Density Tomography Constrained by the Vlasov-Fokker-Planck Equation". In: *Proc. IPAC'24*. JACoW Publishing, July 2024, 2350–2353 pages.
DOI: 10.18429/JACOW-IPAC2024-WEPG55.

[17] Meghana Patil, Anke-Susanne Müller, Christina Widmann, Erik Bründermann, Gudrun Niehues, Johannes Steinmann, Leander Grimm, M. Reissig, Michele Caselle, and Stefan Funkner. "Electro-Optical Spectral Decoding of THz Pulses at MHz Repetition Rates". In: *Proc. IPAC'24*. JACoW Publishing, July 2024, 2347–2349 pages.
DOI: 10.18429/JACOW-IPAC2024-WEPG54.

[18] Stefano Mazzoni, Andriy Nosych, Marco Potenza, Manfred Wendt, Ubaldo Iriso, Andreas Schloegelhofer, Thibaut Lefevre, Bruno Paroli, Georges Trad, Daniele Butti, M. Reissig, Bastian Härer, Gudrun Niehues, Anke-Susanne Müller, Mirko Siano, Laura Torino, and Emily Howling. "CERN's Beam Instrumentation R&D Study for FCC-ee". In: *Proc. IPAC'23*. JACoW Publishing, Sept. 2023, 4653–4656 pages.
DOI: 10.18429/JACOW-IPAC2023-THPL088.

[19] Manfred Wendt, Emanuela Carideo, Bastian Härer, Ubaldo Iriso, Thibaut Lefèvre, Stefano Mazzoni, Toshiyuki Mitsuhashi, Anke-Susanne Müller, Gudrun Niehues, M. Reissig, Andreas Schloegelhofer, and Mirko Siano. "Beam Instrumentation Challenges for FCC-ee". In: *Proc. eeFACT'22*. JACOW Publishing, Geneva, Switzerland, Feb. 2022, pp. 208–217.
DOI: 10.18429/JACoW-eeFACT2022-WEZAS0203.

[20] Meghana Patil, Erik Bründermann, Michele Caselle, Suren Chilingaryan, Timo Dritschler, Andreas Ebersoldt, Stefan Funkner, Andreas Kopmann, Anke-Susanne Müller, Michael Nasse, Gudrun Niehues, M. Reissig, Johannes Steinmann, Marc Weber, and Christina Widmann. "Ultra-Fast Line-Camera KALYPSO for fs-Laser-Based Electron Beam Diagnostics". In: *Proc. IBIC'21*. Vol. IBIC'21. JACoW Publishing, Geneva, Switzerland, 2021, Re of Korea.
DOI: 10.18429/JACOW-IBIC2021-MOOB01.

Bibliography

[21] Helmut Wiedemann. *Particle Accelerator Physics*. eng. 4th ed. Graduate texts in Physics. Cham, Springer, 2015. ISBN: 978-3-319-18316-9.
DOI: 10.1007/978-3-319-18317-6.

[22] *Proceedings of the 2018 CERN-Accelerator-School course on Beam Instrumentation*. 2020.
URL: https://cas.web.cern.ch/previous-schools.

[23] R. W. Assmann et al. "EuPRAXIA Conceptual Design Report". en. In: *The European Physical Journal Special Topics* 229.24 (Dec. 2020), pp. 3675–4284. ISSN: 1951-6355, 1951-6401.
DOI: 10.1140/epjst/e2020-000127-8.

[24] Allan Gillespie. "Bunch Length Diagnostics: Current Status and Future Directions". In: *Proceedings of the 2018 CERN-Accelerator-School course on Beam Instrumentation*. arXiv, 2020, pp. 305–317.
DOI: 10.48550/ARXIV.2005.05715.

[25] M. Benedikt, A. Blondel, O. Brunner, P. Janot, E. Jensen, M. Koratzinos, R. Losito, K. Oide, T. Raubenheimer, and F. Zimmermann. "The FCC-ee R&D programme". en. In: *European Strategy for Particle Physics - Accelerator R&D Roadmap*. CERN Yellow Reports: Monographs, 229 Pages.
DOI: 10.23731/CYRM-2022-001.229.

[26] Bernd Richard Steffen. "Electro-optic methods for longitudinal bunch diagnostics at FLASH". PhD Thesis. Universität Hamburg, 2007.

[27] Nicole Hiller. "Electro-Optical Bunch Length Measurements at the ANKA Storage Ring". en. PhD thesis. Karlsruhe Institute of Technology, 2013.
DOI: 10.5445/IR/1000041159.

[28] I. Wilke, A. M. MacLeod, W. A. Gillespie, G. Berden, G. M. H. Knippels, and A. F. G. van der Meer. "Single-Shot Electron-Beam Bunch Length Measurements". In: *Physical Review Letters* 88.12 (Mar. 2002), p. 124801.
DOI: 10.1103/physrevlett.88.124801.

[29] B. Steffen, Ch Gerth, M. Caselle, M. Felber, T. Kozak, D. R. Makowski, U. Mavrič, A. Mielczarek, P. Peier, K. Przygoda, and L. Rota. "Compact single-shot electro-optic detection system for THz pulses with femtosecond time resolution at MHz repetition rates". In: *Review of Scientific Instruments* 91.4 (Apr. 2020), p. 045123.
DOI: 10.1063/1.5142833.

[30] Eléonore Roussel, Christophe Szwaj, Clément Evain, Bernd Steffen, Christopher Gerth, Bahram Jalali, and Serge Bielawski. "Phase Diversity Electro-optic Sampling: A new approach to single-shot terahertz waveform recording". en. In: *Light: Science & Applications* 11.1 (Jan. 2022), p. 14. ISSN: 2047-7538.
DOI: 10.1038/s41377-021-00696-2.

[31] Quentin Demazeux, Christophe Szwaj, Eléonore Roussel, Bernd Steffen, Marie-Kristin Czwalinna, and Serge Bielawski. "Single-Shot electro-optic detection of broadband THz at EuXFEL and FLASH using diversity scheme with advanced reconstruction algorithms". In: *2025 50th International Conference on Infrared, Millimeter, and Terahertz Waves (IRMMW-THz)*. Helsinki, Finland: IEEE, Aug. 2025, pp. 1–2. ISBN: 979-8-3503-7883-2.
DOI: 10.1109/IRMMW-THz61557.2025.11319759.

[32] Norman, Samuel, Pakuza, Collette, Graham, Darren, Walsh, David, Hibberd, Morgan, and Lefevre, Thibaut. "Fibre-Coupled Oscillator-Driven Electro-Optic Spectral Interferometry as a Longitudinal Bunch Profile Monitor". en. In: (Jan. 2026). Ed. by Kumar,Narender, Apsimon,Robert, Chanwattana,Thankonwat, Chen,Zhichu, Im,Eunhoon, Kwon,Jangwon, Patel,Milaan, Schaa,Volker RW, Thomson,Jana, Wilson,Bradley, and Zhang,Hao, 707–710 pages. ISSN: 2673-5350.
DOI: 10.18429/JACOW-IBIC2025-WEPCO40.

[33] N Hiller and E Huttel. "A Setup for Single Shot Electro Optical Bunch Length Measurements at the ANKA Storage Ring". en. In: *Proc. IPAC'24*. 2011, p. 3.

[34] Patrik Schönfeldt. "Simulation and measurement of the dynamics of ultra-short electron bunch profiles for the generation of coherent THz radiation". PhD thesis. IBPT, 2018.

[35] Stefan Funkner, Edmund Blomley, Erik Bründermann, Michele Caselle, Nicole Hiller, Michael J. Nasse, Gudrun Niehues, Lorenzo Rota, Patrik Schönfeldt, Sophie Walther, Marc Weber, and Anke-Susanne Müller. "High throughput data streaming of individual longitudinal electron bunch profiles". In: *Physical Review Accelerators and Beams* 22.2 (Feb. 2019), p. 022801.
DOI: 10.1103/physrevaccelbeams.22.022801.

[36] CERN Yellow Reports: Monographs. *CERN Yellow Reports: Monographs, Vol. 1 (2022): European Strategy for Particle Physics - Accelerator R&D Roadmap*. en. Mar. 2022.
DOI: 10.23731/CYRM-2022-001.

[37] A. Abada et al. "FCC Physics Opportunities". In: *The European Physical Journal C* 79.6 (June 2019).
DOI: 10.1140/epjc/s10052-019-6904-3.

[38] A. Abada et al. "FCC-ee: The Lepton Collider". en. In: *The European Physical Journal Special Topics* 228.2 (June 2019), pp. 261–623. ISSN: 1951-6401.
DOI: 10.1140/epjst/e2019-900045-4.

[39] A. Abada et al. "FCC-hh: The Hadron Collider". en. In: *The European Physical Journal Special Topics* 228.4 (July 2019), pp. 755–1107. ISSN: 1951-6401.
DOI: 10.1140/epjst/e2019-900087-0.

[40] Andreas Schloegelhofer. "Cherenkov diffraction radiation in beam diagnostics - investigation of a potential tool for FCC-ee". PhD thesis. Vienna, Tech. U., 2020.
URL: https://cds.cern.ch/record/2750140.

[41] Klaus Wille. *Physik der Teilchenbeschleuniger und Synchrotronstrahlungsquellen*. Vieweg+Teubner Verlag, 1992.
DOI: 10.1007/978-3-663-11850-3.

[42] Frank Tecker. *Longitudinal Beam Dynamics in Circular Accelerators*. Nov. 2020. arXiv: 2011.02932 (physics).
DOI: 10.48550/arXiv.2011.02932.

[43] Patrick Schreiber. "Negative Momentum Compaction Operation and its Effect on the Beam Dynamics at the Accelerator Test Facility KARA". de. PhD thesis. Karlsruhe Institute of Technology, 2022.
DOI: 10.5445/IR/1000148354.

[44] John David Jackson. *Klassische Elektrodynamik:* DE GRUYTER, Dec. 2013. ISBN: 978-3-11-033446-3.
DOI: 10.1515/9783110334470.

[45] Alexander Wu Chao, Karl Hubert Mess, Maury Tigner, and Frank Zimmermann. *Handbook of Accelerator Physics and Engineering*. WORLD SCIENTIFIC, May 2012.
DOI: 10.1142/8543.

[46] K. Y. Ng. "Physics of intensity dependent beam instabilities". In: *U.S. particle accelerator school (USPAS 2002)*. Apr. 2002.

[47] Kevin Li. *Collective Effects – an introduction*. Preprint. July 2021. arXiv: 2107.06109 (physics).
DOI: 10.48550/arXiv.2107.06109.

[48] Dassault Systèmes. *CST Studio Suite*. 2024.
URL: https://www.cst.com.

[49] Tomonori Agoh. "Steady fields of coherent synchrotron radiation in a rectangular pipe". In: *Physical Review Special Topics - Accelerators and Beams* 12.9 (Sept. 2009).
DOI: 10.1103/PhysRevSTAB.12.094402.

[50] M. Brosi. "Overview of the Micro-Bunching Instability in Electron Storage Rings and Evolving Diagnostics". In: *Proc. IPAC'21* (Campinas, SP, Brazil). International Particle Accelerator Conference 12. JACoW Publishing, Geneva, Switzerland, Aug. 2021, THXA02, pp. 3686–3691. ISBN: 978-3-95450-214-1.
DOI: 10.18429/JACoW-IPAC2021-THXA02.

[51] JB Murphy, RL Gluckstern, and S Krinsky. "Longitudinal wake field for an electron moving on a circular orbit". In: *Particle Accelerators* 57.BNL-63090 (1996), pp. 9–64.
URL: https://cds.cern.ch/record/1120287/files/p9.pdf.

[52] Philip J. Davis. "Leonhard Euler's Integral: A Historical Profile of the Gamma Function: In Memoriam: Milton Abramowitz". In: *The American Mathematical Monthly* 66.10 (Dec. 1959), p. 849. ISSN: 00029890.
DOI: 10.2307/2309786.

[53] Miriam Brosi, Johannes L. Steinmann, Edmund Blomley, Erik Bründermann, Michele Caselle, Nicole Hiller, Benjamin Kehrer, Yves-Laurent Mathis, Michael J. Nasse, Lorenzo Rota, Manuel Schedler, Patrik Schönfeldt, Marcel Schuh, Markus Schwarz, Marc Weber, and Anke-Susanne Müller. "Fast mapping of terahertz bursting thresholds and characteristics at synchrotron light sources". In: *Physical Review Accelerators and Beams* 19.11 (Nov. 2016), p. 110701.
DOI: 10.1103/PhysRevAccelBeams.19.110701.

[54] A.-S. Muller, I. Birkel, B. Gasharova, E. Huttel, R. Kubat, Y.-L. Mathis, D.A. Moss, W. Mexner, R. Rossmanith, M. Wuensch, P. Wesolowski, F. Perez, M. Pont, and C.J. Hirschmugl. "Far infrared coherent synchrotron edge radiation at ANKA". In: *Proceedings of the 2005 particle accelerator conference*. 2005, pp. 2518–2520.
DOI: 10.1109/PAC.2005.1591164.

[55] Johannes Steinmann, Miriam Brosi, Erik Bründermann, Michele Caselle, Stefan Funkner, Benjamin Kehrer, Anke-Susanne Müller, Michael Nasse, Gudrun Niehues, Lorenzo Rota, Marcel Schuh, Patrik Schönfeldt, Michael Siegel, and Marc Weber. “Turn-by-Turn Measurements for Systematic Investigations of the Micro-Bunching Instability”. en. In: *Proceedings of the 60th ICFA Advanced Beam Dynamics Workshop on Future Light Sources* FLS2018 (2018), China. DOI: 10.18429/JACOW-FLS2018-TUP2WD03.

[56] Benjamin Kehrer. *Time-resolved studies of the micro-bunching instability at KARA*. de. 2019. DOI: 10.5445/IR/1000098584.

[57] Tobias Boltz, Miriam Brosi, Bastian Haerer, Patrik Schönfeldt, Patrick Schreiber, Minjie Yan, and Anke-Susanne Müller. *On the Perturbation of Synchrotron Motion in the Micro-Bunching Instability*. Nov. 2022. DOI: 10.48550/arXiv.2211.15086.

[58] Sebastian Maier. “Systematic Studies of the Micro-Bunching Instability with an Additional Corrugated Structure Impedance at KARA”. de. PhD thesis. Karlsruhe Institute of Technology, 2024. DOI: 10.5445/IR/1000171277.

[59] M. Migliorati, M. Behtouei, E. Carideo, A. Rajabi, Y. Zhang, and M. Zobov. “Studies of FCC-ee Single Bunch Instabilities with an Updated Impedance Model”. en. In: *Journal of Physics: Conference Series* 2687.6 (Jan. 2024). ISSN: 1742-6596. DOI: 10.1088/1742-6596/2687/6/062010.

[60] Erik Brundermann, Heinz-Wilhelm Hubers, and M. F. Kimmitt. *Terahertz techniques*. Springer series in optical sciences 151. Heidelberg ; New York: Springer, 2010. ISBN: 978-3-642-02591-4.

[61] Stefan Funkner, Gudrun Niehues, Michael J. Nasse, Erik Bründermann, Michele Caselle, Benjamin Kehrer, Lorenzo Rota, Patrik Schönfeldt, Marcel Schuh, Bernd Steffen, Johannes L. Steinmann, Marc Weber, and Anke-Susanne Müller. “Revealing the dynamics of ultrarelativistic non-equilibrium many-electron systems with phase space tomography”. en. In: *Scientific Reports* 13.1 (Mar. 2023), pp. 1–11. ISSN: 2045-2322. DOI: 10.1038/s41598-023-31196-5.

[62] Bahaa E. A. Saleh and Malvin Carl Teich. “Electro-optics”. English. In: *Fundamentals of photonics*. Third edition. Wiley series in pure and applied optics. Hoboken, NJ : Wiley-Interscience, 2019. ISBN: 0-471-35832-0. URL: https://search.ebscohost.com/login.aspx?direct=true&db=nlebk&db=nlabk&AN=2037047.

[63] Charles Kittel. *Introduction to solid state physics*. eng. 8. ed., [repr.] Hoboken, NJ: Wiley, 2004. ISBN: 978-0-471-41526-8.

[64] S. Casalbuoni, H. Schlarb, B. Schmidt, P. Schmüser, B. Steffen, and A. Winter. “Numerical studies on the electro-optic detection of femtosecond electron bunches”. In: *Physical Review Special Topics - Accelerators and Beams* 11.7 (July 2008), p. 072802. DOI: 10.1103/physrevstab.11.072802.

[65] Walsh, David, Pacey, Thomas, Snedden, Edward, and Okell William. “Demonstration of an electro-optic spectral interferometry longitudinal profile monitor at Clara”. en. In: *IPAC'2023*. Venice, Italy, Sept. 2023, 4855–4858 pages. DOI: 10.18429/JACOW-IPAC2023-THPL171.

[66] R. Paschotta. *Time–bandwidth product*. RP Photonics Encyclopedia. 2008. DOI: 10.61835/bfb.

[67] B. Pradarutti, G. Matthäus, S. Riehemann, G. Notni, S. Nolte, and A. Tünnermann. "Highly efficient terahertz electro-optic sampling by material optimization at 1060 nm". In: *Optics Communications* 281.19 (Oct. 2008), pp. 5031–5035. ISSN: 0030-4018.
DOI: 10.1016/j.optcom.2008.06.055.

[68] Bang Wu, Lei Cao, Qiang Fu, Ping Tan, and Yongqian Xiong. "Comparison of the Detection Performance of Three Nonlinear Crystals for the Electro-optic Sampling of a FEL-THz Source". In: *Proceedings of the 5th Int. Particle Accelerator Conf.* IPAC2014 (2014), Germany.
DOI: 10.18429/JACOW-IPAC2014-THPRO017.

[69] Steven W. Smith. *Digital signal processing: a practical guide for engineers and scientists.* Demystifying technology series. Amsterdam ; Boston: Newnes, 2003. ISBN: 978-0-7506-7444-7.

[70] F. G. Sun, Zhiping Jiang, and X.-C. Zhang. "Analysis of Terahertz Pulse Measurement with a Chirped Probe Beam". In: *Applied Physics Letters* 73.16 (Oct. 1998), pp. 2233–2235. ISSN: 0003-6951.
DOI: 10.1063/1.121685.

[71] Sophie Walther. "Aufbau und Test eines Einzelschuss-Spektrometers für elektro-optische Bunchlängenmessungen am ANKA Speicherring". Bachelor's Thesis. Karlsruhe: Karlsruhe Institute of Technology, 2013.

[72] L. Rota, M. Caselle, E. Bründermann, S. Funkner, Ch. Gerth, B. Kehrer, A. Mielczarek, D. Makowski, A. Mozzanica, A. -S. Müller, M. J. Nasse, G. Niehues, M. Patil, B. Schmitt, P. Schönfeldt, B. Steffen, and M. Weber. "KALYPSO: Linear array detector for high-repetition rate and real-time beam diagnostics". In: *Nuclear Instruments and Methods in Physics Research Section A: Accelerators, Spectrometers, Detectors and Associated Equipment.* Frontier Detectors for Frontier Physics: 14th Pisa Meeting on Advanced Detectors 936 (Aug. 2019), pp. 10–13. ISSN: 0168-9002.
DOI: 10.1016/j.nima.2018.10.093.

[73] Alexander Papash, Edmund Blomley, Miriam Brosi, Julian Gethmann, Benjamin Kehrer, Anke-Susanne Müller, Marcel Schuh, Patrik Schönfeldt, and Johannes Steinmann. "Non-Linear Optics and Low Alpha Operation at the Storage Ring KARA at KIT". en. In: *Proceedings of the 9th Int. Particle Accelerator Conf.* IPAC2018 (2018). Ed. by Satogata Todd (Ed.) and Schaa RW (Ed.) Volker, 4 pages, 0.776 MB.
DOI: 10.18429/JACOW-IPAC2018-THPMF070.

[74] Alexander Papash, Miriam Brosi, Erhard Huttel, Akira Mochihashi, Anke-Susanne Müller, Robert Ruprecht, Patrick Schreiber, Marcel Schuh, and Nigel Smale. "Different Operation Regimes at the KIT Storage Ring KARA (Karlsruhe Research Accelerator)". en. In: *Proc. IPAC'21.* JACOW Publishing, Geneva, Switzerland, Aug. 2021, pp. 163–166. ISBN: 978-3-95450-214-1.
DOI: 10.18429/JACoW-IPAC2021-MOPAB036.

[75] B. Kehrer, M. Brosi, E. Bründermann, S. Funkner, M.J. Nasse, G. Niehues, M.M. Patil, J.L. Steinmann, and A.-S. Müller. "Diagnostics of longitudinal bunch instabilities at KARA". en. In: *CERN Yellow Reports: Conference Proceedings* Vol. 9.2020 (2020), pp. 23–27.
DOI: 10.23732/CYRCP-2020-009.137.

[76] Tobias Boltz. "Micro-bunching control at electron storage rings with reinforcement learning". phd. Dissertation, Karlsruhe, Karlsruher Institut für Technologie (KIT), 2021.

[77] Luca Scomparin, Michele Caselle, Andrea Santamaria Garcia, Chenran Xu, Edmund Blomley, Timo Dritschler, Akira Mochihashi, Marcel Schuh, Johannes L Steinmann, Erik Bründermann, Andreas Kopmann, Jürgen Becker, Anke-Susanne Müller, and Marc Weber. "Microsecond-latency feedback at a particle accelerator by online reinforcement learning on hardware". In:

Machine Learning: Science and Technology 7.2 (Apr. 2026), p. 025056. ISSN: 2632-2153.
DOI: 10.1088/2632-2153/ae5b20.

[78] Liang Dong and Bryce Samson. *Fiber lasers: basics, technology, and applications.* eng. Boca Raton London New York: CRC Press, 2017. ISBN: 978-1-4987-2554-5.

[79] G. Herink, B. Jalali, C. Ropers, and D. R. Solli. "Resolving the build-up of femtosecond mode-locking with single-shot spectroscopy at 90 MHz frame rate". en. In: *Nature Photonics* 10.5 (May 2016), pp. 321–326. ISSN: 1749-4893.
DOI: 10.1038/nphoton.2016.38.

[80] F Müller. "Ytterbium Fiber Laser for Electro-Optical Pulse Length Measurements at the Swiss-FEL". en. In: *Proceedings of DIPAC09,* Basel, Switzerland, 2009.
URL: https://accelconf.web.cern.ch/d09/papers/tupd31.pdf.

[81] Müller. "Electro-Optical Bunch Length Measurements at the Swiss Light Source". PhD thesis. Bern, Switzerland: Universität Bern, May 2011.

[82] Swamp Optics. *Grenouille – High-Resolution Spectroscopy.* 2024.
URL: https://www.swampoptics.com/grenouille.html (visited on 05/05/2026).

[83] Thorlabs SAS tech. support. *Private Communication.* Email, Spring 2026.

[84] Tobias Bückle. "Bestimmung der Strahlenergie des ANKA-Speicherring mittels resonanter Elektron-Spin-Depolarisation". de. MA thesis. 2008.
DOI: 10.5445/IR/1000022044.

[85] Edmund Blomley, Anke-Susanne Müller, and Manuel Schedler. "Beam Studies with a New Longitudinal Feedback System at the ANKA Storage Ring". en. In: *Proceedings of the 7th Int. Particle Accelerator Conf.* IPAC2016 (2016). Ed. by Petit-Jean-Genaz Christine (Ed.), Kim Eon (Ed.) Dong, Kim Sook (Ed.) Kyung, Ko Soo (Ed.) In, and Schaa RW (Ed.) Volker, 3 pages.
DOI: 10.18429/JACOW-IPAC2016-WEPOR001.

[86] C. Evain, E. Roussel, M. Le Parquier, C. Szwaj, M.-A. Tordeux, J.-B. Brubach, L. Manceron, P. Roy, and S. Bielawski. "Direct Observation of Spatiotemporal Dynamics of Short Electron Bunches in Storage Rings". en. In: *Physical Review Letters* 118.5 (Feb. 2017), p. 054801. ISSN: 0031-9007, 1079-7114.
DOI: 10.1103/PhysRevLett.118.054801.

[87] B. E. Billinghurst, J. C. Bergstrom, C. Baribeau, T. Batten, T. E. May, J. M. Vogt, and W. A. Wurtz. "Longitudinal bunch dynamics study with coherent synchrotron radiation". en. In: *Physical Review Accelerators and Beams* 19.2 (Feb. 2016), p. 020704. ISSN: 2469-9888.
DOI: 10.1103/PhysRevAccelBeams.19.020704.

[88] B Kehrer, A Borysenko, E Hertle, N Hiller, V Judin, and S Marsching. "Numerical Wakefield Calculations for Electro-optical Measurements". en. In: *Proc. IPAC'23* (Shanghai, China). 2013. ISBN: 978-3-95450-122-9.
URL: https://proceedings.jacow.org/IPAC2013/papers/mopme015.pdf.

[89] David Brewster. "X. On the communication of the structure of doubly refracting crystals to glass, muriate of soda, fluor spar, and other substances, by mechanical compression and dilatation. By David Brewster, LL. D. F. R. S. Lond. and Edin. In a letter addressed to the Right Hon. Sir Joseph Banks, Bart. G. C. B. P. R. S". en. In: *Philosophical Transactions of the Royal Society of London* 106 (Dec. 1816), pp. 156–178. ISSN: 0261-0523, 2053-9223.
DOI: 10.1098/rstl.1816.0011.

[90] Andrzej L. Bajor. “Investigation of stress-induced birefringence in large semiconductor wafers by imaging polarimetry”. In: *Polarization Analysis and Measurement II*. Vol. 2265. SPIE, Sept. 1994, pp. 431–442.
DOI: 10.1117/12.186695.

[91] Collaboration: Authors and Editors of the LB Volumes III/17A-22A-41A1b. “Gallium phosphide (GaP), thermodynamical data, vaporization”. en. In: *Group IV Elements, IV-IV and III-V Compounds. Part b - Electronic, Transport, Optical and Other Properties*. Ed. by O. Madelung, U. Rössler, and M. Schulz. Vol. b. Series Title: Landolt-Börnstein - Group III Condensed Matter. Berlin/Heidelberg: Springer-Verlag, 2002, pp. 1–9. ISBN: 978-3-540-42876-3.
DOI: 10.1007/10832182_170.

[92] M. J. Nasse, M. Schuh, S. Naknaimueang, M. Schwarz, A. Plech, Y.-L. Mathis, R. Rossmanith, P. Wesolowski, E. Huttel, M. Schmelling, and A.-S. Müller. “FLUTE: A versatile linac-based THz source”. en. In: *Review of Scientific Instruments* 84.2 (Feb. 2013), p. 022705. ISSN: 0034-6748, 1089-7623.
DOI: 10.1063/1.4790431.

[93] Nasse,Michael, Smale,Nigel, Nabinger,Matthias, Malygin,Anton, Schmelzer,Thiemo, Schaefer,Jens, Schuh,Marcel, Ruprecht,Robert, Blomley,Edmund, Gethmann,Julian, Bernhard,Axel, Wesolowski,Pawel, El Khechen,Dima, Mexner,Wolfgang, Steinmann,Johannes, Xu,Chenran, Santamaria Garcia,Andrea, Brosi,Miriam, Bründermann,Erik, and Mueller,Anke-Susanne. “First THz light generated in high energy section of FLUTE”. en. In: (Nov. 2025). Ed. by Lin,Ming-Chyuan, Sato,Yoichi, Huang,Jui-Che, Button,David, and Chuang,Ping-Shun, 1186–1188 pages. ISSN: 2673-5490.
DOI: 10.18429/JACOW-IPAC2025-TUPM010.

[94] Minjie Yan, Erik BrÃ¼ndermann, Micha Dehler, Thomas Feurer, Stefan Funkner, Mozhgan Hayati, Nicole Hiller, Rasmus Ischebeck, Anke-Susanne Müller, Michael Nasse, Gudrun Niehues, Robert Ruprecht, Manuel Schedler, Volker Schlott, Thiemo Schmelzer, Marcel Schuh, Markus Schwarz, and Bennie Smit. “Design of a Time-resolved Electron Diagnostics Using THz Fields Excited in a Split Ring Resonator at FLUTE”. en. In: *Proceedings of the 5th Int. Beam Instrumentation Conf.* IBIC2016 (2017). Ed. by Costa Isidre (Ed.), Iriso Ubaldo (Ed.), Pérez Francis (Ed.), and Schaa RW (Ed.) Volker, 4 pages.
DOI: 10.18429/JACOW-IBIC2016-TUPG56.

[95] Jens Schäfer. “Feasibility studies for a Transverse Deflecting Structure measurement at FLUTE”. en. PhD thesis. Karlsruher Institut für Technologie (KIT), 2024.
DOI: 10.5445/IR/1000170357.

[96] Nabinger,Matthias, Mueller,Anke-Susanne, Malygin,Anton, Bründermann,Erik, Schaefer,Jens, Steinmann,Johannes, Schuh,Marcel, Noll,Marvin, Fuchs,Matthias, Moser,Matthias, Dehler,Micha, Nasse,Michael, Hayati,Mozhgan, Smale,Nigel, Boine-Frankenheim,Oliver, Ischebeck,Rasmus, Ruprecht,Robert, Glukhov,Sergei, Schmelzer,Thiemo, Feurer,Thomas, Schlott,Volker, and Ollmann,Zoltan. “Terahertz streaking detection for longitudinal bunch diagnostics at FLUTE”. en. In: (Nov. 2025). Ed. by Lin,Ming-Chyuan, Sato,Yoichi, Huang,Jui-Che, Button,David, and Chuang,Ping-Shun, 2822–2825 pages. ISSN: 2673-5490.
DOI: 10.18429/JACOW-IPAC2025-THPM064.

[97] Andrii Borysenko, Edmund Hertle, Nicole Hiller, Vitali Judin, Benjamin Kehrer, Sebastian Marsching, Anke-Susanne Müller, Michael Nasse, Robert Rossmanith, Robert Ruprecht, Marcel Schuh, Markus Schwarz, Bernd Steffen, and Pawel Wesolowski. “Electro-optical Bunch Length Monitor for FLUTE: Layout and Simulations”. en. In: *Proceedings of the 5th Int. Particle Accelerator Conf.* IPAC2014 (2014). Ed. by Petit-Jean-Genaz Christine (Ed.), Arduini Gianluigi (Ed.), Michel

Peter (Ed.), and Schaa RW (Ed.) Volker, 3 pages.
DOI: 10.18429/JACOW-IPAC2014-THPME123.

[98] M. Schuh et al. “RF bunch compression studies for FLUTE”. In: *Proc. IPAC'13.* JACoW Publishing, Geneva, Switzerland, 2013, pp. 2144–2146.
URL: https://jacow.org/IPAC2013/papers/WEPWA009.pdf.

[99] Yuancun Nie, Axel Bernhard, Erik Bründermann, Anke-Susanne Müller, Michael Nasse, Robert Ruprecht, Jens Schäfer, Marcel Schuh, and Yimin Tong. “Full Characterization of the Bunch-Compressor Dipoles for FLUTE”. en. In: *Proceedings of the 12th International Particle Accelerator Conference* IPAC2021 (2021). Ed. by Lin Liu (Ed.), Byrd M. (Ed.) John, Regis Neuenschwander (Ed.), Picoreti Renan (Ed.), and Schaa W. (Ed.) Volker R., 4 pages. ISSN: 2673-5490.
DOI: 10.18429/JACOW-IPAC2021-TUPAB087.

[100] PICMG. *MicroTCA – Open Standard.* 2024.
URL: https://www.picmg.org/openstandards/microtca/ (visited on 04/08/2026).

[101] Sadao Adachi. “Optical dispersion relations for GaP, GaAs, GaSb, InP, InAs, InSb, AlxGa1-xAs, and In1-xGaxAsyP1-y”. In: *Journal of Applied Physics* 66.12 (Dec. 1989), pp. 6030–6040.
DOI: 10.1063/1.343580.

[102] M. Hoek, E.D. Bennet, D. Branford, E.N. Cowie, M. Düren, K. Föhl, D. Glazier, R. Kaiser, A. Lehmann, S. Lu, J. Marton, R. Ostendorf, G. Schepers, C. Schwarz, B. Seitz, A. Teufel, and D. Watts. “Radiation hardness study on fused silica”. en. In: *Nuclear Instruments and Methods in Physics Research Section A: Accelerators, Spectrometers, Detectors and Associated Equipment* 595.1 (Sept. 2008), pp. 190–193. ISSN: 01689002.
DOI: 10.1016/j.nima.2008.07.098.

[103] D. Gamba, R. Corsini, S. Curt, S. Doebert, W. Farabolini, G. Mcmonagle, P.K. Skowronski, F. Tecker, S. Zeeshan, E. Adli, C.A. Lindstrøm, A. Ross, and L.M. Wroe. “The CLEAR User Facility at CERN”. In: *Nuclear Instruments and Methods in Physics Research Section A: Accelerators, Spectrometers, Detectors and Associated Equipment* 909 (2018), pp. 480–483. ISSN: 0168-9002.
DOI: 10.1016/j.nima.2017.11.080.

[104] Kyrre Sjobak et al. “Status of the CLEAR Electron Beam User Facility at CERN”. In: *Proceedings of the 10th International Particle Accelerator Conference* IPAC2019 (2019). Ed. by Boland Mark (Ed.), Tanaka Hitoshi (Ed.), Button David (Ed.), Dowd Rohan (Ed.), Schaa RW (Ed.) Volker, and Tan Eugene (Ed.), 4 pages, 0.190 MB.
DOI: 10.18429/JACOW-IPAC2019-MOPTS054.

[105] Edu Granados, Eric Chevallay, Valentine Fedosseev, and Harsha Panuganti. *Capabilities and Performance of the CLEAR Facility Photo-Injector.* 2020.
DOI: 10.17181/CERN.KPD2.MM9H. Pre-published.

[106] E. Treacy. “Optical Pulse Compression with Diffraction Gratings”. In: *IEEE Journal of Quantum Electronics* 5.9 (Sept. 1969), pp. 454–458. ISSN: 0018-9197, 1558-1713.
DOI: 10.1109/JQE.1969.1076303.

[107] Max Born, Emil Wolf, and Peter Knight. *Principles of Optics.* Seventh anniversary edition, 60th anniversary of first edition, 20th anniversary of seventh edition. Cambridge: Cambridge University Press, 2019. 1 p. ISBN: 978-1-108-47743-7.
DOI: 10.1017/9781108769914.

[108] Oliver Werzer, Stefan Kowarik, Fabian Gasser, Zhang Jiang, Joseph Strzalka, Christopher Nicklin, and Roland Resel. “X-Ray Diffraction under Grazing Incidence Conditions”. In: *Nature Reviews Methods Primers* 4.1 (Feb. 29, 2024), p. 15. ISSN: 2662-8449.
DOI: 10.1038/s43586-024-00293-8.

[109] Sergey A. Stepanov. *X0h X-Ray Server.*
URL: https://x-server.gmca.aps.anl.gov (visited on 06/29/2023).

[110] Sergey A. Stepanov. "X-Ray Server: An Online Resource for Simulations of x-Ray Diffraction and Scattering". In: Optical Science and Technology, the SPIE 49th Annual Meeting. Ed. by Manuel Sanchez Del Rio. Denver, CO, Oct. 21, 2004, pp. 16–26.
DOI: 10.1117/12.557549.

[111] Prabin Dulal, Madan K. Mainali, Suresh Chaulagain, Bishal Shrestha, Emily Amonette, Ambalanath Shan, and Nikolas J. Podraza. "Optical Properties of Fused Silica Glass Using Spectroscopic Ellipsometry from 0.4 meV to 8.5 eV". In: *Surface Science Spectra* 32.2 (Dec. 1, 2025), p. 026001. ISSN: 1055-5269, 1520-8575.
DOI: 10.1116/6.0004538.

[112] M. Naftaly and R.E. Miles. "Terahertz Time-Domain Spectroscopy: A New Tool for the Study of Glasses in the Far Infrared". In: *Journal of Non-Crystalline Solids* 351.40–42 (Oct. 2005), pp. 3341–3346. ISSN: 00223093.
DOI: 10.1016/j.jnoncrysol.2005.08.003.

[113] Andreas Schlögelhofer. "Non-invasive beam diagnostic development for FCC using Cherenkov diffraction radiation in dielectric materials". en. Thesis. Technische Universität Wien, 2024.
DOI: 10.34726/hss.2024.96000.

[114] V L Ginzburg. "Transition Radiation and Transition Scattering". In: *Physica Scripta* T2A (Jan. 1, 1982), pp. 182–191. ISSN: 0031-8949, 1402-4896.
DOI: 10.1088/0031-8949/1982/T2A/024.

[115] U. Happek, A. J. Sievers, and E. B. Blum. "Observation of Coherent Transition Radiation". In: *Physical Review Letters* 67.21 (Nov. 18, 1991), pp. 2962–2965. ISSN: 0031-9007.
DOI: 10.1103/PhysRevLett.67.2962.

[116] A. Murokh, J.B. Rosenzweig, M. Hogan, H. Suk, G. Travish, and U. Happek. "Bunch Length Measurement of Picosecond Electron Beams from a Photoinjector Using Coherent Transition Radiation". In: *Nuclear Instruments and Methods in Physics Research Section A: Accelerators, Spectrometers, Detectors and Associated Equipment* 410.3 (June 1998), pp. 452–460. ISSN: 01689002.
DOI: 10.1016/S0168-9002(98)00177-6.

[117] P. Muggli, M.J. Hogan, C.D. Barnes, D. Walz, P. Krejcik, R.H. Siemann, H. Schlarb, and R. Ischebek. "Coherent Transition Radiation to Measure the SLAC Electron Bunch Length". In: *Proceedings of the 2005 Particle Accelerator Conference.* 2005 Particle Accelerator Conference. Knoxville, TN, USA: IEEE, 2005, pp. 4102–4104. ISBN: 978-0-7803-8859-8.
DOI: 10.1109/PAC.2005.1591731.

[118] W.S.C. Chang. *RF Photonic Technology in Optical Fiber Links.* Cambridge University Press, 2007. ISBN: 978-1-139-43968-8.
URL: https://books.google.de/books?id=Wc-v38fblRIC.

[119] Korysko,Pierre, Malyzhenkov,Alexander, Gilardi,Antonio, Aksoy,Avni, Robertson,C., Granados,Eduardo, Najmudin,I., Wroe,Laurence, Martinez-Calderon,Miguel, Corsini,Roberto, Rieker,Vilde, and Farabolini,Wilfrid. "Operational Improvements and Upgrades of the CLEAR User Facility". In: (Oct. 23, 2024). Ed. by Jaje,Kelly, Bishofberger,Kip, Brody,Ryan, Bruno,Gustavo, Chrin,Jan, Eyberger,Cathy, Montes,Maggie, Skiadopoulos,Denise, Wang,Ling, and Wootton,Kent, 670–673 pages, 0.88 MB. ISSN: 2226-0366.
DOI: 10.18429/JACOW-LINAC2024-THPB017.

[120] Andreas Schloegelhofer. *Private Communication.* Conversation, Spring 2024.

[121] M.M. Patil, M. Caselle, E. Bründermann, S. Chilingarayan, A. Kopmann, G. Niehues, J.L. Steinmann, S. Stankov, C. Widmann, A.-S. Müller, G. Borghi, G. Paternoster, M. Centis Vignali, and M. Boscardin. "KALYPSO LGAD — a MHz repetition rate line camera based on trench isolated low gain avalanche detector". en. In: *Journal of Instrumentation* 20.01 (Jan. 2025), p. C01006. ISSN: 1748-0221.
DOI: 10.1088/1748-0221/20/01/C01006.

Acknowledgments

Funding

I acknowledge the support by the Doctoral School „Karlsruhe School of Elementary and Astroparticle Physics: Science and Technology“. This project has received funding from the European Union’s Horizon 2020 research and innovation programme under grant agreement No 951754.

AI tools

The KI-Toolbox[1] (KIT-hosted model GPT-OSS-120b) has been used in this thesis for occasional code and text refinement.

People

This thesis was made possible by the motivation, support and knowledge of many people in many different ways. I am very grateful for all the help that I received, which enabled me to overcome the challenges along the way, and kept me motivated to continue this project.

I would like to thank Prof. Anke-Susanne Müller for enabling this thesis and for her contagious enjoyment of accelerator physics. I always left our meetings with new ideas and motivation to continue with the project.

Thanks to Prof. Günter Quast for accepting the role as co-referent for my thesis and for the positive and fruitful discussions.

A big thank you goes to Gudrun Niehues, who introduced me to the world of electro-optical beam diagnostics and helped me on an almost daily basis with many minor and major challenges along the way. She kept asking the right questions and provided support and good advice for any situation. I would like to thank Bastian Härer, whose support and motivation led me to start my journey in accelerator physics at IBPT during my master’s thesis and who continued to support and motivate me during my doctoral thesis.

I received great support from my colleagues at IBPT, with many fruitful discussions while ingesting lots of coffee. I would like to thank Robert Ruprecht, Marcel Schuh and Matthias Fuchs for helping me navigate through the administration at KIT and for providing advice to get me started in the world of scientific research. Many thanks to Erik Bründermann, whose extensive knowledge of beam diagnostics and THz-related topics led to many important discussions that started the initial idea of the prism-based EO monitor design for FCC-ee.

During my countless hours in the EO laboratory, I am grateful for the support of Meghana Patil, who helped me during my first measurements with lots of patience and provided immediate support when

[1] https://ki-toolbox.scc.kit.edu/

issues occurred. I also want to thank Stefan Funkner, who was always interested to go deep into discussions and helped to advance the project by asking the right questions.

Running an accelerator like FLUTE and KARA requires lots of knowledge and problem solving of many different systems, and I would like to thank Edmund Blomley for always being supportive and fast to respond, if issues with the control system occurred. I would like to thank Akira Mochihashi for many electron beam injections for my measurements at KARA and Anton Malygin for operating FLUTE during very long measurement days. I would like to thank Johannes Steinmann for making things work with any kind of electronics-related issues.

The exchange with other doctoral students was an important factor for me to discuss new ideas, administrative difficulties, or specific problems that occurred. Most importantly, these discussions never failed to find the humorous side of things. Particularly, I would like to thank Marvin Noll, Jens Schäfer, Felipe Donoso, Matthias Nabinger and Sebastian Maier.

I would like to thank Ling Leander Grimm, Thariq Muhammad and Denis Stiben, who supported me as students in the lab and who helped me improve my understanding of many things by having me explain the details of the experimental setup.

Special thanks go to the people behind the scenes like Steffen Schott and Till Borkowski, who helped designing, specifying and ordering needed hardware; Jürgen Schmid, Andreas Völker and Michael Bank for the installation of the experimental setup and its required infrastructure and Ralf Lang for quickly building missing parts. I am grateful for the support and patience of Deniz Birli, Claudia Lieber, Anne Stößer and Kyra Ohlenschläger with any administrative or organisational issues and questions.

During many workshops, conferences and external experiments, I am grateful to have received support from many more people, who brought new perspectives and additional knowledge. In particular, I want to thank Bernd Steffen, who never hesitated to share his comprehensive knowledge and experience with electro-optical diagnostics and its laser system. A desperate phone call with Bernd usually resulted in newly found motivation and ideas to finally resolve remaining issues. I also want to thank Nicole Hiller, who set the foundation of my thesis by initially building and installing the EO setup at KARA. I would like to thank Svetoslav Stankov, who let me use and introduced me to the X-Ray diffraction device on short notice to measure the lattice orientation of EO crystals.

As the FCC-ee will be hosted at CERN, I got to know many new colleagues during many online meetings, but also during several in person-visits, conferences and two beam times at CLEAR. I am grateful to Thibaut Lefevre, who enabled the close cooperation and took his time to introduce me to the people and facilities at CERN. I had a great time at CLEAR, where successful prototype measurements were only made possible by the many knowledgeable and motivated people. Thus, I would like to thank Pierre Korysko, Antonio Gilardi, Collette Pakuza, Avni Aksoy, Daniele Butti and many more. In particular, I would like to thank Andreas Schlögelhofer, who helped me to quickly solve any issues and provided support during my time at CERN.

I would like to thank Stefano Mazzoni, who tragically passed away in 2025. He was a major driver to enable my experiments at CLEAR and his knowledge, motivation and positive attitude was very inspiring and will be kept in good memory.

Thank you all!

Zum Schluss möchte ich mich bei meiner Familie und meinen Freunden bedanken, die mich durchgängig unterstützt haben, und damit diese Arbeit ermöglicht haben. Insbesondere möchte ich Carl danken, der mich mit seinem ehrlichen Interesse immer wieder motivierte weiter zu machen und gleichzeitig in meiner Freizeit für Ausgleich sorgte. Außerdem möchte ich meinem Bruder und meinen Eltern für ihre durchgängige Unterstützung danken, ohne die ich vermutlich nie diesen Weg eingeschlagen hätte. Ich möchte meiner Frau danken, die mich stets unterstützte und den Rücken frei hielt. Ich bin dankbar für ihre stetige Motivation, obwohl die intensiven Abschnitte meiner Arbeit für sie mindestens ebensoviel Stress bedeuteten wie für mich. Zum Schluss möchte ich meinem Sohn Aron danken, der mich auch zu anstrengenden Zeiten stets zum Lachen und auf andere Gedanken gebracht hat.